

DRONE SUPPORTED PRE-SCAN OPTIMAL ACTIVE SUSPENSION FOR 8X8
VEHICLE

A THESIS SUBMITTED TO
THE GRADUATE SCHOOL OF NATURAL AND APPLIED SCIENCES
OF
MIDDLE EAST TECHNICAL UNIVERSITY

BY

ALPAY SANCAR

IN PARTIAL FULFILLMENT OF THE REQUIREMENTS
FOR
THE DEGREE OF MASTER OF SCIENCE
IN
AEROSPACE ENGINEERING

JUNE 2018

Approval of the thesis:

**DRONE SUPPORTED PRE-SCAN OPTIMAL ACTIVE SUSPENSION FOR 8X8
VEHICLE**

submitted by **ALPAY SANCAR** in partial fulfillment of the requirements for the degree of **Master of Science in Aerospace Engineering Department, Middle East Technical University** by,

Prof. Dr. Halil Kalipçılar
Dean, Graduate School of **Natural and Applied Sciences**

Prof. Dr. Ozan Tekinalp
Head of Department, **Aerospace Engineering**

Assist. Prof. Dr. Ali Türker Kutay
Supervisor, **Aerospace Engineering Department, METU**

Examining Committee Members:

Prof. Dr. Ozan Tekinalp
Aerospace Engineering Department, METU

Assist. Prof. Dr. Ali Türker Kutay
Aerospace Engineering Department, METU

Assoc. Prof. Dr. İlkey Yavrucuk
Aerospace Engineering Department, METU

Assoc. Prof. Dr. Melin Şahin
Aerospace Engineering Department, METU

Prof. Dr. Metin Uymaz Salamcı
Mechanical Engineering Department, Gazi University

Date:

I hereby declare that all information in this document has been obtained and presented in accordance with academic rules and ethical conduct. I also declare that, as required by these rules and conduct, I have fully cited and referenced all material and results that are not original to this work.

Name, Last Name: ALPAY SANCAR

Signature :

ABSTRACT

DRONE SUPPORTED PRE-SCAN OPTIMAL ACTIVE SUSPENSION FOR 8X8 VEHICLE

Sancar, Alpay

M.S., Department of Aerospace Engineering

Supervisor : Assist. Prof. Dr. Ali Türker Kutay

June 2018, 194 pages

In today's world, the number and the usage area of the drones are getting increased rapidly from day to day. On the other hand, despite the fact that air vehicles will probably shape the future, the ground vehicles also will stay essential at least as much as today. In this study, these two separated systems; the drone and the 8x8 land vehicle are considered to work together to solve a problem; personnel comfort for the drastic terrain conditions. A simulation, which includes a quadrotor, which is carrying a laser system for road scanning and a 8x8 full car model with an active suspension system, is created. The study starts with the modeling and simulation of the quadrotor and then continues with the modeling and simulation of the 8x8 vehicle model. For each model, developing the related control theories are the third step and the final step is integration of the models in a simulation world and generation of the scenarios in order to evaluate the advantages and disadvantages of co-working drone and vehicle system. The 8x8 vehicle is considered to use the road distribution information, which comes from the drone that is flying in front of the vehicle and commanded by the vehicle. On the other hand, the active suspension of the vehicle is optimized by the information provided by the drone.

Keywords: Active Suspension, Full Car Modeling, Quadrotor Modeling, Optimal Control, Laser Road Scanning

ÖZ

8X8 ARAÇLAR İÇİN İHA DESTEKLİ ÖNCE DEN YOL TARAMALI OPTİMAL AKTİF SÜSPANSİYON SİSTEMİ

Sancar, Alpay

Yüksek Lisans, Havacılık ve Uzay Mühendisliği Bölümü

Tez Yöneticisi : Dr. Öğr. Üyesi Ali Türker Kutay

Haziran 2018 , 194 sayfa

Bugünün dünyasında insansız hava araçlarının sayısı hızlı bir şekilde günden güne artmaya devam etmektedir. Hava araçlarının geleceği şekillendirecek olma ihtimaline rağmen kara araçları da bir çok bakımdan olmazsa olmaz kalmaya devam edeceklerdir. Bu çalışmada, bu iki birbirinden bağımsız sistemin; insansız hava aracının ve 8x8 kara aracının bir problemi çözmek için beraber çalıştığı bir durum incelenmiştir. Problem, zorlu arazi şartlarında personel konforunun sağlanmasındaki güçlüklerdir. Bu problemi çözmek adına, yol taramak için kullanılan bir lazer sistemi taşıyan dört motorlu insansız hava aracını ve aktif süspansiyona sahip 8 tekerli bir kara aracını içeren simülasyon dünyası yaratılmıştır. Çalışma, 4 motorlu insansız hava aracının modellenmesiyle başlamış, 8x8 aracın modellenmesiyle devam etmiştir. 2 sistem için de duruma özel kontrol teorileri çalışılmış ve uygun kontrolcüler geliştirilmiştir. Bir sonraki aşamada ise bütün modeller tek bir dünyada birleştirilmiş ve senaryolar oluşturulmuştur. Farklı senaryolarda insansız hava aracıyla 8x8 kara aracının beraber çalışması durumunun avantajları ve dezavantajları anlaşılmaya çalışılmıştır. 8x8 aracın aktif süspansiyonun insansız hava aracından gelen yol bilgisiyle optimize edilmesi sağlanmıştır. Paralelde de 8x8 aracın insansız hava aracını kendi önünde kendi hareketiyle senkronize bir şekilde kontrol etmesi kurgulanmıştır.

Anahtar Kelimeler: Aktif Süspansiyon, Bütün Araç Modellemesi, 4 Motorlu Hava Aracı Modellemesi, Optimal Kontrol, Laser Yol Taraması

This thesis dedicated to my dearest family and friends for their encouragement and love,

ACKNOWLEDGMENTS

I am deeply grateful to my supervisor, Assist. Prof. Dr. Ali Türker Kutay, for his guidance and constant encouragement throughout the duration of this thesis.

I would like to thank to my family for their endless support, encouragement, and guidance all along the years of my educational life.

Finally, I also express my sincerest thanks to the coffee shops of Ankara where put me up gently and patiently during the thesis writing period.

TABLE OF CONTENTS

ABSTRACT	v
ÖZ	vii
ACKNOWLEDGMENTS	x
TABLE OF CONTENTS	xi
LIST OF TABLES	xvii
LIST OF FIGURES	xx
LIST OF ABBREVIATIONS AND NOTATIONS	xxvi
CHAPTERS	
1 PROBLEM STATEMENT AND OBJECTIVES	1
1.1 Problem Statement	1
1.2 Scope of the Study	4
2 DESIGN AND MATHEMATICAL MODELING OF A DRONE	7
2.1 Introduction	7
2.2 Literature Survey	7
2.3 Payloads of the Quadrotor	10

2.3.1	Mechanical Parts	11
2.3.2	Electronics	12
2.3.3	Optics	16
2.3.4	Payload Weight and Power Summary	23
2.4	Main Components of the Quadrotor	24
2.5	General Characteristics of the Quadrotor	27
2.6	Equations of Motion of the Quadrotor	29
3	CONTROL AND SIMULATION OF THE QUADROTOR	33
3.1	Control of the Quadrotor	33
3.1.1	Control Modeling	33
3.1.2	PID based Control Approach	35
3.2	Simulation of The Quadrotor	35
3.3	Simulation Results	37
4	MATHEMATICAL MODELING OF THE 8X8 FULL VEHICLE	41
4.1	Introduction	41
4.2	Literature Survey	42
4.2.1	Commercial Active Suspension Systems in Auto- motive Industry	44
4.2.2	Vertical Vibration Models	47
4.2.2.1	Half Car Model	47
4.2.2.2	Full Car model	47
4.2.2.3	Quarter Car Model	48

4.3	Mathematical Modeling of The Quarter Car Model	48
4.4	8x8 Full Car model	49
4.4.1	Mathematical Modeling of The 8x8 Full Car	51
4.4.1.1	Assumptions in Modeling	52
4.4.1.2	Equations of Motion	53
4.5	Comparison of the Quarter Car and the 8x8 Full Car Model	57
5	CONTROL AND SIMULATION OF THE VEHICLE	61
5.1	Control of the Vehicle	61
5.1.1	Introduction	61
5.1.2	Literature Survey	61
5.1.3	LQR Optimal Control Method	63
5.1.4	Preview Control Method	76
5.1.5	Frequency Response Comparison	82
5.2	Simulation of the Vehicle	84
6	THE QUADROTOR-VEHICLE INTEGRATED SIMULATION	87
6.1	Introduction	87
6.2	Control and Optimization Logic	88
6.3	Error Conditions	89
6.4	Integrated and Synchronized Motion Simulations	90
7	RESULTS AND DISCUSSIONS	93
7.1	Generation of Road Profiles	93

7.1.1	Road Type 1: H Standard Road	95
7.1.2	Road Type 2: G Standard Road	96
7.1.3	Road Type 3: B Standard Road	97
7.1.4	Road Type 4: Bump Road	98
7.1.5	Road Type 5: Sinusoidal Road Profile	98
7.2	Analyze Scenarios	99
7.3	Vibration Evaluation	101
7.3.1	Time Domain Evaluation	101
7.3.2	Frequency Domain Evaluation	103
7.4	Results	104
7.4.1	Deterministic Results for H Type Road	104
7.4.1.1	Time Domain Results @ 5 km/h . . .	104
7.4.1.2	Frequency Domain Results @ 5 km/h	109
7.4.1.3	Preview and Optimal Suspension Limits for Ideally Known H Type Road . .	109
7.4.2	Stochastic Results for H Type Road @ 20 km/h . .	113
7.4.2.1	Scenario 1:Quadrotor Speed 20 km/h, Range 5 Meters	114
7.4.2.2	Scenario 2: Quadrotor Speed 20 km/h, Range 100 Meters	116
7.4.3	Deterministic Results for G Type Road	119
7.4.3.1	Time Domain Results @ 20 km/h . . .	119
7.4.3.2	Frequency Domain Results @ 20 km/h	123

7.4.3.3	Preview and Optimal Suspension Limits for Ideally Known G Type Road . .	124
7.4.4	Stochastic Results for G Type Road @ 40 km/h . .	128
7.4.4.1	Scenario 1: Quadrotor Speed 40 km/h, Range 5 Meters	128
7.4.4.2	Scenario 2: Quadrotor Speed 40 km/h, Range 100 Meters	130
7.4.5	Deterministic Results for B Type Road	134
7.4.5.1	Time Domain Results @ 80 km/h . . .	134
7.4.5.2	Frequency Domain Results @ 80 km/h	138
7.4.5.3	Preview and Optimal Suspension Limits for Ideally Known B Type Road . .	139
7.4.6	Stochastic Results for B Type Road @ 40 km/h . .	139
7.4.6.1	Scenario 1: Quadrotor Speed 40 km/h, Range 5 Meters	139
7.4.6.2	Scenario 2: Quadrotor Speed 40 km/h, Range 100 Meters	141
7.4.7	Deterministic Results for the Bump Road	145
7.4.7.1	Time Domain Results @ 40 km/h . . .	145
7.4.7.2	Frequency Domain Results @ 40 km/h	149
7.4.8	Stochastic Results for Road the Bump Road @ 40 km/h	149
7.4.8.1	Scenario 1:Quadrotor Speed 40 km/h, Range 5 Meters	150
7.4.8.2	Scenario 2: Speed 40 km/h Range 100 Meters	152

7.4.9	Roll Channel Analysis	154
7.5	Discussions	158
8	CONCLUSION AND FUTURE WORKS	167
8.1	Conclusion	167
8.2	Future Works	168
	REFERENCES	171
APPENDICES		
A	DRONE PART	177
A.1	Motor Technical Specifications	177
A.2	Quadrotor Inertia Calculations	177
B	VEHICLE PART	181
B.1	Actuator Comparison	181
B.2	A Matrix	185

LIST OF TABLES

TABLES

Table 2.1	Comparative Study for the Flying Objects [3]	10
Table 2.2	Mounting and Casing Mass Parameters	12
Table 2.3	System Specifications for the FOG System [5]	13
Table 2.4	System Specifications for the FOG System [5]	14
Table 2.5	System Specifications for the Flight Computer [6]	14
Table 2.6	System Specifications for the GNSS Antenna [7]	15
Table 2.7	System Specifications for the GNSS Heading [8]	16
Table 2.8	Range Measurement Data Riegl VUX-1HA [14]	22
Table 2.9	Technical Data Riegl VUX-1HA [14]	23
Table 2.10	Payload Mass Budget	23
Table 2.11	Payload Power Budget	24
Table 2.12	Characteristics of MN701SKV280 [15]	25
Table 2.13	Propeller Characteristics [15]	25
Table 2.14	Characteristics of the ESC [16]	26
Table 2.15	Battery Pack Characteristics [17]	27
Table 2.16	Total Mass Budget of the Quadrotor	27
Table 2.17	Total Power Budget of the System	28
Table 2.18	Total Battery Capacity	28

Table 3.1	System Parameters Used in MATLAB/Simulink Model	38
Table 4.1	Parameter Symbols and Names	49
Table 4.2	Parameter Symbols and Names	52
Table 4.3	Quarter Car Simulation Input Parameters and Their Values	58
Table 4.4	Full Car Simulation Input Parameters and Their Values	58
Table 5.1	Thomson T13-B5010MU090-04 [47]	71
Table 5.2	Simulation Input Parameters and Their Values	85
Table 7.1	ISO 8608 Road Profile Classification [50]	94
Table 7.2	Comfort Indications in Public Transport [51]	103
Table 7.3	Time Domain Analyzes Results	108
Table 7.4	Time Domain Analyzes Results (Percental)	108
Table 7.5	Frequency Domain Analyzes Results	109
Table 7.6	Time Domain Analyzes Results for 20 km/h	110
Table 7.7	Preview Suspension Absorb Power @20km/h	111
Table 7.8	Time Domain Analyzes Results for 15 km/h for Optimal Suspension	111
Table 7.9	Optimal Suspension Absorb Power @15km/h	112
Table 7.10	Performance Degradation with Scanned Road for 2 Scenarios	119
Table 7.11	Time Domain Analyzes Results	123
Table 7.12	Time Domain Analyzes Results [Percental]	123
Table 7.13	Frequency Domain Analyzes Results	124
Table 7.14	Time Domain Analyzes Results	125
Table 7.15	Preview Suspension Absorb Power @80km/h	126
Table 7.16	Time Domain Analyzes Results	126
Table 7.17	Optimal Suspension Absorb Power @60km/h	128
Table 7.18	Performance Degradation with Scanned Road for 2 Scenarios	133

Table 7.19 Time Domain Analyzes Results	137
Table 7.20 Time Domain Analyzes Results (Percental)	138
Table 7.21 Frequency Domain Analyzes Results	139
Table 7.22 Time Domain Analyzes Results	144
Table 7.23 Performance Degradation with Scanned Road for 2 Scenarios	145
Table 7.24 Time Domain Results for the Bump Road	148
Table 7.25 Time Domain Percental Results for the Bump Road	148
Table 7.26 Frequency Domain Analyzes Results	149
Table 7.27 Time Domain Analyzes Results for Sinusoidal Road	158
Table 7.28 Time Domain Analyzes Results for Sinusoidal Road (Percental)	158
Table 7.29 Vibration Evaluation for the H Type Road	160
Table 7.30 Vibration Evaluation for the G Type Road	162
Table 7.31 Vibration Evaluation for the G Type Road	164
Table A.1 Test Report Table for the Chosen Motor MN701s KV280	177
Table B.1 Actuator Comparison Table [47]	182

LIST OF FIGURES

FIGURES

Figure 1.1 Schematic of Study	3
Figure 2.1 Payload Product Tree	11
Figure 2.2 Typical Anti-Vibration Mount[4]	12
Figure 2.3 Fiber-Optic Gyro IMU [5]	13
Figure 2.4 Resonan Flight Computer [6]	14
Figure 2.5 GNSS Antenna [7]	15
Figure 2.6 GNSS Heading [8]	15
Figure 2.7 Lehmann and Partner Solution [9]	16
Figure 2.8 Pavemetrics Solution [10]	17
Figure 2.9 Phoenix Scientific Solution [11]	17
Figure 2.10 Phase Shift Methodology [12]	18
Figure 2.11 Phase Shift Methodology [12]	19
Figure 2.12 Point Cloud Example [13]	20
Figure 2.13 Road Surface Consisting of Points [13]	20
Figure 2.14 Detailed Road Profile [13]	21
Figure 2.15 Riegl VUX-AH Laser Scanner [14]	21
Figure 2.16 Point Density vs Drone Velocity for Selected Laser Scanner [14]	22
Figure 2.17 MN701s Quadrotor Motor [15]	24
Figure 2.18 CF-Epoxy Propeller [15]	25

Figure 2.19 Selected Electronic Speed Control Unit [16]	26
Figure 2.20 30000 mAh Battery Pack [17]	26
Figure 2.21 Axis and Rotation Labels for (+) Configuration Drone (Right Hand Rule) [18]	29
Figure 3.1 Drone Simulink Model Structure	36
Figure 3.2 Desired X position vs Actual X Position of the Quadrotor	38
Figure 3.3 Desired Y position vs Actual Y Position of the Quadrotor	39
Figure 3.4 Desired Z position vs Actual Z Position of the Quadrotor	39
Figure 4.1 Active Body System Equipment Representation [38]	45
Figure 4.2 Magic Body System [39]	46
Figure 4.3 Hydractive System [40]	47
Figure 4.4 Quarter Car Model Representation	48
Figure 4.5 8x8 Full Car Representation	50
Figure 4.6 8x8 Full Car Representation	51
Figure 4.7 Small Angle Approximation [42]	52
Figure 4.8 Comparison Between Quarter Car Model, Full Car Model and Measured Data [43]	57
Figure 4.9 Full Car and Quarter Car Comparison	59
Figure 5.1 Suspension Systems Control Theories	62
Figure 5.2 State-Feedback Controller Loop	63
Figure 5.3 Thomson T130 High Precision Electromechanical Actuator [47]	71
Figure 5.4 Suspension 1 Travel for selected Q and R Values on the most drastic Road Condition	74
Figure 5.5 Actuator Forces for selected Q and R Values on the most drastic Road Condition	74
Figure 5.6 Preview Sensor Representation	76
Figure 5.7 Road Disturbance Feed Forward Controller Loop	77

Figure 5.8	Frequency Response Function from Road input to Body Acceleration	83
Figure 5.9	Vehicle Simulink Model Structure	84
Figure 6.1	Quadrotor-Vehicle Working Logic	88
Figure 6.2	Self Corrective Navigation Error	89
Figure 6.3	Point Cloud Density Trend w.r.t. Quadrotor Range and Velocity . .	90
Figure 6.4	Complete Model	91
Figure 7.1	ISO 8608 Road Profile Classification [50]	94
Figure 7.2	ISO8608 Stadar Road Type H	95
Figure 7.3	PSD for the H Road	95
Figure 7.4	ISO8608 Stadar Road Type G	96
Figure 7.5	PSD for the Road Type 2	96
Figure 7.6	ISO8608 Stadar Road Type B	97
Figure 7.7	PSD for the Road Type 3	97
Figure 7.8	Bump Road	98
Figure 7.9	Sinusoidal Road PRofile	99
Figure 7.10	Whole body vibration health guidance caution zones [51]	102
Figure 7.11	Road Profile	105
Figure 7.12	Body Displacement	105
Figure 7.13	Body Acceleration	106
Figure 7.14	Pitch Acceleration	106
Figure 7.15	Actuator Forces for selected Q and R Values on H Type Road . . .	107
Figure 7.16	Suspension 1 Travel for selected Q and R Values on H Type Road .	107
Figure 7.17	Absorb Power	109
Figure 7.18	Road profile	110
Figure 7.19	Preview Suspension Absorb Power @20km/h	111

Figure 7.20 Optimal Suspension Absorb Power @15km/h	112
Figure 7.21 Road profile	113
Figure 7.22 Point Cloud Density Trend w.r.t. Quadrotor Range and Velocity . .	113
Figure 7.23 Stochastic Scenario @20km/h	114
Figure 7.24 Point Cloud Density @20km/h	115
Figure 7.25 Ideal Road vs Scanned Road for 20km/h Quadrotor Speed	115
Figure 7.26 Body Acceleration Responses with Ideal Road and Scanned Road .	116
Figure 7.27 Stochastic Scenario 2 @20km/h, 100 meters	117
Figure 7.28 Point Cloud Density @20km/h, Range: 100 meters	117
Figure 7.29 Ideal Road vs Scanned Road for 20km/h Quadrotor Speed and 100 meters range	118
Figure 7.30 Body Acceleration Responses with Ideal Road and Scanned Road for Scenario 2	118
Figure 7.31 G Type Road Profile for 20km/h)	120
Figure 7.32 Body Displacement	120
Figure 7.33 Body Acceleration	121
Figure 7.34 Pitch Acceleration	121
Figure 7.35 Actuator Forces and Limits	122
Figure 7.36 Suspension Travels and Limits	122
Figure 7.37 Absorb Power	124
Figure 7.38 Road Profile	125
Figure 7.39 Preview Suspension Absorb Power @80 km/h	126
Figure 7.40 Road Profile	127
Figure 7.41 Optimal Suspension Absorb Power @60 km/h	127
Figure 7.42 Quad. Range =5 meters and Target Velocity= 40 km/h	129
Figure 7.43 Point Cloud Density for Range =5 meters and Target Velocity= 40 km/h	129

Figure 7.44 Ideal Road vs Scanned Road	130
Figure 7.45 Vertical Acceleration for Ideal Road and Scanned Road	130
Figure 7.46 Quad. Range =100 meters and Target Velocity= 40 km/h	131
Figure 7.47 Point Cloud Density for Range =100 meters and Target Velocity= 40 km/h	132
Figure 7.48 Ideal Road vs Scanned Road for Scenario 2	132
Figure 7.49 Vertical Acceleration for Ideal Road and Scanned Road for Sce- nario 2	133
Figure 7.50 Road Profile for Each Axes (Delay=0.045sc => Vehicle Velocity 80km/h)	134
Figure 7.51 Vertical Displacement for Vehicle Speed= 80 km/h	135
Figure 7.52 Vertical Acceleration for Vehicle Speed=80km/h	135
Figure 7.53 Pitch Acceleration for Vehicle Speed=80km/h	136
Figure 7.54 Actuator Forces and Limits	136
Figure 7.55 Suspension Travels and Limits	137
Figure 7.56 Preview Suspension Absorb Power @80 km/h	138
Figure 7.57 Quad. Range =5 meters and Target Velocity= 40 km/h	140
Figure 7.58 Point Cloud Density for Range =5 meters and Target Velocity= 40 km/h	140
Figure 7.59 Ideal Road vs Scanned Road for Scenario 1	141
Figure 7.60 Vertical Acceleration for Ideal Road and Scanned Road for Sce- nario 1	141
Figure 7.61 Quad. Range =100 meters and Target Velocity= 40 km/h	142
Figure 7.62 Point Cloud Density for Range =100 meters and Target Velocity= 80 km/h	143
Figure 7.63 Ideal Road vs Scanned Road for Scenario 2	143
Figure 7.64 Vertical Acceleration for Ideal Road and Scanned Road for Sce- nario 2	144
Figure 7.65 Bump Road	146

Figure 7.66 40 km/h Vehicle and Quadrotor Velocity - Vertical Body Displacement	146
Figure 7.67 40 km/h Vehicle and Quadrotor Velocity - Vertical Body Acceleration	147
Figure 7.68 40 km/h Vehicle and Quadrotor Velocity - Pitch Acceleration for the Vehicle	147
Figure 7.69 Absorbed Power vs Frequency Bands	149
Figure 7.70 Scenerio 1 Quad. Range=5 meters and Target Velocity=40km/hours	150
Figure 7.71 Cloud Point Density for Scenerio 1 (Quad Range=5 meter, Velocity=40km/h)	151
Figure 7.72 Scanned Road vs Ideal Road for Scenerio 1 (Quad Range=5 meter, Velocity=40km/h)	151
Figure 7.73 Body Displacements for Scanned Road and Ideal Road	152
Figure 7.74 Scenerio 2 Quad. Range=100 meters and Target Velocity=40km/hours	153
Figure 7.75 Cloud Point Density for Scenerio 2 (Quad Range=100 meter, Velocity=40km/h)	153
Figure 7.76 Road Profile with Max. Error vs Zero Error	154
Figure 7.77 Suspension Behavior with Road Profile with Max. Error	154
Figure 7.78 Sinusoidal Road Profile	155
Figure 7.79 Roll Acceleration	155
Figure 7.80 Body Acceleration	156
Figure 7.81 Pitch Acceleration	156
Figure 7.82 Actuator Forces	157
Figure 7.83 Suspension Travel for Tyre 1	157
Figure B.1 T Series Actuator	181
Figure B.2 Definition of Forces	181

LIST OF ABBREVIATIONS AND NOTATIONS

ABBREVIATIONS

COG	Center of Gravity
MOI	Moment of Inertia
PI	Proportional–Integral
PID	Proportional–Integral–Derivative
LQR	Linear–quadratic regulator
UAV	Unmanned Air Vehicles
RAMS	Reliability, Availability, Maintainability, and Safety
IMU	Internal Measurement System
GNSS	Global Navigation Satellite System
RPM	Rotations Per Minute
GPS	Global Positioning System
INS	Internal Navigation System
LIDAR	Light Detection and Ranging
ESC	Electronic Speed Control
NATO	North Atlantic Treaty Organization

NOTATIONS

Chapter 2

M_{motor}	[kg] Quadrotor Motor Mass (Per motor)
M_{ESC}	[kg] Quadrotor ESC Mass (Per motor)
M_{Hub}	[kg] Quadrotor Hub Mass
M_{arm}	[kg] Quadrotor Arm Mass (Per motor)
L_{motor}	[m] Quadrotor Motor Length

L_{Hub}	[m] Quadrotor Hub Length
L_{arm}	[m] Quadrotor Arm Length
R_{motor}	[m] Quadrotor Motor Radius
R_{Hub}	[m] Quadrotor Hub Radius
H_{motor}	[m] Quadrotor Motor Height
H_{Hub}	[m] Quadrotor Hub Height
$X_{motor2cg}$	[m] Distance between Motor-COG (Center of Gravity)
X_{ESC2cg}	[m] Distance between ESC-COG
X_{arm2cg}	[m] Distance between ARM-COG
X_{motor}	[m] Distance of Each Motor to COG
$J_{x_{motor}}$	[kg/m ²] Motor MOI (Moment of Inertia) around x axis
$J_{y_{motor}}$	[kg/m ²] Motor MOI around y axis
$J_{z_{motor}}$	[kg/m ²] Motor MOI around z axis
$J_{x_{ESC}}$	[kg/m ²] ESC MOI around x axis
$J_{y_{ESC}}$	[kg/m ²] ESC MOI around y axis
$J_{z_{ESC}}$	[kg/m ²] ESC MOI around z axis
$J_{x_{Hub}}$	[kg/m ²] Hub MOI around x axis
$J_{y_{Hub}}$	[kg/m ²] Hub MOI around y axis
$J_{x_{arm}}$	[kg/m ²] Arm MOI around x axis
$J_{y_{arm}}$	[kg/m ²] Arm MOI around y axis
$J_{z_{arm}}$	[kg/m ²] Arm MOI around z axis
$J_{x_{TOTAL}}$	[kg/m ²] Total MOI around x axis
$J_{y_{TOTAL}}$	[kg/m ²] Total MOI around y axis
$J_{z_{TOTAL}}$	[kg/m ²] Total MOI around z axis
J^{body}	[kg/m ²] Total Quadrotor MOI Matrix
J_m	[kg/m ²] Motor MOI for Rotating Components
$C_{b i}$	Transformation Matrix
$(r_x, r_y, r_z)_i$	[m] Quadrotor Inertia Frame Positions
$(x, y, z)_b$	[m]Quadrotor Body Frame Positions
$V_{x,y,z}$	[m/s]Total Magnitude of Velocities in each Direction
\mathcal{T}	[Joule]Kinetic Energy
\mathcal{V}	[Joule]Potential Energy
C_{Thrust}	[Ns ²] Quadrotor Thrust Coefficient
C_{Drag}	[Nm s ²] Quadrotor Drag Coefficient

Ω_i	[deg/s] Quadrotor Propeller Angular Rate
$\ddot{\phi}, \ddot{\theta}, \ddot{\psi}$	[deg/s ²] Euler Angular Accelerations
$\ddot{x}, \ddot{y}, \ddot{z}$	[m/s ²] Translational Accelerations
g	[m/s ²] Gravity

Chapter 3

ϕ, θ, ψ	[deg] Quadrotor Euler Angles
P, Q, R	[deg/s] Quadrotor Body Angular Velocities
X, Y, Z	[m] Quadrotor Translational Positions
U, V, W	[m/s] Quadrotor Translational Velocities
$\mathcal{U}_{altitude} = \mathcal{U}_1$	Control Input for Altitude
$\mathcal{U}_{roll} = \mathcal{U}_2$	Control Input for Roll
$\mathcal{U}_{pitch} = \mathcal{U}_3$	Control Input for Pitch
$\mathcal{U}_{yaw} = \mathcal{U}_4$	Control Input for Yaw
e	PID Error for the System
K_p	PID Proportional Term
K_i	PID Integral Term
K_d	PID Derivative Term
T_i	PID Integral Time
T_d	PID Derivative Time

Chapter 4

i	”i” Term Indicates the Related Suspensions
$m_{uf_i} = m_{ur_i}$	[kg] Unsprung Mass for Suspensions
m_s	[kg] Total Mass of the Vehicle
I_p	[kgm ²] Pitch Inertia
I_r	[kgm ²] Roll Inertia
$k f_i$	[N/m] Spring Stiffness
$kt f_i$	[N/m] Tire Stiffness for Suspension
$b f_i$	[Ns/m] Damping Coefficient
a	[m] Dist. from vehicle cog to first axe
d	[m] Dist. from vehicle cog to second axe

e	[m] Dist. from vehicle cog to third axle
b	[m] Dist. from vehicle cog to fourth axle
T_f	[m] First Two Axle Half Threat
T_r	[m] Last Two Axle Half Threat
$Z_{r,i}$	[m] Road Inputs
$Z_{u,i}$	[m] Vertical Distances of the Unsprung masses
$Z_{s,i}$	[m] Vertical Distances of the Sprung masses
u_i	[N] Input forces
F_i	[N] Summation of Spring and Damper Forces

Chapter 5

A, B, B_2	State Matrices
C, D, D_2	Measurement Matrices
K, K_x	Gain Matrix of State-Feedback Controller
$u_{x,i}$	[N] Input Forces for State-Feedback Controller
K_w	Gain Matrix of Disturbance Feed-Forward Controller
$u_{w,i}$	[N] Input Forces for Disturbance Feed-Forward Controller
$u_{pre,i}$	[N] Input Forces for Preview Suspensions
w_i	[m] Road Inputs
\mathcal{J}	Objective Function
\mathcal{F}	Feasible Criterion Space
\mathcal{H}	Hamiltonian Function
Q	Weighting Matrix of States
R	Weighting Matrix of Inputs
λ	Dynamic Lagrange Multipliers
P	Ricatti Matrix
ξ	Ricatti Vector

CHAPTER 1

PROBLEM STATEMENT AND OBJECTIVES

1.1 Problem Statement

Most drones are either toys for fun or flying robots for commercial purposes or high-tech weapons for military. The recreational drones, which are produced for the consumers, are the most numerous by far and second group, which are the reason of nearly 90 percent of drone spending, are the military unmanned air vehicles. Military drones are generally used in environment where the situation is considered too risky or difficult for a human-being. They are widely used for lethal and situational awareness purposes.

Considering the ground vehicles in the category; wheeled vehicles and tracked vehicles, in recent years a trend is rising to prominence. The trend is that the wheeled vehicles are appearing as substitute for the tracked vehicles. The reason for that wheeled vehicles have advantages in terms of high mobility, high maintainability, small footprint and also low cost in comparison with the tracked versions. In military field, ground vehicles are used for different purposes such as personnel carrier, infantry fighting vehicles, mortar carrier, mobile gun carrier, air-defense system carrier and command post. Most of the time, these vehicles are forced into driving on difficult terrain conditions. Considering the drastic off-road conditions, multi-wheeled ground vehicles come into prominence. 8x8 vehicles provide tactical and technical advantage. Considering the confine situations in difficult terrain conditions, 8x8 vehicles bring advantages with their superior mobility and payload capacity.

On drastic terrain condition, in a 8x8 heavy vehicle, the most difficult situation occurs

for the personnel. It is the vibration coming from the road distributions. Generally, personnel comfort is one of the most important parameters that has to be considered when designing the suspension system for a vehicle. The ideal suspension system has to strengthen the personnel comfort and vehicle performance by providing the directional control and also has to provide maximum isolation between the personnel and the road disturbance. Fundamentally, there are three kinds of suspension systems; passive suspension system, semi-active suspension system and active suspension system [1]. Passive suspension systems are only consist of a damper element and a spring element. The damper dissipates the energy, which is stored by the spring system. Passive suspension systems have constant parameters, which have to be selected based on the problem to solve. The problem can be either personnel comfort, handling performance, ride performance or all of them according to the operational role. However, the passive suspension system has disadvantages for 8x8 wheeled military vehicles because of the wide range of the payload, road, off-road and operational parameters. At this point, semi active and active suspension solutions gain importance due to the advantage that they can vary their parameters based on the situational conditions. Active suspension system has an additional element to the spring and damper elements. This additional element actuates force to the system between the tire and the body of the vehicle. The actuating forces for the active suspensions are controlled by the state-feedback and feed-forward control theories, which are the function of the selected states of the whole system. Moreover, active suspension system performance can be increased by using the upcoming road information. The road profile can be scanned by a laser scanner system which can be mounted on the vehicle or on a separated system such as a drone or a different ground vehicle. This kind of suspension systems are called as the preview suspension systems. Finally, the problem statement of this study is that *what performance gains in personnel comfort can be achieved with a drone supported preview active suspension system for high tonnage 8x8 armored vehicles.?*

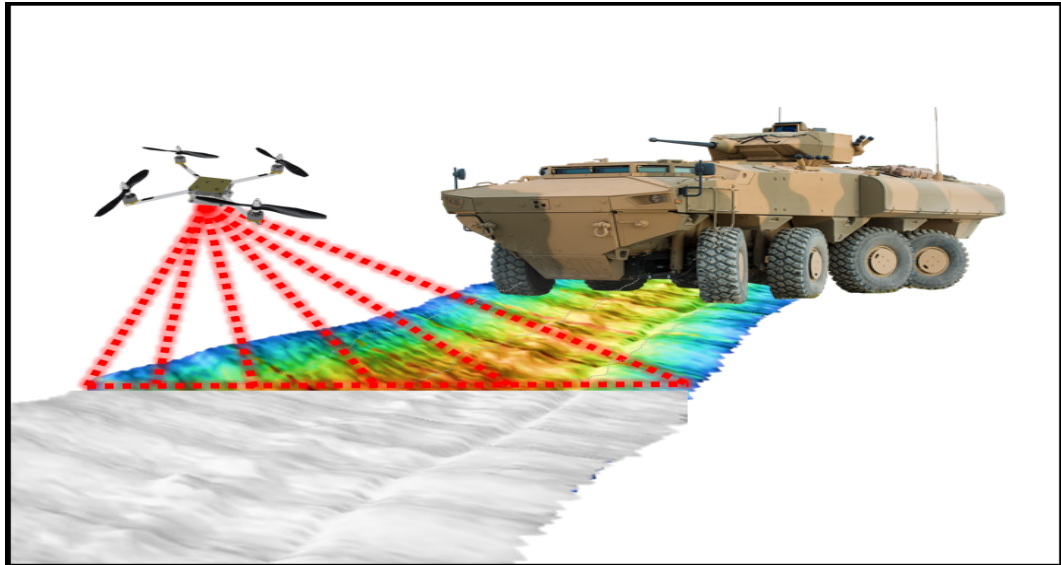


Figure 1.1: Schematic of Study

Why drone?

When considering the defense industry, drones have great numbers of usage field.

- Lethality
- Intelligence, Surveillance, Reconnaissance
- Situational Awareness

For the lethality purposes, the drone which is used in this study can carry a weapon system. Moreover, when we consider the intelligence, surveillance and reconnaissance advantages of the drone system, the drone can provide detailed information about the enemy territory. On the other hand the drone can listen the mobile conversations of the enemy and also can provide aerial monitoring in order to improve the situational awareness of the vehicle. Beside all these unlimited capabilities and the benefits of the drone system, this study also focuses on an additional supplementary and complementary benefit of the drone, which is providing the ground surface information in order to enhance the mobility performance of the vehicle by improving both the handling and ride comfort capabilities through preview active suspension system.

- Situational Awareness \Rightarrow Aerial Monitoring \Rightarrow Road Profile Scanning

Using a separated drone system has some serious advantages rather than stationary laser scanner systems, which are mounted on the vehicle. The mounted systems can only scan the road in front of the vehicle with a very limited range. But when we consider the highly terrain off-road conditions, a 360 degree independent road scanning, which can be provided by the drone system, come into prominence. The scanning range of the independent drone system can be considered as approximately unlimited in comparison with the stationary systems. Moreover, the stationary systems can be useless when the vehicle encounters an high obstacle such as wall in front of the vehicle, on the other hand, a drone system can provide unlimited scanning behind any obstacles or wall. Since the study focuses on the military field, the drone system is decided to be used for providing the upcoming road data to the suspension systems in order to enhance the mobility and situational awareness capabilities of the vehicle.

1.2 Scope of the Study

The first objective of this study is to use active suspension systems in order to overcome the personnel comfort problems for a heavy weight 8x8 military vehicle. Moreover, the active suspension system is enhanced by using the road distribution information, which is obtained by scanning of the road via an unmanned air vehicle. The major contribution of this study is to investigate the drone supported optimization of the active suspension systems.

The first study is modeling the drone. The drone parameters are selected by taking into consideration of the weight and volume of the laser road scanning system. Then PI (Proportional–integral)and PID (Proportional–Integral–Derivative) control approaches are developed in order to control the attitudes of the systems. Principally, the drone tracks and scans the path, which is generated by the 8x8 vehicle.

The second study is modeling the vehicle suspension system. Firstly, a quarter car model is developed prelusively and then a 8x8 full car vibration model is built to simulate the whole coupled dynamics of 8 suspension systems. LQR optimal control approach is applied to the vibration model to improve the personnel comfort of the vehicle. Then, as a second control approach, the LQR (Linear Quadratic Regulator)

optimization of the active suspension system is enhanced by the road information, which is coming from the drone. The second suspension approach is called as the preview suspension system.

Finally, the drone model and the vehicle model are integrated in a simulation world. Then, laser scanning errors are implemented to the simulation world. Different scenarios with different road types are generated in order to evaluate the preview optimal active suspension system performance against the passive suspension system and the standard optimal suspension system on different road conditions.

This thesis does not deal with the production of the drone and optimal active suspension systems, but it studies the effects of the drone supported suspension system on the personnel comfort, while taking into the account of the laser scanner error parameters.

In summary, the goals of the study and the corresponding chapters for the related objectives can be summarized as:

- Understand the feasibility of the usage of air vehicles for the purpose of road scanning. (Chapter 2)
- Design a road scanning aimed drone and select appropriate components. (Chapter 2)
- Understand the potential and constraints of the road scanning via drone system. (Chapter 2)
- Control, model and simulate the drone. (Chapter 3)
- Characterize the laser scanner error with respect to drone velocity and range. (Chapter 2, 6 and 7)
- Understand the feasibility of the usage of optimal control for the suspension systems. (Chapter 4, 5 and 7)
- Understand the potential and the constraints for the preview active suspension systems. (Chapter 4, 5 and 7)
- Model and simulate the 8x8 full car vibration model. (Chapter 4)
- Control the 8x8 suspension system. (Chapter 5)
- Integrate the vehicle and the drone simulations. (Chapter 6)
- Generate ISO standard road profiles. (Chapter 7)

- Analyze and compare the drone supported preview suspension system against the standard optimal suspension system and the passive suspension system with respect to pitch, roll and vertical motion. (Chapter 7)
- Analyze with the different road types such as ISO standard roads, bump road and sinusoidal road.(Chapter 7)

CHAPTER 2

DESIGN AND MATHEMATICAL MODELING OF A DRONE

2.1 Introduction

Flying objects attract engineers for different kind of research and development projects in any discipline of engineering. When considering the defense industry, drones have great numbers of usage field. A drone can carry a weapon while gathering situational information such as the exact location of the enemy or the details about the enemy territory. Military drones have been changing the face of wars, and completely changing the way that many countries go about their defense strategies.

Among the unlimited possibilities of the drone usage, this study focuses on the usage of the drone, which has ability to scan the road distributions in order to enhance the suspension performance against personnel comfort problems. For the best performance, a shelf product high technology laser scanner system is selected to be mounted on the quadrotor system and to scan the road with high accuracy and precision in order to serve a precise position information to the vehicle.

2.2 Literature Survey

There are many types of drones. For this study, it is necessary to design a multicopter, which is able to carry the payload(laser scanning system, IMU system, GPS etc.) and able to fly stably. The number of motors are generally used for categorization of the multirotors. The general types of multirotors can be categorized as: [2]

- Bicopter
- Tricopter
- Quadcopter
- Hexacopter
- Octocopter

Bicopter: The Bicopter has two rotors. It is known as the cheapest multicopter configuration since it needs only two motors and two servos, which are used for arranging the tilt angle. Because of having only two propulsive forces, this configuration has the least lifting payload power but it has advantages because of having low maintenance costs.

Tricopter: The Tricopter has three rotors. "T" shape and "Y" shape configurations are more common tricopter configurations. It is still relatively cheap multicopter configuration since it has only three propellers. The tricopter configurations are known as one of the least stable configurations. On the other hand, it has relatively more yaw authority comparing to the quadrotor. In other words, the tricopter uses servos to make yaw maneuver, and therefore, it loses relatively less thrust.

Quadcopter: A quadrotor has 4 propellers, which are typically 90 degrees apart for the common X4 configuration. Because of the simplest mechanism and relatively high payload capacity, quadrotor is one of the most popular and widely used multicopter type. Most popular configurations are "X" and "+" configurations. For the photography quadrotors, the "X" configuration is more useful since the camera has a clear view in the middle of the propellers.

Hexacopter: Hexacopter has 2 most common configurations; axial and coaxial configurations. Axial hexacopter has 6 rotors mounted at intervals of 60 degrees. Coaxial one has a "Y" shape and its propeller mounted 120 degrees apart. Coaxial one has two propellers on per arm, one above and the other. Hexacopters have more lifting power than the quadrotors since it has two more motors. The most important disadvantages of this configuration are larger sizes and being more expensive.

Octocopter: Octocopters are also have axial and coaxial configurations. The axial ones have 8 motors on the same level and mounted 45 degrees apart. Octocopters

have more lifting capacity and redundancy than the quadrotors and hexarotors, on the other hand, it is the most expensive one because of having huge number of motors and propellers. The coaxial ones also have 8 rotors but these rotors are mounted on only four arms, one above and the other.

After all, when the military conditions are considered, due to the mechanical simplicity and the operational maintainability, the quadrotor configuration comes in to prominence. Additionally, using four power sources provide quite high lift and also decrease the necessity of rotating of the rotors at high rotations per minute (RPMs). Having relatively small propellers and rotor sizes are also scarce advantages for the military and the law enforcement due to the fact that the safety of the equipments decrease as the number and the size of the rotor increases. Another benefit of the quadrotor is the swift maneuverability and this capability makes the quadrotor more safe to fly outdoors in bad weather conditions.

Furthermore, another important thing is that having four motors lead to be capable of carrying relatively high payloads. Since, it is necessary to have a road scanning drone, incorporating of different technologies such as scanning systems, internal navigation system (INS) and global positioning system (GPS) is indispensable, and therefore, having satisfactory payload capacity gains even more importance in the scope of this study.

Next table summarizes the capabilities of widely used drone types and answers the question that why quadrotor is selected for this study. [3]

Table 2.1: Comparative Study for the Flying Objects [3]

Skills	SR	AR	CR	TR	B	BL	IL	Quadrotor
Payload	5	5	10	7	2	5	2	9
Power Cost	5	5	6	5	10	9	9	2
Control Cost	3	3	9	5	8	5	1	8
Maneuverability	10	5	6	8	1	8	8	8
Mechanical Simplicity	1	7	8	2	10	2	2	10
Aerodynamics Complexity	1	1	2	1	7	1	1	10
Low Speed Flight	10	8	10	8	9	5	5	10
High Speed Flight	5	10	2	5	1	7	7	7
Survivability	1	7	7	1	8	5	7	2
Stationary Flight	10	10	10	10	7	2	5	10
TOTAL	51	61	70	52	63	49	47	75

where "SR" is single rotor, "AR" is axial rotor, "CR" is coaxial rotor, "TR" is tandem rotor, "B" is blimp, "BL" is bird-like drone and "IL" is insect-like drone and the scores ranged from 1 (Poor) to 10 (Excellent).

As can be seen on the Table 2.1, quadrotor and coaxial multirotor configurations come into prominence. Although the coaxial drones is the best one when the payload capacity is considered, because of the great mobility, simplicity and RAMS (Reliability, Availability, Maintainability, and Safety) advantages, quadrotor configuration is selected to be used in this study.

2.3 Payloads of the Quadrotor

Among all of the comparing parameters, which are evaluated in the previous section, payload capacity is one of the important ones. Therefore, payload and lift capacity are the most critical design constraints. Rotors, propellers, electronic control units (ESC) and all of the critical subsystems of the quadrotor are selected to meet the payload requirement of the system.

The product tree of the payloads of the system has three main subcategories; mechanical components, electronic components and optic components. Mechanical subsystems of the payload are mainly consist of the casing and mounting parts of the other

payloads such as scanner. Electronic subsystems mainly include the internal navigation system components and optic part is the laser scanner system.

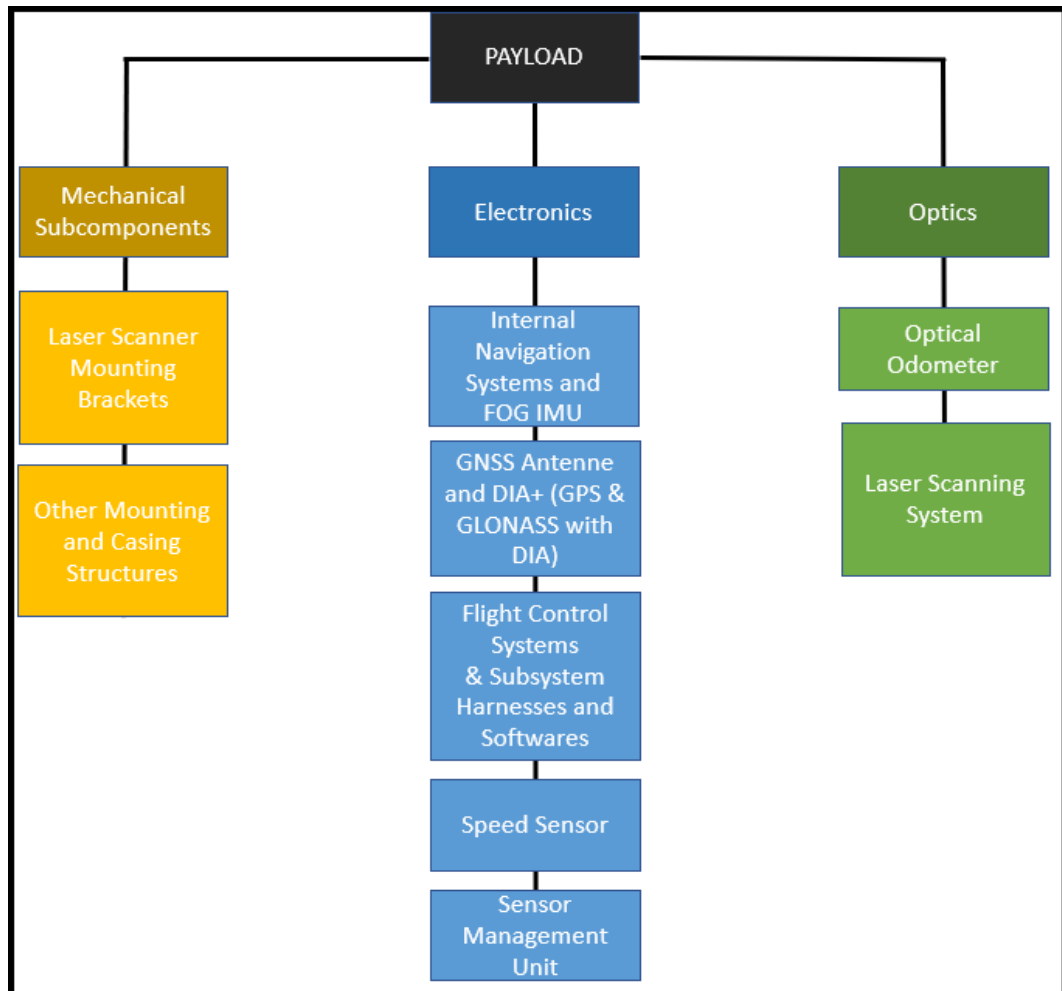


Figure 2.1: Payload Product Tree

2.3.1 Mechanical Parts

Mechanical parts are mainly consist of the laser scanner mounting structures and the other casing and mounting brackets. Since, sampling rate of the laser scanners are quite fast, the system does not need any gimbal system. On the other hand, an anti-vibration mount improves the stability of the laser scanner. The anti-vibration damper provides isolation for the vibrations, which are common during an UAV (Unmanned Air Vehicle) flight. Eliminating the vibration improves the quality, precision and

accuracy of the measured data. Figure 2.2 shows a typical anti-vibration mount.



Figure 2.2: Typical Anti-Vibration Mount[4]

Table 2.2: Mounting and Casing Mass Parameters

Characteristics	
Weight of the anti-vibration mount	0.5 kg
Other Mounting and Casing Weights	approx. 8 kg

2.3.2 Electronics

Internal Measurement System (IMU): The role of the navigation system is to provide precise positioning for the system. One of the important subsystem of the Internal navigation system (INS) is the IMU system. There are two different types of widely used IMU systems in order to measure velocity and orientation;

- Micro-electro-mechanical gyro (MEMS)
- Fibre-Optic Gyro (FOG)

Since the fiber-optic gyros offer the lowest acceleration/gyro bias, lowest random walk and also highest mean time between failures, the fiber-optic option is selected to be used in the system. The LN-200E [5] is a small, lightweight FOG system and it is

an appropriate product to be integrated to a quadrotor system. The LN-200 has three solid state fiber optic gyros with three solid-state micro-electro-mechanical gyros. Moreover, in LN200E system, fiber optic path length is increased by adding more fiber onto coil and accelerometer processing is also increased. Therefore, the gyro performance is increased. Other advantage of this gyro system is that the low power consumption of the system. Figure 2.3 shows the FOG IMU system.



Figure 2.3: Fiber-Optic Gyro IMU [5]

Important System Specifications for the FOG System are stated in the following two tables.

Table 2.3: System Specifications for the FOG System [5]

Performance	
Accelerometer	
Bias Repeatability	300 micro g, 1 sigma
Scale Factor Accuracy	100 ppm, 1 sigma
Gyro	
Bias Repeatability	0.5 degree/hr, 1 sigma
Scale Factor Accuracy	100 ppm, 1 sigma
Random Walk (max)	0.05 degree/hour

Table 2.4: System Specifications for the FOG System [5]

Characteristics	
Weight	0.75 kg
Power Consumption	900 mA, 12 W

Flight Computer:

Resonan flight computer [6] is selected for the system.



Figure 2.4: Resonan Flight Computer [6]

System control computer specifications are showed in the next table.

Table 2.5: System Specifications for the Flight Computer [6]

Characteristics	
Weight	0.46 kg
Power Consumption	960 mA , 13-16 W

Global Navigation Satellite System (GNSS) Antenna and DIA+ System:

TW5340 Multi-Constellation GNSS Smart Antenna [7] is considered to be used for the quadrotor. The TW5340 is a multi-constellation GNSS antenna, which provides simultaneous GPS/GLONASS /SBAS reception. It is used for precise tracking and positioning applications.



Figure 2.5: GNSS Antenna [7]

Table 2.6: System Specifications for the GNSS Antenna [7]

Characteristics	
Weight	0.135 kg
Power Consumption	100 mA

Additionally, Victornav VN300 [8] GNSS heading is used . VN300 includes 72 channel L1 GNSS receiver and 5 Hz of solution update rate.

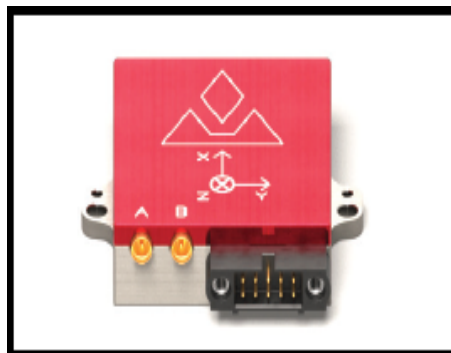


Figure 2.6: GNSS Heading [8]

Table 2.7: System Specifications for the GNSS Heading [8]

Characteristics	
Weight	0.030 kg
Power Consumption	140 mA, 1.5W

GNSS system also has sensor management and control unit, which controls, fuses and evaluates all of the sensor data.

2.3.3 Optics

Due to the purpose of this study, optic part is the most important part of the system. Active suspension system will be optimized with the help of the information obtained by the optics such as laser scanner. For this reason, the precise and accurate data obtained by the scanners gain importance for the success of the integrated system.

Road Scanning Systems:

Mobile mapping systems (MMS) are consist of internal navigation system and optic measurement sensors, which are mounted on a moving system such as vehicles, drones etc. In the following section, the theory behind the road scanning and the specifications of the selected road scanning system will be summarized.

Commercial System Examples:

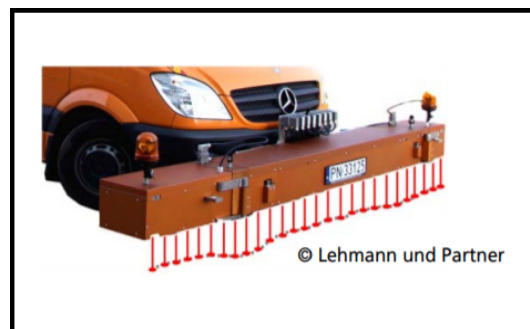


Figure 2.7: Lehmann and Partner Solution [9]

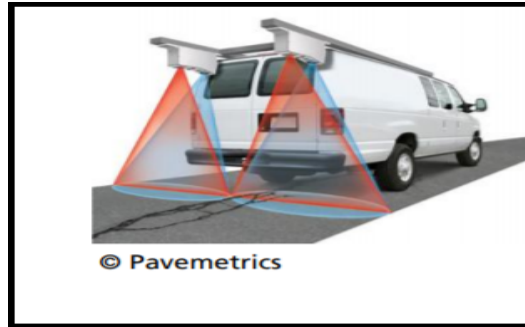


Figure 2.8: Pavemetrics Solution [10]



Figure 2.9: Phoenix Scientific Solution [11]

Figure 2.7 shows the Lehmann and Partner solution [9] for the road scanning. Laser distance sensors, mounted on a bar with a length of 3.3 meters, are used. Measurement device for measurement of transverse profile is also used in this system. On the other hand, Pavemetrics [10] uses high-speed cameras, optics and laser line projectors to detect the road distributions and 3d pavement profile for the scanning road. Figure 2.9 shows the pavement and crack scanner system of the Phoenix Scientific. [11] One of the disadvantages of all of those systems is that they use expensive and unsafe laser Class 3B scanners. Moreover, the laser Class 3B sensors are relatively bulky and they are not appropriate for the drone systems.

Theory of the Pavement Profile Scanning:

The core of the system is the laser scanner, which measures the road distributions. The main components of the laser scanner;

- Distance Measurement Module
- Angular Measurement Module
- Optical Beam Steering Module

A single laser scanner is capable of scanning road profile. The scanner is suitable for drones with respect to its volume and weight and capable of measuring the road between the altitudes of 3 meters and 100 meters. Phase shift methodology is used to obtain the time of flight of the laser beam, which is used for measuring the height of the road surface.

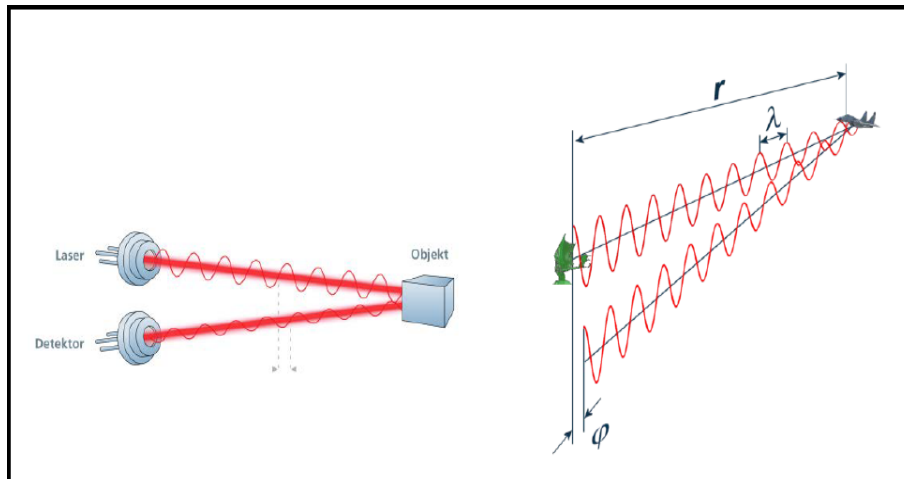


Figure 2.10: Phase Shift Methodology [12]

Phase shift method is a very rapid solution for the range measurements. It is capable of detecting millions of points per second according to the capability of the laser scanner.

Moreover, for the distance measurements, the phase shift methodology is the precise method and it gives quite good results for the close range scanning.

On the other hand, standard pulse-based methodology is less accurate and slower methodology in contrast with the phase-shift and additionally, the pulse-based methodology includes higher noise.

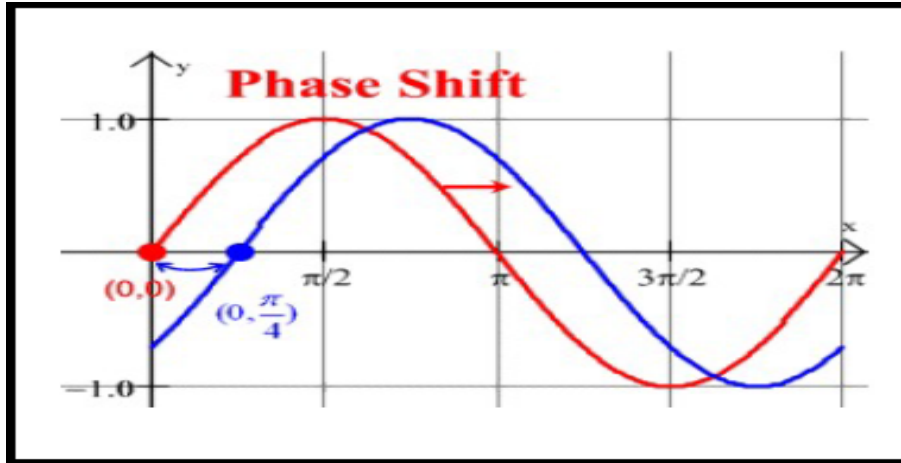


Figure 2.11: Phase Shift Methodology [12]

A laser beam is sent out and comes back to the laser scanner. The range between the system and the target point and also the time of flight are obtained by measuring the shift in the wavelength of the reflecting infrared laser signal. In Figure 2.11, the red line is the transmitted beam from the transmitter and the blue line is the reflecting beam, which goes to the receiver of the system. The difference between the two peaks of the red and the blue lines (as seen in Figure 2.11) is the phase shift [12].

$$\text{Phase Shift} = 2\pi(\text{Time of Flight}) \times (\text{Modulation Frequency}) \quad (2.1)$$

The other important parameter for the road scanning systems is the point density. The number of laser reflections per unit area is generally called as the point density. The number of the point density is highly dependent on the hardware capability of the laser scanner, data collection rate of the scanner, the range between the scanner and the target, the size of the target and the speed of the scanning system. In the most advanced laser scanning shelf products, the effective measurement rate can be up to 1000000 measurements per second per scanner, which provides highly accurate and precise data of a target objects' point cloud density. Then, high point cloud density of the point clouds collected with the help of the laser scanners provide mapping of the road distributions, vertical road surface objects, holes and cracks on the road profile.

The laser collects 3D points and post processing of this data generates the road distribution profiles for the suspension system. Figure 2.12 shows the typical point density for a road profile and the colors vary according to the height of the related point. Figure 2.13 shows the whole picture[13].

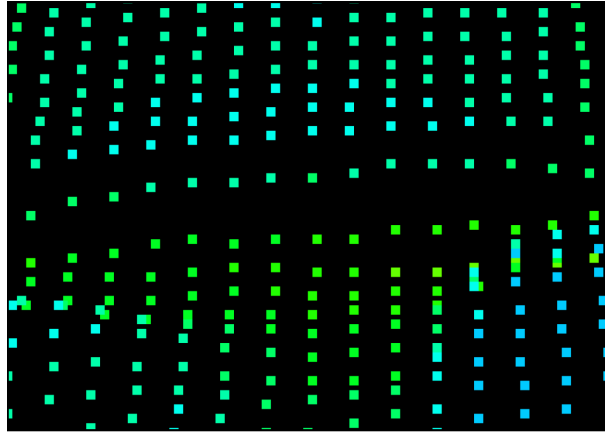


Figure 2.12: Point Cloud Example [13]

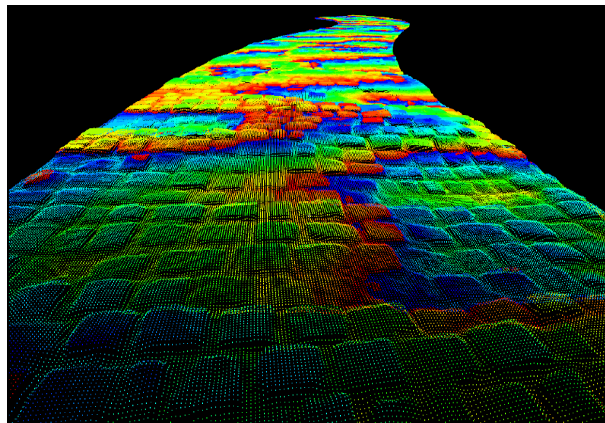


Figure 2.13: Road Surface Consisting of Points [13]

Exact location of the scanner is measured by post-processing of the information obtained by the GNSS system, which uses the data collected by the GNSS antennas mounted on the drone system. The GNSS information is corrected by the internal measurement unit (IMU) outputs, which include the geospatial positions and orientations of the scanner system. Each point data measured by the scanner systems are saved with the combined location and orientation

information.

As a result of the scanners output and post processing and interpolation tools a very detailed road profile can be obtained.

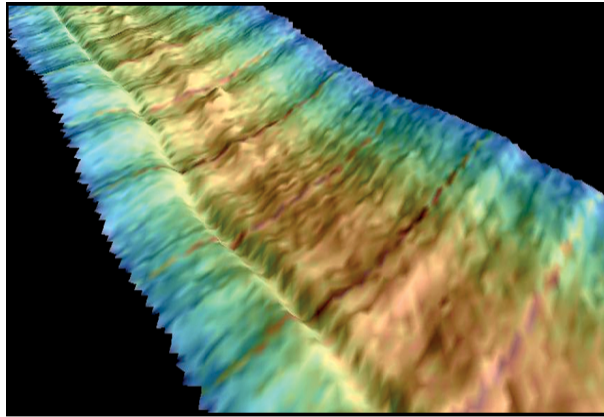


Figure 2.14: Detailed Road Profile [13]

Selected System Technical Specifications:

Riegl VUX-1HA [14] model laser scanner is selected as a laser scanner component in this study.



Figure 2.15: Riegl VUX-AH Laser Scanner [14]

This scanner can collect at rates up to 1 MHz (1,000,000 points /sec) at a repeatability of 5 mm and accuracy of 3 mm. In other words, it provides maximum effective

measurement rate of up to 1 MHz. VUX-1HA kinematic light detection and ranging sensor (LIDAR) is produced and developed for mobile purposes with a capability of scanning with 360-degrees field of view. The laser captures up to 4800 3D points/sqm at 25 km/h and 1200 points/sqm at 100 km/h. Therefore, it is capable of enabling acquisition of point clouds even at high speeds of the drone.

Figure 2.16 shows the graphical trend at 5 meters altitude of flight.

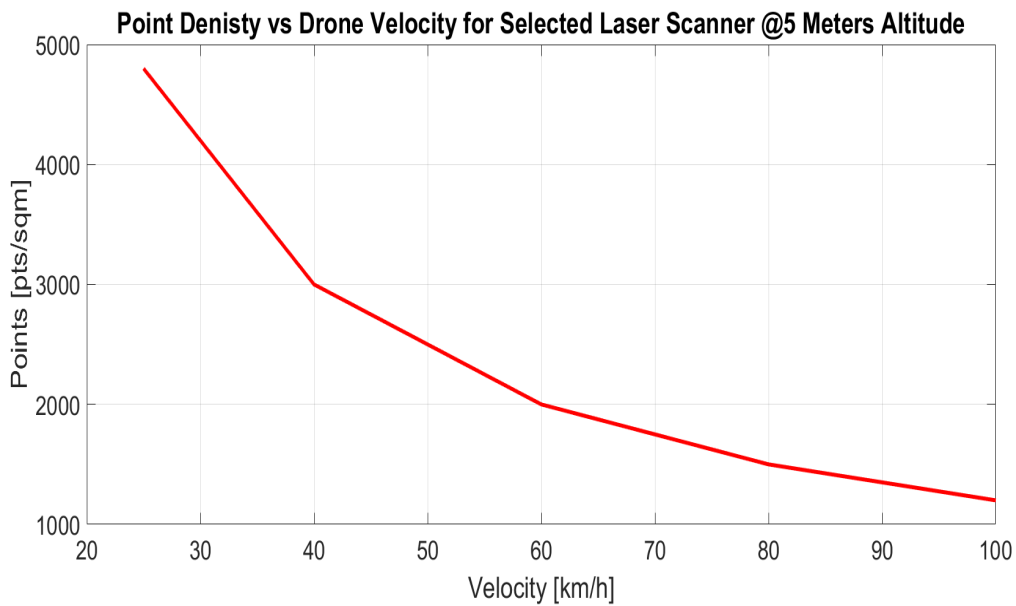


Figure 2.16: Point Density vs Drone Velocity for Selected Laser Scanner [14]

Performance and general specifications of the laser system:

Table 2.8: Range Measurement Data Riegl VUX-1HA [14]

Range Measurement Performance	
Minimum Range	1.2 m
Accuracy	5 mm
Precision	3 mm
Max. Effective Measurement Rate	up to 1000000 meas./sec.

Table 2.9: Technical Data Riegl VUX-1HA [14]

Scanner Performance	
Scanning Mechanism	Rotating Mirror
Field of View (selectable)	360 degree,, full circle”
Scan Speed (selectable)	250 Scans/sec
Angle Measurement Resolution	0.001 degree
Data Interface	
Configuration	LAN 10/100/1000 Mbit/sec
Scan Data Output	LAN 10/100/1000 Mbit/sec or USB
GNSS Interface	Serial RS232 Interface
Internal Memory	250 Gbyte SSD
Characteristics	
Power Consumption	3250 Ma, 65 Watt
Weight	3.5 kg

2.3.4 Payload Weight and Power Summary

Payload mass and power budgets can be seen in the Tables 2.10 and 2.11.

Table 2.10: Payload Mass Budget

Payload Mass Budget	
Mechanical Parts	
Anti-vibration mount	0.5 kg
Other Mounting and Casing Weights	approx. 8 kg
Electronic Parts	
FOG IMU Related System	0.75 kg
Flight Computer	0.46 kg
GNSS Anttena Related Systems	0.135 kg
GNSS Haading	0.030 kg
Optical Parts	
Laser Scanner Systems	3.5 kg
Other Optical Sensors (Odometer etc.)	0.1 kg.
TOTAL	
Quadrotor Hub Total Mass	13.475 kg

Table 2.11: Payload Power Budget

Payload Power Budget	
Electronic Parts	
FOG IMU Related System	900 mA
Flight Computer	960 mA
GNSS Antenna Related Systems	100 mA
GNSS Haading	140 mA
Optical Parts	
Laser Scanner Systems	3250 mA
Other Optical Sensors (Odometer etc.)	200 mA
TOTAL	
Quadrotor Hub Total Power Budget	5550 mA

2.4 Main Components of the Quadrotor

Motor: Since the payload mass is quite high, powerful propeller systems are necessary to provide enough lift to carry the payload. MN701S [15] is selected because of the advantages of high thrust and long lifespan. The MN701s rotor provides 6.4 kilogram lift at 75 percent throttle and 3634 revolutions per minute. A 8 mm steel shaft and relatively strong bearings provide quite high impact resistance, stability, durability and also the improved lifespan. T-shaped shaft also guarantees the safety and reliability of the rotor system even under high revolution of the propellers without rotor damages. Detailed thrust performance table of the corresponding motor can be found in Appendix A1.



Figure 2.17: MN701s Quadrotor Motor [15]

General characteristics of the selected rotor:

Table 2.12: Characteristics of MN701SKV280 [15]

Characteristics	
Motor Weight	355 g
Power Consumption @ 66% Throttle	28000 mA
Prop. Recommendation	24-26"

Propeller:

Propeller is selected to be compatible with the motor systems of the quadrotor. Propeller length is quite high in order to help the motors to provide the required lift for the payload. The propeller set is a lightweight product because of the material which is a mixture of the carbon fiber and epoxy.



Figure 2.18: CF-Epoxy Propeller [15]

Table 2.13: Propeller Characteristics [15]

Characteristics	
Propeller Weight	87 g
Diameter/Pitch	660.4 mm / 215.9 mm
Material	Carbon Fiber+Epoxy

Electronic Speed Control Unit:

Electronic speed control unit (ESC) is a control component that manipulates the speed of a electric motor. There should be one ESC for each electric motor system for the quadrotor. ESC system should be selected to be compatible with the motor and propeller configuration. All of the main components of the quadrotor such as propellers, rotors and electronic control units have to work in harmony with each other

properly. Alpha 60A HV ESC [16] is the selected system for the quadrotor . Alpha ESCs are more efficient compared with the other commercial ESCs. Combination with the appropriate rotor and propeller configuration provides long flight time. The other important advantage of this ESC is that the improved stability as compared with the other ESCs.

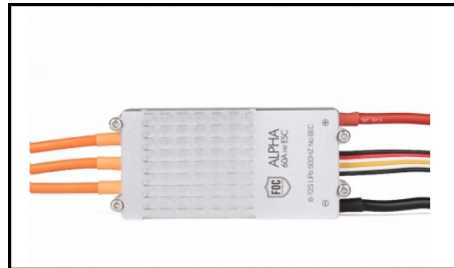


Figure 2.19: Selected Electronic Speed Control Unit [16]

General characteristics of the ESC system:

Table 2.14: Characteristics of the ESC [16]

Characteristics	
ESC Weight	73 g
Power Consumption	60 mA

Battery:

Tattu 30000mAh lipo battery pack [17] is selected for the system. Tattu battery provides higher capacity than other comparable size packs. Additionally, it has longer life cycle and it is almost double that of standard lipoly technology.



Figure 2.20: 30000 mAh Battery Pack [17]

Table 2.15: Battery Pack Characteristics [17]

Characteristics	
Capacity	30000 mAh
Weight	3673 g

2.5 General Characteristics of the Quadrotor

Mass Budget:

Total mass budget of the quadrotor can be seen in the next table.

Table 2.16: Total Mass Budget of the Quadrotor

Total Mass Budget	
Total Payload Mass (See Table 2.8 for details)	13.475 kg
Battery x1	3673 g
Rotor x 4	355 g x 4 = 1420 g
Propellers x 4	87 g x 4 = 348 g
ESC x 4	73 g x 4 = 292 g
Other masses	approx. 1500 g.
Gross Weight	approx. 20708 g

Quadrotor maximum allowable lift is $9040 \times 4 = 36160$ gram force for the maximum RPM. For 66 percent of throttle, the capacity reduces $5355 \times 4 = 21420$ gram force. Therefore, it is obvious that the mass budget of the quadrotor is appropriate. These values are measured at an ambient temperature of 34.5 degrees celcius at the ground level. Also the motor temperature is motor surface temperature at 100 percent throttle running 10 minutes [15]. Thrust factor for the 66 percent of throttle;

$$C_{Thrust} = \frac{Thrust@66Percent}{(RPM@66Percent)^2}$$

$$C_{Thrust} = \frac{5355}{(3322)^2} \tag{2.2}$$

$$C_{Thrust} = 4.8524 * 10^{-4} N/RPM^2$$

Total moment of inertia of the quadrotor system (J^{body}) and motor moment of inertia for rotating components (J_m) are stated below. For detailed calculations see Appendix A.2.

$$\begin{aligned}
 J^{body} &= \begin{bmatrix} J_{xTOTAL} & 0 & 0 \\ 0 & J_{yTOTAL} & 0 \\ 0 & 0 & J_{zTOTAL} \end{bmatrix} \\
 &= \begin{bmatrix} 0.2604kg/m^2 & 0 & 0 \\ 0 & 0.2604kg/m^2 & 0 \\ 0 & 0 & 0.4892kg/m^2 \end{bmatrix}
 \end{aligned} \tag{2.3}$$

$$J_m = 6.8183 * 10^{-4}kg/m^2 \tag{2.4}$$

Power Budget:

Total power budget of the quadrotor is summarized in the next table. Detailed power consumption of the payload components can be seen in the Table 2.9.

Table 2.17: Total Power Budget of the System

Total Power Budget	
Total Payload Power Consumption (See Table 2.9 for details)	5550 mA
Motors Power Consumption @ 66 percent Throttle x 4	28960 mA x 4 = 115840 mA
ESC x 4	60 mA x 4 = 240 mA
TOTAL Power Consumption	approx. 121630 mA

And the battery capacity of the system:

Table 2.18: Total Battery Capacity

Total Power Capacity	
Lipo Batterys' x 1	30000mAh

$$\Delta t = \frac{\text{Battery Capacity (mAh)}}{\text{Required Current(mA)}} = \frac{30000}{121630} \cong 0.25 \text{ hours} = 15 \text{ minutes} \quad (2.5)$$

It means that between two battery replacement, the quadrotor is capable of scanning the road distribution for 15 minutes.

2.6 Equations of Motion of the Quadrotor

Before building the mathematical model and equations of motion, it is important to identify the coordinate system that is used. The coordinate system can be different according to the configuration that is used in the model. The coordinate system can be located differently whether you use (+) configuration or (X) configuration. In the plus configuration, the "x" axis towards to the motor 1 from the center of the quadrotor and also the "y" axis lie along the arm of rotor 2. Lastly, the "z" axis points upward.[18] In this study the "+" configuration, which can be seen in the Figure 2.21, is used.

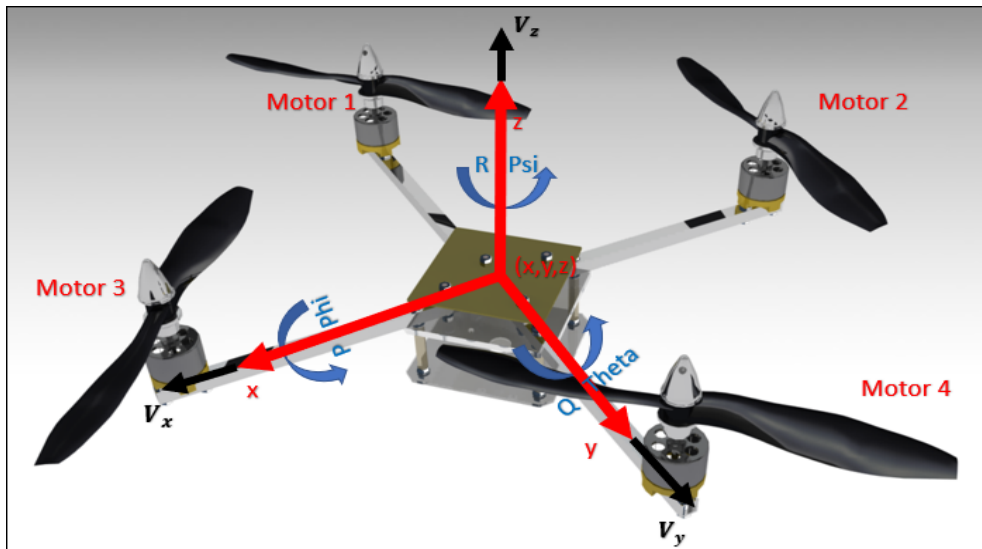


Figure 2.21: Axis and Rotation Labels for (+) Configuration Drone (Right Hand Rule) [18]

Following equation is the ZYX rotation matrix from inertial frame to the body frame.

In this equation, c and s represent cosine and sine respectively.

$$C_{b|i} = \begin{bmatrix} c(\theta)c(\psi) & c(\theta)s(\psi) & -s(\theta) \\ (-s(\psi)c(\phi) + s(\theta)s(\phi)c(\psi)) & (c(\psi)c(\phi) + s(\theta)s(\phi)s(\psi)) & c(\theta)s(\phi) \\ (s(\psi)s(\phi) + s(\phi)s(\theta)c(\psi)) & (-s(\phi)c(\psi) + c(\phi)s(\theta)s(\psi)) & c(\theta)c(\phi) \end{bmatrix} \quad (2.6)$$

And for any point in earth frame the positions may be represented as:

$$\begin{bmatrix} r_x \\ r_y \\ r_z \end{bmatrix}_i = C_{b|i_{3x3}} * \begin{bmatrix} x \\ y \\ z \end{bmatrix}_b \quad (2.7)$$

The total magnitude of the velocities in each direction are also given by:

$$V^2 = V_x^2 + V_y^2 + V_z^2 \quad (2.8)$$

Since the inertia matrix is diagonal, the kinetic energy formula can be expressed as:

$$\mathcal{T} = \frac{1}{2}I_{xx}(\dot{\phi} - \dot{\psi}s(\theta))^2 + \frac{1}{2}I_{yy}(\dot{\theta}c(\phi) + \dot{\psi}s(\phi)c(\theta))^2 + \frac{1}{2}I_{zz}(\dot{\theta}s(\phi) + \dot{\psi}c(\phi)c(\theta))^2 \quad (2.9)$$

The potential energy is also formulated as:

$$\mathcal{V} = g \int (-s(\theta)x + s(\phi)c(\theta)y + c(\phi)c(\theta)z) dm r \quad (2.10)$$

By using the lagrangian $\mathcal{L} = \mathcal{T} - \mathcal{V}$:

$$\Gamma_i = \frac{d}{dt} \left(\frac{\partial \mathcal{L}}{\partial \dot{q}_i} \right) - \frac{\partial \mathcal{L}}{\partial q_i} \quad (2.11)$$

This equation is the general representation of the equation of motion with the generalized coordinate system \dot{q}_i .

On the other hand, there are nonconservative moments, which are based on the thrust imbalance between motor 2 and motor 4, between motor 1 and motor 3 and between the motors 1, 3 and 2, 4 respectively.

$$\left\{ \begin{array}{l} \text{Between Rotors 2 and 4} \Rightarrow C_{Thrust} X_{motor} (\Omega_4^2 - \Omega_2^2) \\ \text{Between Rotors 1 and 3} \Rightarrow C_{Thrust} X_{motor} (\Omega_3^2 - \Omega_1^2) \\ \text{Between Rotors (1,3) and (2,4)} \Rightarrow C_{Drag} (\Omega_1^2 - \Omega_2^2 + \Omega_3^2 - \Omega_4^2) \end{array} \right. \quad (2.12)$$

By taking the nonconservative moments into account, the equations of motion for three euler angles becomes:

$$\left\{ \begin{array}{l} \ddot{\phi} = \frac{J_{yTOTAL} - J_{zTOTAL}}{J_{xTOTAL}} \dot{\theta} \dot{\psi} - \frac{J_{motor}}{J_{xTOTAL}} (\Omega_1^2 - \Omega_2^2 + \Omega_3^2 - \Omega_4^2) C_{drag} + \\ \quad \frac{1}{J_{yTOTAL}} C_{Thrust} X_{motor} (\Omega_4^2 - \Omega_2^2) \\ \ddot{\theta} = \frac{J_{zTOTAL} - J_{xTOTAL}}{J_{yTOTAL}} \dot{\phi} \dot{\psi} - \frac{J_{motor}}{J_{yTOTAL}} (\Omega_1^2 - \Omega_2^2 + \Omega_3^2 - \Omega_4^2) C_{drag} + \\ \quad \frac{1}{J_{yTOTAL}} C_{Thrust} X_{motor} (\Omega_3^2 - \Omega_1^2) \\ \ddot{\psi} = \frac{J_{xTOTAL} - J_{yTOTAL}}{J_{zTOTAL}} \dot{\phi} \dot{\theta} - \frac{C_{Drag} (\Omega_1^2 - \Omega_2^2 + \Omega_3^2 - \Omega_4^2)}{J_{zTOTAL}} \end{array} \right. \quad (2.13)$$

Three equations of translational accelerations of the quadrotor systems:

$$\left\{ \begin{array}{l} \ddot{x} = \frac{(s\psi s\phi + c\psi s\theta c\phi)}{MTOTAL} (\Omega_1^2 + \Omega_2^2 + \Omega_3^2 + \Omega_4^2) C_{Thrust} \\ \ddot{y} = \frac{(-c\psi s\phi + s\psi s\theta c\phi)}{MTOTAL} (\Omega_1^2 + \Omega_2^2 + \Omega_3^2 + \Omega_4^2) C_{Thrust} \\ \ddot{z} = g - \frac{1}{MTOTAL} (c\psi c\phi) (\Omega_1^2 + \Omega_2^2 + \Omega_3^2 + \Omega_4^2) C_{Thrust} \end{array} \right. \quad (2.14)$$

This state equations allow us to determine the euler angles and the positions of the quadrotor in X, Y and Z directions of the inertial frame.

It is important to mention that in these state equations there are two important assumptions:

- The hub forces and rolling moments are neglected.
- Thrust and drag coefficients are constant for all RPMs of the propellers.

CHAPTER 3

CONTROL AND SIMULATION OF The QUADROTOR

3.1 Control of the Quadrotor

In this study for the control of the system the PID control approaches are used and the PID terms are tuned in the simulations manually. Manual PID tuning is done by changing the PID terms by looking at the response of the system at the end of the each separate simulations. The goal is to obtain the desired and appropriate system response by arranging the integral terms K_i , derivative term K_d and the proportional term K_p . When the desired response is reached then the PID terms are fixed. Although the manual terms seem to be simple and kind of trial and error approach, this methodology requires a lot time and experience.

Widely-used approaches to tune the PID terms [19]:

- Manual Tuning Method (Selected)²
- Ziegler-Nichols Tuning Method
- Cohen-Coon Tuning Method
- PID Tuning by using third party software (ex. MATLAB)

3.1.1 Control Modeling

In the light of the state equations represented in the section 2.6, the control model is generated. The assumptions :

- The hub forces and rolling moments are neglected.

- Thrust and drag coefficients are constant for all RPMs of the propellers.

are valid for modeling the control system. The assumptions are important to simplify the system model in order to construct a real-time closed control loop. In order to model the control loop, the state equations should be written in the state-space form.

States for the system:

$$X_{States} = \{P, Q, R, \phi, \theta, \psi, U, V, W, X, Y, Z\}^T \quad (3.1)$$

where P, Q and R are the body angular velocities and ϕ, θ and ψ are the euler angles. Also, U, V and W are the translational velocities and X, Y and Z are the translational positions.

After defining the simplify model and the states, the next step is to define the control inputs that will close the control loop in order to provide a real time control for the system.

The input vector for controlling the model:

$$\mathcal{U} = \{\mathcal{U}_{altitude}, \mathcal{U}_{roll}, \mathcal{U}_{pitch}, \mathcal{U}_{yaw}\}^T \quad (3.2)$$

where:

$$\begin{cases} \mathcal{U}_{altitude} = \mathcal{U}_1 = (\Omega_1^2 + \Omega_2^2 + \Omega_3^2 + \Omega_4^2)C_{Thrust} \\ \mathcal{U}_{roll} = \mathcal{U}_2 = (\Omega_4^2 - \Omega_2^2)C_{Thrust} \\ \mathcal{U}_{pitch} = \mathcal{U}_3 = (\Omega_1^2 - \Omega_3^2)C_{Thrust} \\ \mathcal{U}_{yaw} = \mathcal{U}_4 = (-\Omega_1^2 + \Omega_2^2 - \Omega_3^2 + \Omega_4^2)C_{Drag} \end{cases} \quad (3.3)$$

3.1.2 PID based Control Approach

By using the PID control approaches, one can obtain the optimum control dynamics with response with short response time, increased stability and minimized oscillations. Using the derivative gain P_d , the system gains capability to minimize the overshoot and oscillations. The proportional, derivative and integrative terms are arranged manually to get the desired response in the simulations. For a quadrotor system to fly properly, the response of the controllers have to be stable without any oscillations in any situation and under any noise. [20]

The generalized equation for the PID is:

$$PID = K_p = (e + \frac{1}{T_i} \int_0^t e dt + T_d \frac{de}{dt}) \quad (3.4)$$

where e is the error for the system and

$$T_i = K_p / K_i \quad (3.5)$$

and

$$T_d = K_d / K_p \quad (3.6)$$

are the integral and derivative times respectively.

3.2 Simulation of The Quadrotor

For the simulations, Matlab/SIMULINK software is used.

The whole structure blocks of the system, which is consist of path generating model block, which obtains the information from the 8x8 vehicle, the core system model block and the controller block and also relations, inputs and outputs for these blocks can be shown in the next figure.

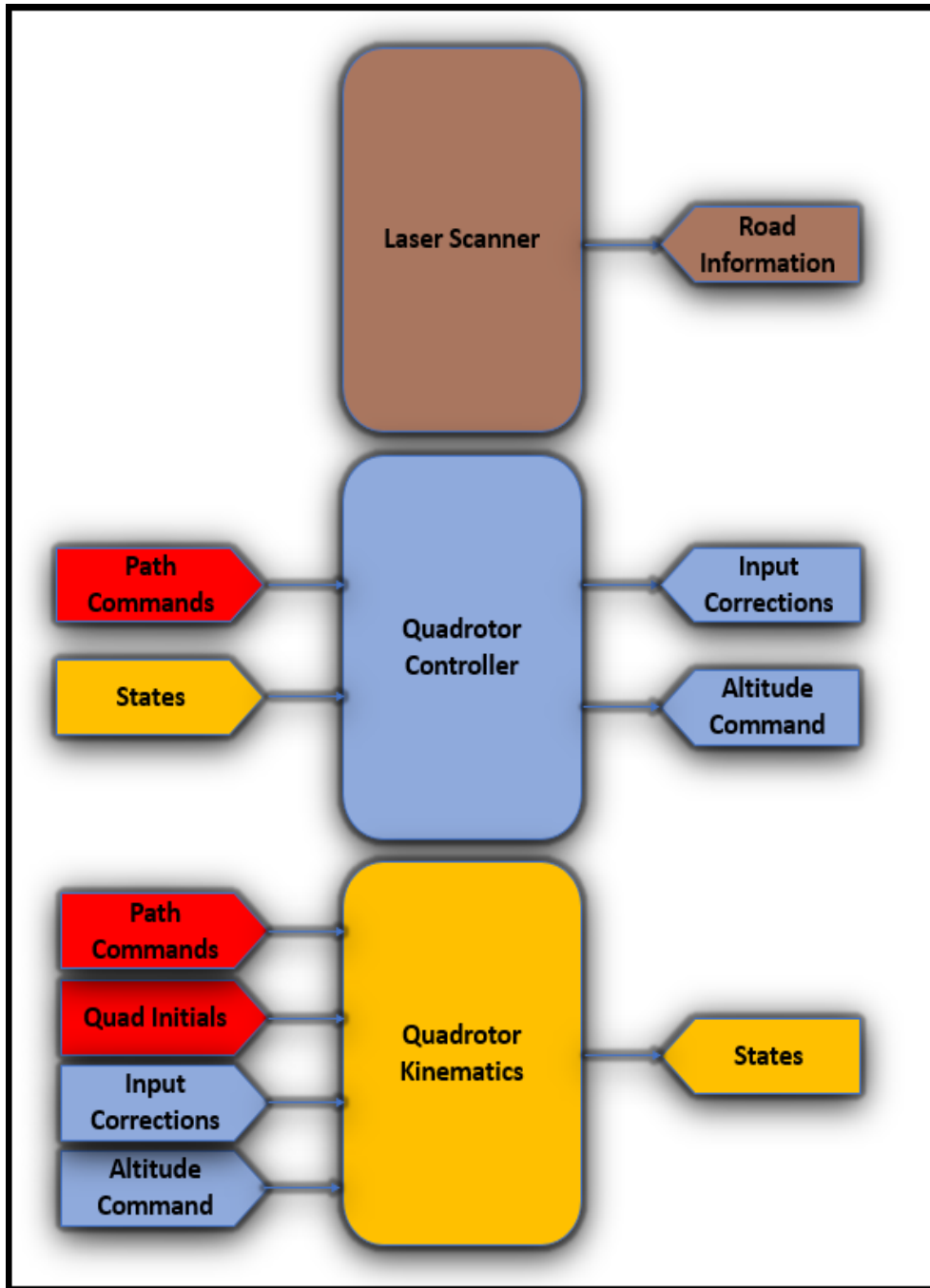


Figure 3.1: Drone Simulink Model Structure

Laser Scanner Block:

This block provides the road heights for eight wheels. In full drone and vehicle integrated simulation, this information comes from the laser scanner system mounted on the drone. Only the laser scanner based errors such as point cloud density with respect to the range and the velocity of the quadrotor is modeled in the simulations. Accuracy of the laser scanner is also taken to the account. Navigation based errors are assumed to be eliminated with the help of the self corrective navigation system, which is mentioned in Chapter 6.

Quadrotor Controller Block:

This block includes the PID controllers, which control the attitudes of the quadrotor. Path commands come from the vehicle.

Quadrotor Kinematics Block:

This block is the core block of the quadrotor system. The inputs of this block come from the controller block and the outputs are the updated state vector, which goes back to the controller blocks in order to have a closed loop control. In the scope of the study, the quadrotor is commanded by the 8x8 vehicle. Therefore the red inputs come from the vehicle. This block also includes the ω calculations and also all of the state equations modeling, which are euler angle equations and the position equations. The block also includes the euler angle and Ω^2 calculations.

3.3 Simulation Results

Next table summarizes the system parameters, which are used in the simulations.

Parameter Description	Symbol	Value
Distance of each rotors to the COG	X_{motor}	0.45m
Rotor Mass	M_{motor}	0.437 kg (1 Rotor+1 Prop.)
Rotor Height	H_{motor}	0.0394 m
Rotor Radius	R_{motor}	0.079 m
ESC Mass	X_{ESC}	0.073 kg

Table 3.1 continued from previous page

Parameter Description	Symbol	Value
ESC Width	W_{ESC}	0.0325 m
ESC Length	L_{ESC}	0.071 m
Distance of each ESC to the COG	X_{ESC}	0.1 m
Hub Mass	M_{Hub}	17.748 kg
Hub Radius	R_{Hub}	0.1 m
Hub Length	L_{Hub}	0.1 m
Quad Total Mass	M_{TOTAL}	20.708 kg
Quad Total Inertia around X axis	J_x	0.2604 kg/m^2
Quad Total Inertia around Y axis	J_y	0.2604 kg/m^2
Quad Total Inertia around Z axis	J_z	0.4892 kg/m^2
Thrust Coefficient	C_{Thrust}	$4.8524 \times 10^{-4} N/RPM^2$

Table 3.1: System Parameters Used in MATLAB/Simulink Model

In Figure 3.2, Figure 3.3 and Figure 3.4 the desired X, Y and Z positions and the response of the quadrotor to this desired path can be seen. The paths are generated randomly.

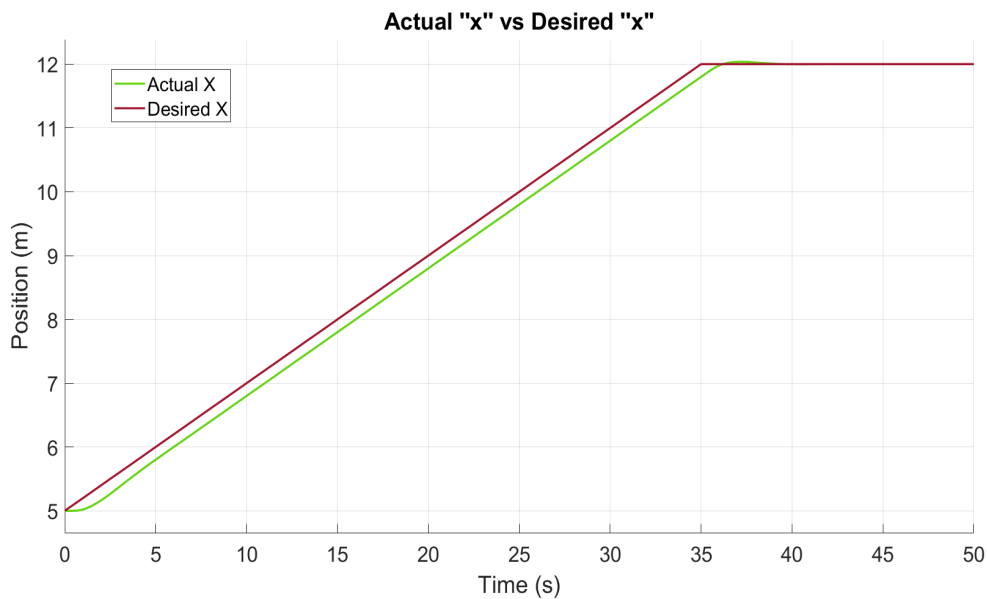


Figure 3.2: Desired X position vs Actual X Position of the Quadrotor

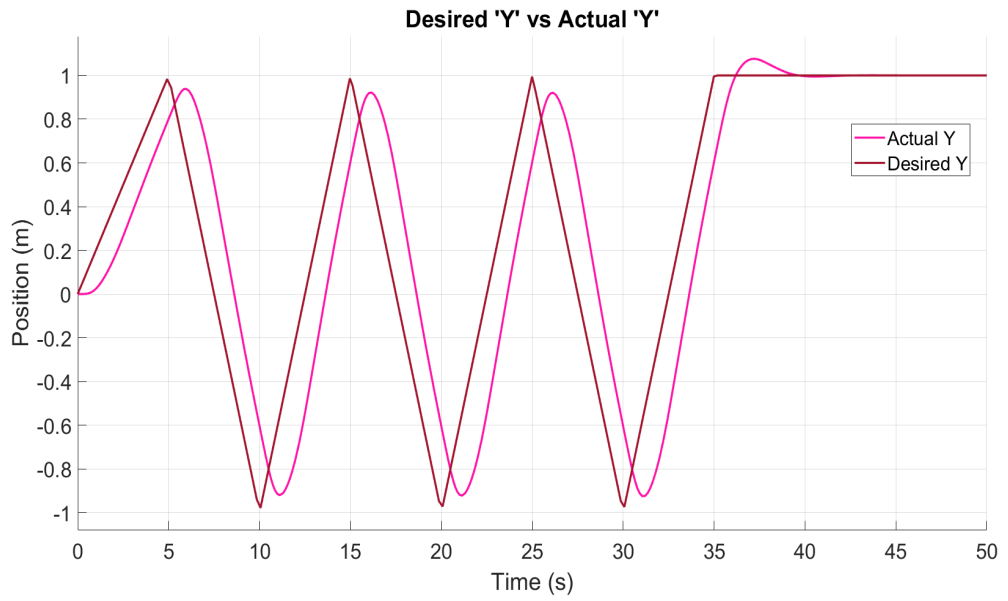


Figure 3.3: Desired Y position vs Actual Y Position of the Quadrotor

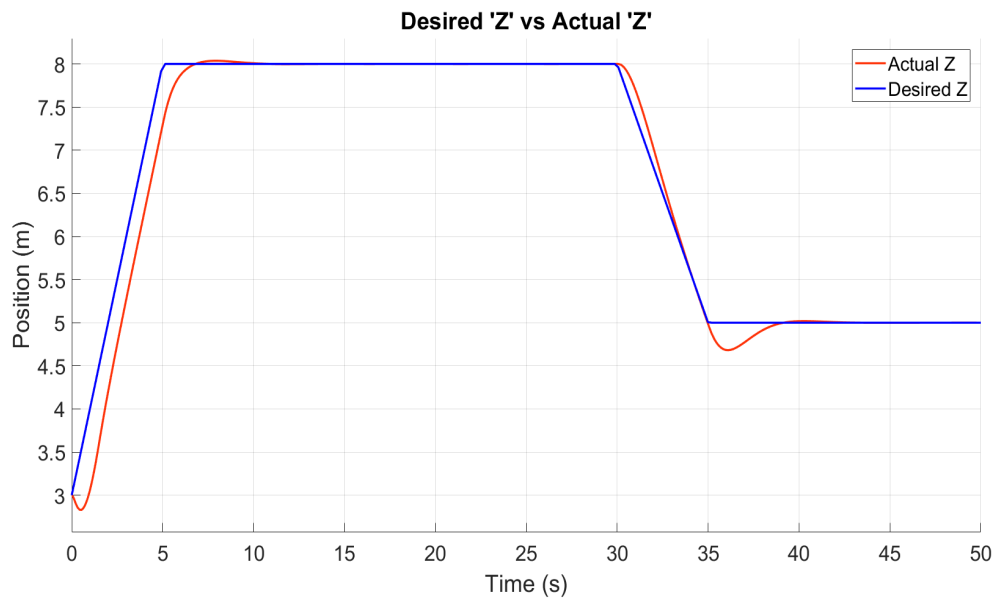


Figure 3.4: Desired Z position vs Actual Z Position of the Quadrotor

CHAPTER 4

MATHEMATICAL MODELING OF The 8X8 FULL VEHICLE

4.1 Introduction

The study proposes LQR control based active suspension system modeling and simulation for 8x8 high tonnages armored vehicle to provide personnel comfort in hard off-road conditions. A full car vibration model is used to simulate all the dynamics of a real vehicle suspension. The governing differential equations of motion of a 8x8 heavy weight vehicle for active optimal control are derived analytically. The equations of states are formulated and an optimal control gain is calculated for optimal results. Furthermore, a feed-forward gain is also calculated to be used for preview optimal controller. Eight actuators, one for each suspension systems are used. Various ISO standard road inputs are generated in order to simulate asphalt and off-road terrain types, which will be stated in chapter 7 in more details. After generating the road inputs and obtaining the feedback gain matrix for the feedback actuators, the standard optimal suspension, preview optimal suspension and the passive suspension systems are compared and it is observed that the active suspension system with preview optimal actuator feedback forces is better than the passive system, which does not have actuator system and the standard optimal system, which does not have the preview sensors. The results will be considered in chapter 7 in more detail. Simulations using MATLAB/Simulink environment shows that the preview active suspension system provides better personnel comfort for 8x8 high tonnages land vehicles.

4.2 Literature Survey

On drastic terrain conditions, in a 8x8 heavy vehicle, the most difficult situation occurs for the personnel based on the vibration coming from the road distributions. Generally, personnel comfort is one of the most important parameters that have to be considered when designing the suspension system for a vehicle. The ideal suspension system has to strengthen the personnel comfort by providing the directional control and also has to provide maximum isolation between the personnel and the road disturbance. Fundamentally, there are three kind of suspension systems; passive suspension system, semi-active suspension system and active suspension system.

Passive suspension systems consist of a damper and a spring and the damper dissipates the energy, which is stored by the spring system. Passive suspension systems have constant parameters and these parameters have to be selected according to the problem to be solved. The problem can be either personnel comfort, handling performance, ride performance or all of them according to the operational role. However, the passive suspension system have disadvantages for 8x8 wheeled military vehicles because of the wide range of the payload, road, off-road and operational parameters. At this point, semi active and active suspension solutions gain importance due to the advantage that they can vary their critical parameters according to the situational conditions. In other words, the semi-active suspension systems have capability to manipulate the damping coefficient. One of the method to change the behavior of the shock absorbers is changing the intensity of the magnetic field [22],[23],[24],[25]. Another method is regulating the controller orifice [26].

Active suspension systems have an additional element to the spring and damper elements. This additional element actuates force to the system between the tire and the body of the vehicle. The actuating forces for all suspensions are controlled by the smart control theories, which are the function of the selected states of the whole system. The complexity, power consumption and the relatively high cost can be counted as disadvantages of the active suspension systems.

The objective of this study is to use active suspension system to provide personnel comfort for a heavy weight 8x8 military vehicle. Moreover, the standard optimal ac-

tive suspension system is enhanced by using the road distribution information, which is obtained by the scanning of the road via laser sensors mounted on a quadrotor system. The major contribution of this study is to investigate the quadrotor supported optimization of the active suspension systems for the purpose of enhanced personnel comfort.

Vehicle suspension systems are typically evaluated by its road handling, ride comfort and personnel comfort performances. For the past two decades, researchers have been developing suspension system concepts in order to improve the performance. It is an obvious fact that the quarter car model, half car model and full car model are used to investigate the suspension systems, which can be categorized in three groups; active suspension systems, semi-active suspension systems and passive suspension systems.[27]

Suspension system of most vehicles includes passive spring and damper systems. Passive suspension system is more frequently used suspension systems, which are used as conventional suspension systems. Passive suspension systems have constant damper and spring coefficients and these constant parameters cause poor road handling capability and poor passenger comfort.

Semi active suspension system can manipulate the amount of dissipative power by controlling the damping coefficient in viscous damper.

Active suspension systems use some actuator sources with spring and damper forces and under advantages of this controllable actuator forces, it can reduce the amount of necessary power to provide desired personnel comfort performance.

In modeling and simulation environment, suspension systems can be examined in different fidelity level models such as quarter car, half car and full car model. In quarter car model, there is no effects of the pitch and roll motion. In half car model, pitch angle is a variable for the performance. Beside all these, in full car model both pitch motion and roll motion are included in equations of motion and the fidelity of the model is higher than the others because all of the coupled dynamics of all of the suspension system are taken into account. Therefore, full car model is generated for this model even the pitch and roll motion analyzes are not in the scope of this study.

The other important object of this study is to investigate the behavior of the optimal controllers against the different road types such as bumpy road, off-road and asphalt.

Furthermore, a feed-forward optimal gain is calculated for preview optimal controller. In this kind of suspension system, it is assumed that the vehicle knows the upcoming road distributions. In the results and discussion part, preview optimal controller is compared to the passive suspension and the standard optimal controller.

4.2.1 Commercial Active Suspension Systems in Automotive Industry

Mercedes's Active Body Control:

Active body controller ABC [38] is the technology that Mercedes has developed to provide active suspension system. This technology offers the customer improved ride comfort and road handling by eliminating the body roll of the vehicle by controlling the chassis motion for all of the driving conditions such as accelerating, braking or cornering.

This system works with the help of an internal computer system, which detects the chassis motions by using the information, which come from the thirteen sensors and manipulate the motion of the active suspension system by providing an actuator force arising with the hydraulic actuators mounted between the chassis and each wheel. Every ten milliseconds, the body movement information is updated and the monitoring of the body motion always continuous to provide uninterrupted control for the active suspension system. Hydraulic pressure is also monitored by the pressure sensors mounted at each hydraulic cylinders. The effect of the hydraulic actuators appears almost instantaneously and the counter forces are generated by the active suspension system in order to absorb the wheel motion arises due to the pavement distributions.

The ABC system can also be used for raising or arising the vehicle chassis in order to provide appropriate response to the vehicle loading (i.e passengers or cargo).

As a result of the ABC, mercedes offers the customers grater comfort, for example, the body roll angle can be reduced almost 45 percent from the value, which can be seen when the ABC system is closed.

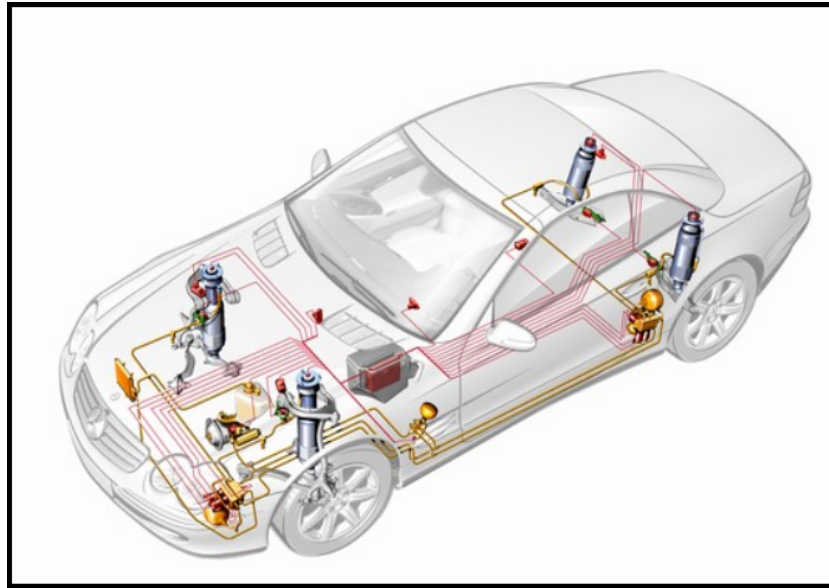


Figure 4.1: Active Body System Equipment Representation [38]

Mercedes's Magic Body Control:

Mercedes magic body control MBC [39] is the next generation active suspension system of the active body control system. As it mentioned in the previous part of this section, the ABC system acts on each actuator to adjust the actuator force on each active suspension instantaneously and independently with the help of the hydraulic pistons to generate a quick response to the pavement distributions in order to provide ride comfort and road handling. But the critical parameter is the reaction and response time. The suspension responses to the road distributions quickly after the tire has encountered them.

The important difference between the ABC system and MBC system appears at this point. Because in MBC system the vehicle knows what is coming in advance, with precisely and accurately and down to every imperfection and the hydraulic actuators actuate forces at each suspension system so accurately that any surface disturbance could be absorbed.

In MBC system, a camera mounted at the top of the windshield scans the upcoming pavement and after analyzing the data, it is delivered to the ABC system. The sensor

scans the road ahead, which is an area between 4.5 meters to 13.5 meters in front of the vehicle and even 10 centimeters distributions can be detected by this system. Therefore, the vehicle knows the information what the wheels encounter and the exact time of the encountering. Figure 4.2 shows the general working principle of the magic body control.

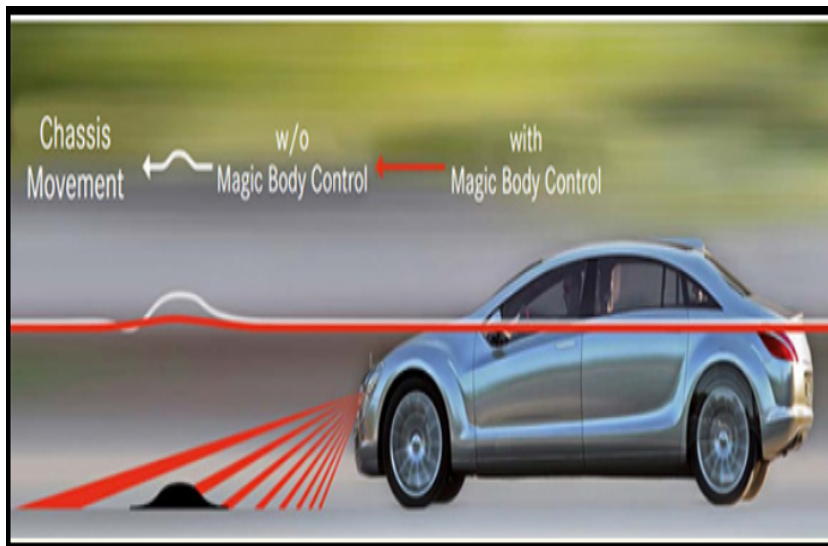


Figure 4.2: Magic Body System [39]

Citroen’s Hydractive System:

The main advantage of the hydractive system of the Citroen [40] is that it gives the vehicle the capability of adapting the damping force and its flexibility. It can vary the configuration of the suspension from the performance based options to the comfort based options with the help of a third sphere and a stiffness regulator mounted on each axle of the vehicle chassis. The system also benefits the data coming from the sensors such as height sensor, tire sensor and it also uses the information of brake pressure and engine speed. By doing this, the system is capable to arrange and control the roll, pitch and vertical motion of the vehicle.

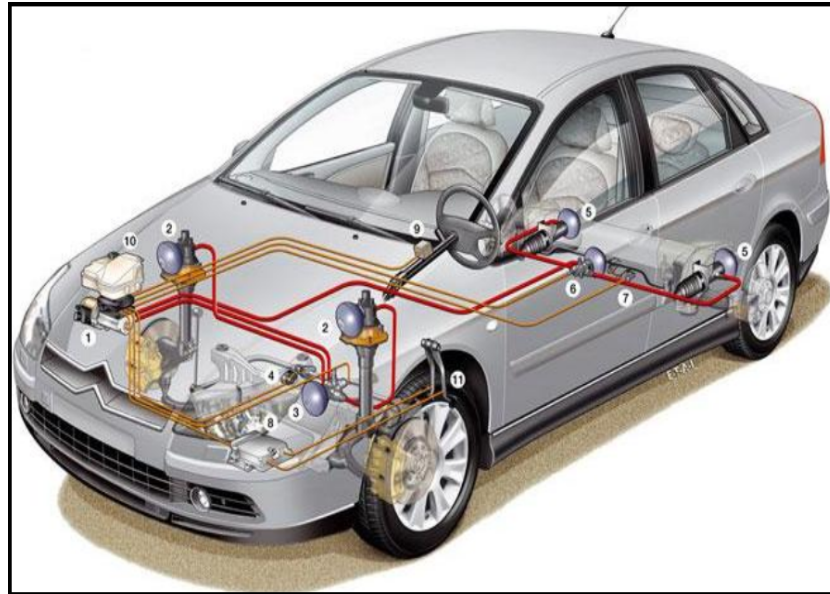


Figure 4.3: Hydractive System [40]

4.2.2 Vertical Vibration Models

4.2.2.1 Half Car Model

A half car model is used to investigate suspension system of the vehicle in a bit more advanced way than the quarter car version. Since in half car model, only one side of the vehicle including all of the wheels of this side is modeled and by doing this, only the pitch motion of the vehicle can be simulated [27]. All of the assumptions for the quarter car model are also valid for this model.

4.2.2.2 Full Car model

In full car model representation, in addition to the half car model, both side of the vehicle is modeled. Full car model provides information about vertical motion, pitch motion and roll motion of the chassis[27]. More accurate analysis can be achieved by using so-called full car model [22],[33]. All of the roll, pitch and vertical motion state equations are implemented to the model and this provides complete analyze for the suspension system. Next figure shows a generalized form of the 4x4 full car model.

4.2.2.3 Quarter Car Model

Quarter car model is the most simplified model that is used for examining the behaviour of the suspension system. Quarter car models are the most commonly used models in the literature [28],[29],[30],[31],[32]. As assumptions of the quarter car modeling, there is no rotational motion around the wheel and the body. The tire can be modeled with only linear spring or with linear spring and damper couple. Additionally, the tire is assumed to be always in contact with the pavement. All of the friction forces based on the road surfaces are also neglected and also residual structural damping is also assumed to be negligible [27]. In quarter car model, only the vertical body displacement can be examined, the rolling and pitching motion can not be simulated.

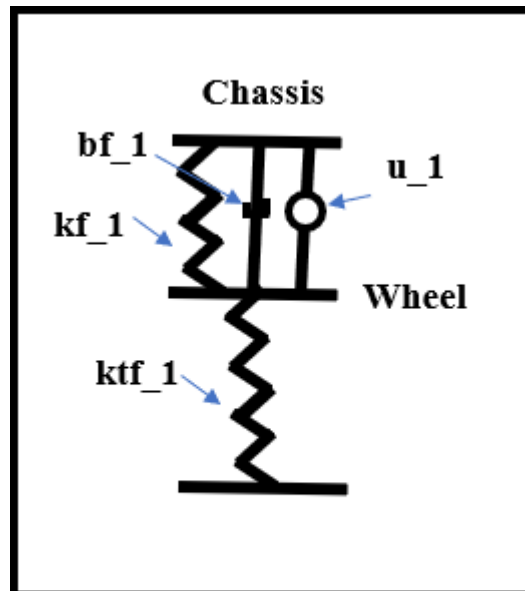


Figure 4.4: Quarter Car Model Representation

4.3 Mathematical Modeling of The Quarter Car Model

The assumptions for the simplest vehicle model are as follows: the wheel system is modeled by using only spring element, all of the rotational motions in tire and chassis

system are neglected, all of the components are linear, continuous ground contact and no friction between the road and the tire.

Table 4.1 states the parameters symbols and names, which are used in the equations of motions of the quarter car model.

Table 4.1: Parameter Symbols and Names

Parameter Description	Symbol
Unsprung Mass for Suspension	$mu f_1$
Total mass of the system	ms
Suspension Spring Stiffness	$k f_1$
Tire Spring Stiffness	$kt f_1$
Damping Coefficient	$b f_1$

Equation of bouncing motion of the sprung mass:

$$\ddot{x}ms = -F_1 + u_1 \quad (4.1)$$

Governing equations of the vertical motion of unsprung masses are represented as:

$$\ddot{z}_{u_1}mu f_1 = F_1 T_f - Z_{U_1}kt f_1 - U_1 + Z_{r_1}kt f_1, \quad (4.2)$$

The governing equations for F term is specified as:

$$F_1 = b_{f_1}(\dot{Z}_{s_1} - \dot{Z}_{u_1}) + k_{f_1}(Z_{s_1} - Z_{u_1}) \quad (4.3)$$

4.4 8x8 Full Car model

Eight conventional quarter-car vibration models, which simulate each suspensions, are connected to get a 8x8 full car model. The resulting vehicle model has been implemented in MATLAB/Simulink environment.

Quarter car models are very often used because of being simple and it can simulate the basic characteristics of full car model. The spring, damper and an actuator placed between the sprung and unsprung masses compose a single suspension system.

By linking the eight quarter car models, a full car model can be designed in order to get a higher fidelity suspension model. The roll, pitch, yaw and the bouncing motions can be represented around the X, Y and Z axis. Figure 4.5 and Figure 4.6 show the 8x8 full car model with 22 degrees of freedom(DOF). Eight independent unsprung masses and the sprung mass are linked with a spring, damper and a force actuator. The intersection point of the roll axis and the pitch axis is also the center of gravity point of the vehicle. In Figure 4.5 and Figure 4.6, θ indicates the pitch angle and ϕ indicates the roll angle. For eight different suspensions, eight different number notations are used and 1, 2, 11, 22, 33, 44, 3, and 4 represent the related suspension system in the figures and equations. [41]

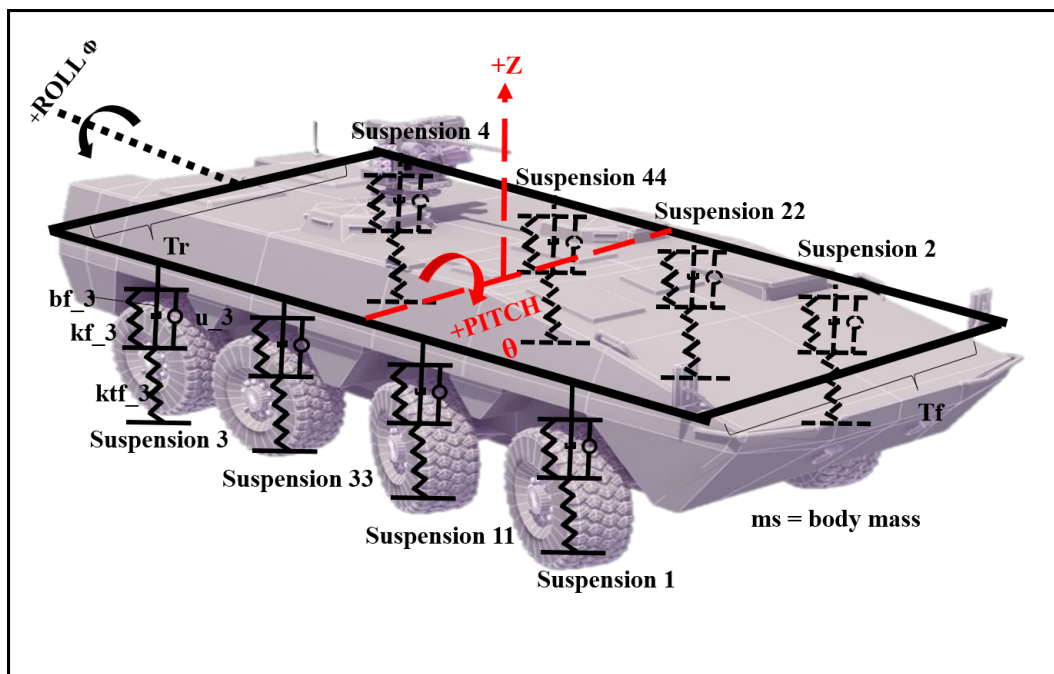


Figure 4.5: 8x8 Full Car Representation

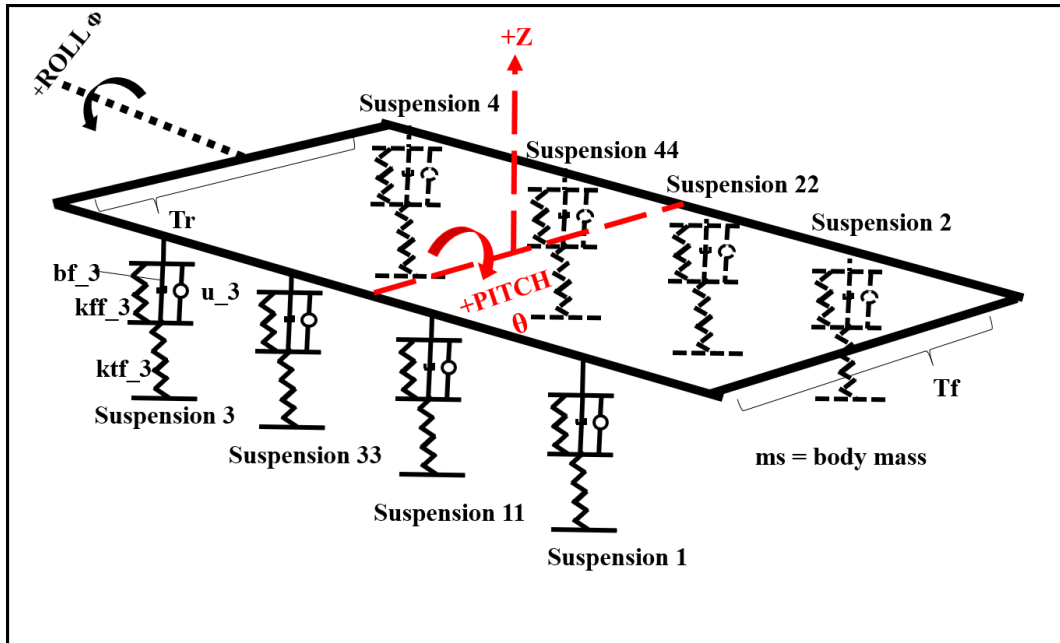


Figure 4.6: 8x8 Full Car Representation

4.4.1 Mathematical Modeling of The 8x8 Full Car

Table 4.2 states the parameters symbols and names, which are used in the equations of motions of the 8x8 full car model.

Parameter Description	Symbol
Unsprung Mass for Suspensions	$mu f_i$
Total mass of the vehicle	ms
Pitch Inertia	I_p
Roll Inertia	I_r
Suspension Spring Stiffness	$k f_i$
Tire Spring Stiffness	$kt f_i$
Suspension Damping Coefficient	$b f_i$
Dist. from vehicle cog to first axe	a
Dist. from vehicle cog to second axe	d
Dist. from vehicle cog to third axe	e
Dist. from vehicle cog to fourth axe	b

Table 4.2 continued from previous page

First Two Axle Half Threat	T_f
Last Two Axle Half Threat	T_r

Table 4.2: Parameter Symbols and Names

The forces on the sprung mass are based on the springs, dampers, and the actuators between the vehicle body and unsprung masses. A linear spring is used to simulate the wheel motion. Damping motion is based on the tire is neglected. The full car vibration model does not include the lateral and longitudinal forces and also wheel model and steering model. The road is assumed to slip under the 8x8 vehicle. The vibration model, which is used in the simulations, includes all of the coupled dynamics based on eight different suspension systems.

4.4.1.1 Assumptions in Modeling

The mathematical model of the 8x8 full car is constructed by simplifying the system by making several assumptions such as:

- Small displacement assumption is made. In other words, stiffness of the system is considered as constant.
- Small angle approximation is made since the difference between angles is so small.

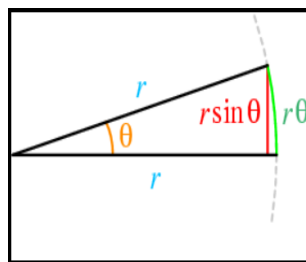


Figure 4.7: Small Angle Approximation [42]

- All of the components are considered as linear.

- Gravity is ignored since all of the displacements are obtained by considering the equilibrium conditions.
- Continuous ground contact.
- The vehicle is assumed as a rigid body.
- Wheel system is modeled by using only spring element. No damping element in wheel model.

4.4.1.2 Equations of Motion

Equation of bouncing motion of the sprung mass:

$$\ddot{x}_{ms} = -F_1 - F_2 - F_{11} - F_{22} - F_{33} - F_{44} - F_3 - F_4 + u_1 + u_2 + u_{11} + u_{22} + u_{33} + u_{44} + u_3 + u_4 \quad (4.4)$$

Equation of the pitch motion of the sprung mass:

$$\ddot{\theta}I_p = F_1a + F_2a + F_{11}d + F_{22}d - F_{33}e - F_{44}e - F_3b - F_4b - u_1a - u_2a - u_{11}d - u_{22}d + u_{33}e + u_{44}e + u_3b + u_4b, \quad (4.5)$$

Equation of the roll motion of the sprung mass:

$$\ddot{\phi}I_r = F_1T_f - F_2T_f + F_{11}T_f - F_{22}T_f + F_{33}T_r - F_{44}T_r + F_3T_r - F_4T_r - u_1T_f + u_2T_f - u_{11}T_f + u_{22}T_f - u_{33}T_r + u_{44}T_r - u_3T_r + u_4T_r, \quad (4.6)$$

Governing equations of the vertical motion of unsprung masses are represented as:

$$\ddot{z}_{U_1}muf_1 = F_1 - u_1 + ktf_1(Z_{r1} - Z_{U1}), \quad (4.7)$$

$$\ddot{z}_{U_2}muf_2 = F_2 - u_2 + ktf_2(Z_{r2} - Z_{U2}), \quad (4.8)$$

$$\ddot{z}_{U_{11}} m u f_{11} = F_{11} - u_{11} + k t f_{11} (Z_{r11} - Z_{U_{11}}), \quad (4.9)$$

$$\ddot{z}_{U_{22}} m u f_{22} = F_{22} - u_{22} + k t f_{22} (Z_{r22} - Z_{U_{22}}), \quad (4.10)$$

$$\ddot{z}_{U_{33}} m u f_{33} = F_{33} - u_{33} + k t f_{33} (Z_{r33} - Z_{U_{33}}), \quad (4.11)$$

$$\ddot{z}_{U_{44}} m u f_{44} = F_{44} - u_{44} + k t f_{44} (Z_{r44} - Z_{U_{44}}), \quad (4.12)$$

$$\ddot{z}_{U_3} m u f_3 = F_3 - u_3 + k t f_3 (Z_{r3} - Z_{U_3}), \quad (4.13)$$

$$\ddot{z}_{U_4} m u f_4 = F_4 - u_4 + k t f_4 (Z_{r4} - Z_{U_4}), \quad (4.14)$$

And the related kinematic equations are specified as:

$$Z_s - \phi_s T_f - \theta_s a = Z_{s1} \quad (4.15)$$

$$\dot{Z}_s - \dot{\phi}_s T_f - \dot{\theta}_s a = \dot{Z}_{s1} \quad (4.16)$$

$$Z_s + \phi_s T_f - \theta_s a = Z_{s2} \quad (4.17)$$

$$\dot{Z}_s + \dot{\phi}_s T_f - \dot{\theta}_s a = \dot{Z}_{s2} \quad (4.18)$$

$$Z_s - \phi_s T_f - \theta_s d = Z_{s11} \quad (4.19)$$

$$\dot{Z}_s - \dot{\phi}_s T_f - \dot{\theta}_s d = \dot{Z}_{s11} \quad (4.20)$$

$$Z_s + \phi_s T_f - \theta_s d = Z_{s22} \quad (4.21)$$

$$\dot{Z}_s + \dot{\phi}_s T_f - \dot{\theta}_s d = \dot{Z}_{s22} \quad (4.22)$$

$$Z_s - \phi_s T_r + \theta_s e = Z_{s33} \quad (4.23)$$

$$\dot{Z}_s - \dot{\phi}_s T_r + \dot{\theta}_s e = \dot{Z}_{s33} \quad (4.24)$$

$$Z_s + \phi_s T_r + \theta_s e = Z_{s44} \quad (4.25)$$

$$\dot{Z}_s + \dot{\phi}_s T_r + \dot{\theta}_s e = \dot{Z}_{s44} \quad (4.26)$$

$$Z_s - \phi_s T_r + \theta_s b = Z_{s3} \quad (4.27)$$

$$\dot{Z}_s - \dot{\phi}_s T_r + \dot{\theta}_s b = \dot{Z}_{s3} \quad (4.28)$$

$$Z_s + \phi_s T_r + \theta_s b = Z_{s4} \quad (4.29)$$

$$\dot{Z}_s + \dot{\phi}_s T_r + \dot{\theta}_s b = \dot{Z}_{s4} \quad (4.30)$$

The governing equations for F terms are specified as:

$$F_1 = b_{f1}(\dot{Z}_{s1} - \dot{Z}_{u1}) + k_{f1}(Z_{s1} - Z_{u1}) \quad (4.31)$$

$$F_2 = b_{f2}(\dot{Z}_{s2} - \dot{Z}_{u2}) + k_{f2}(Z_{s2} - Z_{u2}) \quad (4.32)$$

$$F_{11} = b_{f11}(\dot{Z}_{s11} - \dot{Z}_{u11}) + k_{f11}(Z_{s11} - Z_{u11}) \quad (4.33)$$

$$F_{22} = b_{f22}(\dot{Z}_{s22} - \dot{Z}_{u22}) + k_{f22}(Z_{s22} - Z_{u22}) \quad (4.34)$$

$$F_{33} = b_{f33}(\dot{Z}_{s33} - \dot{Z}_{u33}) + k_{f33}(Z_{s33} - Z_{u33}) \quad (4.35)$$

$$F_{44} = b_{f44}(\dot{Z}_{s44} - \dot{Z}_{u44}) + k_{f44}(Z_{s44} - Z_{u44}) \quad (4.36)$$

$$F_3 = b_{f3}(\dot{Z}_{s3} - \dot{Z}_{u3}) + k_{f3}(Z_{s3} - Z_{u3}) \quad (4.37)$$

$$F_4 = b_{f4}(\dot{Z}_{s4} - \dot{Z}_{u4}) + k_{f4}(Z_{s4} - Z_{u4}) \quad (4.38)$$

Body mass and unsprung masses are represented as m_s and m_{uf_i} , respectively. I_p and I_r are the pitch inertia and the roll inertia of the system. Spring stiffness and tire stiffness are represented as k_{f_i} and k_{t_i} , respectively, and b_{f_i} is the damping coefficient. Distance between the center of gravity and first axle, second axle, third axle and fourth axle represented as a , d , e and b , respectively. The first axle is the closest to the front of the vehicle. Finally, first two axle width represented as T_f and T_r while the first two axle half threat and the last the axle half width represented as T_f and T_r .

Further, Z_{r_i} represents the road inputs at the related individual tire for all of the eight suspension systems. Z_{u_i} are the vertical distances of the unsprung masses and the x is the vertical distance of the whole body. Additionally, u_i terms indicate the input forces for all eight suspension systems, which are generated by the actuators with the inputs, which are coming from the optimal controller, where $i = [1, 2, 11, 22, 33, 44, 3, 4]$ and each "i" term indicates the related suspensions, which are represented in Figure 4.5 and 4.6.

4.5 Comparison of the Quarter Car and the 8x8 Full Car Model

The most importance difference between the quarter car model and full car model is the capabilities of the models. By using quarter car model, which is the most simplest model, only vertical motion of a quarter vehicle can be analyzed. On the other hand, full car model provides analyzes for all of the motions such as: pitch motion, roll motion and vertical motion. Since this study focuses on the evaluation of the personnel comfort for a 8x8 heavy weight vehicle, all of the motions have to be taken into account in order to make more realistic analyzes.

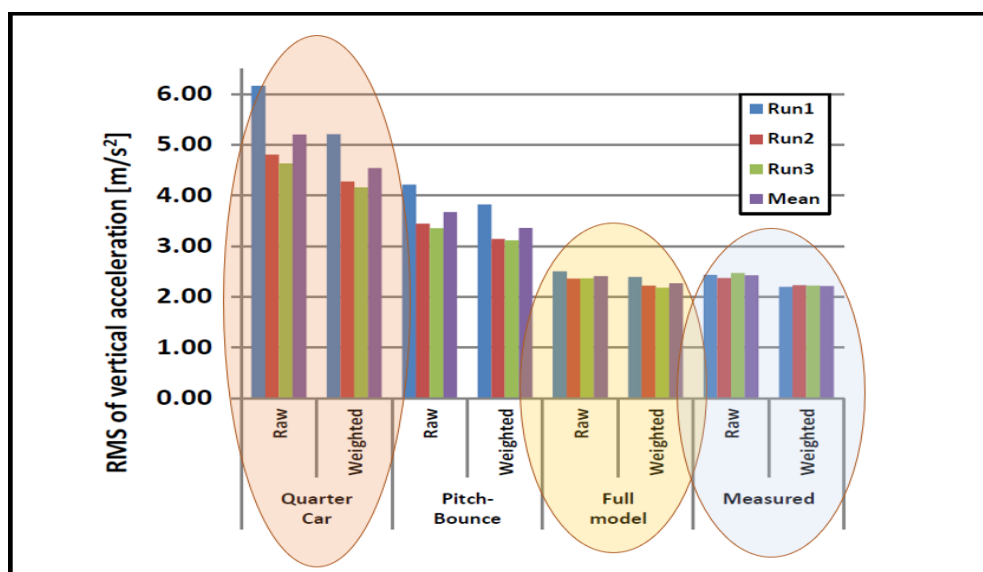


Figure 4.8: Comparison Between Quarter Car Model, Full Car Model and Measured Data [43]

Furthermore, Hamersma and Els, S. from the University of Pretoria had made a comparison of quarter car model and full car model with experimental data [43]. Their paper compares the response of the quarter car and full car model with the measured response of a real car. When they consider the ride comfort mode, the error for the quarter car model was 114 percent with respect to the RMS value of the vertical acceleration value while the error of the full car model 1 percent with respect to the RMS value of the vertical acceleration in comparison with the measured data. Their result proves that there is an important discrepancy between the results of quarter car

simulation results and the measured results and also their study is an evident that the full car model provides much more realistic and acceptable results than the quarter car model when comparing RMS values of the body acceleration of the chassis. Their suggestion for the researchers in the field of active suspension control is that in order not to encounter with the erroneous conclusions, the limitations of the quarter car model for the comfort problems has to be taken into account.

Table 4.3: Quarter Car Simulation Input Parameters and Their Values

Parameter Description	Symbol	Value
Unsprung Mass for Suspensions	m_{uf_1}	200kg
Total Mass of the Vehicle	m_s	3100kg
Spring Stiffness	k_{f_1}	180000N/m
Tire Stiffness for Suspension	kt_{f_1}	400000N/m
Damping Coefficient	b_{f_1}	20000Ns/m

Table 4.4: Full Car Simulation Input Parameters and Their Values

Parameter Description	Symbol	Value
Unsprung Mass for Suspensions	$m_{uf_i} = m_{ur_i}$	200kg
Total Mass of the Vehicle	m_s	25000kg
Pitch Inertia	I_p	90000kgm ²
Roll Inertia	I_r	30000kgm ²
Spring Stiffness	k_{f_i}	180000N/m
Tire Stiffness for Suspension	kt_{f_i}	400000N/m
Damping Coefficient	b_{f_i}	20000Ns/m
Dist. from vehicle cog to first axe	a	2m
Dist. from vehicle cog to second axe	d	1m
Dist. from vehicle cog to third axe	e	1m
Dist. from vehicle cog to fourth axe	b	2m
First Two Axle Half Threat	T_f	1.3m
Last Two Axle Half Threat	T_r	2.6m

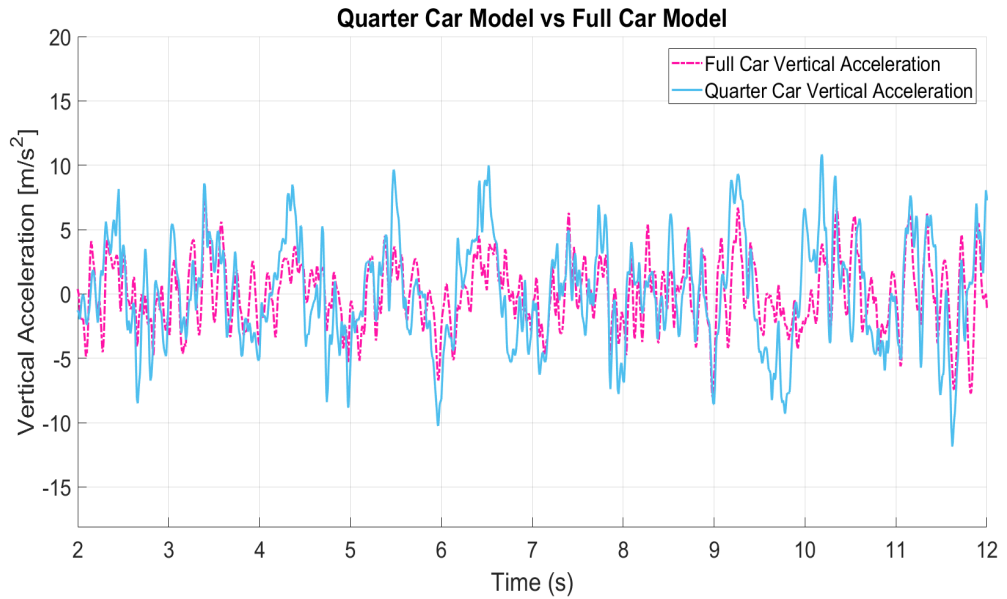


Figure 4.9: Full Car and Quarter Car Comparison

The Figure 4.9 shows the quarter car and full car simulation results for this study with the values of the parameters in the tables above. The RMS of the vertical acceleration for quarter car model is 4.9136 ,while the RMS value for the full car model is 2.8367. This result also supports the results of the paper of the Pretoria University [43].

As a result of the study of the Pretoria University [43] and the pitch and roll evaluation capability of the full car model, the 8x8 full car model is constructed and used in the simulations of this study in order to evaluate the personnel comfort more realistically. Furthermore, in the controller design processes, the full car model is also used to determine the design matrices Q and R since the vertical acceleration information is directly related with the force and thus with the required actuator force which is generated by using the controller design parameters.

CHAPTER 5

CONTROL AND SIMULATION OF The VEHICLE

5.1 Control of the Vehicle

5.1.1 Introduction

Passive suspension systems provide options to the customers; comfort and performance. On the other hand, active suspension systems create a chance to control the conflicting parameters of control and performance. By doing this, active suspension systems provide improvement in both side of the vehicle along with vertical body control. This chapter discourses the control and the simulation of the active suspension system in MATLAB / Simulink environment.

5.1.2 Literature Survey

In the light of the trend that wheeled vehicles are replacing tracked vehicles in defense industry, suspension systems have an important role on improving the mobility capabilities. Researchers have been working on active and semi-active suspension systems for years and numerous papers have been published as a result of those studies. However, almost all of the studies are limited to commercial 4x2 or 4x4 automobile industries. On the other hand, this thesis develops a structure for a 8x8 vehicle. Goodall and Kortum [54] published an overview about the active suspension systems used in automobiles and trains. Suspension control theories are generally investigated based on six different control algorithms; classic control [55], optimal control [56], nonlinear control [57], robust control [58], adaptive control [59] and intelligent

control [60].

One of the most straightforward and widely-used approach for active suspensions is the sky-hook control methodology, which is used to hang up the vehicle chassis on a virtual sky. In the literature, there are lots of applications using the sky-hook theorem and a quarter car model for the analysis [22], [28], [26]. Furthermore, tire oscillations are taken into account in ground-hook control methodology [34].

Intelligence based algorithms such as fuzzy logic have advantages of providing good performance for body acceleration and road handling, however these algorithms can cause serious stability issues. Nonlinear adaptive approaches enhance the performance of active suspension systems but those studies need Lyapunov adaptation. Nonlinear backstepping theories are apt to be adaptive to the different road distributions; on the other hand, they have highly nonlinear dynamics. Sliding mode controls are highly robust approaches to the uncertainties but those approaches need some different techniques such as nonlinear gains, dynamic extensions or higher order sliding mode control in order to overcome the chattering, which is a high-frequency motion that causes the fact that no ideal sliding mode can be obtained in real world.

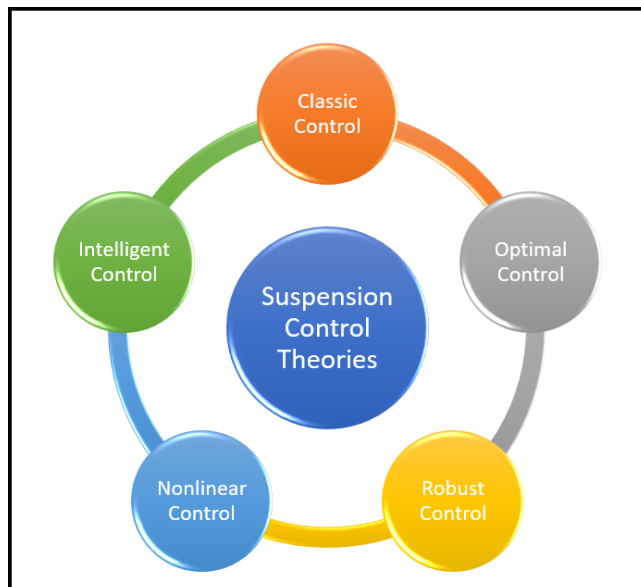


Figure 5.1: Suspension Systems Control Theories

One of the most powerful methodology for controlling the linear systems is the linear quadratic regulator method. This technique requires an optimal controller gain which can be easily obtained by using the solution of the algebraic ricatti equation. In the literature, there are several applications of the LQR methodology [35],[36],[37].

Beyond all of these control approaches, this thesis focuses on the optimal control theories. Considering the complicated 8x8 vehicle suspension structure, using optimal controller overcomes the difficulties based on the systems, which have powerful couplings between their states. Furthermore, the optimal controller provides an easy way to minimize the pre-defined performance parameter. On the other hand, optimal controller approaches are not capable of being adaptive to the differing system parameters. To overcome those drawbacks, some extra methods such as observers, gain scheduling systems or extra gains, which make the system road-adaptive, can be used. In this study, feed forward gain is used for the prescan suspension system.

5.1.3 LQR Optimal Control Method

To develop optimal control structure and calculate feedback gains, the block diagram, which is shown in Figure 5.2, is used.

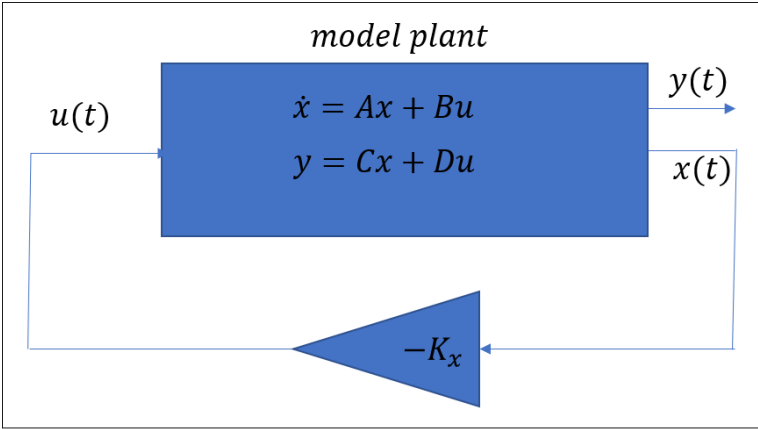


Figure 5.2: State-Feedback Controller Loop

The state space equation of the system based on the Figure 5.2 is specified as:

$$\begin{cases} \dot{x} = Ax + Bu \\ y = Cx + Du \end{cases} \quad (5.1)$$

where x is the state vector of 22 variables.

$$x = \{\phi_s, \theta_s, Z_s, Z_{U1}, Z_{U2}, Z_{U11}, Z_{U22}, Z_{U33}, Z_{U44}, Z_{U3}, Z_{U4}, \dot{\phi}_s, \dot{\theta}_s, \dot{Z}_s, \dot{Z}_{U1}, \dot{Z}_{U2}, \dot{Z}_{U11}, \dot{Z}_{U22}, \dot{Z}_{U33}, \dot{Z}_{U44}, \dot{Z}_{U3}, \dot{Z}_{U4}\}^T \quad (5.2)$$

and

$$\dot{x} = \{x_{12}, x_{13}, x_{14}, x_{15}, x_{16}, x_{17}, x_{18}, x_{19}, x_{20}, x_{21}, x_{22}, \ddot{\phi}_s, \ddot{\theta}_s, \ddot{Z}_s, \ddot{Z}_{U1}, \ddot{Z}_{U2}, \ddot{Z}_{U11}, \ddot{Z}_{U22}, \ddot{Z}_{U33}, \ddot{Z}_{U44}, \ddot{Z}_{U3}, \ddot{Z}_{U4}\}^T \quad (5.3)$$

Additionally, the vector U gives the eight control forces for the eight hydraulic actuators that generate force between sprung and unsprung masses for related suspension systems.

$$u = \begin{pmatrix} u_1 \\ u_2 \\ u_{11} \\ u_{22} \\ u_{33} \\ u_{44} \\ u_3 \\ u_4 \end{pmatrix} \quad (5.4)$$

Equation 5.1 is used to obtain the state space form, which is necessary to apply the linear control theories with the help of the system matrices; A and B .

The linear quadratic regulator methodology is a well known process for active suspension system. The most important benefit of the approach is that the performance

parameters can be tuned according to the optimization purposes. In this study the LQR methodology has been used to improve the personnel comfort for 8x8 full car. In preview suspension system the LQR gain is enhanced by a feed-forward gain in order to make the suspension system road-adaptive. The controller design equations to obtain the controller gains are states below in detail [44].

The new actuator force vector is:

$$u(t) = -K_x x(t) \quad (5.5)$$

where K is the feedback gain vector, which is calculated in this study with the help of MATLAB optimization toolbox.

One of the purpose of the study is to determine an optimal gain K and eight actuator forces based on this K in order to optimize the suspensions to improve the personnel comfort. The performance characteristics are represented by the performance index \mathcal{J} , and the optimal controller is designed to minimize this performance function, which is;

$$\mathcal{J} = \int_0^{\infty} \mathcal{F}(u, x, t) = \int_0^{\infty} (x^T Q(t)x + u^T R(t)u) dt \quad (5.6)$$

The matrix $Q(t)$ is symmetric and positive semi-definite and also the matrix $R(t)$ is positive semi definite matrix. Relatively high elements of $Q(t)$ compared to the $R(t)$ result in tight control and small errors in the states with considerable inputs.

Generally, in optimization problems, the objective is not to minimizing of all of the states, only minimize a selected output according to the $y(t)$. So, the objective function becomes:

$$\mathcal{J} = \int_0^{\infty} (y^T Q_y(t)x + u_y^T R(t)u) dt \quad (5.7)$$

where $Q_y(t)$ is the weighting matrix of measured output and $R_u(t)$ is the weighting matrix of inputs.

When we substitute $y(t)$ from 5.1 to 5.7, the equation becomes:

$$\begin{aligned}
\mathcal{J} &= \int_0^{\infty} [Cx + Du]^T Q_y (Cx + Du) + u^T R_u u \\
&= \int_0^{\infty} [x^T (C^T Q_y C)x + 2x^T (C^T Q_y D)u + u^T (D^T Q_y D + R_u)u] dt \\
&= \int_0^{\infty} [x^T Q x + u^T R u] dt
\end{aligned} \tag{5.8}$$

In the equation 5.8, the N term is omitted and taken as zero. To solve the LQR problem, among the alternative methodologies, the Pontryagin's maximum principle is used in this study. This methodology says that the optimal input of the system that minimizes the J has also to minimize the so-called Hamiltonian.

$$\begin{aligned}
\mathcal{H}(u, x, \lambda, t) &= \mathcal{F}(u, x, t) + \lambda^T (Ax + Bu) \\
&= x^T Q x + u^T R u + \lambda^T (Ax + Bu)
\end{aligned} \tag{5.9}$$

where λ is the dynamic lagrange multipliers. Then when we combine the equations 5.6 and 5.10, the objective function can be written as:

$$\begin{aligned}
\mathcal{J}(u, x, \lambda, t) &= \int_0^{\infty} \mathcal{F}(u, x, t) = \int_0^{\infty} \mathcal{H} - \lambda^T (Ax + Bu) \\
&= - \int_0^{\infty} \lambda^T \dot{x} dt + \int_0^{\infty} \mathcal{H} dt
\end{aligned} \tag{5.10}$$

Then the partial integration of the term which includes lagrange multiplier

$$\begin{aligned}
\mathcal{J}(u, x, \lambda, t) &= - \lambda^T x \Big|_0^{\infty} + \int_0^{\infty} \dot{\lambda}^T x dt + \int_0^{\infty} \mathcal{H} dt \\
&= \lambda_0^T x_0 + \int_0^{\infty} \dot{\lambda}^T x dt + \int_0^{\infty} \mathcal{H} dt
\end{aligned} \tag{5.11}$$

where, for the initial condition:

$$x_0 = x(0) \tag{5.12}$$

and for the the asymptotic value:

$$x(\infty) = 0 \tag{5.13}$$

At this point, if the $\delta(x)$ and $\delta(u)$ variations of the states and the inputs are introduced, the first order Taylor series expansion of the objective function about the optimal point can be derived as:

$$\mathcal{J}(u + \delta(u), x + \delta(x), \lambda, t) \approx \mathcal{J}(u, x, \lambda, t) + \left[\left(\frac{\partial \mathcal{J}}{\partial x} \right)^T \delta(x) + \left(\frac{\partial \mathcal{J}}{\partial u} \right)^T \delta(u) \right] \quad (5.14)$$

The first order term of the expansion must be vanished according to the necessary condition of the local extremum:

$$\begin{aligned} \delta(j) &= \mathcal{J}(u + \delta(u), x + \delta(x), \lambda, t) - \mathcal{J}(u, x, \lambda, t) \\ &= \left[\left(\frac{\partial \mathcal{J}}{\partial x} \right)^T \delta(x) + \left(\frac{\partial \mathcal{J}}{\partial u} \right)^T \delta(u) \right] = 0 \end{aligned} \quad (5.15)$$

This condition can be satisfied if and only if:

$$\begin{aligned} \left(\frac{\partial \mathcal{J}}{\partial x} \right) &= 0 \\ \left(\frac{\partial \mathcal{J}}{\partial u} \right) &= 0 \end{aligned} \quad (5.16)$$

By using the equation 5.11, the first part of the equation 5.16 becomes:

$$\left(\frac{\partial \mathcal{J}}{\partial x} \right) = 0 = \int_0^\infty \dot{\lambda} dt + \int_0^\infty \left(\frac{\partial \mathcal{H}}{\partial x} \right) \Rightarrow \dot{\lambda} = - \frac{\partial \mathcal{H}}{\partial x} \quad (5.17)$$

Or by using the equation 5.9:

$$\dot{\lambda} = -2Qx - A^T \lambda \quad (5.18)$$

By using the equations 5.11 and 5.16, it can be derived that:

$$\begin{aligned} \frac{\partial \mathcal{J}}{\partial U} = 0 &= \frac{\partial \mathcal{H}}{\partial u} \\ &= 2Ru + B^T \lambda \end{aligned} \quad (5.19)$$

which can be obtained for the optimal input as:

$$u(t) = -R^{-1}\left(\frac{1}{2}B^T\lambda\right) \quad (5.20)$$

Equation 5.20 proves that the input function $u(t)$ is depend on the states and co-state vector λ_t . By using the riccati equation, the λ_t term can be omitted.

$$\lambda = 2Px \quad (5.21)$$

Where P is the riccati matrix. Finally the optimal control for state-feedback controller becomes:

$$u(t) = -R^{-1}B^TPx = -K_x \quad (5.22)$$

And Riccati equation has to be satisfied by the matrix P :

$$A^TP + PA - PBR^{-1}B^TP + Q = 0 \quad (5.23)$$

where Q is the weighting matrix and the R is the cost constant. Since the 8x8 vehicle has 22 states, which are stated above, the size of the Q matrix is 22x22 and since the system has 8 input forces for 8 suspension system, the size of the R matrix is 8x8. Furthermore, A widespread usage of the Q matrix and the R matrix is diagonal.

$$Q_{22 \times 22} = \begin{bmatrix} q_1 & 0 & \cdot & \cdot & \cdot & 0 \\ 0 & q_2 & \cdot & \cdot & \cdot & \cdot \\ \cdot & \cdot & \cdot & \cdot & \cdot & \cdot \\ \cdot & \cdot & \cdot & \cdot & \cdot & \cdot \\ \cdot & \cdot & \cdot & \cdot & q_{21} & 0 \\ 0 & \cdot & \cdot & \cdot & 0 & q_{22} \end{bmatrix}_{22 \times 22} \quad (5.24)$$

and R Matrix:

$$R_{8 \times 8} = \begin{bmatrix} r_1 & 0 & \cdot & \cdot & \cdot & \cdot & \cdot & 0 \\ 0 & r_2 & \cdot & \cdot & \cdot & \cdot & \cdot & \cdot \\ \cdot & \cdot & \cdot & \cdot & \cdot & \cdot & \cdot & \cdot \\ \cdot & \cdot & \cdot & \cdot & \cdot & \cdot & \cdot & \cdot \\ \cdot & \cdot & \cdot & \cdot & r_7 & 0 & \cdot & \cdot \\ 0 & \cdot & \cdot & \cdot & 0 & r_8 & \cdot & \cdot \end{bmatrix}_{8 \times 8} \quad (5.25)$$

The first step to obtain the Q and R matrices is to decide the most influential $q_i =$ and r_i values when considering the vertical acceleration response of the system. Since a complete simulation is constructed in order to evaluate all of the system responses, the trial and error method is used to eliminate the relatively less influential $q_i =$ and r_i values. After conducting several simulation runs, it is observed that the most influential states for the vertical acceleration response are the unsprung mass velocities. Therefore, all of the $q_i =$ values except from the unsprung mass velocities remain as zero and the $q_i =$ values for the unsprung mass velocities are considered as the same value since all of them are the velocities related with the corresponding suspension system. On the other hand, since the cost of each actuator input are assumed as the same, all of the $r_i =$ values are selected as the same value. The new formation of the Q and R matrices become:

$$Q_{22 \times 22} = q * \begin{bmatrix} 0 & \cdot & \cdot & \cdot & \cdot & \cdot & \cdot & \cdot & \cdot & 0 \\ \cdot & \cdot & \cdot & \cdot & \cdot & \cdot & \cdot & \cdot & \cdot & \cdot \\ \cdot & \cdot & \cdot & \cdot & \cdot & \cdot & \cdot & \cdot & \cdot & \cdot \\ \cdot & \cdot & 0 & \cdot & \cdot & \cdot & \cdot & \cdot & \cdot & \cdot \\ \cdot & \cdot & \cdot & 1_{(15,15)} & \cdot & \cdot & \cdot & \cdot & \cdot & \cdot \\ \cdot & \cdot & \cdot & \cdot & 1_{(16,16)} & \cdot & \cdot & \cdot & \cdot & \cdot \\ \cdot & \cdot & \cdot & \cdot & \cdot & \cdot & \cdot & \cdot & \cdot & \cdot \\ \cdot & \cdot & \cdot & \cdot & \cdot & \cdot & \cdot & \cdot & \cdot & \cdot \\ \cdot & \cdot & \cdot & \cdot & \cdot & \cdot & \cdot & 1_{(21,21)} & 0 & \cdot \\ 0 & \cdot & \cdot & \cdot & \cdot & \cdot & \cdot & 0 & 1_{(22,22)} & \cdot \end{bmatrix}_{22 \times 22} \quad (5.26)$$

and

$$R_{8 \times 8} = r * \begin{bmatrix} 1 & 0 & . & . & . & 0 \\ 0 & 1 & . & . & . & . \\ . & . & . & . & . & . \\ . & . & . & . & . & . \\ . & . & . & . & 1 & 0 \\ 0 & . & . & . & 0 & 1 \end{bmatrix}_{8 \times 8} \quad (5.27)$$

The next step is selecting the q and r values. The q and r values are obtained by considering the system constraints which are stated in the next subsection.

Constraints of the Optimization Problem:

The design of the controller requires constraints in order to obtain more closer results to the actual situation. In other words, the definite non-negative weighting matrix Q and definite positive cost matrix R have to be designed by taking the constraints into account. The optimization of the objective function \mathcal{J} does not ensure that all of system parameters and requirements stay in the limitations. Therefore, according to Paucer, W. [45] the Q and R matrices have to be selected by considering the system limitations in order not to violate the constraints and in order to be more closer to the actual situation.

When we consider the optimization problem of this study, the most important constraints are the **actuator limits** and the **suspension travel limits** for each suspension systems.

Actuator Limit: When we consider the optimization problem of this study, the first and the most important system constraint, that has to be satisfied when selecting the Q and R matrices that minimize the cost function \mathcal{J} , is the actuator capacities for the active suspension system.

In the active suspension system, the most critical element is the force actuating element. For the force actuating system, a precision linear electromechanical actuator system is selected to be used in the active suspension system. Precision linear actuators provide better performance than the hydraulic or pneumatic systems in the

Table 5.1: Thomson T13-B5010MU090-04 [47]

Characteristics	
Maximum Linear Force ($F_{\{x\}}$)	60000N
Weight (Per Actuator)	42.5 kg

light of the advantages of simpler and smaller installation, lower energy consumption, easier control, higher accuracy, less maintenance and less noise. In other words, using electromechanical actuators improves the controllability, accuracy and reliability [46]. Detailed comparison of the electromechanical actuator with the hydraulic actuator and pneumatic actuator is stated in the Table B.1 in Appendix B.1 [47].

In the light of the information in the Table B.1 in Appendix B.1 [47], it is decided to use the electromechanical actuator. Since the vehicle is heavy weight 8x8 off-road vehicle a high precision and high force capacity electromechanical actuator, which is the T130 model of the Thomson Company [47], is selected.

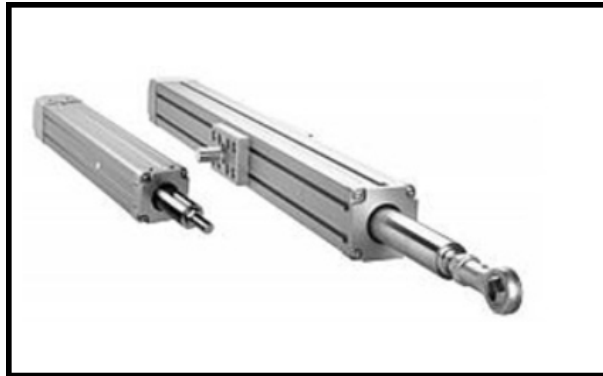


Figure 5.3: Thomson T130 High Precision Electromechanical Actuator [47]

Therefore, the limit of the actuator force ($actlimit$) is considered as 60 000N in the simulations and this information is used to obtain the q and r values.

Suspension Travel Limit:

Suspension travel is the mechanical limit of the suspension movement. The upper limit of the suspension travel is considered to hit the suspension limiter or suspension stop, being determined by the variable $suspm_{max}$. In any time, the suspension should

not hit suspension stop bumps [48]. According to Gillespie (1992) [48], the author states that for most of the passenger cars, the upper limit of the suspension travel is between 0.177 and 0.2032 meters. On the other hand, in this thesis the corresponding vehicle is not a standard passenger car, the vehicle is a 8x8 military off-road vehicle. Therefore, by considering the suspension size and total mass of the 8x8 military land vehicle, the $suspmax$ is considered as 0.4 meters for this heavy weight 8x8 land vehicle [49]. Timomey, which is a company that produces independent suspension systems, also states that their off-highway 87150 series product provides 400 mm suspension travel negotiates the roughest terrain while maintaining traction on all-wheel for final drive and through drive axles for 8x8 configurations [49].

Finally, the optimization problem becomes to minimize the root mean square of the vertical acceleration of the vehicle body under:

$$\begin{cases} F_{actuator,i} \leq actlimit = 60000N & \text{where } i = 1, 2, 3, 4, 5, 6, 7, 8 \\ Z_{s,i} - Z_{u,i} \leq suspmax = 0.4m & \text{where } i = 1, 2, 3, 4, 5, 6, 7, 8 \end{cases} \quad (5.28)$$

The next step is to find the Q and R matrices that minimize the vertical acceleration. In order to find the design matrices, the most drastic off-road condition, that passive suspension can handle, is considered. The most drastic condition is determined by using the ISO 8608 road profile standard [50], ISO 2631 mechanical vibration and shock evaluation of human exposure to whole body vibration standard [51] and US Army ride dynamics and evaluation of human exposure to whole body vibration procedure [52]. According to the references [50], [51] and [52], when the vehicle uses the passive suspension system with a speed of 5km/h on a H standard road [51], the vehicle exceeds the absorb power limit, which is 6 watt according to the reference [52]. Therefore 5 km/h speed for passive suspension system on a H type road is selected as the most drastic condition, that pushes the limits of the force actuator and suspension travel. Detailed expressions of absorb power, road types and corresponding standards will be stated in Chapter 7.

After deciding the limits of the optimization problem and the most drastic condition, the final step is to determine the Q and R values that pushes the limit of the optimization problem on the most drastic condition. It is obvious that to choose large Q matrix

and small R matrix, minimizes the vertical acceleration value in time domain [53]. Therefore, the q value has been increased and the r value has been decreased until the suspension travel and actuator force push the limit of the optimization problem, which are stated as $actlimit$ and $suspmax$, on the most drastic condition, which is determined above. The q value has been increased, and the r value has been decreased until the saturation starts on the limits of suspension travel and actuator force. Finally, the q is obtained as $8x10^7$ and r is obtained as 0.3.

$$Q_{22 \times 22} = 8x10^7 * \begin{bmatrix} 0 & \cdot & \cdot & \cdot & \cdot & \cdot & \cdot & \cdot & \cdot & 0 \\ \cdot & \cdot & & & & & & & & \cdot \\ \cdot & & \cdot & & & & & & & \cdot \\ \cdot & & & 0 & & & & & & \cdot \\ \cdot & & & & 1_{(15,15)} & & & & & \cdot \\ \cdot & & & & & 1_{[(16,16)} & & & & \cdot \\ \cdot & & & & & & \cdot & & & \cdot \\ \cdot & & & & & & & \cdot & & \cdot \\ \cdot & & & & & & & & 1_{(21,21)} & 0 \\ 0 & \cdot & \cdot & \cdot & \cdot & \cdot & \cdot & \cdot & 0 & 1_{(22,22)} \end{bmatrix}_{22 \times 22} \quad (5.29)$$

and

$$R_{8 \times 8} = 0.3 * \begin{bmatrix} 1 & 0 & \cdot & \cdot & \cdot & \cdot & \cdot & 0 \\ 0 & 1 & \cdot & \cdot & \cdot & \cdot & \cdot & \cdot \\ \cdot & \cdot & \cdot & \cdot & \cdot & \cdot & \cdot & \cdot \\ \cdot & \cdot & \cdot & \cdot & \cdot & \cdot & \cdot & \cdot \\ \cdot & \cdot & \cdot & \cdot & \cdot & \cdot & \cdot & \cdot \\ \cdot & \cdot & \cdot & \cdot & \cdot & 1 & 0 & \cdot \\ 0 & \cdot & \cdot & \cdot & \cdot & 0 & 1 & \cdot \end{bmatrix}_{8 \times 8} \quad (5.30)$$

The limits for actuator force and suspension travel on the selected most drastic road condition for passive suspension system can be seen in the next two figures.

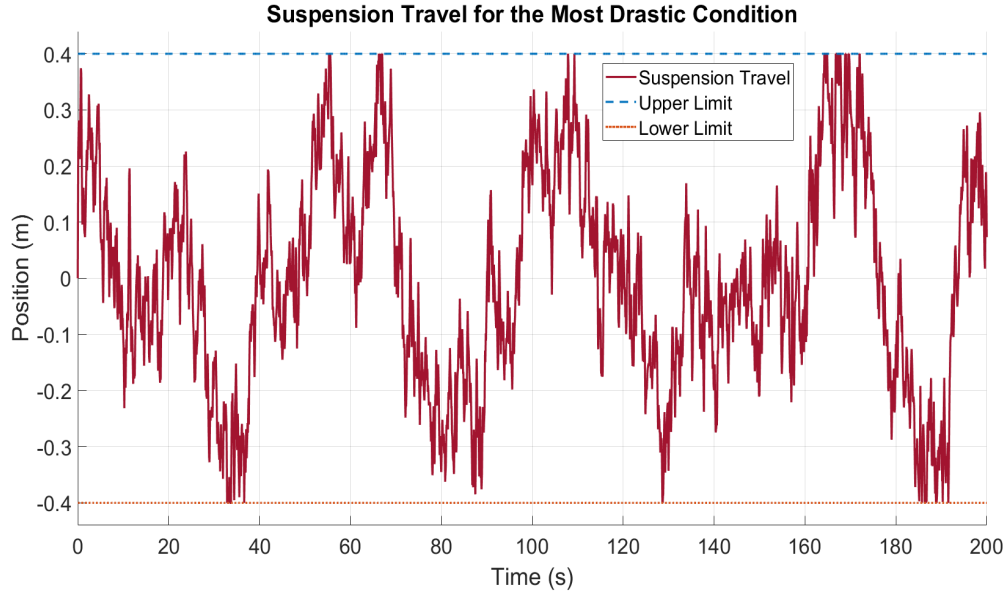


Figure 5.4: Suspension 1 Travel for selected Q and R Values on the most drastic Road Condition

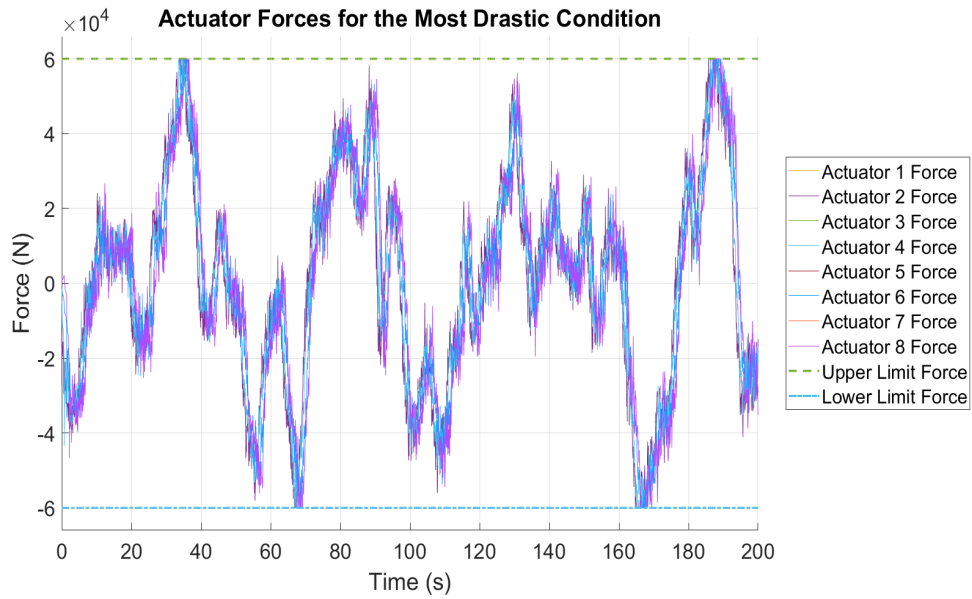


Figure 5.5: Actuator Forces for selected Q and R Values on the most drastic Road Condition

Finally, K_x matrix:

$$K_{x,(8 \times 22)} = \begin{bmatrix} K_{x,(:,1:8)} & K_{x,(:,9:14)} & K_{x,(:,15:20)} & K_{x,(:,21:22)} \end{bmatrix} \quad (5.31)$$

and $K_{x,(:,1:8)}$, $K_{x,(:,9:16)}$, $K_{x,(:,17:22)}$ are derived as shown below:

$$K_{x,(:,1:8)} = \begin{pmatrix} 0 & 0 & 0 & -17114 & -3612.1 & -14371.0 & -868.3 & -8883.5 \\ 0 & 0 & 0 & -3612 & -17114.7 & -868.3 & -14371.0 & 4619.1 \\ 0 & 0 & 0 & -14371 & -868.3 & -12999.1 & 503.5 & -10255.4 \\ 0 & 0 & 0 & -868 & -14371.0 & 503.5 & -12999.1 & 3247.3 \\ 0 & 0 & 0 & -8883 & 4619.1 & -10255.4 & 3247.3 & -12999.1 \\ 0 & 0 & 0 & 4619 & -8883.5 & 3247.3 & -10255.4 & 503.5 \\ 0 & 0 & 0 & -6139 & 7362.9 & -8883.5 & 4619.1 & -14371.0 \\ 0 & 0 & 0 & 7362 & -6139.8 & 4619.1 & -8883.5 & -868.3 \end{pmatrix} \quad (5.32)$$

$$K_{x,(:,9:14)} = \begin{pmatrix} 4619.1 & -6139.8 & 7362.9 & -2829.4 & -4477.9 & 2211.9 \\ -8883.5 & 7362.9 & -6139.8 & 2829.4 & -4477.9 & 2211.9 \\ 3247.3 & -8883.5 & 4619.1 & -2829.4 & -2239.0 & 2211.9 \\ -10255.4 & 4619.1 & -8883.5 & 2829.4 & -2239.0 & 2211.9 \\ 503.5 & -14371.0 & -868.3 & -2829.4 & 2239.0 & 2211.9 \\ -12999.1 & -868.3 & -14371.0 & 2829.4 & 2239.0 & 2211.9 \\ -868.3 & -17114.7 & -3612.1 & -2829.4 & 4477.9 & 2211.9 \\ -14371.0 & -3612.1 & -17114.7 & 2829.4 & 4477.9 & 2211.9 \end{pmatrix} \quad (5.33)$$

$$K_{x,(:,15:20)} = \begin{pmatrix} -5763.2 & 10.5 & 48.0 & 1.7 & 30.4 & -15.8 \\ 10.5 & -5763.2 & 1.7 & 48.0 & -15.8 & 30.4 \\ 48.0 & 1.7 & -5776.3 & -2.7 & 34.8 & -11.4 \\ 1.7 & 48.0 & -2.7 & -5776.3 & -11.4 & 34.8 \\ 30.4 & -15.8 & 34.8 & -11.4 & -5776.3 & -2.7 \\ -15.8 & 30.4 & -11.4 & 34.8 & -2.7 & -5776.3 \\ 21.6 & -24.6 & 30.4 & -15.8 & 48.0 & 1.7 \\ -24.6 & 21.6 & -15.8 & 30.4 & 1.7 & 48.0 \end{pmatrix} \quad (5.34)$$

$$K_{x,(:,21:22)} = \begin{pmatrix} 21.6 & -24.6 \\ -24.6 & 21.6 \\ 30.4 & -15.8 \\ -15.8 & 30.4 \\ 48.0 & 1.7 \\ 1.7 & 48.0 \\ -5763.2 & 10.5 \\ 10.5 & -5763.2 \end{pmatrix} \quad (5.35)$$

5.1.4 Preview Control Method

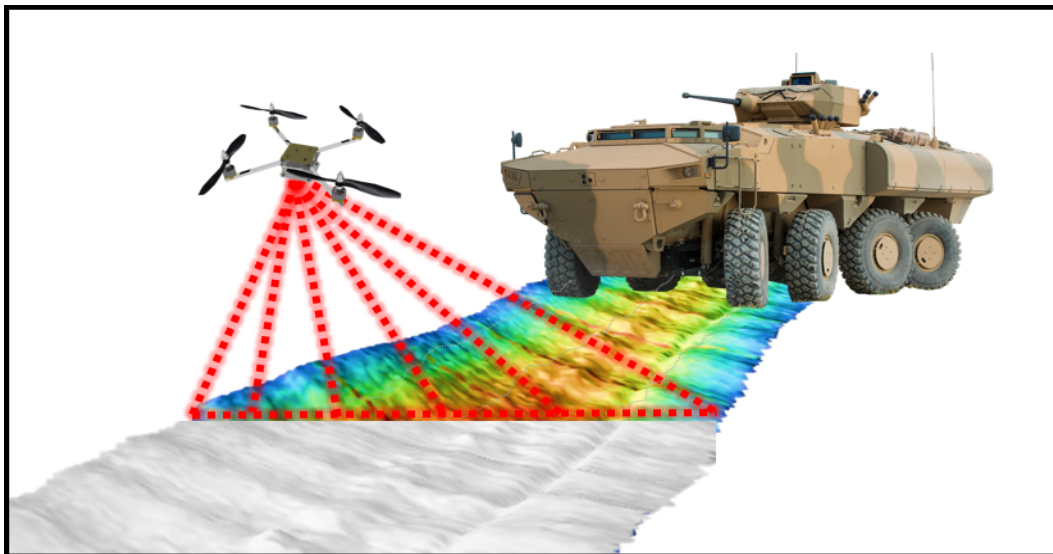


Figure 5.6: Preview Sensor Representation

To develop preview optimal control structure and calculate feedback gains, the block diagram, which is shown in Figure 5.7, is used.

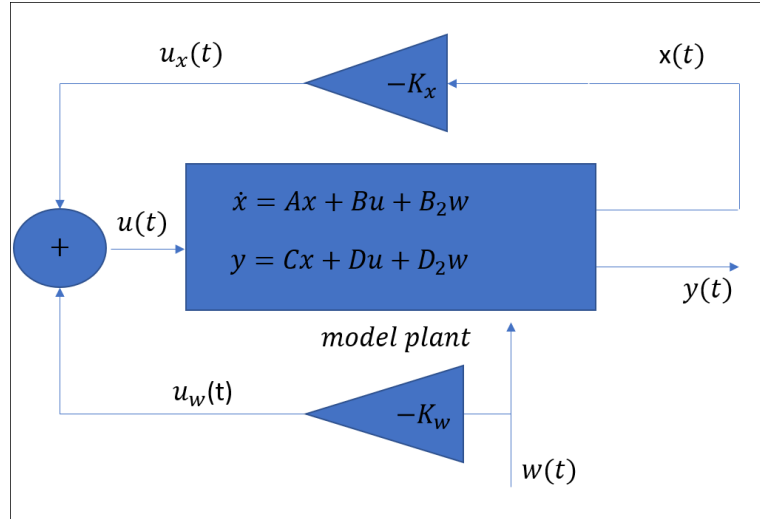


Figure 5.7: Road Disturbance Feed Forward Controller Loop

Consider the system 5.1 including the road disturbances w .

$$\begin{cases} \dot{x} = Ax + Bu + B_2w \\ y = Cx + Du + D_2w \end{cases} \quad (5.36)$$

Where x is the state vector of 22 variables. The road disturbance vector $w(t) \in \mathfrak{R}$ is assumed to be scanned by the laser scanner sensors in real time. When we substitute the the output function $y(t)$ from the state equation 5.36 into the equation 5.7:

The vector w gives the road inputs, which include eight road distributions for the corresponding suspensions.

$$w = \left\{ w_1, w_2, w_{11}, w_{22}, w_{33}, w_{44}, w_3, w_4 \right\}^T \quad (5.37)$$

$$\begin{aligned}
\mathcal{J} &= \int_0^\infty [Cx + Du + D_2w]^T Q_y (Cx + Du + D_2w) + u^T R_u u \\
&= \int_0^\infty [x^T (C^T Q_y C)x + 2x^T (C^T Q_y D)u + u^T (D^T Q_y D + R_u)u] dt \\
&+ \int_0^\infty [2x^T C^T Q_y D_2w + 2w^T D_2^T Q_y Du + w^T D_2^T Q_y D_2w] dt \quad (5.38) \\
&= \int_0^\infty [(x^T Qx + u^T Ru) + (w^T R_2w)] dt \\
&= \int_0^\infty \mathcal{F}(u, x, w, t) dt
\end{aligned}$$

In the equation 5.38, the N terms are assumed to be zero. The important difference is that this equation is also dependent to the road disturbance $w(t)$. In other words, the control methodology has to be function of both the states and the road disturbances. The road distribution is measurable data with the help of the preview sensor over the entire time domain.

Pontryagin's maximum principle is used to solve the optimal problem with road disturbances. The Hamiltonian of the linear system 5.36 is;

$$\begin{aligned}
H(u, x, w, \lambda, t) &= \mathcal{F}(u, x, w, t) + \lambda^T (Ax + Bu + B_2w) \\
&= (x^T Qx + u^T Ru) + (w^T R_2w) + \lambda^T (Ax + Bu + B_2w) \quad (5.39)
\end{aligned}$$

According to the Pontryagin's maximum principle theorem, the necessary condition for a local minimum is given by the Euler-Lagrange equation.

$$\dot{\lambda} = -\frac{\partial \mathcal{H}}{\partial x} = -(2Qx + A^T \lambda) \quad (5.40)$$

Therefore, the equation for the optimal control:

$$0 = -\frac{\partial \mathcal{H}}{\partial u} = 2Ru + B^T \lambda \quad (5.41)$$

By using the equation 5.41

$$u(t) = u_{pre} = R^{-1}\left(\frac{1}{2}B^T\lambda\right) \quad (5.42)$$

In equation 5.42, the lagrange equation has to be eliminated by using a ricatti transformation.

$$\lambda = 2(Px - \xi) \quad (5.43)$$

In equation 5.43 P is the ricatti matrix and ξ is the ricatti vector. Therefore:

$$u(t) = u_{pre} = -R^{-1}(B^T Px - B^T \xi) \quad (5.44)$$

where

$$\begin{aligned} u_x &= -R^{-1}(B^T P)x \\ u_w &= -R^{-1}(-B^T \xi) \end{aligned} \quad (5.45)$$

In equation 5.45, the u_x term is the state feedback actuator input term and the u_w is the feed-forward control input, which uses the upcoming road disturbances.

Now, take a derivative of equation 5.43:

$$\dot{\lambda} = 2(P\dot{x} + \dot{P}x - \dot{\xi}) \quad (5.46)$$

Substituting the equation 5.43 in the equation 5.40 yields

$$\dot{\lambda} = -2[Qx + A^T(Px - \xi)] \quad (5.47)$$

Equate the equations 5.46 and 5.47 to each other:

$$(P\dot{x} + \dot{P}x - \dot{\xi}) = -[Qx + A^T(Px - \xi)] \quad (5.48)$$

Substituting the \dot{x} into the equation yields:

$$(P(Ax + Bu + B_2w) + \dot{P}x - \dot{\xi}) = -[Qx + A^T(Px - \xi)] \quad (5.49)$$

and

$$(\dot{P}x + PAx + A^T Px + Qx) + PBu - [\dot{\xi} + A^T \xi - PB_2w] = 0 \quad (5.50)$$

Substituting the control input equation yields:

$$\begin{aligned} (\dot{P}x + PAx + A^T Px + Qx) + PB[-R^{-1}(B^T P)x] \\ + PB[-R^{-1}(-B^T \xi)] - [\dot{\xi} + A^T \xi - PB_2w] = 0 \end{aligned} \quad (5.51)$$

or

$$\begin{aligned} [\dot{P} + PA + A^T P - PBR^{-1}(B^T P) + Q]x - \dot{\xi} \\ - [A^T + PBR^{-1}B^T]\xi + PB_2w = 0 \end{aligned} \quad (5.52)$$

Now, differential Riccati matrix equation and differential Riccati vector equation become:

$$\begin{cases} [\dot{P} + PA + A^T P - PBR^{-1}(B^T P) + Q] = 0 \\ \dot{\xi} - [A^T + PBR^{-1}B^T]\xi + PB_2w = 0 \end{cases} \quad (5.53)$$

According to the equation 5.45:

$$\begin{cases} u_x = -R^{-1}(B^T P)x \\ K_x = -R^{-1}(B^T P) \end{cases} \quad (5.54)$$

Substituting the K_x equation into the Riccati vector equation yields:

$$\dot{\xi} + [A^T + PBK_x]\xi + PB_2w = 0 \quad (5.55)$$

Then, the Ricatti vector can be determined by:

$$\xi = -[A^T + K_x^T B^T]^{-1} + P B_2 w \quad (5.56)$$

Finally, combining the K_x equation 5.54 and ricatti vector equation 5.56, the preview controller input u_w in the equation 5.45 can be derived:

$$u_w = -R^{-1}[B^T[A^T + K_x^T B^T]^{-1} P B_2] w \quad (5.57)$$

and

$$K_w = -R^{-1}[B^T[A^T + K_x^T B^T]^{-1} P B_2] \quad (5.58)$$

when we compute the K_w matrix:

$$K_{w_{8 \times 8}} = \begin{bmatrix} K_{w_{(:,1:4)}} & K_{w_{(:,5:8)}} \end{bmatrix} \quad (5.59)$$

$$K_{w_{(:,1:4)}} = \begin{bmatrix} 17115 & 3612 & 14371 & 868 \\ 3612 & 17115 & 868 & 14371 \\ 14371 & 868 & 12999 & -504 \\ 868 & 14371 & -504 & 12999 \\ 8884 & -4619 & 10255 & -3247 \\ -4619 & 8884 & -3247 & 10255 \\ 6140 & -7363 & 8884 & -4619 \\ -7363 & 6140 & -4619 & 8884 \end{bmatrix}_{8 \times 8} \quad (5.60)$$

$$K_{w(:,5:8)} = \left\{ \begin{array}{cccc} 8884 & -4619 & 6140 & -7363 \\ -4619 & 8884 & -7363 & 6140 \\ 10255 & -3247 & 8884 & -4619 \\ -3247 & 10255 & -4619 & 8884 \\ 12999 & -504 & 14371 & 868 \\ -504 & 12999 & 868 & 14371 \\ 14371 & 868 & 17115 & 3612 \\ 868 & 14371 & 3612 & 17115 \end{array} \right\}_{8 \times 8} \quad (5.61)$$

Consequently, the preview control or preview actuator force matrix is defined by:

$$u(t) = u_{pre} = u_x + u_w = -K_x x - K_w w \quad (5.62)$$

5.1.5 Frequency Response Comparison

The frequency response function from the road distribution to vertical acceleration can be derived and is represented in Figure 5.8. This diagram shows the system responses for different frequencies and it can be considered as the ratio of the amplitude of the energy transmitted from the road and the tire after the acceleration of the vehicle. In the Figure 5.8, the first peak corresponds to the resonant frequency of the suspension system itself and the second peak corresponds to the resonant frequency of the tire. The resonant frequency for the suspension system is around 1.4 Hertz and the resonant frequency for the tire is around 9.8 Hertz as it can be seen in the Figure 5.8. The resonant frequencies have the highest values since the amplification at resonance which by coincidence lies particularly in the same frequency domain as the maximum of the input spectrum. At it can be seen in the figure 5.8, using preview suspension system suppresses the resonant frequencies.

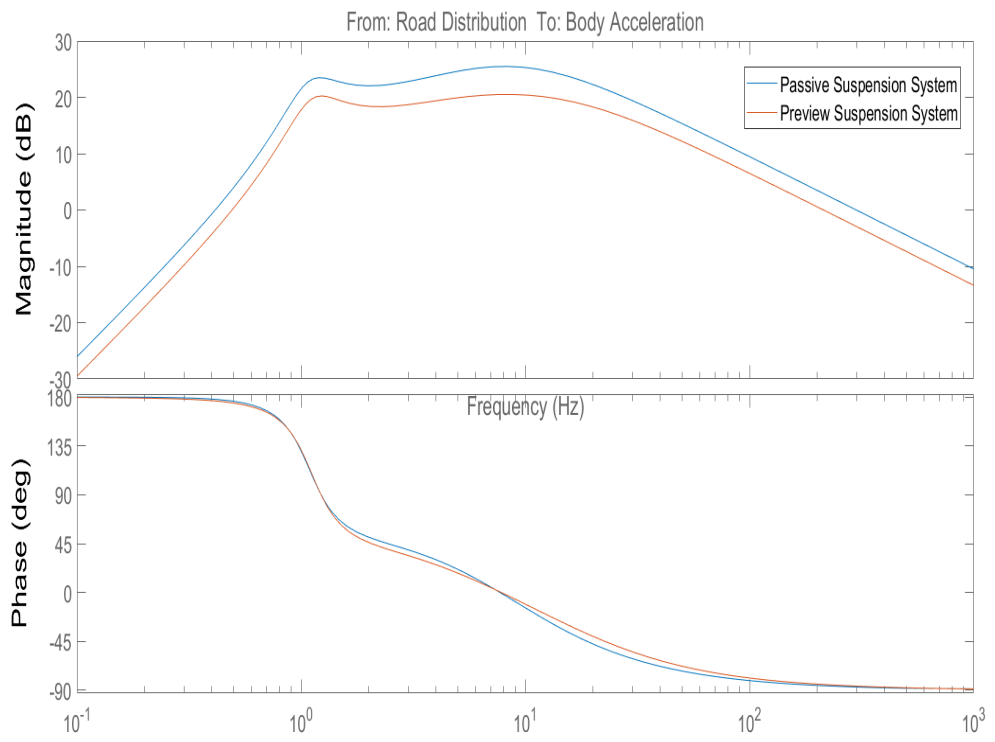


Figure 5.8: Frequency Response Function from Road input to Body Acceleration

5.2 Simulation of the Vehicle

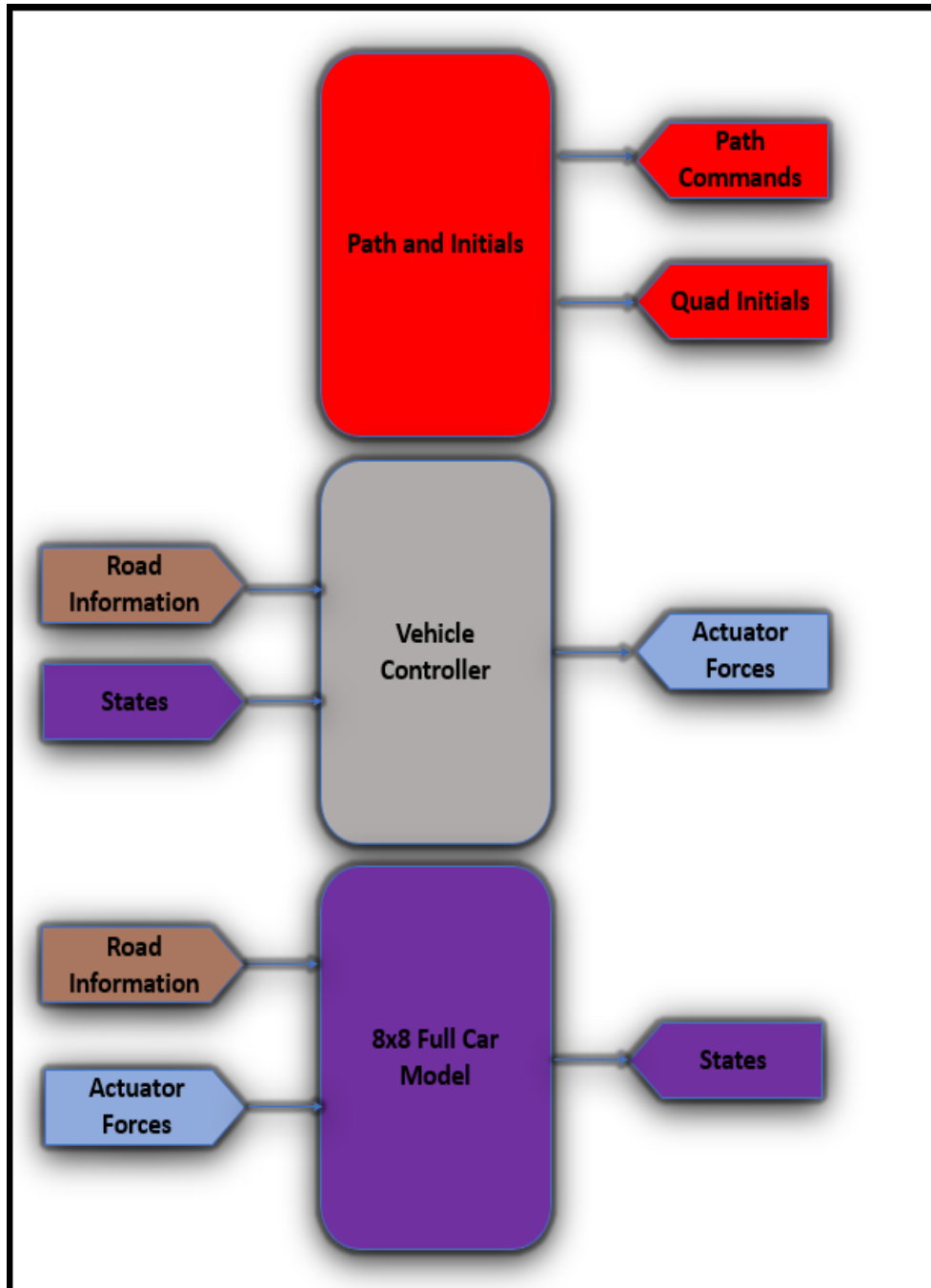


Figure 5.9: Vehicle Simulink Model Structure

Table 5.2: Simulation Input Parameters and Their Values

Parameter Description	Symbol	Value
Unsprung Mass for Suspensions	$mu f_i = mur_i$	200kg
Total Mass of the Vehicle	ms	25000kg
Pitch Inertia	I_p	90000kgm ²
Roll Inertia	I_r	30000kgm ²
Spring Stiffness	$k f_i$	180000N/m
Tire Stiffness for Suspension	$kt f_i$	400000N/m
Damping Coefficient	$b f_i$	20000Ns/m
Dist. from vehicle cog to first axe	a	2m
Dist. from vehicle cog to second axe	d	1m
Dist. from vehicle cog to third axe	e	1m
Dist. from vehicle cog to fourth axe	b	2m
First Two Axle Threat	$T f$	2.6m
Last Two Axle Threat	$T r$	2.6m
First Two Axle Half Threat	T_f	1.3m
Last Two Axle Half Threat	T_r	2.6m

For the simulations Matlab/SIMULINK software is used. Whole Simulation is consist of state equations block, which includes pitch, roll and vertical equations of the vehicle and also controller block for the vehicle and road input generator block. Figure 5.9 shows the general structure of the vehicle simulation model and Table 5.2 the values of the parameters, which are used in the simulations, are stated.

8x8 Full Car Model Block:

This block is the core block of the vehicle simulation since it includes all of the state equations, kinematic equations and unsprung mass equations for each of the eight suspension system.

Vehicle Controller Block:

Vehicle controller blocks is the block that decides the control approach for the vehicle and produce the actuator forces. The controller block includes two different switches: the first switch is the decision between the active suspension system and the passive suspension system and the second switch is for selecting the controller

approach among the standard optimal controller and the preview optimal controller.

Path and Initials Block:

The outputs of this block are the path command and initials for the quadrotor systems, since the quadrotor is assumed to be commanded by the vehicle system.

CHAPTER 6

The QUADROTOR-VEHICLE INTEGRATED SIMULATION

6.1 Introduction

One of the main goals of this study is to understand the working principles of the quadrotor-vehicle synchronized motions and affects of the possible errors to this integrated mutual relation and affects on the suspension systems surely.

The main logic is based on the usage data monitored by the laser scanner mounted on the quadrotor system by suspension system. In other words, vehicle commands the quadrotor system and quadrotor system optimizes the vehicles suspension system for comfort purposes by serving the road information.

In real world, there are lots of error parameters, which can disturb the vehicle-quadrotor integrated motions. The most important and dominant error source is based on the working conditions of the laser scanner due to the fact that point density of the scanning area is directly related with the velocity of the quadrotor and altitude of the quadrotor. Environmental and climatic effects such as gusts, dynamic weather, continuous wind are assumed to be zero in this thesis. In this study, the desired logic of the operational conditions states that the quadrotor flies at an altitude of 5 meters in front of the car almost at the same speed as the vehicle. All of the scanning error parameters is considered for the ideal operational conditions. Transmission loss between the vehicle and the quadrotor is also assumed to be zero for this thesis.

Finally, Navigation errors are also eliminated because of the self-corrective navigation system, which allows instantaneous update for the navigation by using the laser

scanner accuracy and precision. Figure 6.2 shows the self corrective navigation conditions.

6.2 Control and Optimization Logic

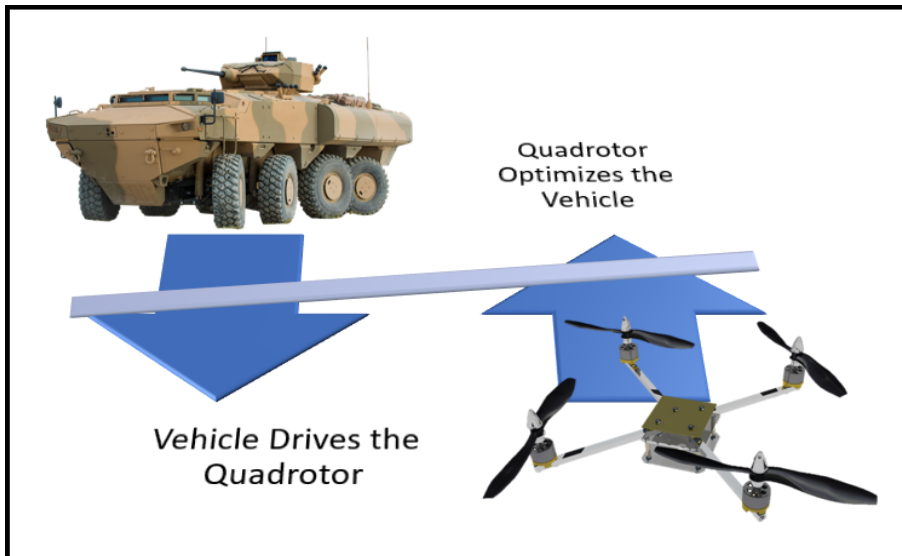


Figure 6.1: Quadrotor-Vehicle Working Logic

This study simulates the mutual motions of the quadrotor and the 8x8 heavy weight armored vehicle. Figure 6.1 shows the fundamental logic of the system. Base of the quadrotor is the top of the vehicle and when the vehicle begins to accelerate and also if the road scanning is necessary, the quadrotor flies suddenly after the motion of the vehicle. Desired speed and desired location of the quadrotor are always controlled by the vehicle during the operation. The desired location of the quadrotor is 20 meters in front of the car and 5 meters in height in normal operation conditions. When the dangerous operational conditions and unexpected situation are considered, the quadrotor is apt to heighten up to 800 meters depends on the instant battery and payload condition.

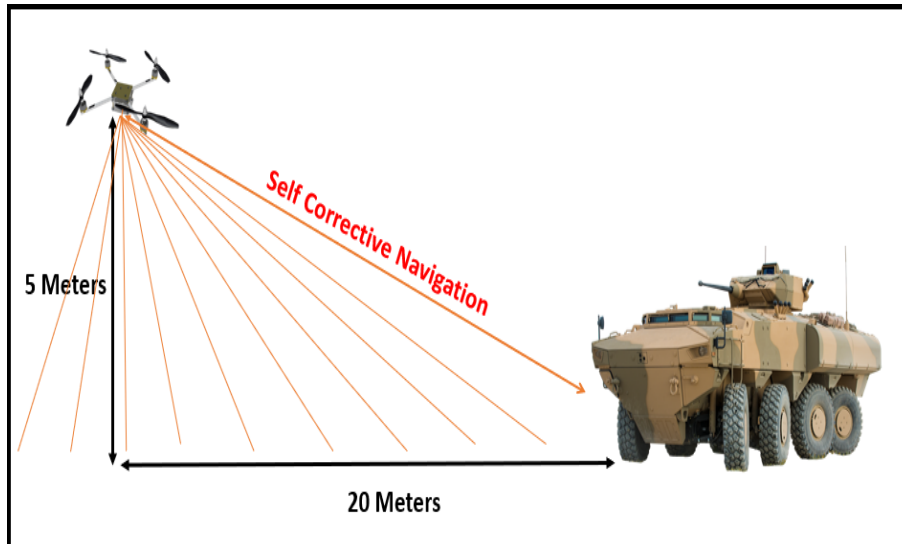


Figure 6.2: Self Corrective Navigation Error

Figure 6.2 shows one of the important innovations of the system. In this mutual motion, the laser scanner system is used to update the navigation and by doing so, it is assumed that it makes possible to eliminate the navigation error during the flight.

6.3 Error Conditions

The only error parameter, which is used as a disturbance for road scanning, is the laser scanner error, which is the most dominant error condition. As it is stated in the previous section the system uses the laser scanner to update and correct the navigation data, which is accumulated in time during the flight. Other error sources based on the real world are neglected in this study. The transmission loss due to the RF transmission is also assumed to be zero.

Laser Scanner Error: For the selected laser system, the measurement accuracy and precision is quite small since it has a superior measurement capability even under drastic weather conditions. It is one of the best long range, high speed, high accuracy mobile mapping system in the world.

Since scanner’s repeatability is quite high (up to 1 MHZ pts/sec), the scanner does not require any gimbal system and vibration isolated mounting system is enough to reach to the desired accuracy and precision. This repeatability also provides 5 mm accuracy and 3 mm precision.

The laser is also apt to scan almost 5000 points at 25 km/h and 1000 points at 100 km/h. Complete trend with respect to the quadrotor range and velocity is showed in the next figure.

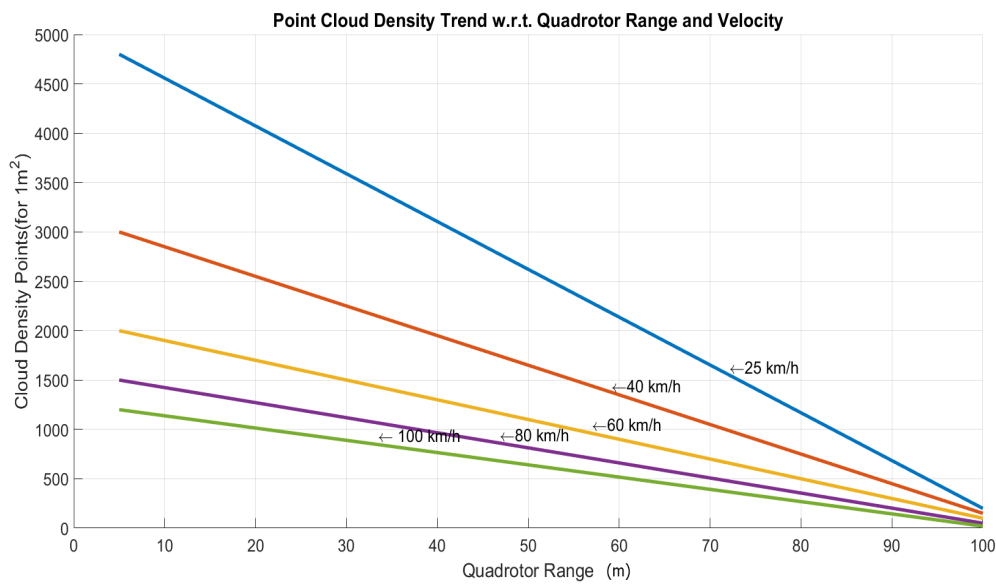


Figure 6.3: Point Cloud Density Trend w.r.t. Quadrotor Range and Velocity

6.4 Integrated and Synchronized Motion Simulations

Vehicle model and the quadrotor model are integrated in Matlab/SIMULINK environment. The whole picture can be seen in Figure 6.4. All of the results, which are shown in the results part, are determined using this complete model.

The complete model is consist of 8x8 full car vehicle model, which includes the equation of motions for the suspension system, vehicle controller model, which has the optimal control and preview control algorithms, vehicle driver model, which provides the path information to the quadrotor, laser scanner model, which generates the road information in order to optimize the vehicle suspension systems, quadrotor

controller block, which consists of attitude controllers for the quadrotor and quadrotor kinematics block, which includes all of the quadrotor rotational and translational dynamics equations for the quadrotor.

All of the blocks are communicated and linked to each other and work collaboratively and appropriately.

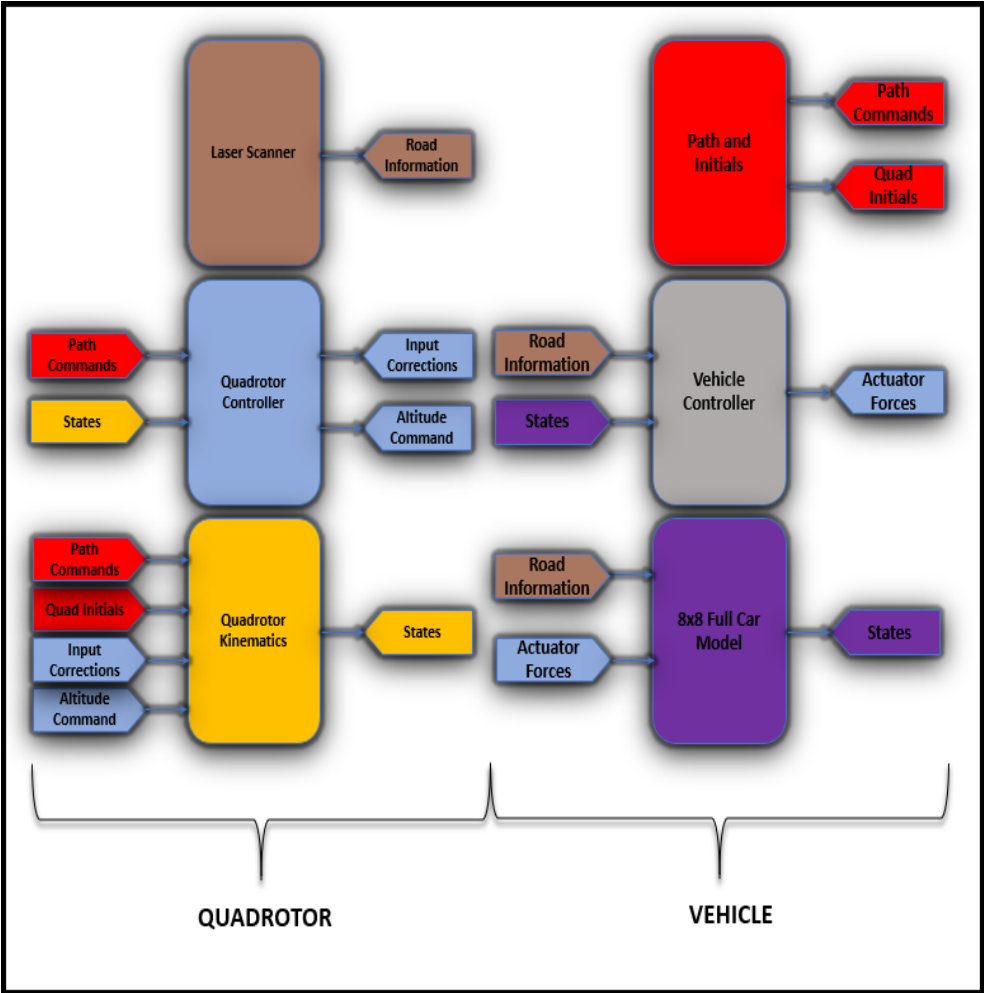


Figure 6.4: Complete Model

CHAPTER 7

RESULTS AND DISCUSSIONS

7.1 Generation of Road Profiles

ISO standard longitudinal road profiles are generated for this study in order to evaluate the suspension responses. In stochastic simulations the ideal road is exposed to the laser scanner errors in order to generate the scanned road profile. For the off-road profiles (H,G) and asphalt profile (B) generations, the ISO 8608 road profile classification standard, which was prepared by the International Organization for the Standardization (ISO), is used. Based on the power spectral densities (PSDs) the ISO has published the road classes between the letters "A" and "H" as shown in Table 7.1 and Figure 7.1. The roughness of the road increases from the "A" class to the "H" class.[50]

The road profiles are generated by using the PSD function. Characteristic conditions of the road profiles are represented by the PSDs with the wave number.

The final form of the parametric road spectrum is given by :

$$S(n) = \begin{cases} S(n_0)\left(\frac{n}{n_0}\right)^{-w} & 0.01 < n \leq 10 \\ 0 & otherwise \end{cases} \quad (7.1)$$

where, $S(n_0)$ is the component for roughness, where n_0 is given by:

$$n_0 = 1\left[\frac{rad}{m}\right] = \frac{1}{2\pi}\left[\frac{cyc}{m}\right] \quad (7.2)$$

and w is the waviness and n is the reference wave number.

Table 7.1: ISO 8608 Road Profile Classification [50]

Road class	S(n ₀) [10 ⁻⁶ m ³ /rad]			w
	Minimum value	Mean value	Maximum value	
A (Very good)	-	1	2	2
B (Good)	2	4	8	
C (Average)	8	16	32	
D (Poor)	32	64	128	
E (Very poor)	128	256	512	
F	512	1024	2048	
G	2048	4096	8192	
H	8192	16384	-	

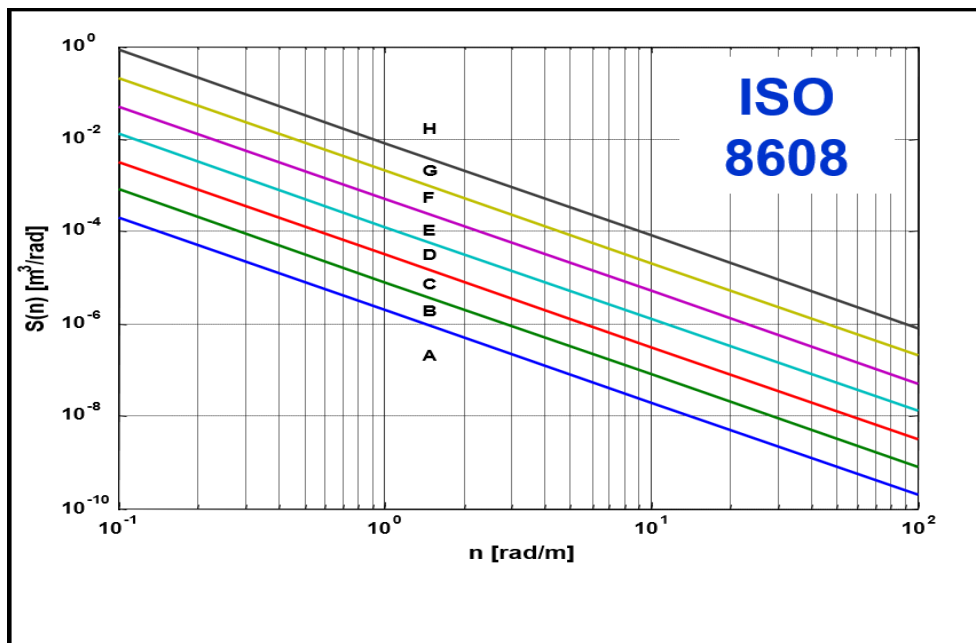


Figure 7.1: ISO 8608 Road Profile Classification [50]

7.1.1 Road Type 1: H Standard Road

In order to understand the limits of the suspension system and to design the controller based on the most drastic road conditions, the most drastic road profile, which is the H standard road, is used. The length of the road is 277 meters.

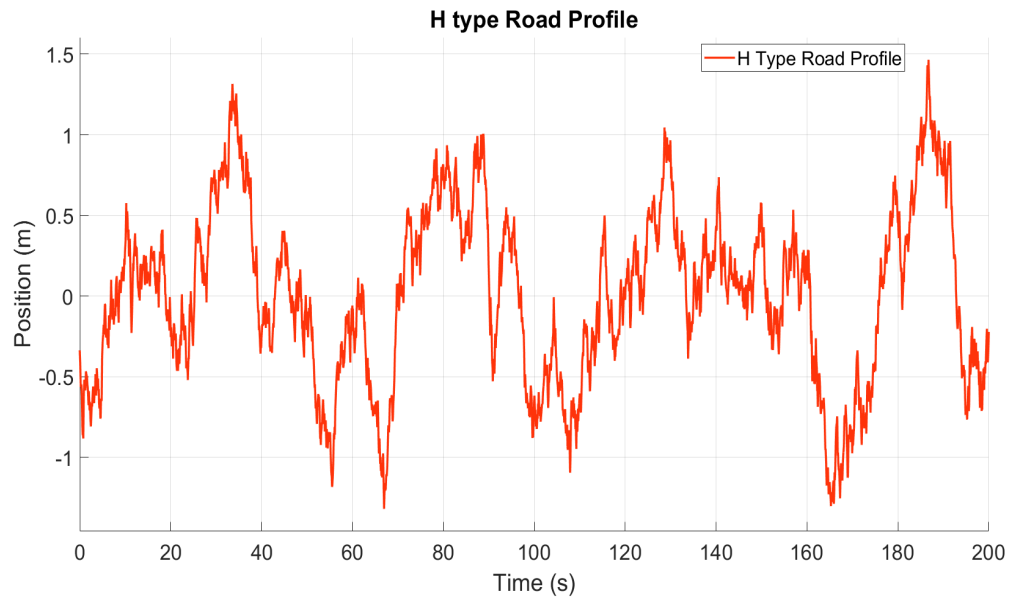


Figure 7.2: ISO8608 Standard Road Type H

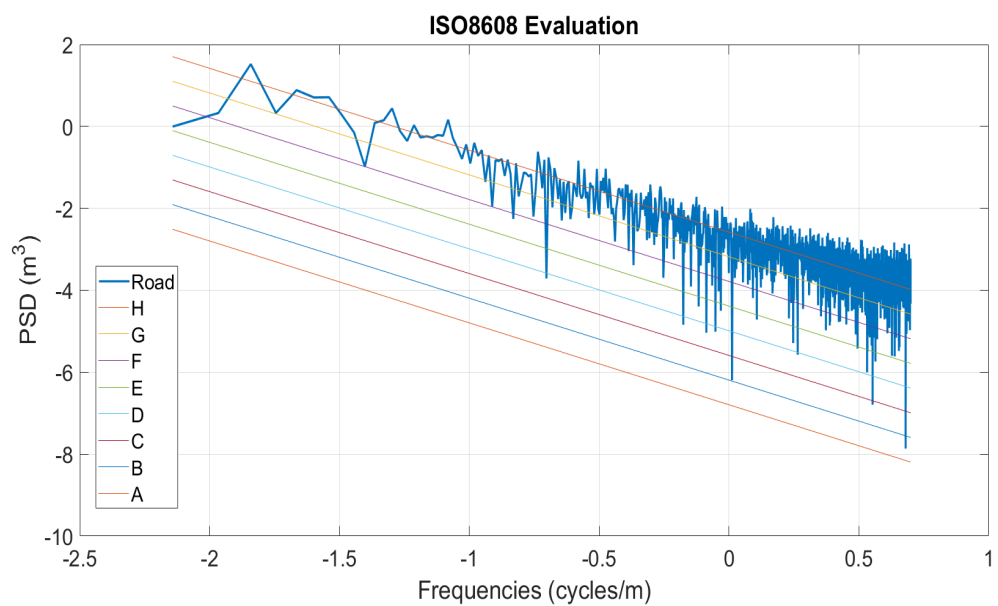


Figure 7.3: PSD for the H Road

7.1.2 Road Type 2: G Standard Road

Road type 2 is generated to simulate the highly terrain road conditions according to the classification, which is represented in the ISO 8608 standard. The length of the road is 555 meters.

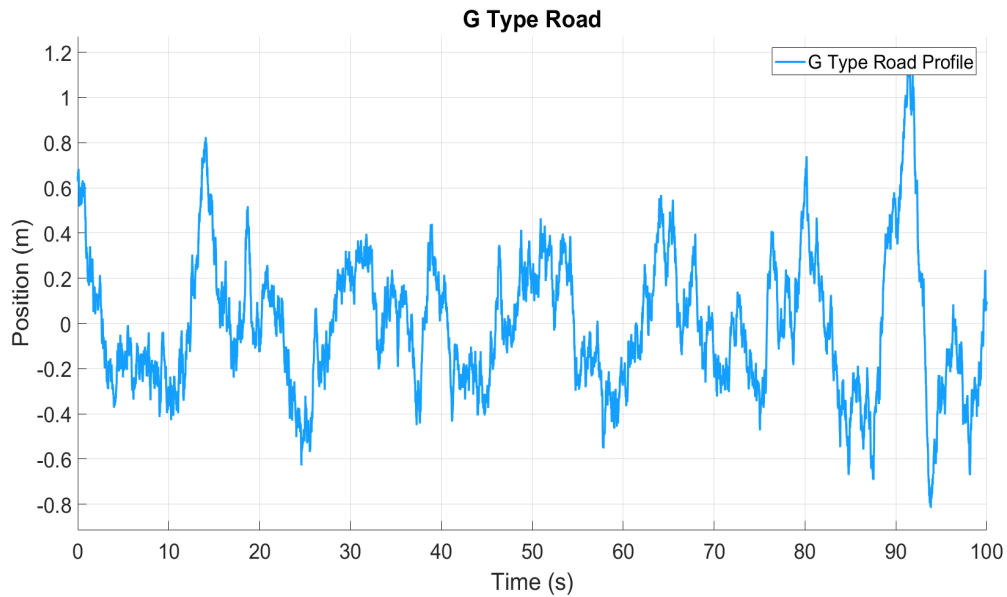


Figure 7.4: ISO8608 Standard Road Type G

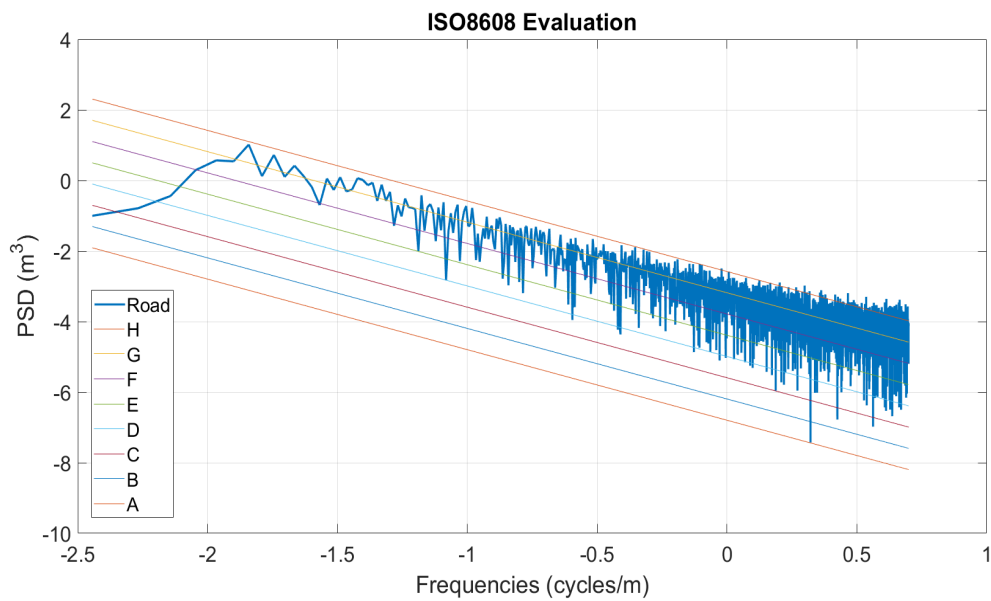


Figure 7.5: PSD for the Road Type 2

7.1.3 Road Type 3: B Standard Road

Road 3 is generated to simulate the paved road conditions according to the classification, which is represented in the ISO 8608 standard. The length of the road is 1111 meters.

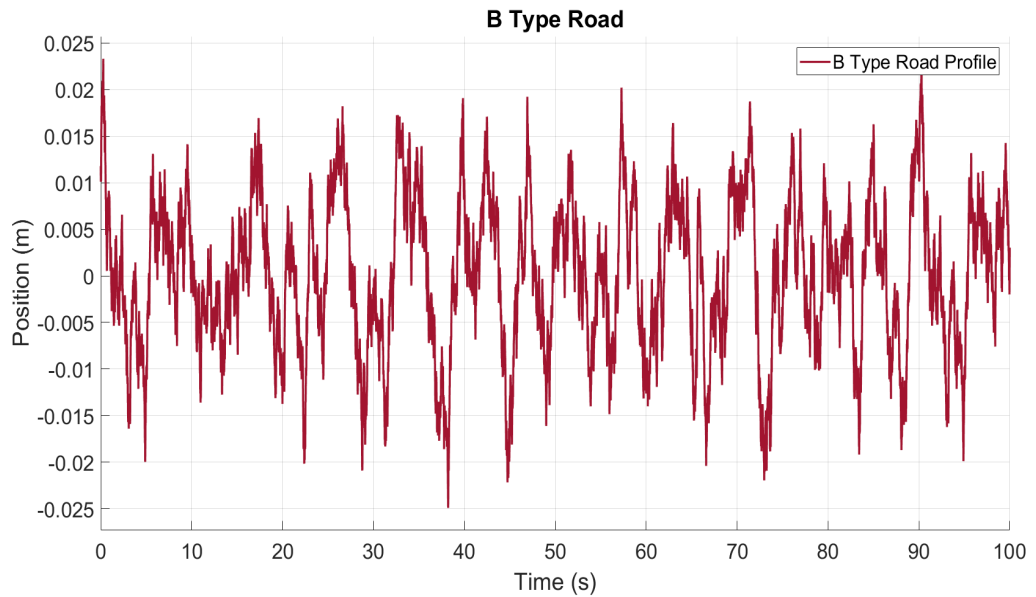


Figure 7.6: ISO8608 Standard Road Type B

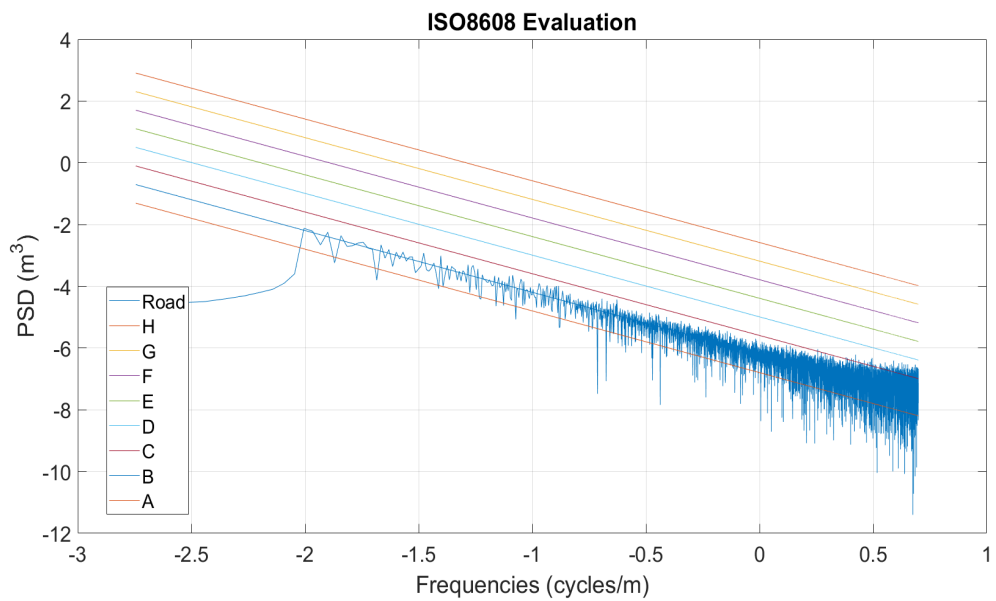


Figure 7.7: PSD for the Road Type 3

7.1.4 Road Type 4: Bump Road

A bump input is subjected to the 4 axes with a corresponding phase delay based on the desired speed of the vehicle. The road input is at a height of 0.2 meters and at a width of 1 meters.

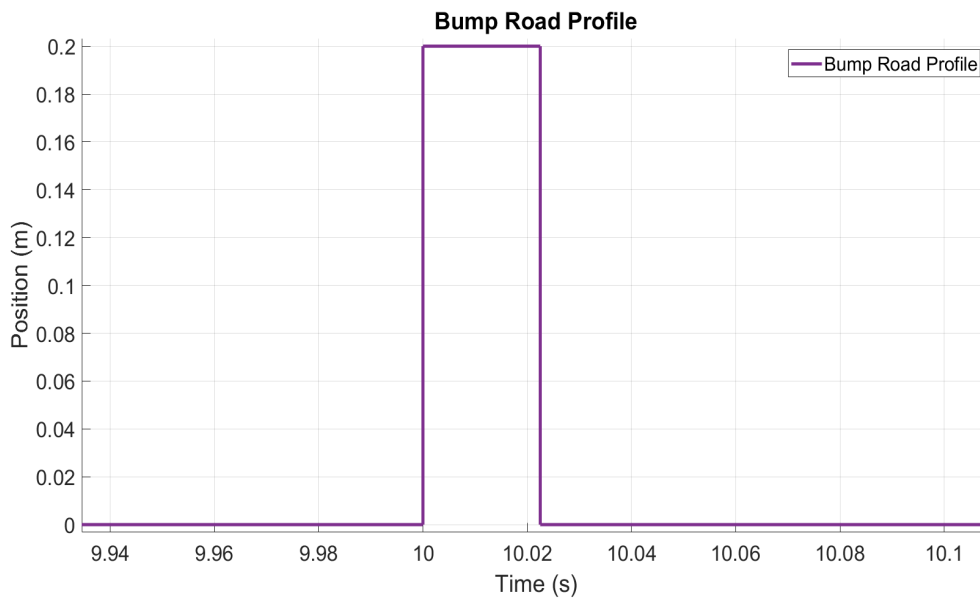


Figure 7.8: Bump Road

7.1.5 Road Type 5: Sinusoidal Road Profile

A sinusoidal input is given to the one side of the vehicle with a corresponding phase delay based on the desired speed of the vehicle. The sinusoidal road profile is used to evaluate the roll performance of the vehicle. The length of one of the sinusoidal bump is 1 meter and the amplitude of one of the sinusoidal bump is 40 centimeters.

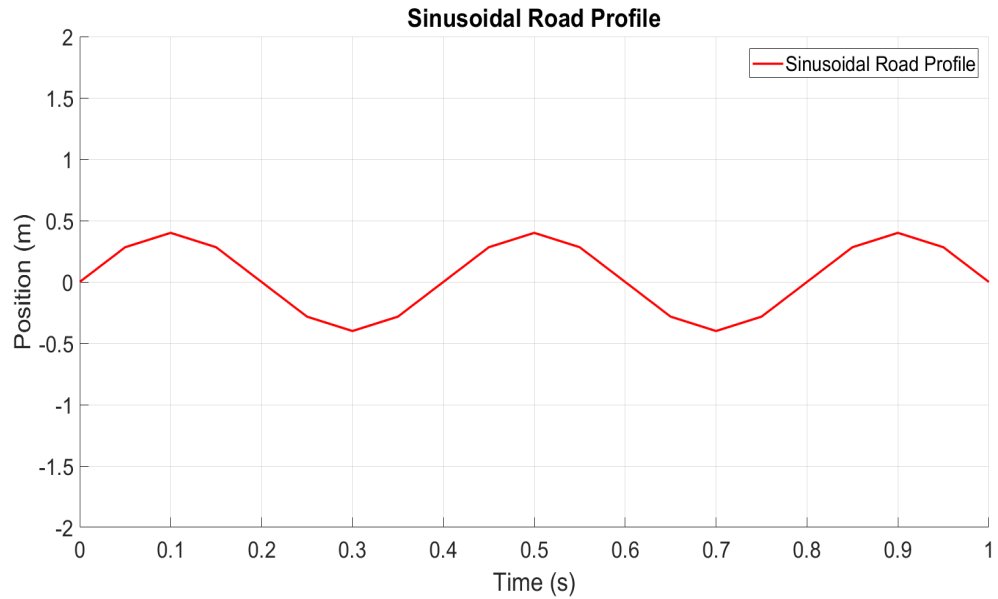


Figure 7.9: Sinusoidal Road PRofile

7.2 Analyze Scenarios

In this section, MATLAB/Simulink simulation results are presented for a 8x8 full car. By using the obtained P and Q parameters, an optimum feedback gain matrix is calculated with the help of the Matlab optimization toolbox. Furthermore, a feed-forward gain is also calculated for the preview version of the optimal controller. Standard optimal and preview controllers are compared to the passive suspension system. In the simulations, a quadrotor is used to carry the laser scanner and according to the motion of the quadrotor, laser scanner error characterization is made for each run of the simulations. For the simulations, only the laser scanner error is taken into account since the navigation errors are eliminated by using the self-corrective navigation system, which is mentioned in Sec. 6.2.

For the deterministic results, it is assumed that the road profile is scanned ideally and there is no error conditions. The preview controller uses the exact road profiles, which are exactly same as the real road. On the other hand, in stochastic simulations, at this time, the error conditions based on the laser scanner, which is mounted on the quadrotor system, are taken into account and the disruption on the road profiles and

affects of the scanned road on the vertical acceleration of the vehicle are evaluated.

By using the ISO 8608 standard, the most drastic road profile, which is the H type road, is selected to evaluate the limits of the suspension system. The controller is design by using the most drastic road conditions. For the H type road, 5 km/h is the limit speed for the vehicle with the passive suspension system. On the other hand, 20 km/h is the limit speed for the suspension system that uses the preview sensor. The reasons on determining the limit velocities will be stated in the results part in more details. In the stochastic results section of the H type road, two different scenario is used. The first and the second scenario describes the situations that the altitude of the quadrotor is 5 meters, which is the minimum range, and 100 meters, which is the maximum range, respectively.

According to the ISO 8608, as an example of highly terrain of off-road conditions, "G" type road is used as the third type of road profile for the off-road analyzes. Because of the capacity of the vehicle, for this type of road, relatively low vehicle speed, which is 20 km/h is used for the simulations. In the stochastic results section of the G type road, two different scenario is used. The first and the second scenario describes the situations that the altitude of the quadrotor is 5 meters, which is the minimum range, and 100 meters, which is the maximum range, respectively.

Finally, as an implementation of the paved road conditions, "B" standard road is generated and used for the asphalt road simulations. 80 km/h vehicle speed is used in the simulations. In the stochastic results section of the B type road, two different scenario is used. The first and the second scenario describes the situations that the altitude of the quadrotor is 5 meters, which is the minimum range, and 100 meters, which is the maximum range, respectively. In the stochastic scenarios, the speed of the vehicle is 40 km/h due to the limits of the quadrotor velocity.

For the bump road analyzes, suspension system is analyzed by using the vehicle speed of 40 km/h. Vehicle velocity is simulated by applying phase delay to the road input. In other words, different axes of the vehicle are subjected to the road disturbances in different times respectively. For the stochastic runs, it is provided that the quadrotor flies approximately 20-30 meters ahead of the vehicle and at a altitude of 5 meters. Maximum error conditions refer the 40 km/h quadrotor speed and 100 meters quadro-

tor altitude.

Finally, a sinusoidal road is used to evaluate the roll performance of the vehicle. In this simulations, a sinusoidal road bump series, which have bump length of 1 meter and bump amplitude of 40 centimeters, is given to the one side of the vehicle with a corresponding phase delay, which generates a speed of 10 km /hours for the vehicle.

7.3 Vibration Evaluation

The evaluation comparisons can be categorized into two different categorizes: the time domain analyzes and the frequency domain analyzes. In order to simplify and standardize the vibration evaluation for the different suspension types, ISO 2631 standard, which is called as "Mechanical vibration and shock evaluation of human exposure to whole body vibration" is used [51]. For the time domain analyzes, the RMS value, the frequency weighted RMS value and the MAX value of the vertical acceleration are calculated in order to evaluate the suspension performances and for the frequency domain analyzes the PSD and the absorb power are calculated and the comparisons are made based on the ISO 2631 standard [51] and US Army body vibration procedure [52].

7.3.1 Time Domain Evaluation

The objectives of the time domain analyzes are to isolate the acceleration events with respect to time, to correlate the acceleration information with other information and to check the limits against the requirements for the vehicle. In time domain analyzes, the root mean square (RMS) and the maximum value of the data can be used in order to compare the suspension types. According to the ISO 2631 standard [51], for the whole body analyses by using the vertical acceleration, the frequency weighted rms acceleration in the frequency range 0.5 to 80 Hz can be used to determine the effects of exposure to vibration on health since the frequency ranges for the effects of degraded health, comfort and perception are 0.5 Hz to 80 Hz. In this study, a butterworth second order bandpass filter with a sample frequency of 2000 Hz is used to filter the raw vertical acceleration value in order to obtain the frequency-weighted RMS

value. Additionally, based on frequency-weighted RMS values, the 2631 standard [51] makes an representation of "Health Guidance Caution Zone" which can be seen in Figure 7.10. In this figure, for exposures below the zone health risks are not clearly specified; between the lines there is potential health risks and above the zone, the health risks are most likely. This recommendation is generally based on exposure duration between 4 hours and 8 hours.

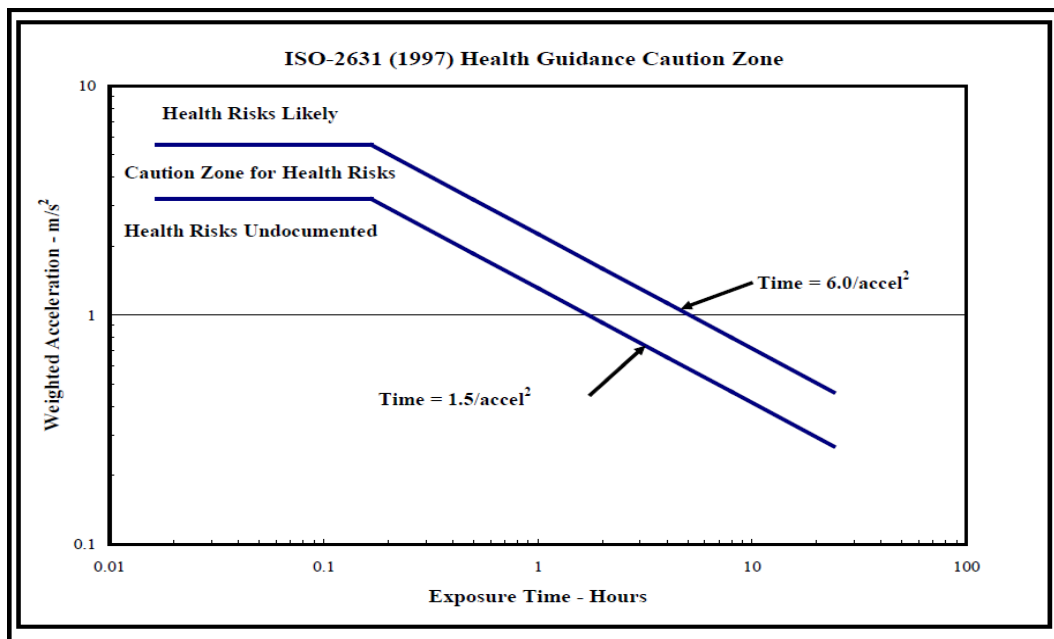


Figure 7.10: Whole body vibration health guidance caution zones [51]

Despite the information in Figure 7.10, in standard ISO 2631 [51] a limit RMS value for the personnel comfort is not defined. The following RMS values, which are stated in the Table 7.2, are helpful to understand the reactions to the various magnitudes of vibration in public transport. It has to be mentioned that the reactions at different vibration magnitudes are totally depend on the expectations of the passenger with regard to the duration of the trip and the type of the activities (listening, reading, etc.) that the passenger tries to accomplish and several different factors (environmental noise, temperature, etc.).

Table 7.2: Comfort Indications in Public Transport [51]

Less than $0.315m/s^2$	not uncomfortable
$0.315m/s^2$ to $0.63m/s^2$	a little uncomfortable
$0.5m/s^2$ to $1m/s^2$	fairly uncomfortable
$0.8m/s^2$ to $1.6m/s^2$	uncomfortable
$1.25m/s^2$ to $2.5m/s^2$	very uncomfortable
Greater than $2m/s^2$	extremely uncomfortable

Time domain analyzes are the basic and the fundamental methodology to evaluate the vibration performance of the suspension systems. The methodology is based on the descriptive statistics and provides good display approximation for time histories for the vertical acceleration.

7.3.2 Frequency Domain Evaluation

According to the ISO 2631 standard [51] and US army body vibration procedure [52], in order to show the speed limiting effects over drastic road condition, the absorb power technique is used. It is a methodology for measuring the response of the personnel to the vibration based on the road disturbances. Absorb power is a measure of the rate which energy is absorbed by the passenger subjected to the vibration which results from the road input. When we consider the military ground vehicles negotiating the drastic road conditions, the absorb power is accepted as the measure of personnel tolerance to the vibrational effects. The absorb power for a specific road can be calculated by multiplying the power spectral density of the vertical acceleration by the related transfer function and integrating the resulting spectrum. Being a scalar value is one of the most important advantages of the absorb power and can be summarized for the complex systems, such as vehicles, to obtain a single scalar value which emphasizes the total average absorb power for the corresponding road and speed. According to the US army body vibration procedure [52], which is derived by using the ISO 2631 standard [51], basically, a standard personnel comfort test procedure consist of determining the maximum speed at which the vertical average absorbed power value reaches an upper limit value of 6 watts for all of the road type. In other words, according to the military standards, the military ground vehicle

must be capable of producing a ride of 6 watts or less for the personnel based on the vertical acceleration for a given speed and road type. This speed limiting criteria is used as one of the mobility limiting factors in the North America Treaty Organization (NATO) reference mobility model[52].

The absorb power can be calculated from:

$$P_{abs} = \sum_1^i (C_{abs,i}) A_{abs,i}^2 \quad (7.3)$$

Where, P_{abs} is the absorb power in watts, $A_{abs,i}$ is the RMS acceleration in ft/sec^2 within the i^{th} spectral band and $C_{abs,i}$ is the absorb power constant within the i^{th} spectral band. See reference [51], [52] and [61] for detailed calculations and information for the absorb power constants.

7.4 Results

7.4.1 Deterministic Results for H Type Road

Deterministic results refer the situations that there is no error based on laser scanner and the road information, which is used by the simulations, is exactly true data.

7.4.1.1 Time Domain Results @ 5 km/h

0.72 seconds time delay is applied to the road profile for different axes in order to simulate the 5 km/h vehicle velocity. The length of the road is 277 meters and the time of the drive is 200 seconds. Figure 7.11 shows the road profile.

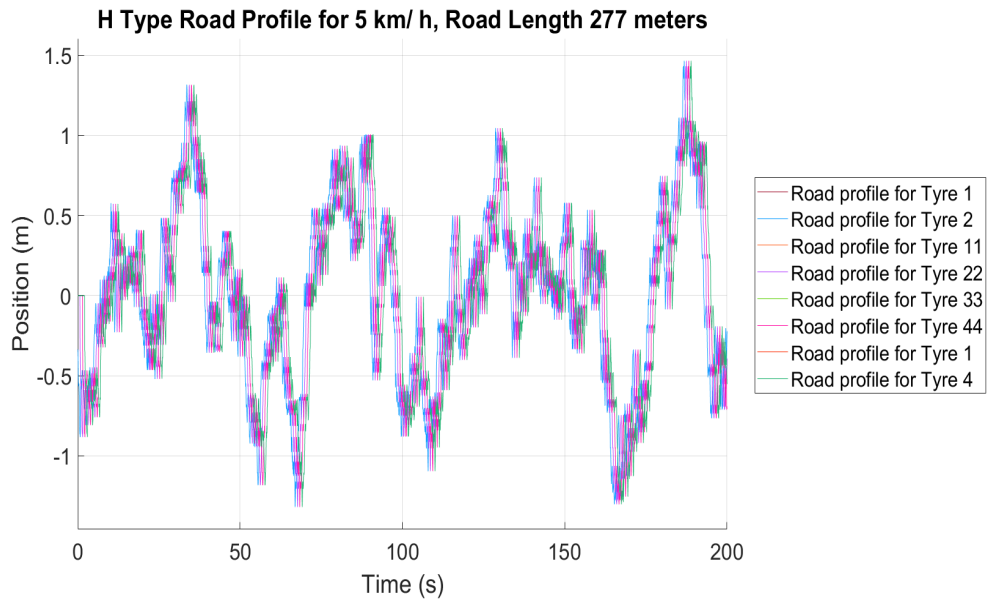


Figure 7.11: Road Profile

Figure 7.12, Figure 7.13 and Figure 7.14 show the vertical body displacement, vertical body acceleration and pitch acceleration for all suspension types, respectively.

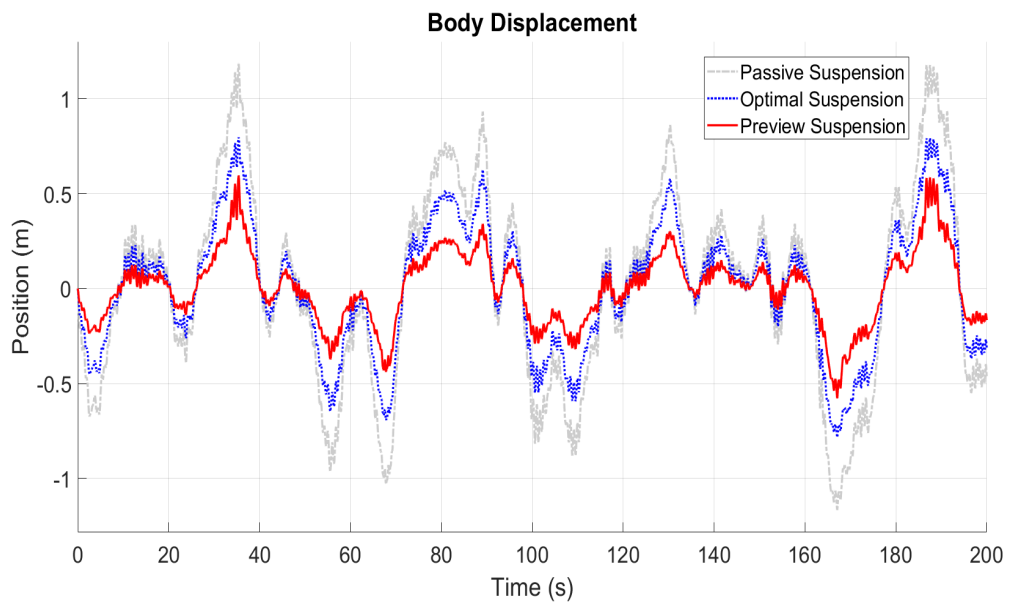


Figure 7.12: Body Displacement

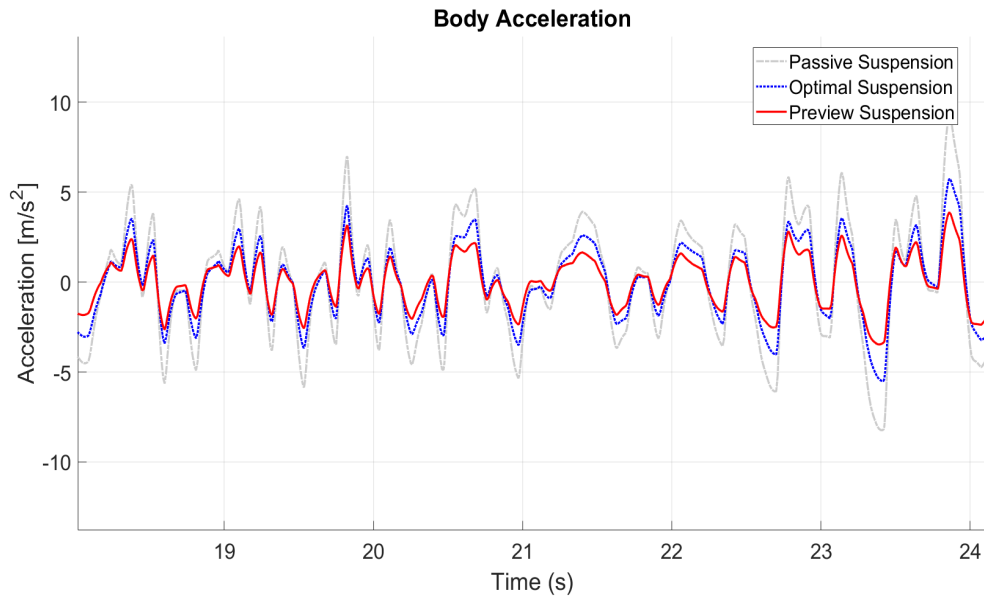


Figure 7.13: Body Acceleration

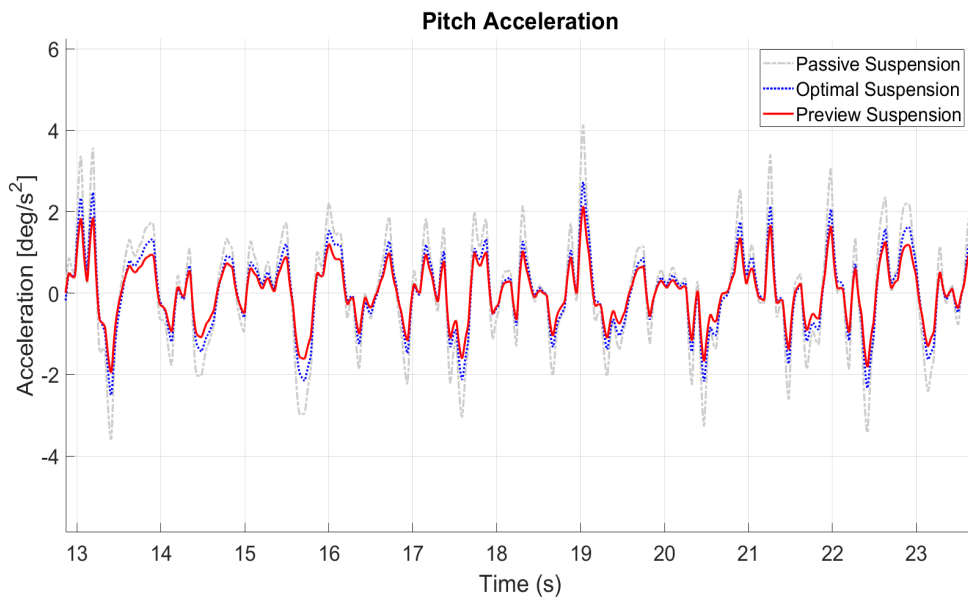


Figure 7.14: Pitch Acceleration

Figure 7.15 and 7.16 show the actuator forces for all tires and suspension travel for the tire 1, respectively.

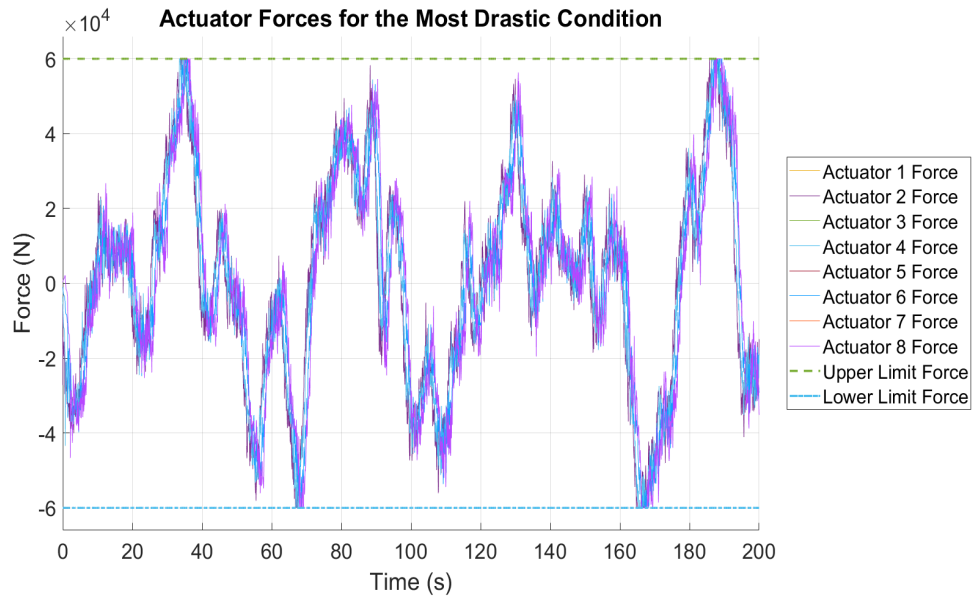


Figure 7.15: Actuator Forces for selected Q and R Values on H Type Road

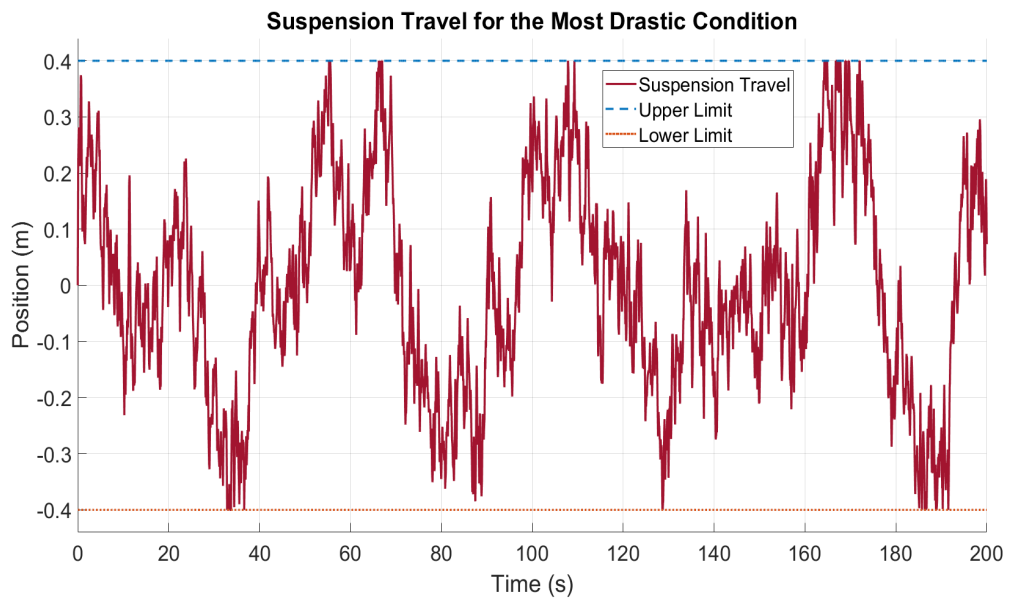


Figure 7.16: Suspension 1 Travel for selected Q and R Values on H Type Road

Table 7.3 and Table 7.4 summarize the performances of the different suspension system types against the H type road profile with the velocity of 5 km/h. The meanings and the consequences of the values are explained in detail in the discussion section.

Table 7.3: Time Domain Analyzes Results

Time Domain Analyzes Results							
Susp. Types	Vertical Acceleration			Vertical Disp.		Pitch Acc.	
	Raw RMS	Weighted RMS	Max	RMS	Max	RMS	Max
Vehicle Velocity 5 km/h							
Passive	3.284	2.929	12.630	0.514	1.183	1.485	5.747
Optimal	2.175	1.965	7.939	0.344	0.796	1.065	4.101
Preview	1.718	1.498	6.595	0.194	0.596	0.911	3.959

Table 7.4: Time Domain Analyzes Results (Percental)

Time Domain Analyzes Results							
Susp. Types	Vertical Acceleration			Vertical Disp.		Pitch Acc.	
	Raw RMS	Weighted RMS	Max	RMS	Max	RMS	Max
Vehicle Velocity 5 km/h							
Passive							
Optimal	33.8%	32.9%	37.1%	33.1%	32.7%	28.2%	28.6%
Preview	47.7%	48.9%	47.8%	62.2%	49.6%	38.6%	31.1%

7.4.1.2 Frequency Domain Results @ 5 km/h

Figure 7.17 shows the comparison of the different suspension systems based on the absorb power in frequency domain. Additionally, Table 7.5 shows the total average absorb power for the speed of 5 km/h and the road type of H. The meanings and the consequences of the values are explained in detail in the discussion section.

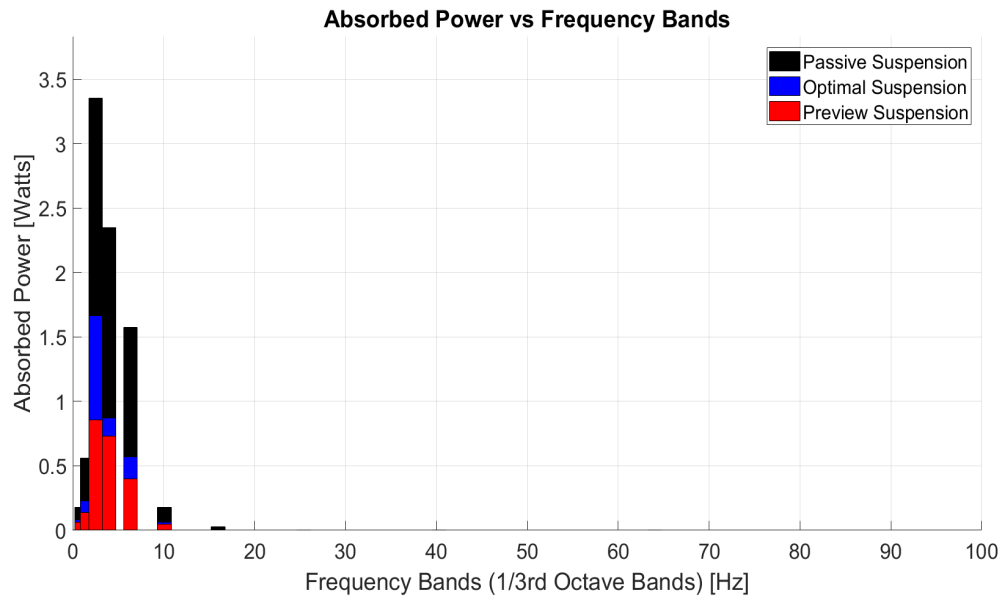


Figure 7.17: Absorb Power

Table 7.5: Frequency Domain Analyzes Results

Frequency Domain Analyzes Results	
	Total Absorb Power [Watts]
	Vehicle Velocity 5 km/h
Passive	8.23 W
Optimal	3.50 W
Preview	2.24 W

7.4.1.3 Preview and Optimal Suspension Limits for Ideally Known H Type Road

Preview Suspension Limits on H Road

Table 7.6: Time Domain Analyzes Results for 20 km/h

Time Domain Analyzes Results							
Susp. Types	Vertical Acceleration			Vertical Disp.		Pitch Acc.	
	Raw RMS	Weighted RMS	Max	RMS	Max	RMS	Max
Vehicle Velocity 20 km/h							
Preview	2.7177	1.8988	14.7769	0.2226	0.5953	2.4826	8.9265

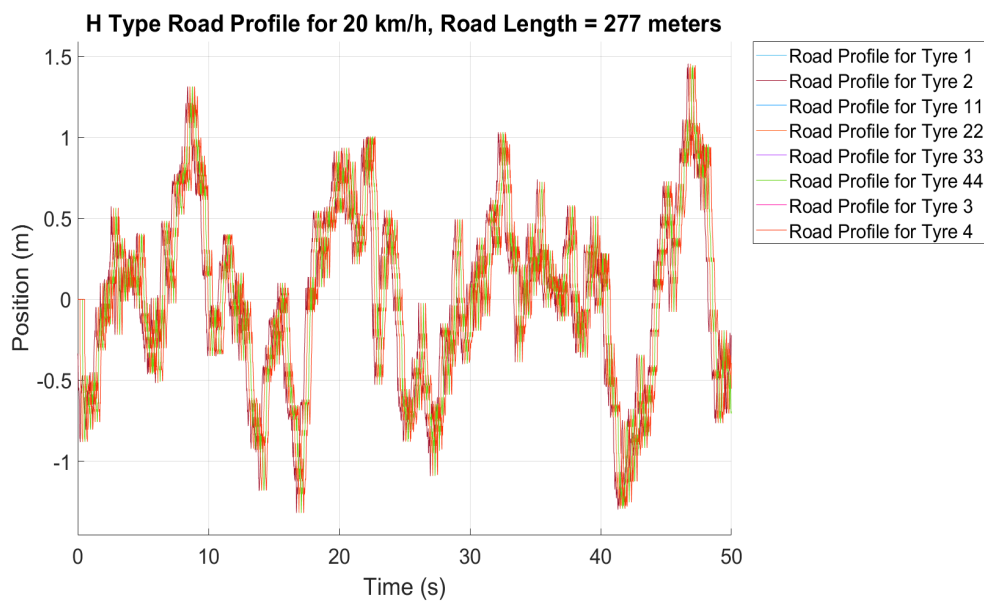


Figure 7.18: Road profile

In order to understand the limits of the vehicle with preview suspension system, the speed of the vehicle has increased until the total absorb power value reaches the maximum allowable value, which is 6 watt. By doing so, it is observed that 20 km/h is the limit speed for the preview suspension system on the same H type road conditions, while the limit is 5 km/h for the passive suspension system. In this simulations, it is assumed that the road profile is known ideally by the vehicle suspensions. Figure 7.18 shows the 277 meters road profile with a time of drive of 50 seconds and Table 7.6 shows the time domain results of the preview suspension system with a vehicle velocity of 20 km/h on the H type road conditions. Finally Figure 7.19 shows the absorb with respect to the frequency bands and the Table 7.7 shows the total average

absorb power with maximum speed of preview suspension system on the H type road.

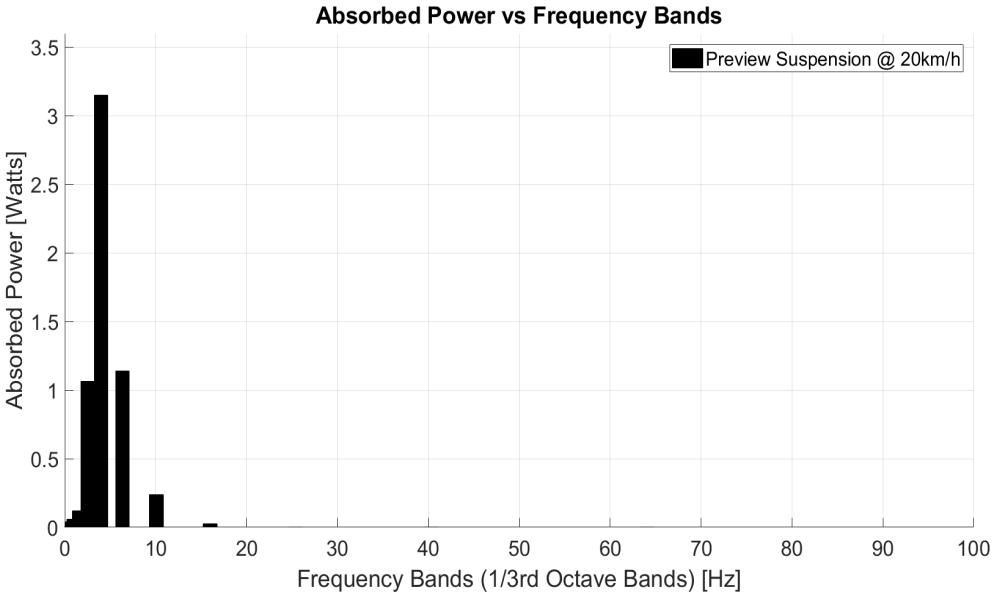


Figure 7.19: Preview Suspension Absorb Power @20km/h

Table 7.7: Preview Suspension Absorb Power @20km/h

Frequency Domain Analyzes Results	
	Total Absorb Power [Watts]
	Vehicle Velocity 20 km/h
Preview Suspension	5.81 W

Optimal Suspension Limits on H Road

Table 7.8: Time Domain Analyzes Results for 15 km/h for Optimal Suspension

Time Domain Analyzes Results							
Susp. Types	Vertical Acceleration			Vertical Disp.		Pitch Acc.	
	Raw RMS	Weighted RMS	Max	RMS	Max	RMS	Max
Vehicle Velocity 15 km/h							
Preview	2.6536	1.8653	9.0885	0.3599	0.7992	2.4190	7.8790

In this simulations, it is assumed that the road profile is known ideally by the vehicle

suspensions. Figure 7.21 shows the 277 meters road profile with a time of drive of 66 seconds and Table 7.8 shows the time domain results of the optimal suspension system with a vehicle velocity of 15 km/h on the H type road conditions. Finally Figure 7.20 shows the absorb with respect to the frequency bands and the Table 7.9 shows the total average absorb power with maximum speed of optimal suspension system on the H type road.

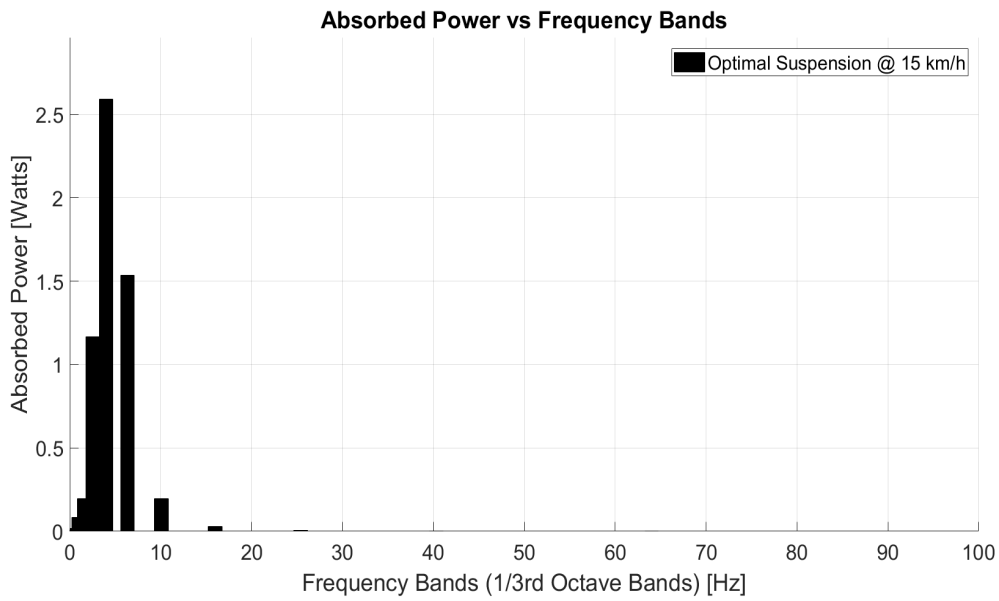


Figure 7.20: Optimal Suspension Absorb Power @15km/h

Table 7.9: Optimal Suspension Absorb Power @15km/h

Frequency Domain Analyzes Results	
	Total Absorb Power [Watts]
	Vehicle Velocity 15 km/h
Preview Suspension	5.83 W

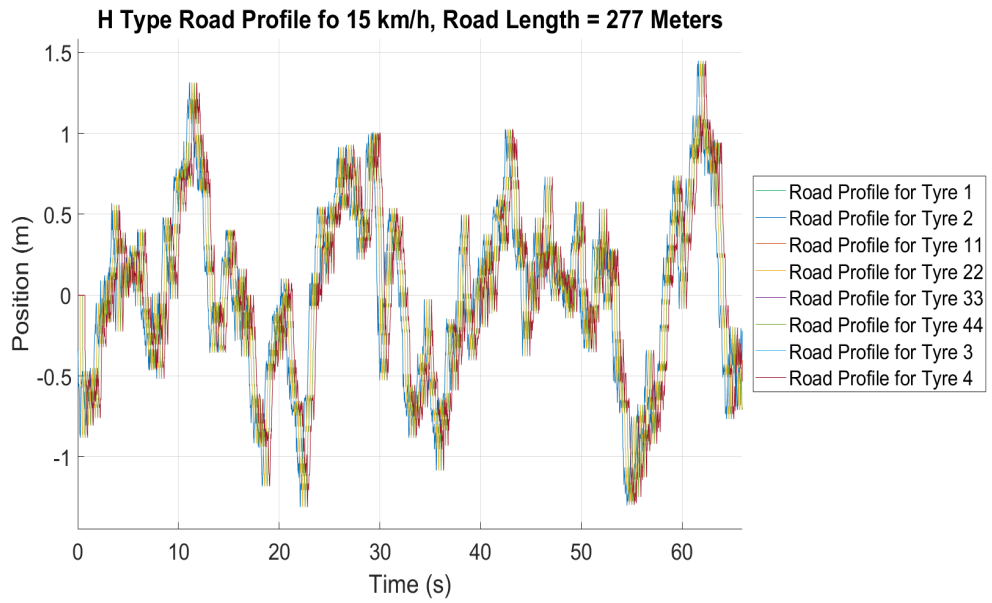


Figure 7.21: Road profile

7.4.2 Stochastic Results for H Type Road @ 20 km/h

For the stochastic results, the quadrotor based error parameters are taken into account and the affect of the errors is evaluated. Figure 7.22 shows the general point cloud density trend with respect to quadrotor range and velocity.

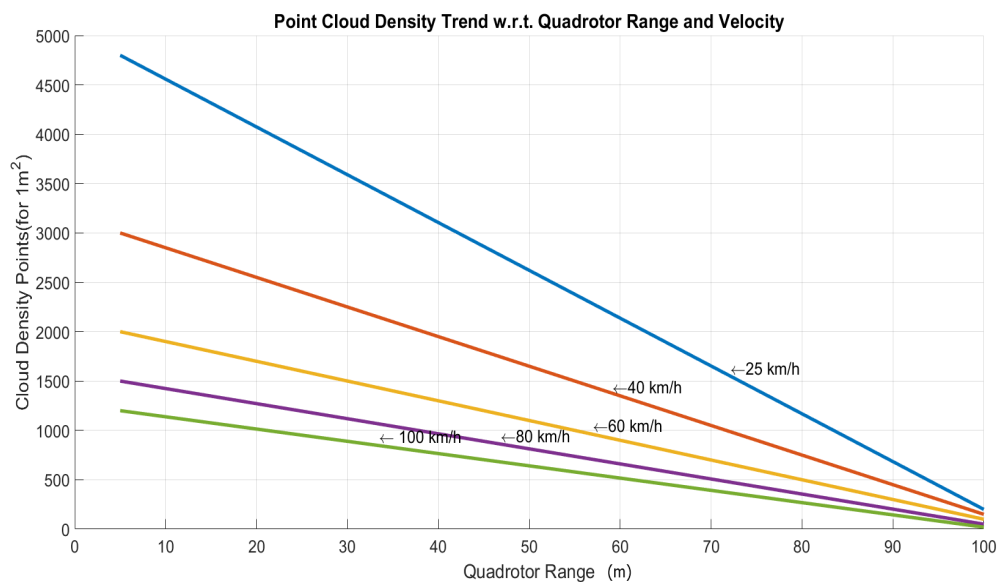


Figure 7.22: Point Cloud Density Trend w.r.t. Quadrotor Range and Velocity

7.4.2.1 Scenario 1:Quadrotor Speed 20 km/h, Range 5 Meters

Figure 7.23 shows the relative motion of the quadrotor and the vehicle on X and Z axes. There is no motion on the Y axes. The altitude of the vehicle is assumed as zero and the altitude of the quadrotor is 5 meters. Figure 7.24 shows the scanned points per square meter. The point cloud density is depend on the range and speed of the quadrotor and the Figure 7.24 shows that the point cloud density decreases from 4800 points to the 4730 points as the quadrotor accelerates to the 20 km/h. Therefore, the maximum distance between two scanned points is around 1.465 centimeters. Additionally, Figure 7.25 and Figure 7.26 show the difference between the ideal road and the scanned road and the differences of the responses of the preview suspension system to the ideal road and the scanned road.

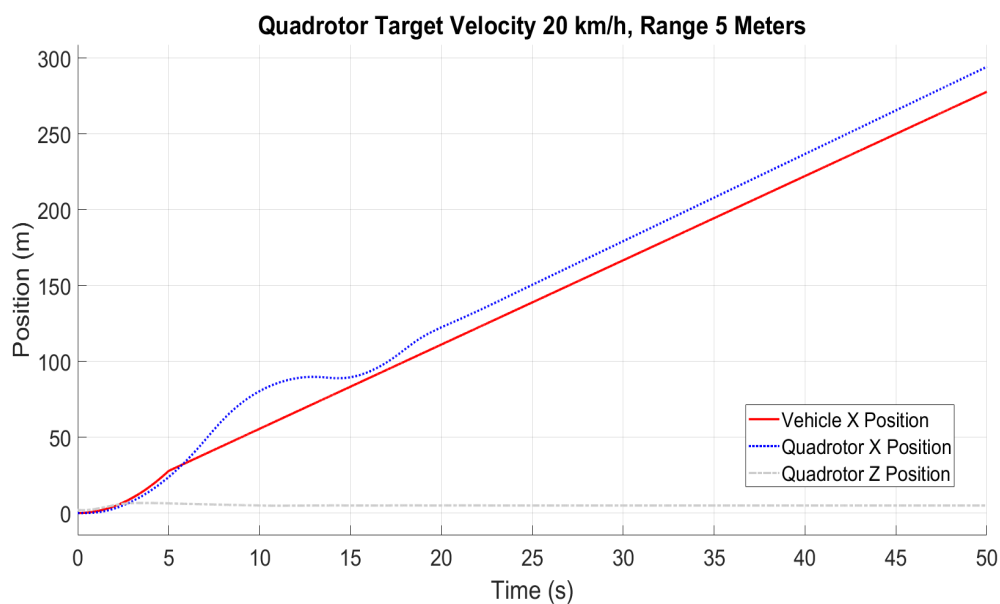


Figure 7.23: Stochastic Scenario @20km/h

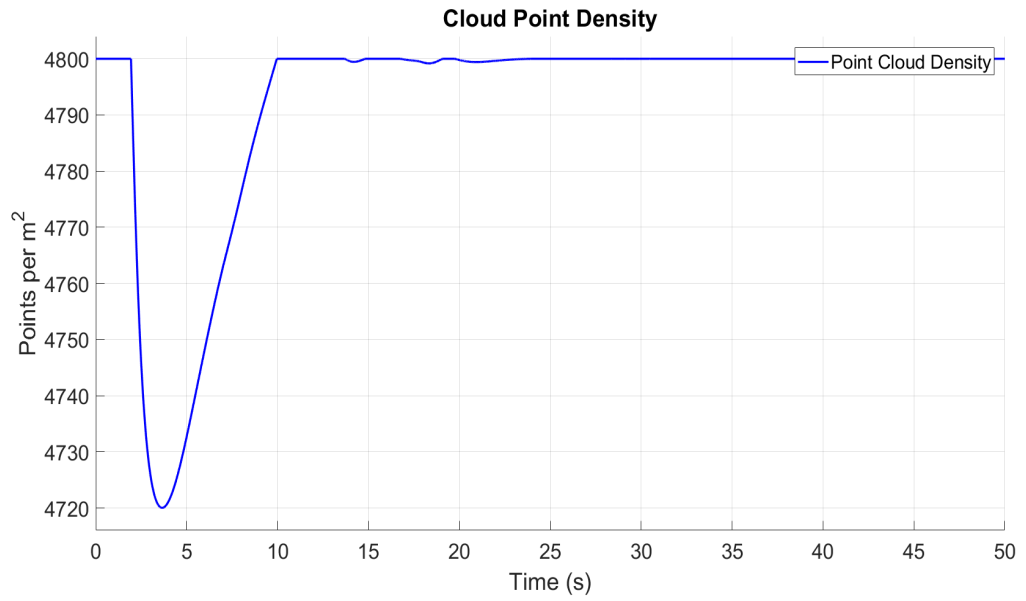


Figure 7.24: Point Cloud Density @20km/h

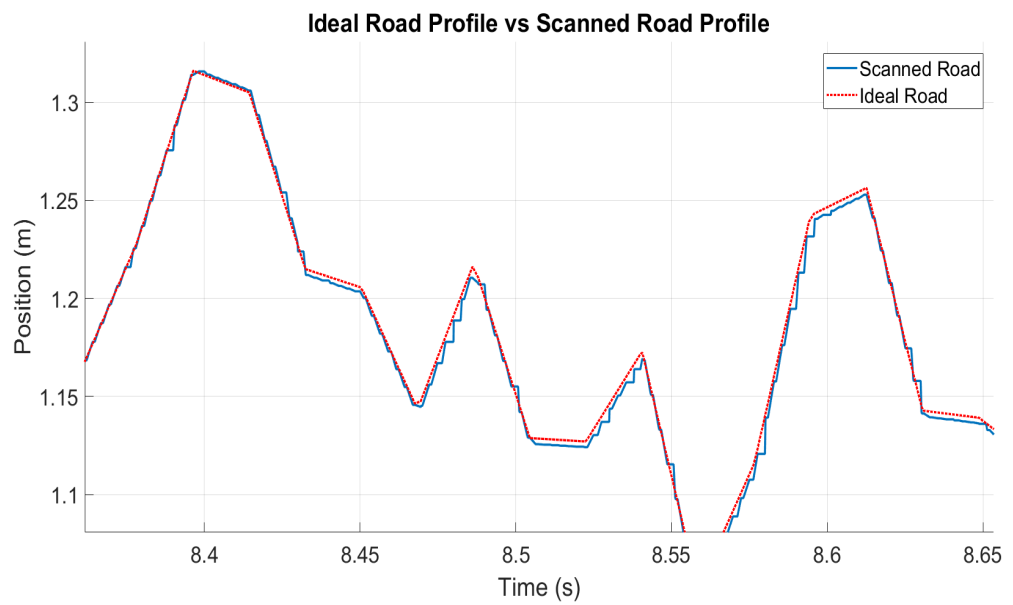


Figure 7.25: Ideal Road vs Scanned Road for 20km/h Quadrotor Speed

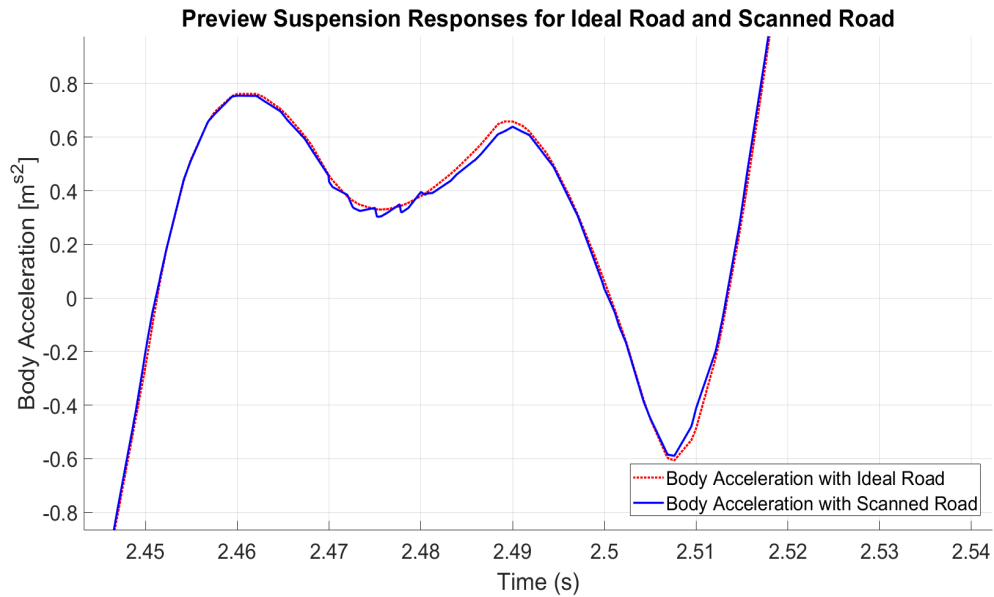


Figure 7.26: Body Acceleration Responses with Ideal Road and Scanned Road

7.4.2.2 Scenario 2: Quadrotor Speed 20 km/h, Range 100 Meters

In order to see the suspensions responses more clearly, the quadrotor is flied at an altitude of 100 meters, thus, the error values are increased. The scenario 2 is generated to investigate the "maximum error" situations, which refers the error when the quadrotor flies at an altitude of 100 meters for the given speed based on the vehicle speed. The Figure 7.27 shows the second scenario.

Figure 7.29 shows the scanned road under maximum error conditions and the ideal road. The disruption for the road is clearly seen in the figure. At this time the maximum distance between two scanned points is around 7.609 centimeters. Figure 7.28 also shows the scanned points per meter square under the maximum error conditions. Finally, Figure 7.30 shows the preview suspension response to the road which is scanned with the maximum error.

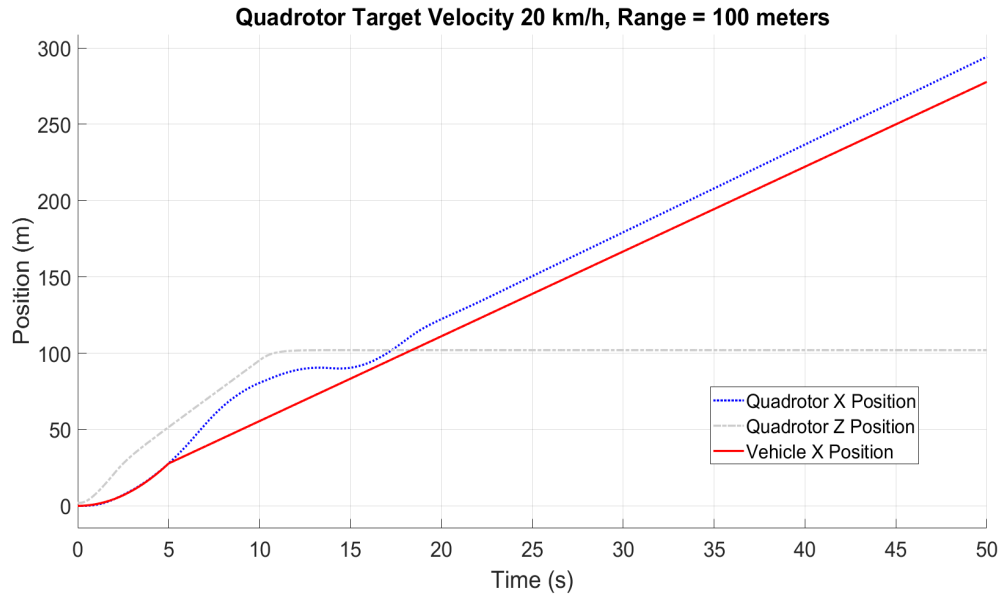


Figure 7.27: Stochastic Scenario 2 @20km/h, 100 meters

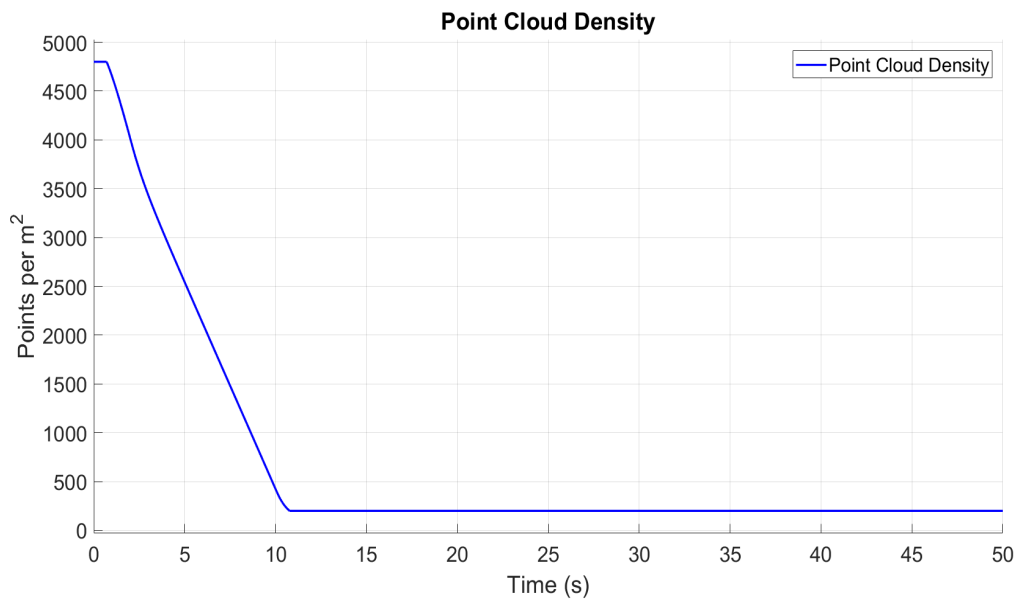


Figure 7.28: Point Cloud Density @20km/h, Range: 100 meters

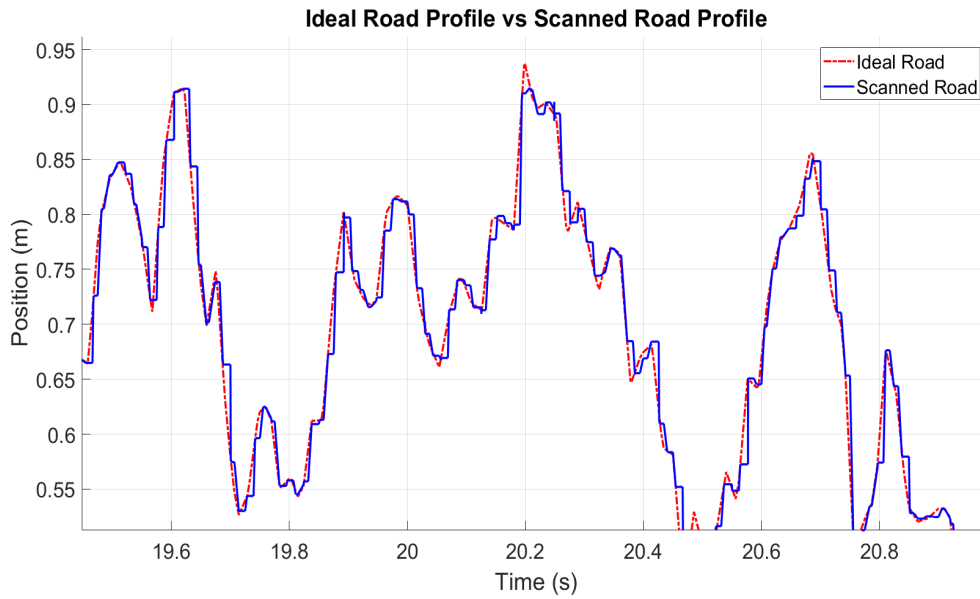


Figure 7.29: Ideal Road vs Scanned Road for 20km/h Quadrotor Speed and 100 meters range

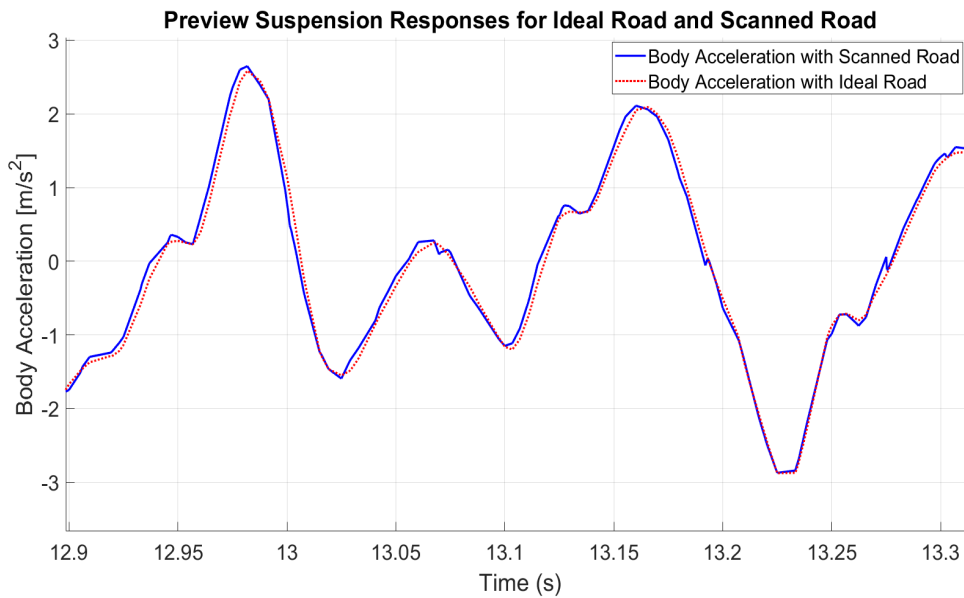


Figure 7.30: Body Acceleration Responses with Ideal Road and Scanned Road for Scenario 2

Table 7.10 shows performance degradation with for two different scenarios against to the ideal road responses.

Table 7.10: Performance Degradation with Scanned Road for 2 Scenarios

Performance Degradation with Scanned Road for 2 Scenarios							
Susp. Types	Vertical Acceleration			Vertical Disp.		Pitch Acc.	
	Raw RMS	Weighted RMS	Max	RMS	Max	RMS	Max
	Vehicle Velocity 20 km/h						
Preview Suspension w/ Ideal Road	-	-	-	-	-	-	-
Preview Suspension w/ Scanned Road [SC1]	-0.4%	-0.4%	-3.4%	-1.3%	-0.1%	-0.6%	-0.9%
Preview Suspension w/ Scanned Road [SC2]	-0.8%	-0.5%	-3.5%	-1.7%	-0.1%	-0.6%	-1%

7.4.3 Deterministic Results for G Type Road

Deterministic results refer the situations that there is no error based on laser scanner and the road information, which is used by the simulations, is exactly true data.

7.4.3.1 Time Domain Results @ 20 km/h

0.18 seconds time delay is applied to the road profile in order to simulate the 20 km/h vehicle velocity. The length of the road is 555 meters and the time of the drive is 100 seconds. Figure 7.31 shows the road profile.

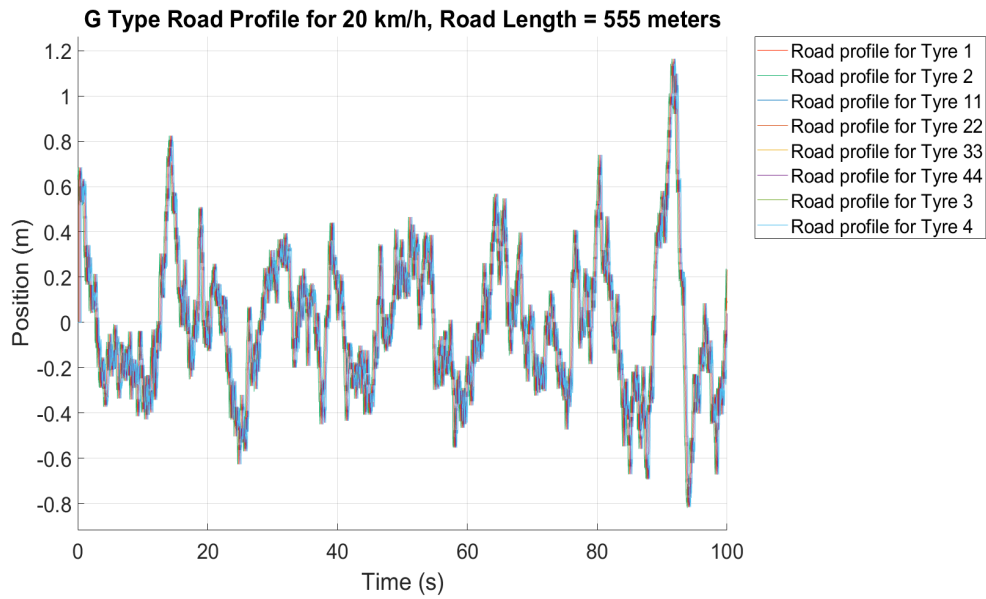


Figure 7.31: G Type Road Profile for 20km/h)

Figure 7.32, Figure 7.33 and Figure 7.34 show the vertical body displacement, vertical body acceleration and pitch acceleration for all suspension types, respectively.

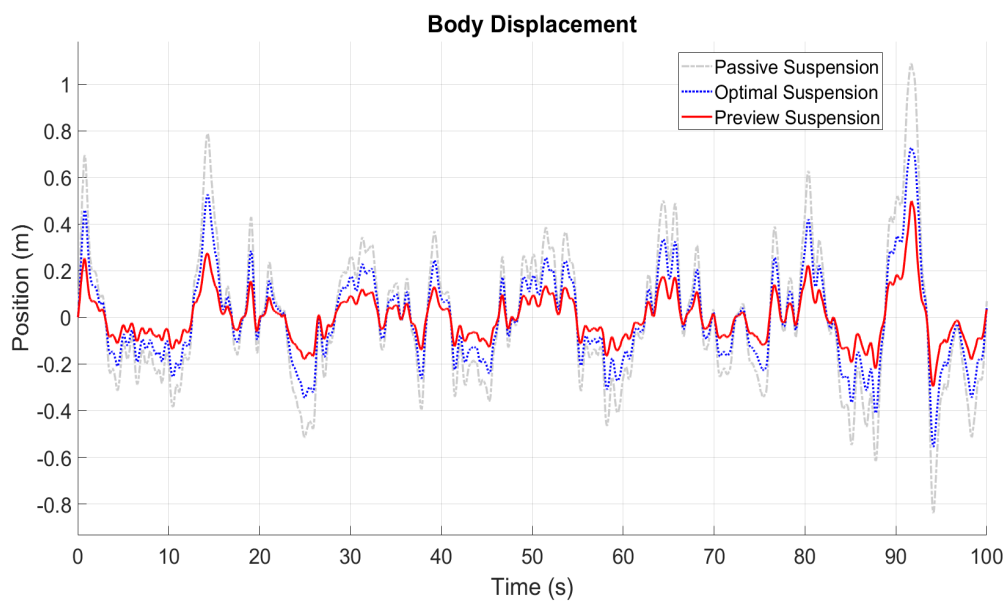


Figure 7.32: Body Displacement

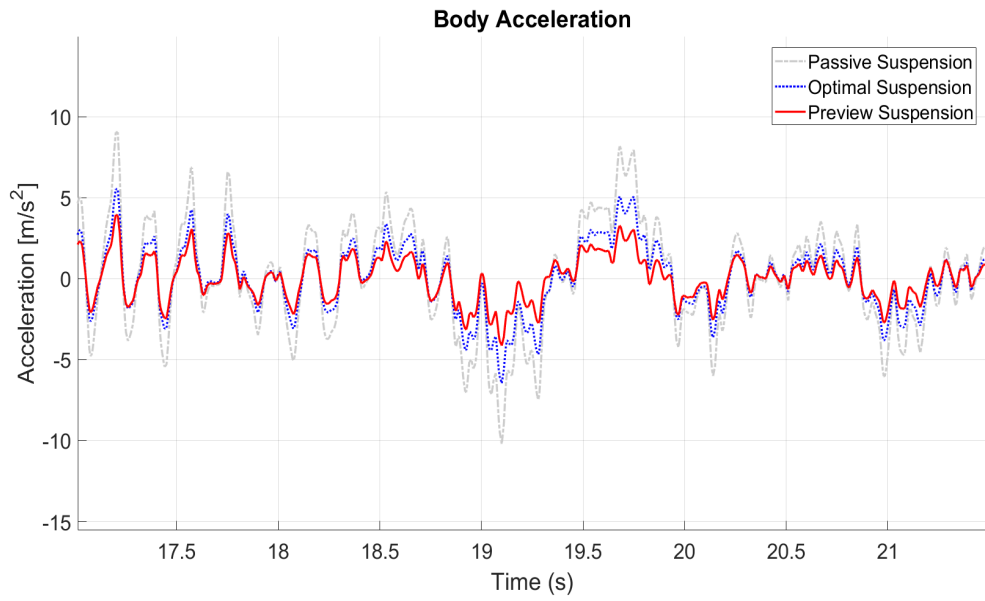


Figure 7.33: Body Acceleration

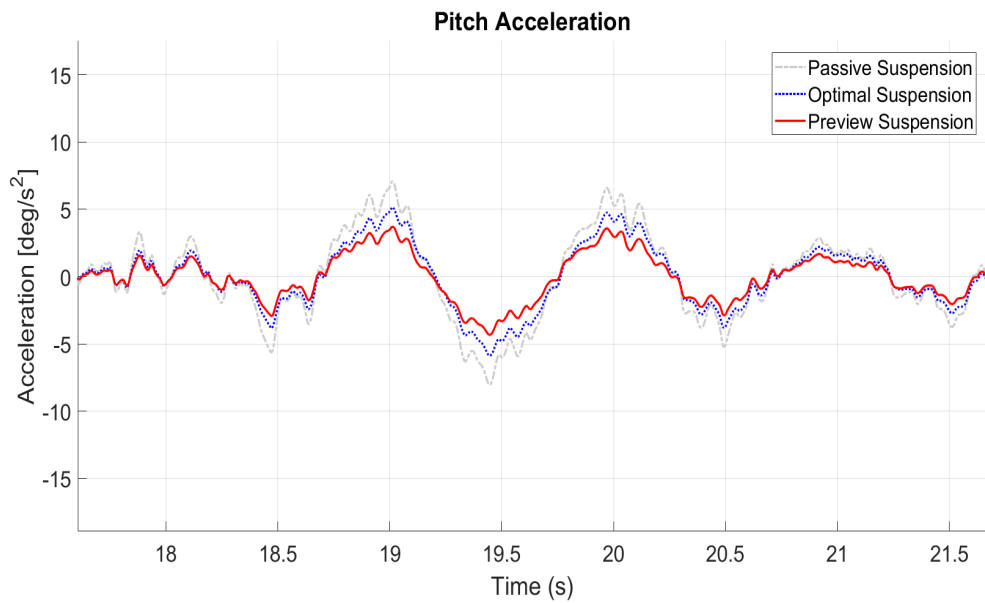


Figure 7.34: Pitch Acceleration

Figure 7.35 and 7.36 show the actuator forces for all tires and suspension travel for the tire 1, respectively.

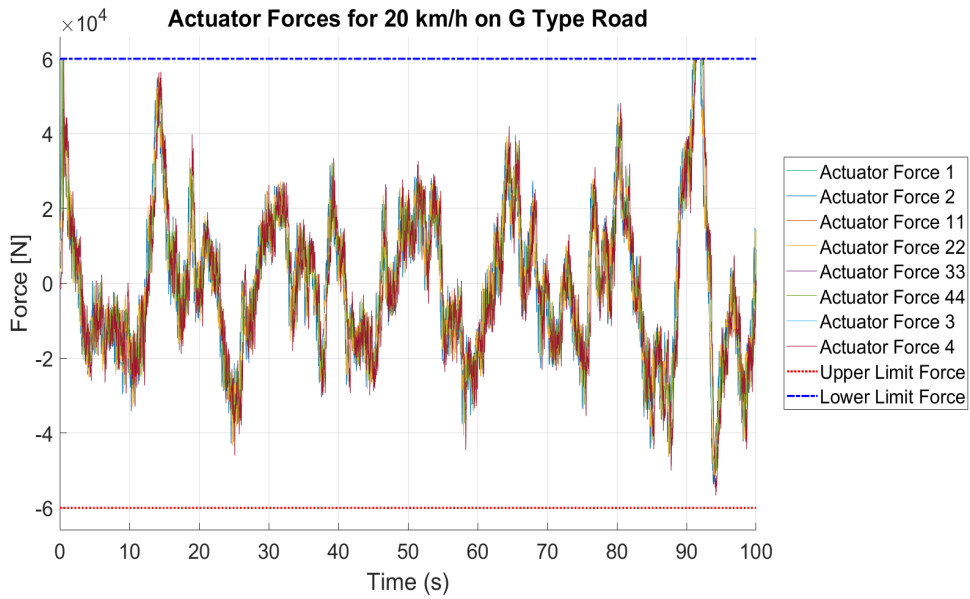


Figure 7.35: Actuator Forces and Limits

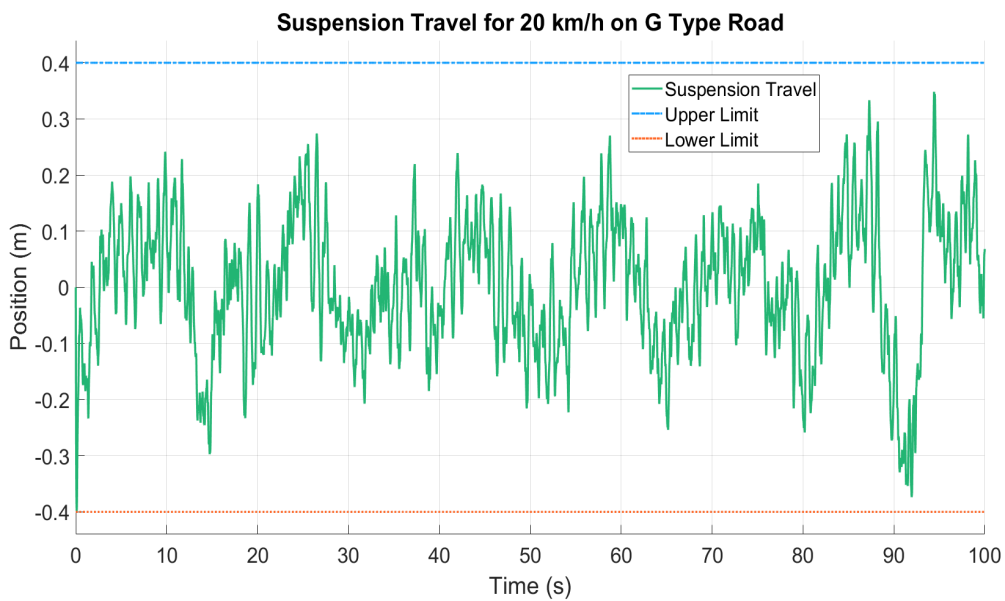


Figure 7.36: Suspension Travels and Limits

Table 7.11 and Table 7.12 summarize the performances of the different suspension system types against the G type road profile with the velocity of 20 km/h. The meanings and the consequences of the values are explained in detail in the discussion section.

Table 7.11: Time Domain Analyzes Results

Time Domain Analyzes Results							
	Vertical Acceleration			Vertical Disp.		Pitch Acc.	
Susp. Types	Raw RMS	Weighted RMS	Max	RMS	Max	RMS	Max
	Vehicle Velocity 20 km/h						
Passive	2.839	2.103	17.915	0.292	1.087	2.283	11.990
Optimal	1.730	1.332	10.732	0.190	0.728	1.649	7.888
Preview	1.236	0.866	8.398	0.102	0.498	1.231	7.527

Table 7.12: Time Domain Analyzes Results [Percental]

Time Domain Analyzes Results							
	Vertical Acceleration			Vertical Disp.		Pitch Acc.	
Susp. Types	Raw RMS	Weighted RMS	Max	RMS	Max	RMS	Max
	Vehicle Velocity 20 km/h						
Passive							
Optimal	39.1%	36.7%	40.1%	34.7%	33.0%	27.8%	34.2%
Preview	56.5%	58.8%	53.1%	65.2%	54.2%	46.1%	37.2%

7.4.3.2 Frequency Domain Results @ 20 km/h

Figure 7.37 shows the comparison of the different suspension systems based on the absorb power in frequency domain. Additionally, Table 7.13 shows the total average absorb power for the speed of 20 km/h and the road type of G. The meanings and the consequences of the values are explained in detail in the discussion section.

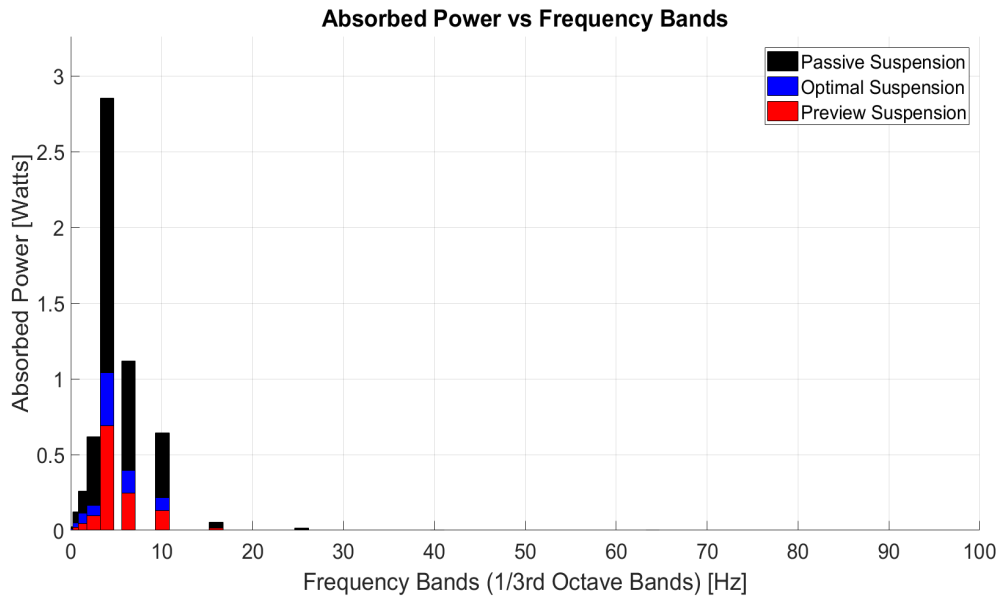


Figure 7.37: Absorb Power

Table 7.13: Frequency Domain Analyzes Results

Frequency Domain Analyzes Results	
	Total Absorb Power [Watts]
	Vehicle Velocity 20 km/h
Passive	5.84 W
Optimal	2.07 W
Preview	1.28 W

7.4.3.3 Preview and Optimal Suspension Limits for Ideally Known G Type Road

Preview Suspension Limits on G Road In order to understand the limits of the vehicle with preview suspension system on G type road, the speed of the vehicle has increased until the total absorb power value reaches the maximum allowable value, which is 6 watt. By doing so, it is observed that at 80 km/h, which is the maximum speed for the vehicle, the absorb power value is still below the allowable value, which is 6 watts. Therefore, we can say that the limit velocity for the preview suspension system is 80 km/h, while the limit for the passive suspension system is 20 km/h on the G type road profile. In this simulations, it is assumed that the road profile is known

ideally by the vehicle suspensions.

Figure 7.38 shows the 555 meters road profile with a time of drive of 25 seconds and Table 7.14 shows the time domain results of the preview suspension system with a vehicle velocity of 80 km/h on the G type road conditions. Finally Figure 7.39 shows the absorb with respect to the frequency bands and the Table 7.15 shows the total average absorb power with maximum speed of preview suspension system on the G type road.

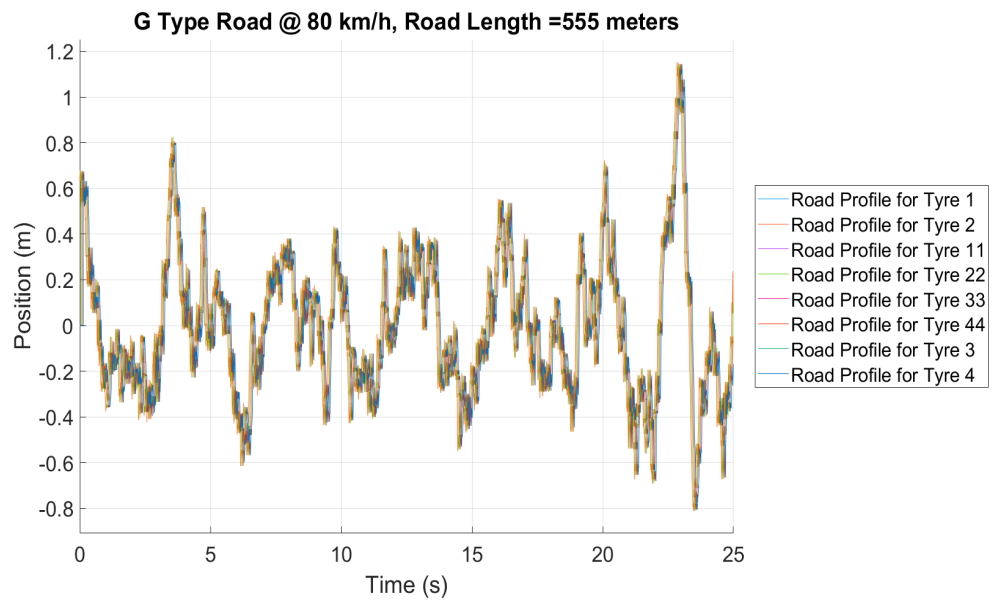


Figure 7.38: Road Profile

Table 7.14: Time Domain Analyzes Results

Time Domain Analyzes Results							
Susp. Types	Vertical Acceleration			Vertical Disp.		Pitch Acc.	
	Raw RMS	Weighted RMS	Max	RMS	Max	RMS	Max
Vehicle Velocity 80 km/h							
Preview	5.3597	4.9019	21.0216	0.1527	0.5013	1.8355	7.2279

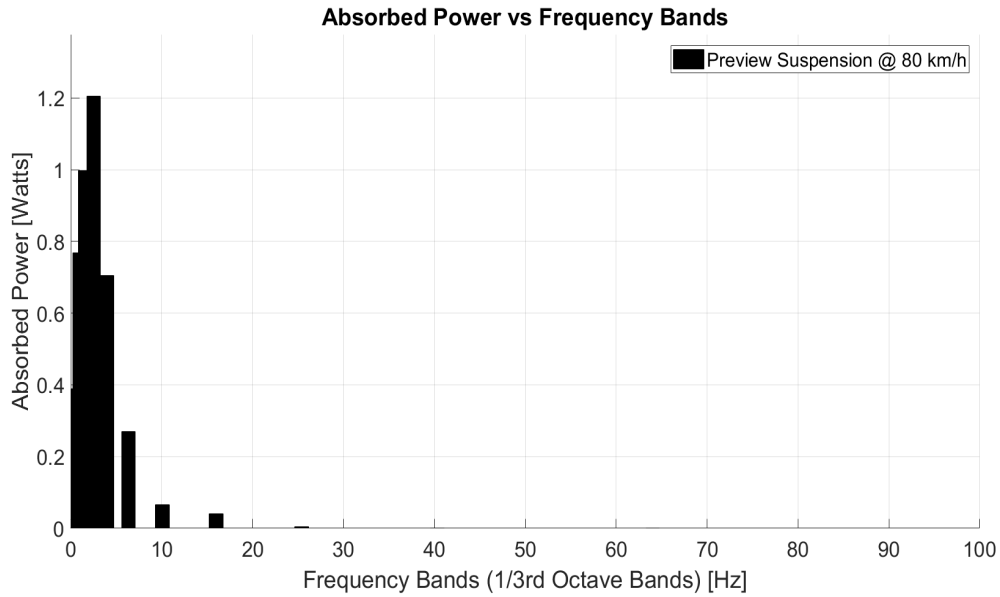


Figure 7.39: Preview Suspension Absorb Power @80 km/h

Table 7.15: Preview Suspension Absorb Power @80km/h

Frequency Domain Analyzes Results	
	Total Absorb Power [Watts]
	Vehicle Velocity 80 km/h
Preview Suspension	4.47 W

Optimal Suspension Limits on G Road

Table 7.16: Time Domain Analyzes Results

Time Domain Analyzes Results							
Susp. Types	Vertical Acceleration			Vertical Disp.		Pitch Acc.	
	Raw RMS	Weighted RMS	Max	RMS	Max	RMS	Max
	Vehicle Velocity 60 km/h						
Preview	6.0959	4.7365	16.9728	0.2374	0.8509	2.1462	7.0057

In this simulations, it is assumed that the road profile is known ideally by the vehicle suspensions. Figure 7.40 shows the 555 meters road profile with a time of drive of 33 seconds and Table 7.16 shows the time domain results of the optimal suspension

system with a vehicle velocity of 60 km/h on the G type road conditions. Finally Figure 7.41 shows the absorb with respect to the frequency bands and the Table 7.17 shows the total average absorb power with maximum speed of optimal suspension system on the G type road.

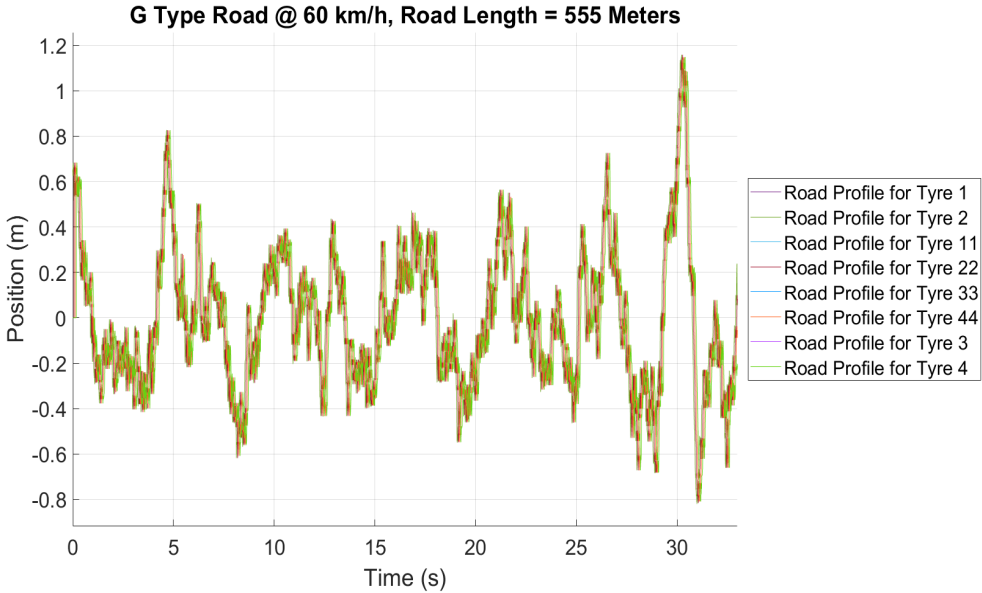


Figure 7.40: Road Profile

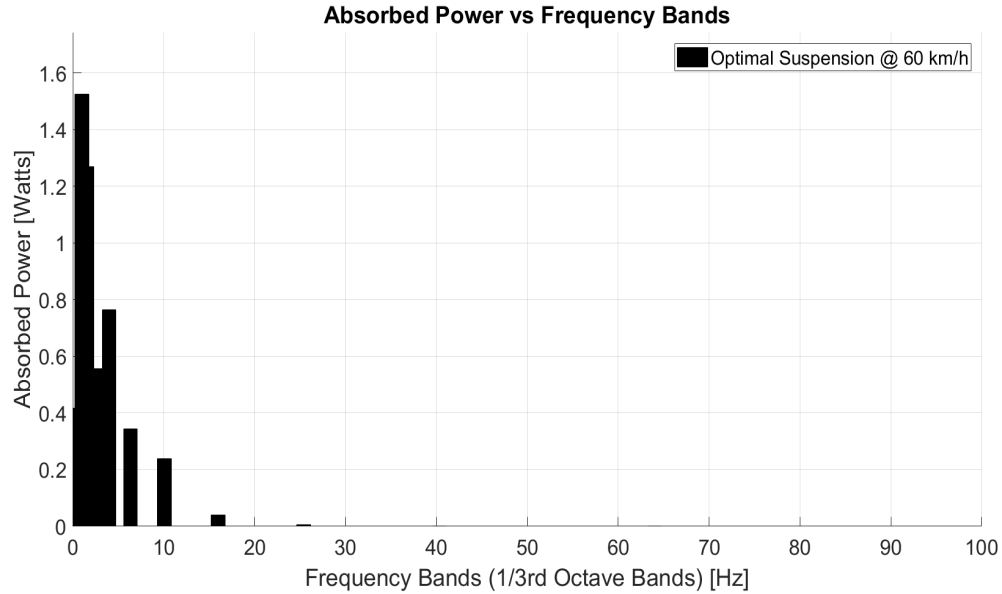


Figure 7.41: Optimal Suspension Absorb Power @60 km/h

Table 7.17: Optimal Suspension Absorb Power @60km/h

Frequency Domain Analyzes Results	
	Total Absorb Power [Watts]
	Vehicle Velocity 60 km/h
Preview Suspension	5.19 W

7.4.4 Stochastic Results for G Type Road @ 40 km/h

For the stochastic results, the quadrotor based error parameters are taken into account and the affect of the errors is evaluated. Figure 7.22 shows the general point cloud density trend with respect to quadrotor range and velocity.

7.4.4.1 Scenario 1: Quadrotor Speed 40 km/h, Range 5 Meters

Figure 7.42 shows the relative motion of the quadrotor and the vehicle on X and Z axes. There is no motion on the Y axes. The altitude of the vehicle is assumed as zero and the altitude of the quadrotor is 5 meters. Figure 7.43 shows the scanned points per square meter. The point cloud density is depend on the range and speed of the quadrotor and the Figure 7.43 shows that the point cloud density decreases from 4800 points to the 3000 points as the quadrotor accelerates to the 40 km/h. Therefore, the maximum distance between two scanned points is around 1.86 centimeters. Additionally, Figure 7.44 and Figure 7.45 show the difference between the ideal road and the scanned road and the differences of the responses of the preview suspension system to the ideal road and the scanned road.

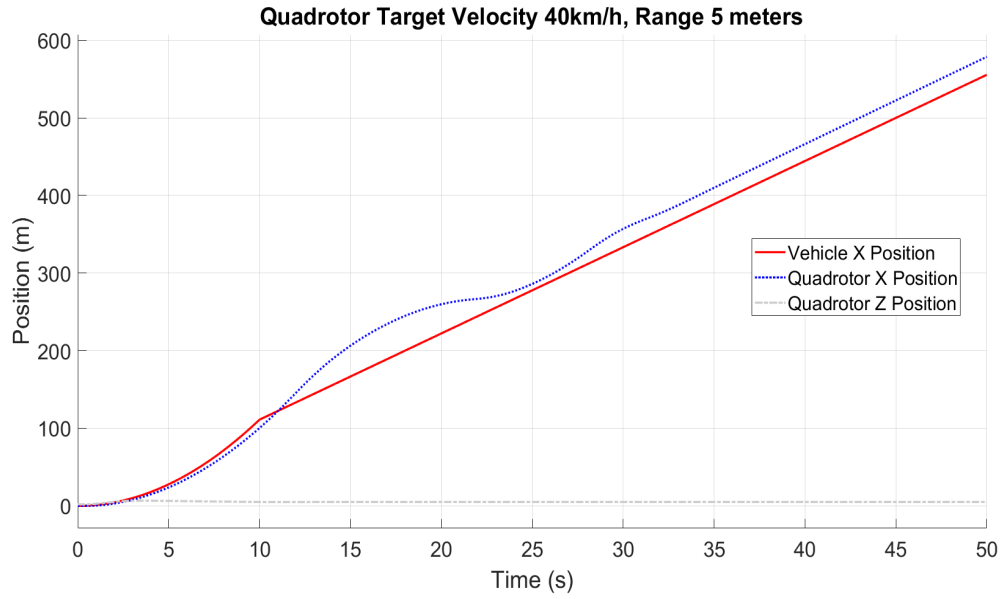


Figure 7.42: Quad. Range =5 meters and Target Velocity= 40 km/h

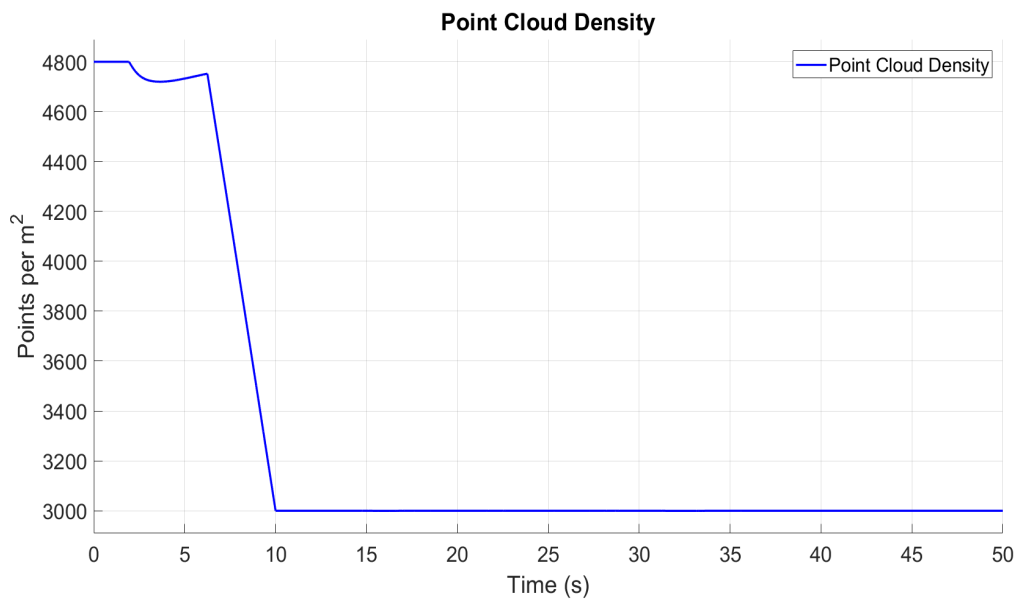


Figure 7.43: Point Cloud Density for Range =5 meters and Target Velocity= 40 km/h

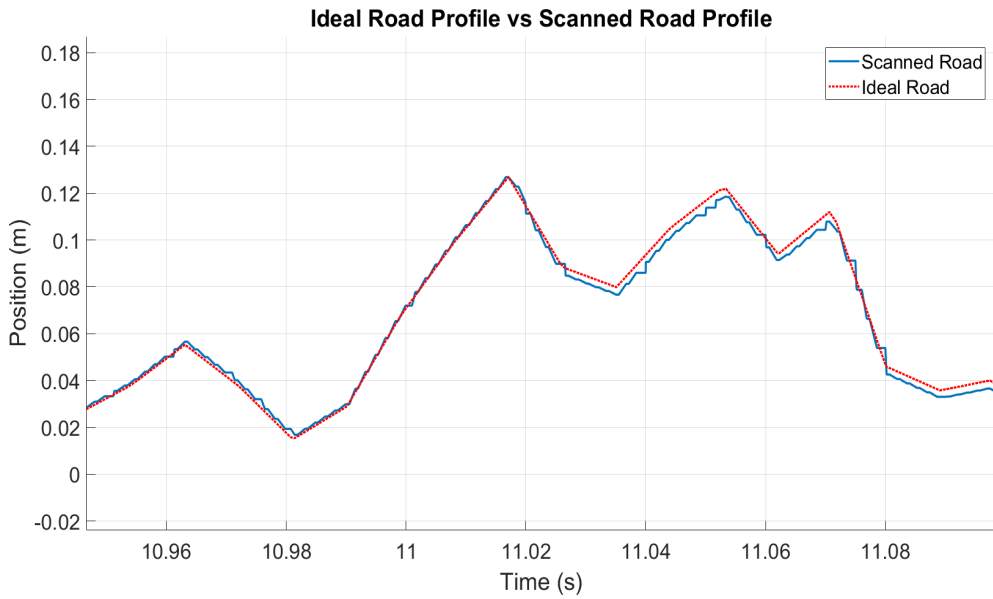


Figure 7.44: Ideal Road vs Scanned Road

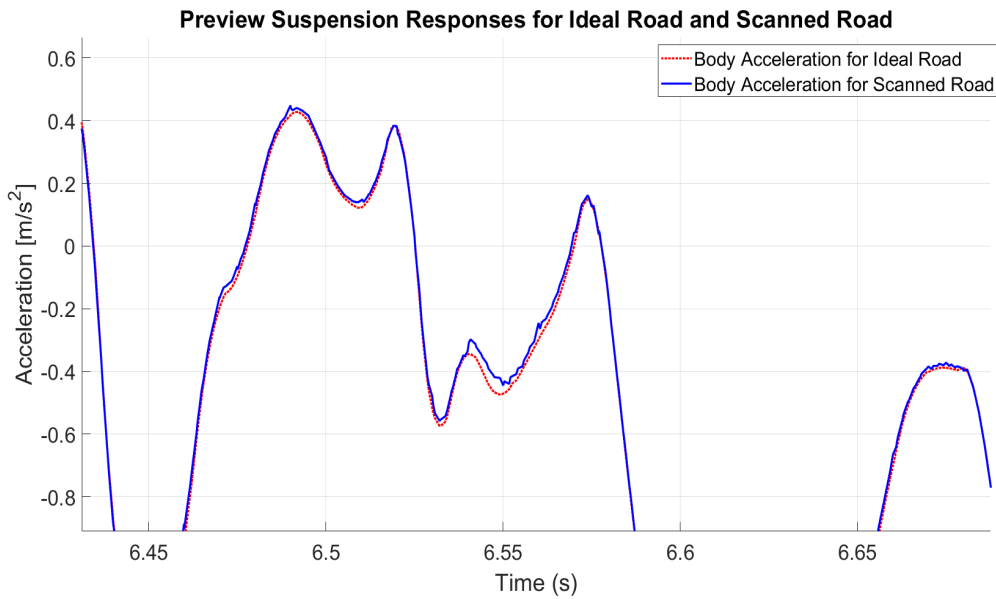


Figure 7.45: Vertical Acceleration for Ideal Road and Scanned Road

7.4.4.2 Scenario 2: Quadrotor Speed 40 km/h, Range 100 Meters

In order to see the suspensions responses more clearly, the quadrotor is flid at an altitude of 100 meters, thus, the error values are increased. The scenario 2 is gener-

ated to investigate the "maximum error" situations, which refers the error when the quadrotor flies at an altitude of 100 meters for the given speed based on the vehicle speed. The Figure 7.46 shows the second scenario.

Figure 7.48 shows the scanned road under maximum error conditions and the ideal road. The disruption for the road is clearly seen in the figure. At this time the maximum distance between two scanned points is around 7.609 centimeters. Figure 7.47 also shows the scanned points per meter square under the maximum error conditions. Finally, Figure 7.49 shows the preview suspension response to the road which is scanned with the maximum error.

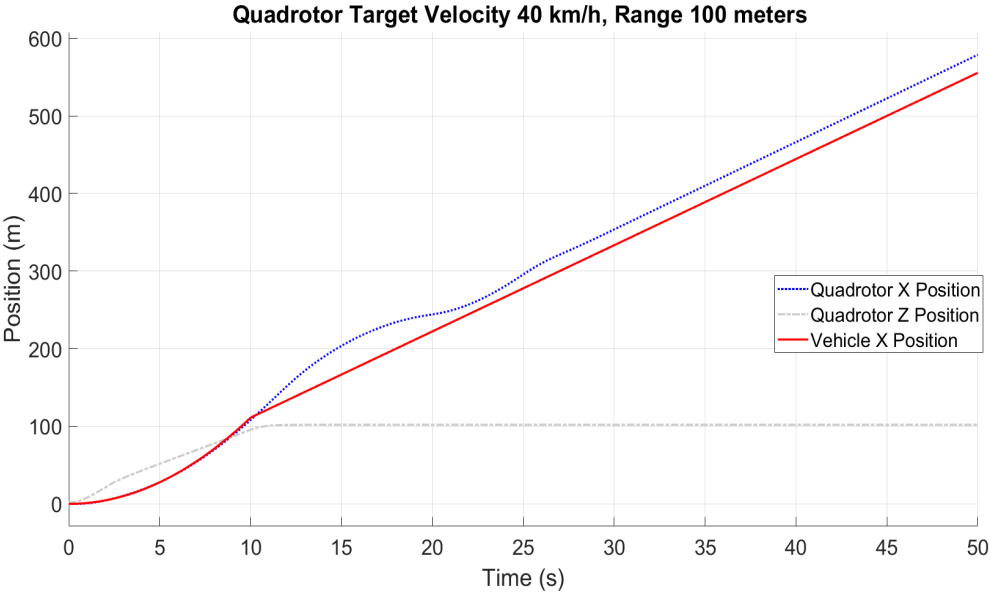


Figure 7.46: Quad. Range =100 meters and Target Velocity= 40 km/h

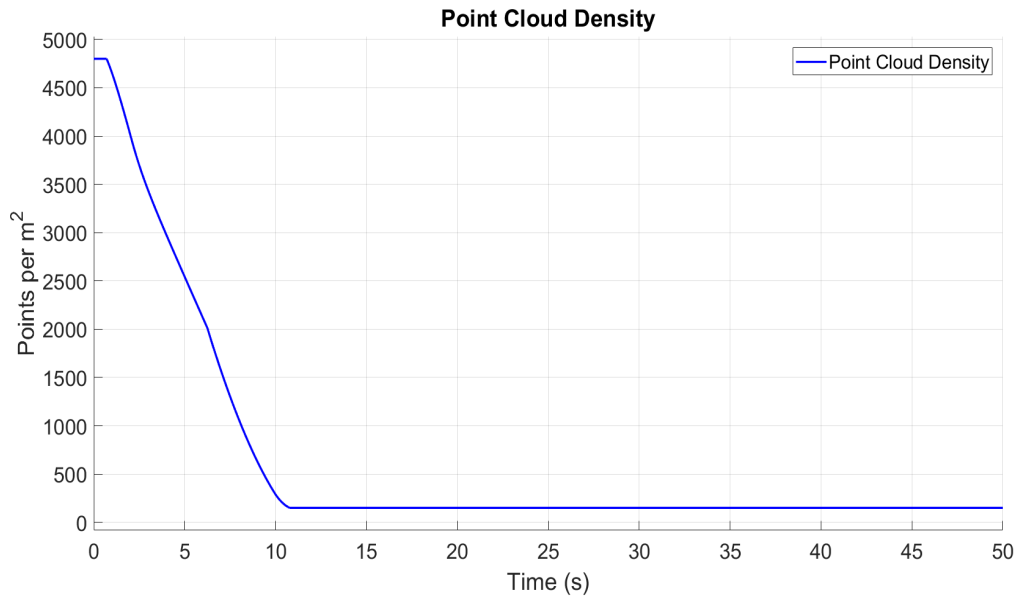


Figure 7.47: Point Cloud Density for Range =100 meters and Target Velocity= 40 km/h

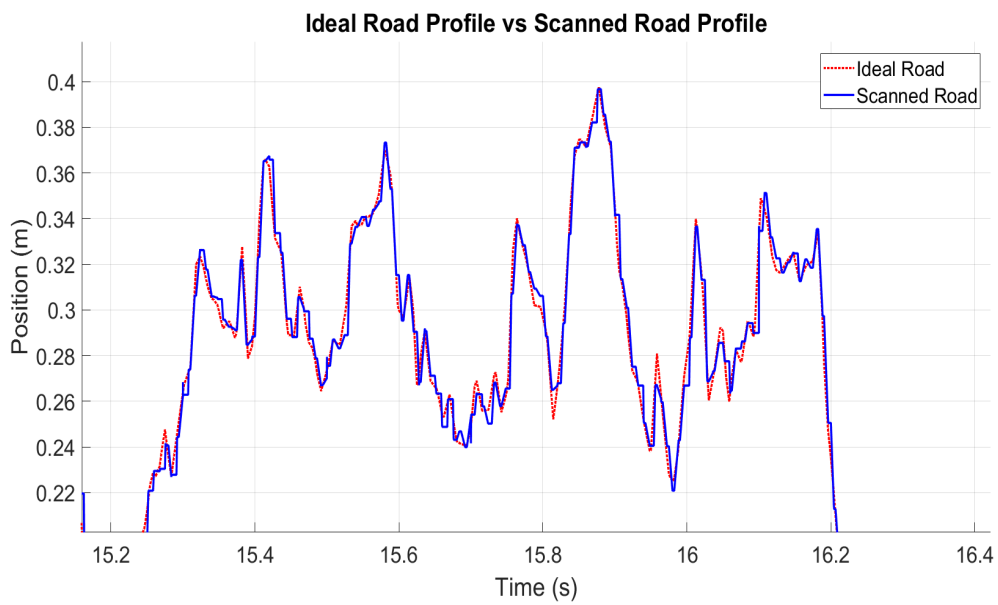


Figure 7.48: Ideal Road vs Scanned Road for Scenario 2

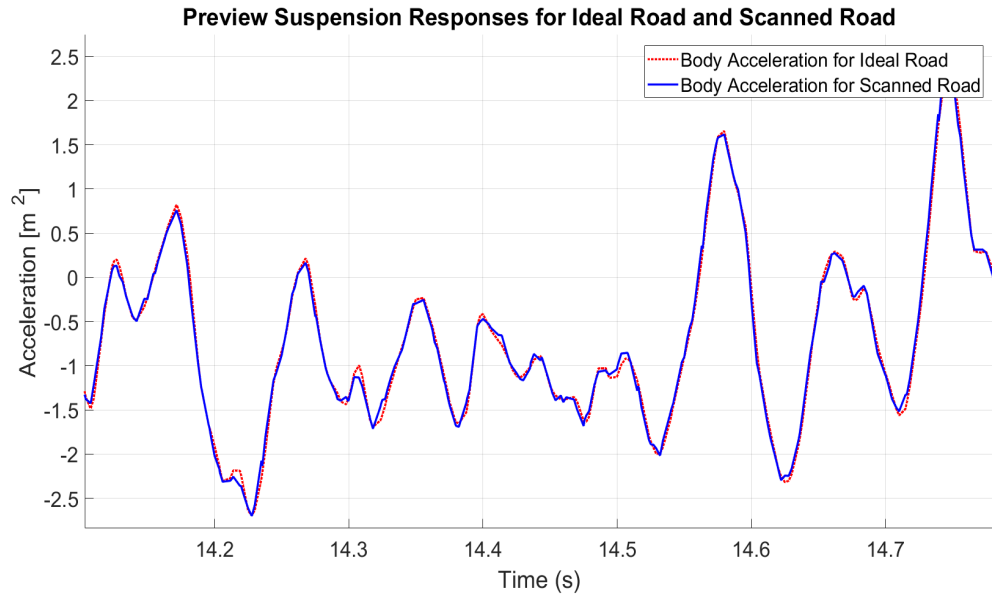


Figure 7.49: Vertical Acceleration for Ideal Road and Scanned Road for Scenario 2

Table 7.18 shows performance degradation with for two different scenarios against to the ideal road responses.

Table 7.18: Performance Degradation with Scanned Road for 2 Scenarios

Performance Degradation with Scanned Road for 2 Scenarios							
Susp. Types	Vertical Acceleration			Vertical Disp.		Pitch Acc.	
	Raw RMS	Weighted RMS	Max	RMS	Max	RMS	Max
Vehicle Velocity 40 km/h							
Preview Susp. w/ Ideal Road	-	-	-	-	-	-	-
Preview Susp. w/ Scan. Road [1]	-0.18%	-0.29%	-0.3%	-0.0%	-0.04%	-0.09%	-0.0%
Preview Susp. w/ Scan. Road [2]	-0.33%	-0.6%	-0.48%	-0.6%	-0.1%	-0.6%	-1%

7.4.5 Deterministic Results for B Type Road

Deterministic results refer the situations that there is no error based on laser scanner and the road information, which is used by the simulations, is exactly true data.

7.4.5.1 Time Domain Results @ 80 km/h

0.0450 seconds time delay is applied to the road profile in order to simulate the 80 km/h vehicle velocity. The length of the road is 1111 meters and the time of drive is 50 seconds. Figure 7.50 shows the road profile.

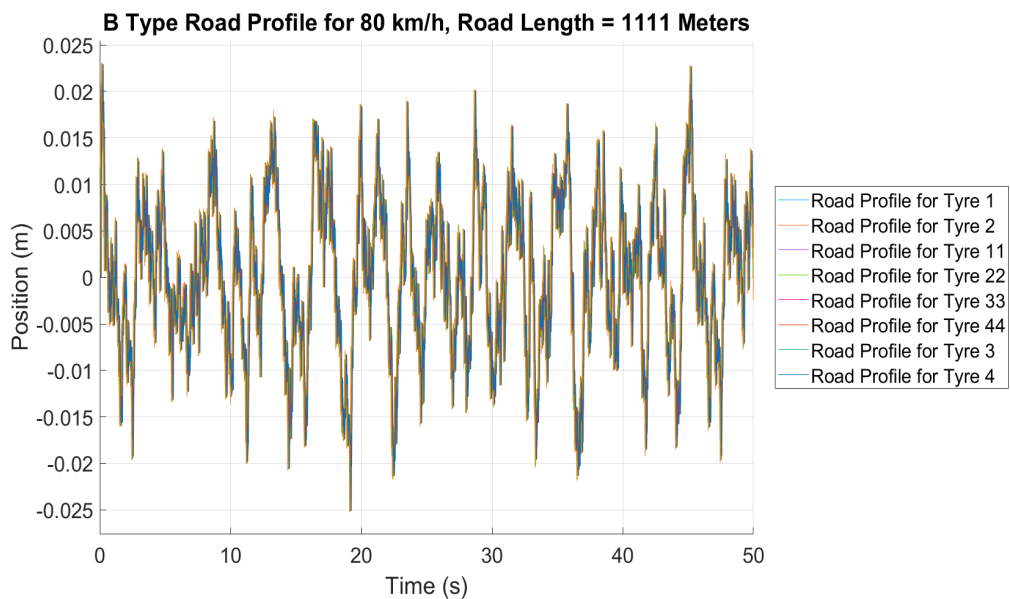


Figure 7.50: Road Profile for Each Axes (Delay=0.045sc => Vehicle Velocity 80km/h)

Figure 7.51, Figure 7.52 and Figure 7.53 show the vertical body displacement, vertical body acceleration and pitch acceleration for all suspension types, respectively.

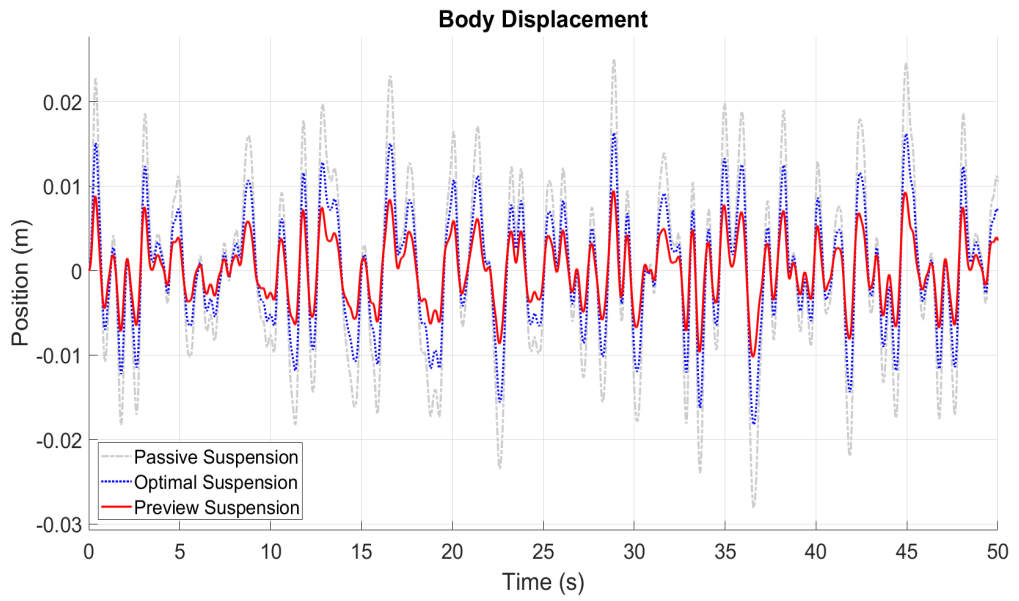


Figure 7.51: Vertical Displacement for Vehicle Speed= 80 km/h

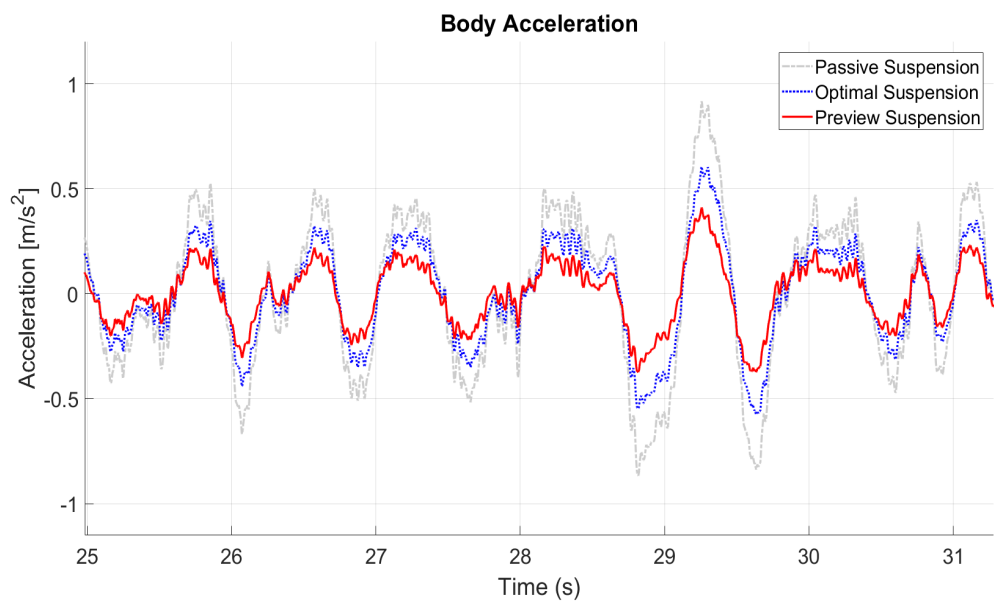


Figure 7.52: Vertical Acceleration for Vehicle Speed=80km/h

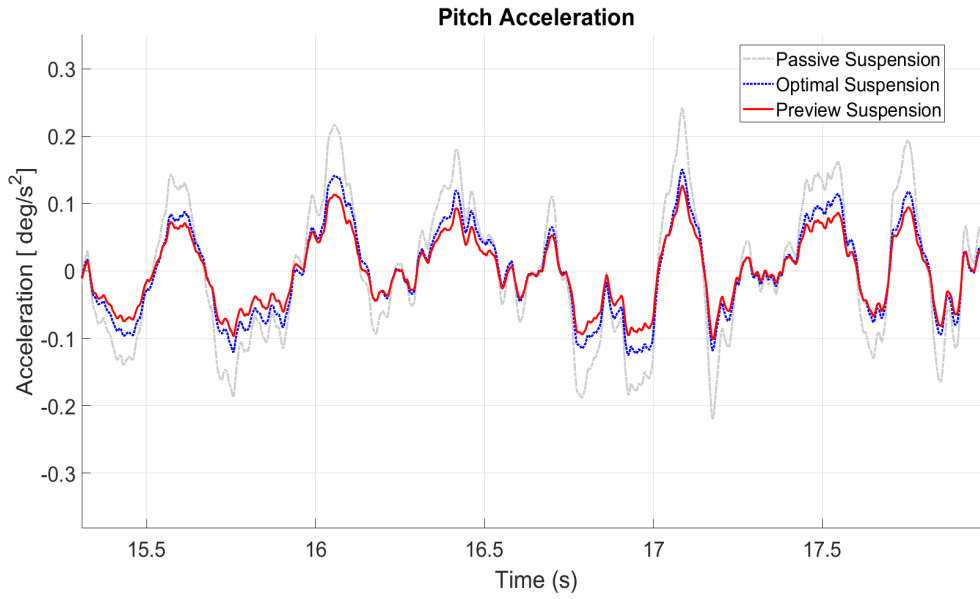


Figure 7.53: Pitch Acceleration for Vehicle Speed=80km/h

Figure 7.54 and 7.55 show the actuator forces for all tires and suspension travel for the tire 1, respectively.

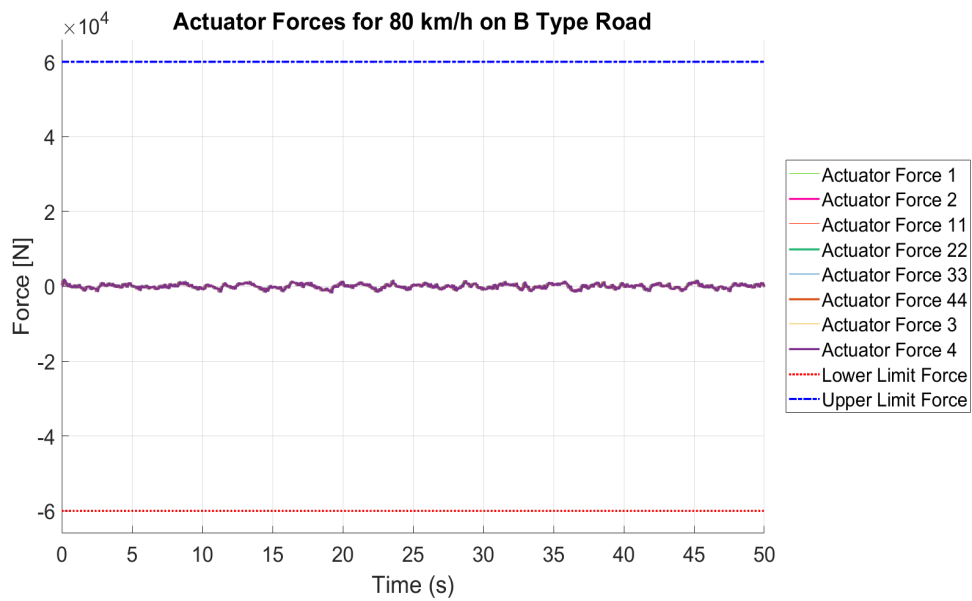


Figure 7.54: Actuator Forces and Limits



Figure 7.55: Suspension Travels and Limits

Table 7.19 and Table 7.20 summarize the performances of the different suspension system types against the B type road profile with the velocity of 80 km/h. The meanings and the consequences of the values are explained in detail in the discussion section.

Table 7.19: Time Domain Analyzes Results

Time Domain Analyzes Results							
Susp. Types	Vertical Acceleration			Vertical Disp.		Pitch Acc.	
	Raw RMS	Weighted RMS	Max	RMS	Max	RMS	Max
Vehicle Velocity 80 km/h							
Passive	0.348	0.124	1.161	0.010	0.025	0.100	0.340
Optimal	0.239	0.080	0.770	0.007	0.016	0.067	0.225
Preview	0.148	0.057	0.488	0.004	0.010	0.052	0.180

Table 7.20: Time Domain Analyzes Results (Percental)

Time Domain Analyzes Results (Percental)							
Susp. Types	Vertical Acceleration			Vertical Disp.		Pitch Acc.	
	Raw RMS	Weighted RMS	Max	RMS	Max	RMS	Max
	Vehicle Velocity 80 km/h						
Passive							
Optimal	33.74%	35.22%	33.67%	34.31%	35.06%	33.50%	33.81%
Preview	57.51%	53.68%	57.90%	62.75%	62.15%	47.70%	47.19%

7.4.5.2 Frequency Domain Results @ 80 km/h

Figure 7.56 shows the comparison of the different suspension systems based on the absorb power in frequency domain. Additionally, Table 7.21 shows the total average absorb power for the speed of 80 km/h and the road type of G. The meanings and the consequences of the values are explained in detail in the discussion section.

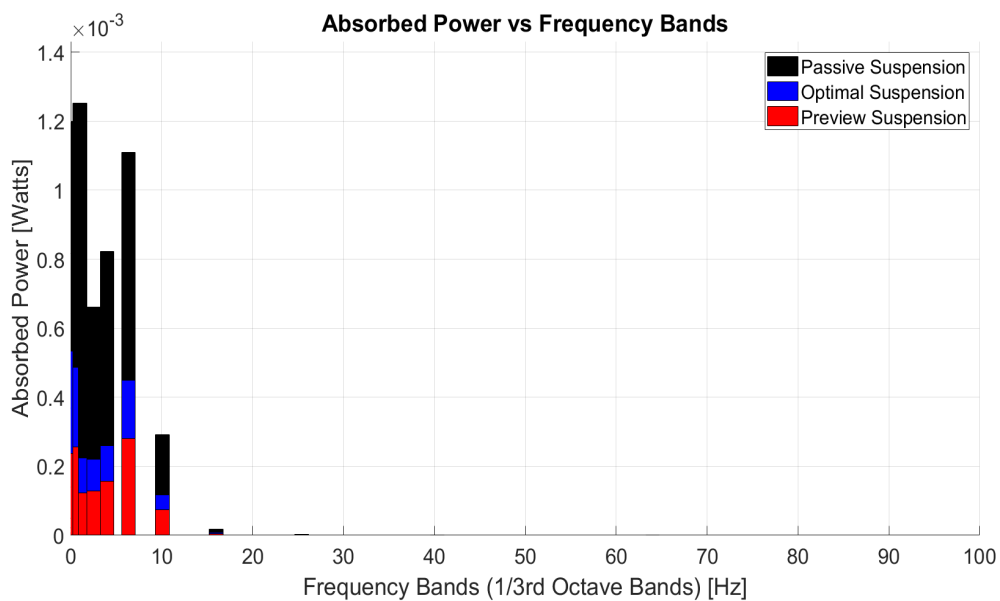


Figure 7.56: Preview Suspension Absorb Power @80 km/h

Table 7.21: Frequency Domain Analyzes Results

Frequency Domain Analyzes Results	
	Total Absorb Power [Watts]
	Vehicle Velocity 80 km/h
Passive	0.012 W
Optimal	0.002 W
Preview	0.001 W

7.4.5.3 Preview and Optimal Suspension Limits for Ideally Known B Type Road

Since the limit of the vehicle is assumed to be 80 km/h and the absorb power is under the limit of 6 watt value, it can be say that the preview and optimal suspension speed limit is 80 km/h for this type of road.

7.4.6 Stochastic Results for B Type Road @ 40 km/h

For the stochastic results, the quadrotor based error parameters are taken into account and the affect of the errors is evaluated. Figure 7.22 shows the point cloud density trend with respect to quadrotor range and velocity.

7.4.6.1 Scenario 1: Quadrotor Speed 40 km/h, Range 5 Meters

Figure 7.57 shows the relative motion of the quadrotor and the vehicle on X and Z axes. There is no motion on the Y axes. The altitude of the vehicle is assumed as zero and the altitude of the quadrotor is 5 meters. Figure 7.58 shows the scanned points per square meter. The point cloud density is depend on the range and speed of the quadrotor and the Figure 7.58 shows that the point cloud density decreases from 4800 points to the 3000 points as the quadrotor accelerates to the 40 km/h. Therefore, the maximum distance between two scanned points is around 1.86 centimeters. Additionally, Figure 7.59 and Figure 7.60 show the difference between the ideal road and the scanned road and the differences of the responses of the preview suspension system to the ideal road and the scanned road.

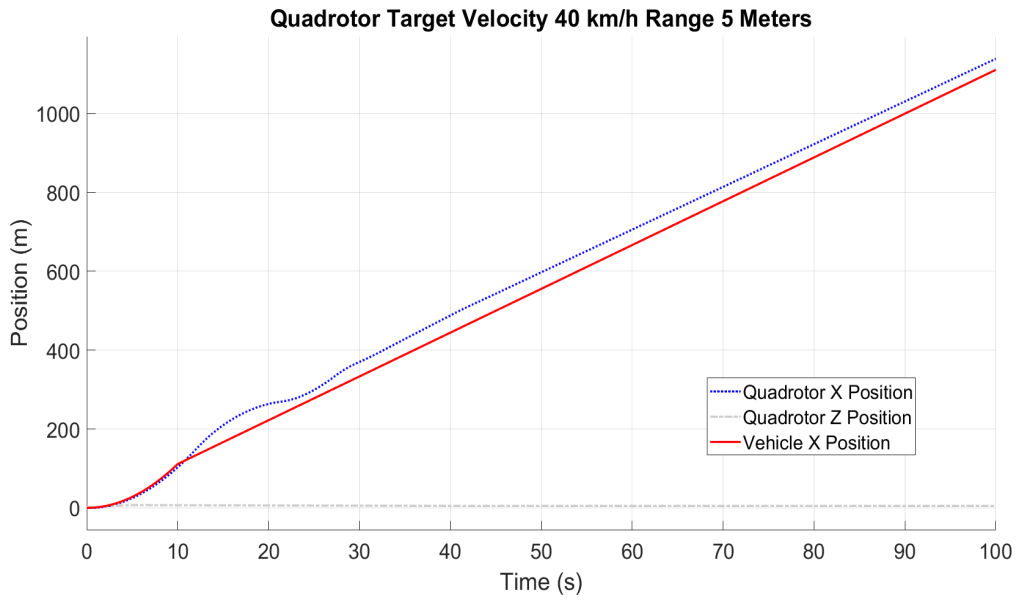


Figure 7.57: Quad. Range =5 meters and Target Velocity= 40 km/h

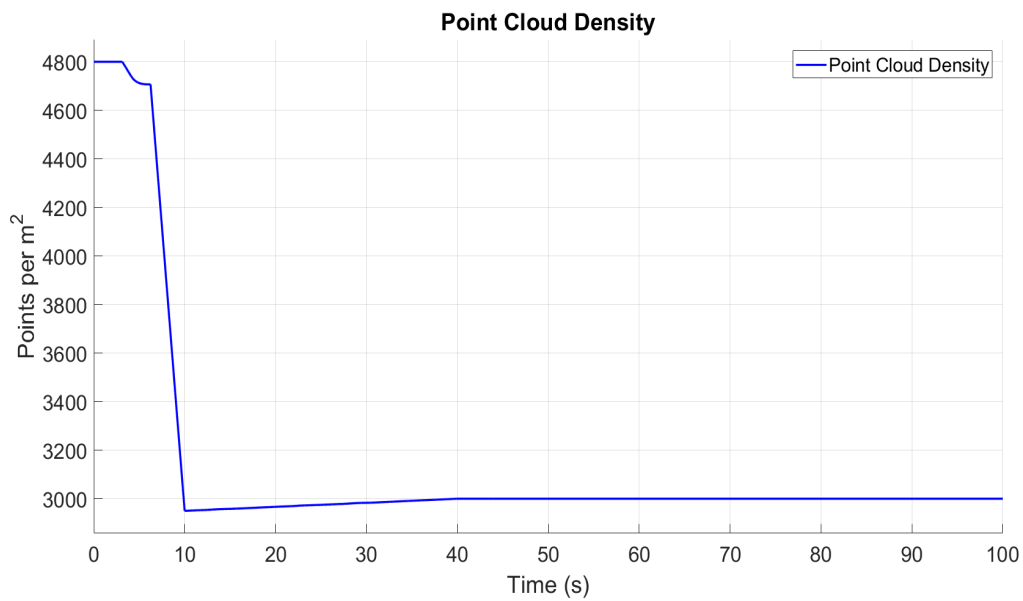


Figure 7.58: Point Cloud Density for Range =5 meters and Target Velocity= 40 km/h

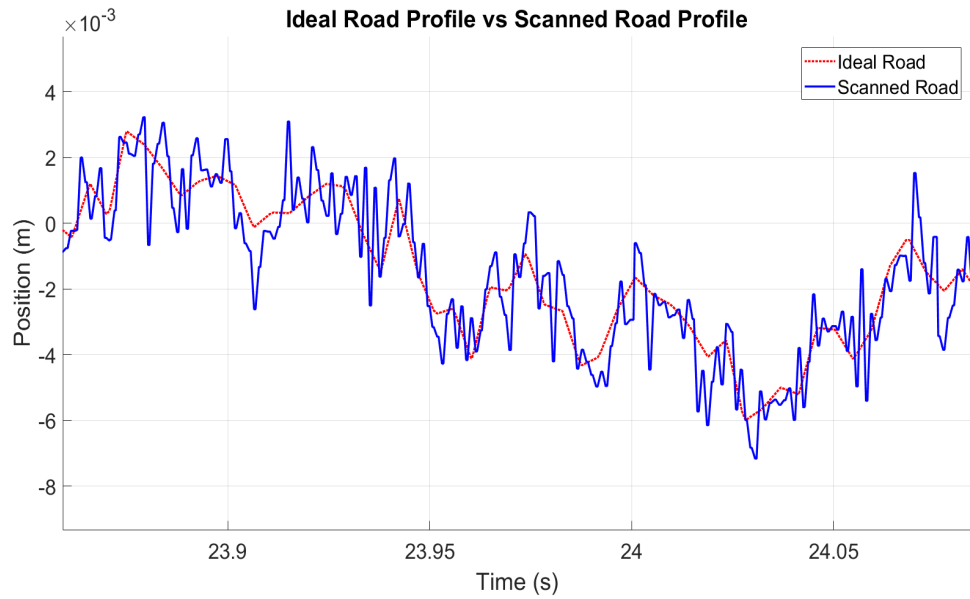


Figure 7.59: Ideal Road vs Scanned Road for Scenario 1

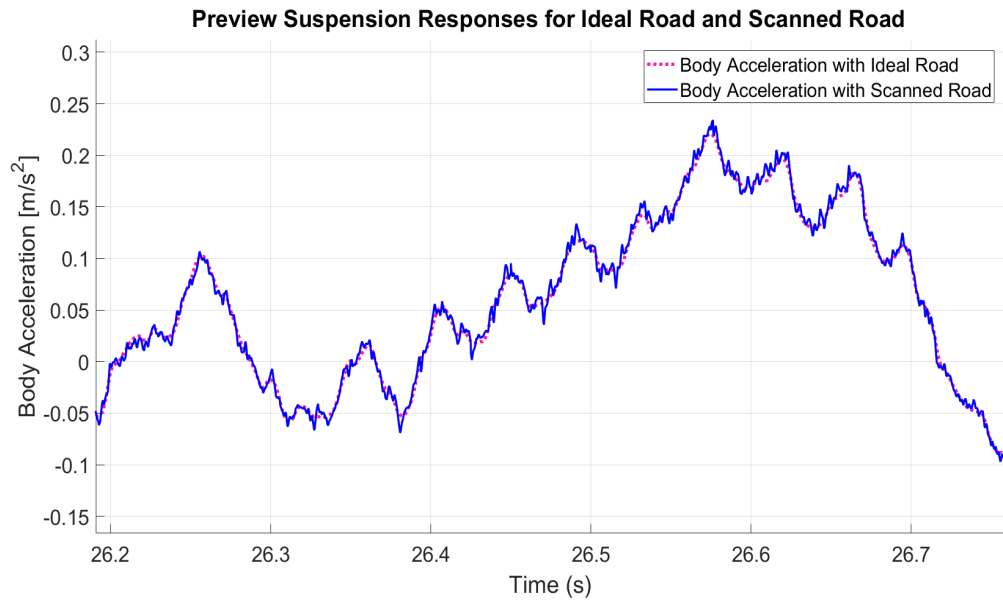


Figure 7.60: Vertical Acceleration for Ideal Road and Scanned Road for Scenario 1

7.4.6.2 Scenario 2: Quadrotor Speed 40 km/h, Range 100 Meters

In order to see the suspensions responses more clearly, the quadrotor is flid at an altitude of 100 meters, thus, the error values are increased. The scenario 2 is gener-

ated to investigate the "maximum error" situations, which refers the error when the quadrotor flies at an altitude of 100 meters for the given speed based on the vehicle speed. The Figure 7.61 shows the second scenario.

Figure 7.63 shows the scanned road under maximum error conditions and the ideal road. The disruption for the road is clearly seen in the figure. At this time the maximum distance between two scanned points is around 7.609 centimeters. Figure 7.62 also shows the scanned points per meter square under the maximum error conditions. Finally, Figure 7.64 shows the preview suspension response to the road which is scanned with the maximum error.

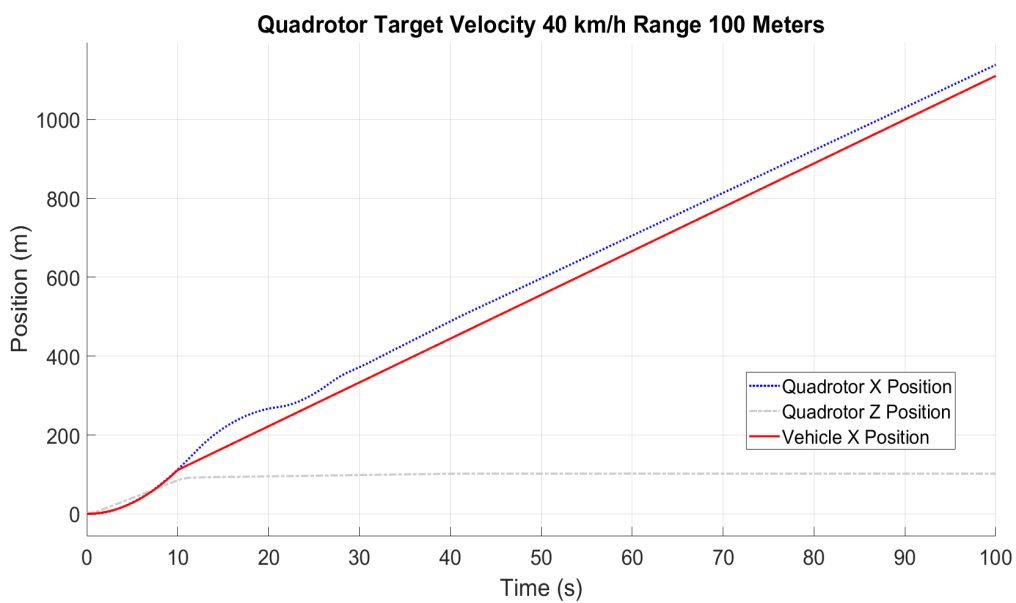


Figure 7.61: Quad. Range =100 meters and Target Velocity= 40 km/h

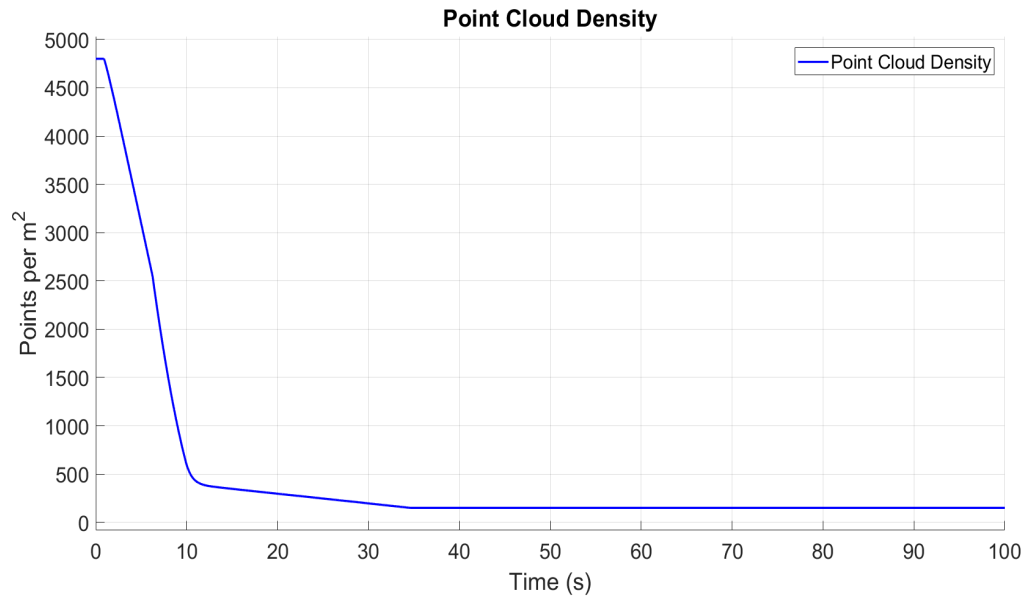


Figure 7.62: Point Cloud Density for Range =100 meters and Target Velocity= 80 km/h

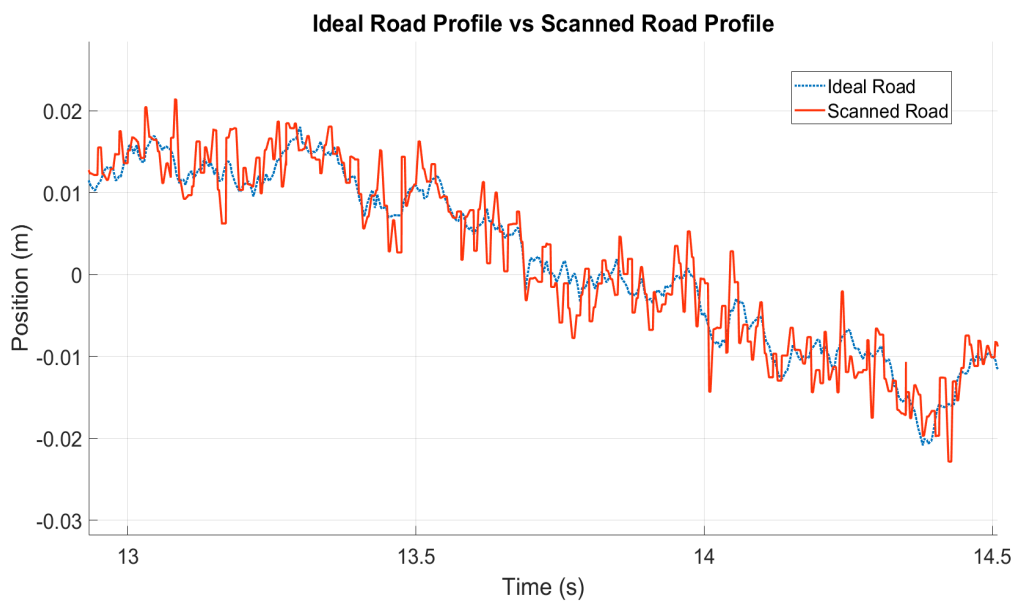


Figure 7.63: Ideal Road vs Scanned Road for Scenario 2

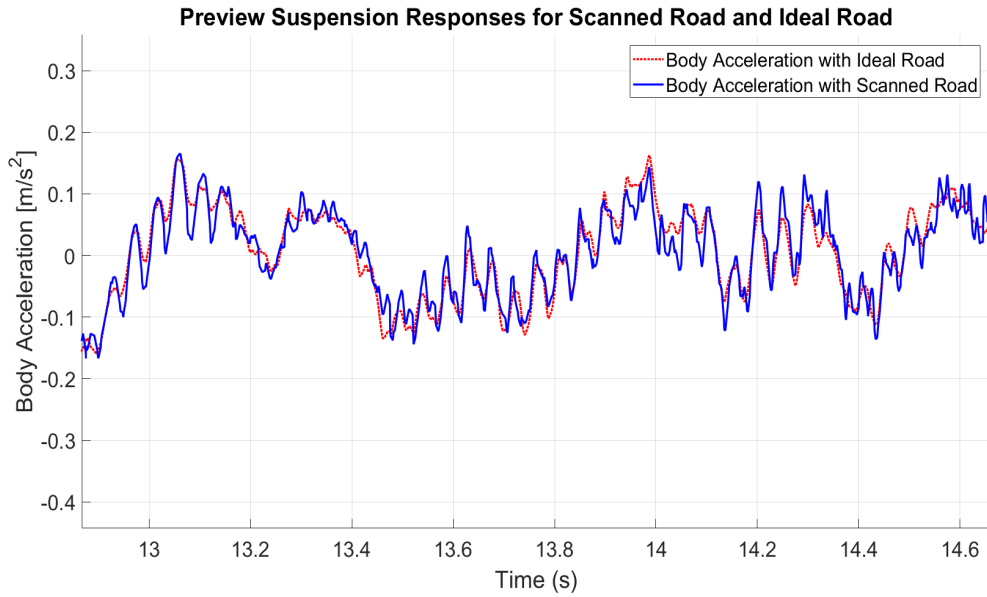


Figure 7.64: Vertical Acceleration for Ideal Road and Scanned Road for Scenario 2

Table 7.22 and the Table 7.23 shows performance degradation with for two different scenarios against to the ideal road responses.

Table 7.22: Time Domain Analyzes Results

Time Domain Analyzes Results							
Susp. Types	Vertical Acceleration			Vertical Disp.		Pitch Acc.	
	Raw RMS	Weighted RMS	Max	RMS	Max	RMS	Max
Vehicle Velocity 40 km/h							
Preview Suspension w/ Ideal Road	0.0788	0.0298	0.2505	0.0032	0.0098	0.0464	0.1596
Preview Suspension w/ Scanned Road [SC1]	0.0791	0.0301	0.2579	0.0033	0.0099	0.0466	0.1612
Preview Suspension w/ Scanned Road [SC2]	0.0828	0.0327	0.2990	0.0035	0.0100	0.0473	0.1622

Table 7.23: Performance Degradation with Scanned Road for 2 Scenarios

Performance Degradation with Scanned Road for 2 Scenarios							
Susp. Types	Vertical Acceleration			Vertical Disp.		Pitch Acc.	
	Raw RMS	Weighted RMS	Max	RMS	Max	RMS	Max
Vehicle Velocity 40 km/h							
Preview Susp. w/ Ideal Road							
Preview Susp. w/ Scan. Road [1]	-0.38%	-1.01%	-2.95%	-3.13%	-1.02%	-0.43%	-1.0%
Preview Susp. w/ Scan. Road [2]	-5.08%	-9.73%	-7.74%	-9.38%	-2.04%	-1.94%	-1.6%

7.4.7 Deterministic Results for the Bump Road

Deterministic results refer the situations that there is no error based on laser scanner and the road information, which is used by the simulations, is exactly true data.

7.4.7.1 Time Domain Results @ 40 km/h

A bump input is subjected to the 4 axes with a corresponding phase delay based on the desired speed of the vehicle. The road input is at a height of 0.2 meters and at a width of 1 meters. Vehicle velocity is 40 km/h and time of the drive is 50 seconds. Figure 7.65 shows the road profile.

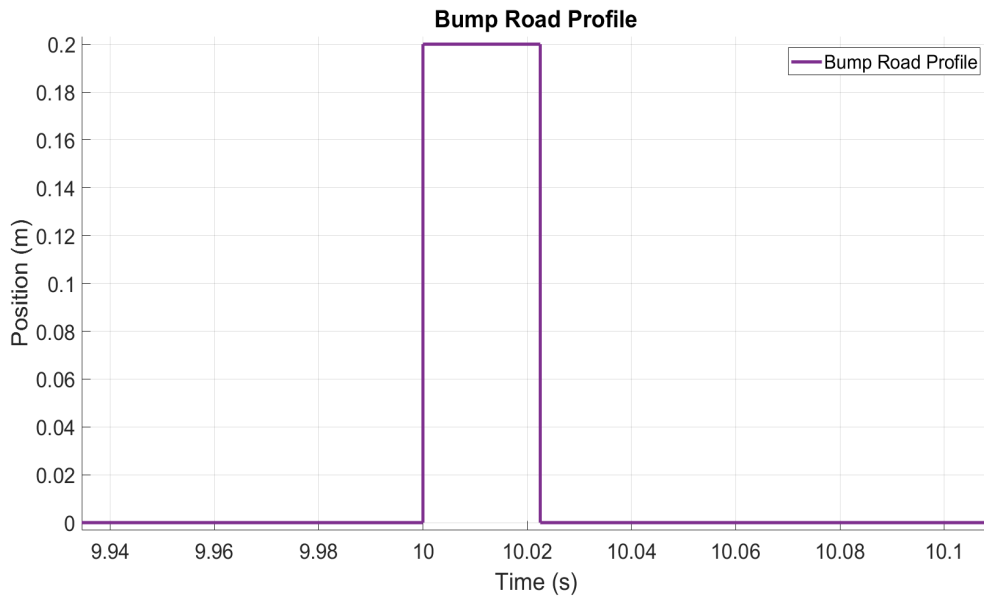


Figure 7.65: Bump Road

Figure 7.66, Figure 7.67 and Figure 7.69 show the vertical body displacement, vertical body acceleration and pitch acceleration for all suspension types, respectively.

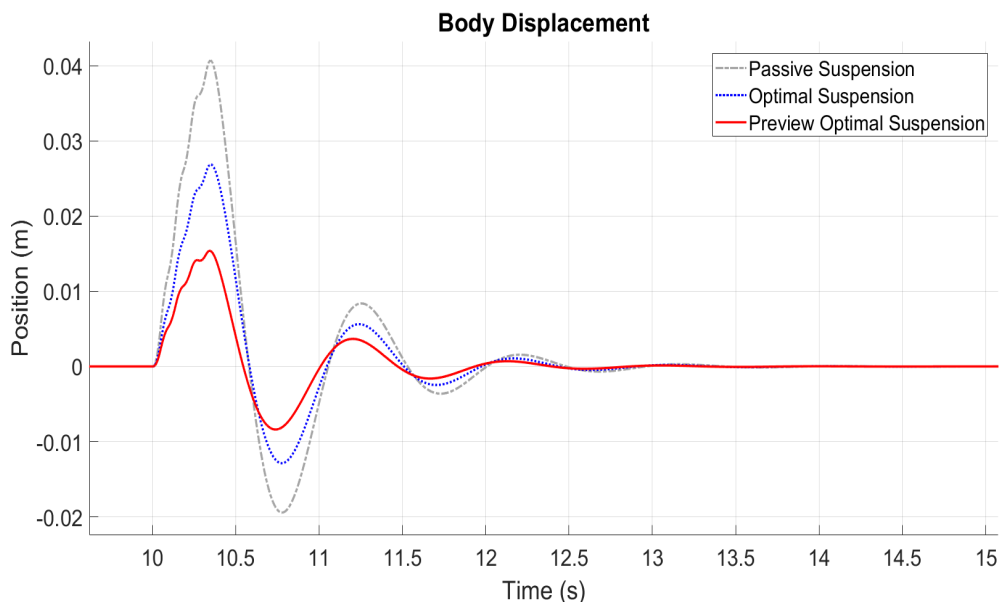


Figure 7.66: 40 km/h Vehicle and Quadrotor Velocity - Vertical Body Displacement

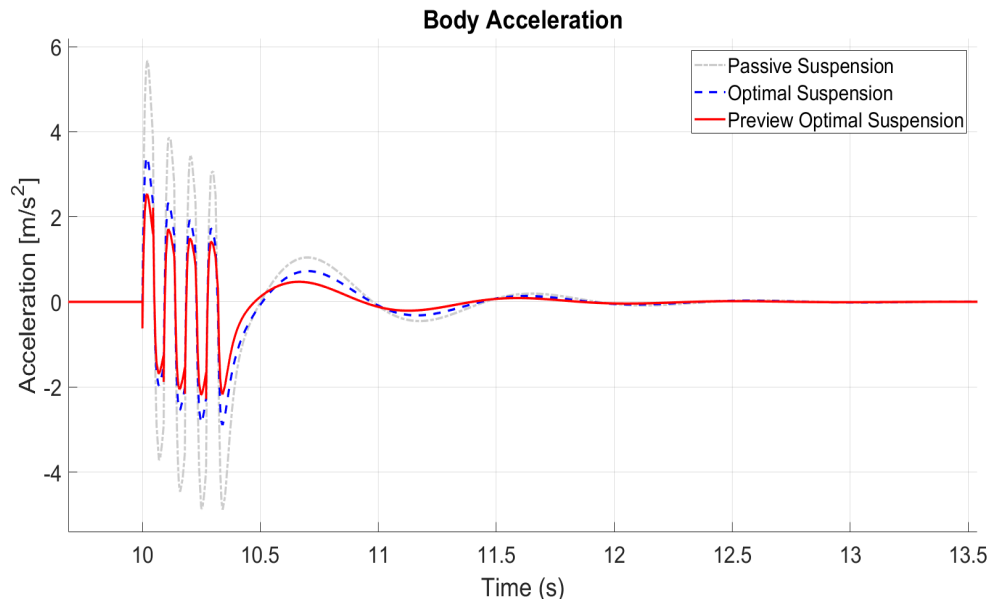


Figure 7.67: 40 km/h Vehicle and Quadrotor Velocity - Vertical Body Acceleration

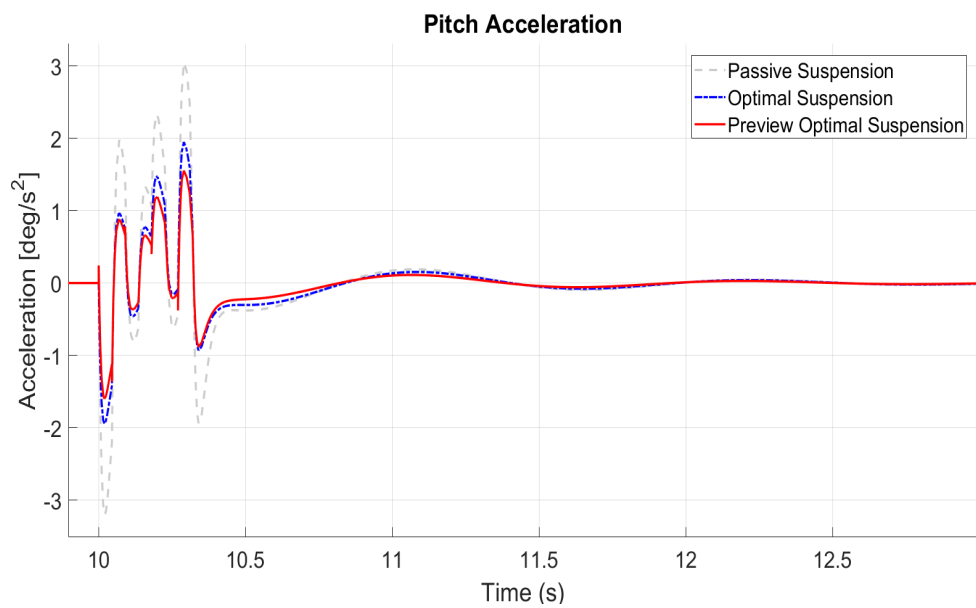


Figure 7.68: 40 km/h Vehicle and Quadrotor Velocity - Pitch Acceleration for the Vehicle

Table 7.24 and Table 7.25 summarize the performances of the different suspension system types against the bump road profile with the velocity of 40 km/h. The meanings and the consequences of the values are explained in detail in the discussion section.

Table 7.24: Time Domain Results for the Bump Road

Time Domain Analyzes Results							
Susp. Types	Vertical Acceleration			Vertical Disp.		Pitch Acc.	
	Raw RMS	Weighted RMS	Max	RMS	Max	RMS	Max
Vehicle Velocity 40 km/h							
Passive	0.456	0.296	5.670	0.004	0.041	0.193	3.052
Optimal	0.265	0.177	3.402	0.003	0.027	0.120	1.951
Preview	0.207	0.132	2.539	0.002	0.015	0.098	1.555

Table 7.25: Time Domain Percental Results for the Bump Road

Time Domain Analyzes Results							
Susp. Types	Vertical Acceleration			Vertical Disp.		Pitch Acc.	
	Raw RMS	Weighted RMS	Max	RMS	Max	RMS	Max
Vehicle Velocity 40 km/h							
Passive							
Optimal	41.8%	40.1%	40.0%	33.3%	33.9%	37.8%	36.1%
Preview	54.6%	55.2%	55.2%	61.5%	62.2%	49.2%	49.0%

7.4.7.2 Frequency Domain Results @ 40 km/h

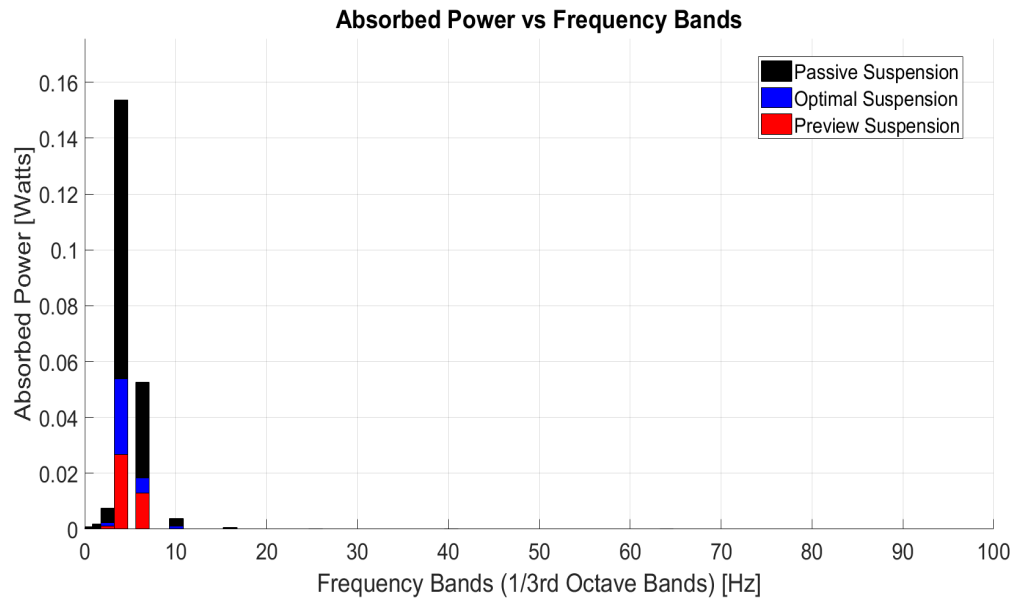


Figure 7.69: Absorbed Power vs Frequency Bands

Table 7.26: Frequency Domain Analyzes Results

Frequency Domain Analyzes Results	
	Total Absorb Power [Watts]
	Vehicle Velocity 40 km/h
Passive	0.22 W
Optimal	0.08 W
Preview	0.04 W

7.4.8 Stochastic Results for Road the Bump Road @ 40 km/h

For the stochastic results, the quadrotor based error parameters are taken into account and the affect of the errors is evaluated. Figure 7.22 shows the general point cloud density trend with respect to quadrotor range and velocity.

7.4.8.1 Scenario 1:Quadrotor Speed 40 km/h, Range 5 Meters

Figure 7.70 shows the relative motion of the quadrotor and the vehicle on X and Z axes. There is no motion on the Y axes. The altitude of the vehicle is assumed as zero and the altitude of the quadrotor is 5 meters. Figure 7.71 shows the scanned points per square meter. The point cloud density is depend on the range and speed of the quadrotor and the Figure 7.71 shows that the point cloud density decreases from 4800 points to the 3000 points as the quadrotor accelerates to the 40 km/h. Therefore, the maximum distance between two scanned points is around 1.86 centimeters. Additionally, Figure 7.72 and Figure 7.72 show the difference between the ideal road and the scanned road and the differences of the responses of the preview suspension system to the ideal road and the scanned road.

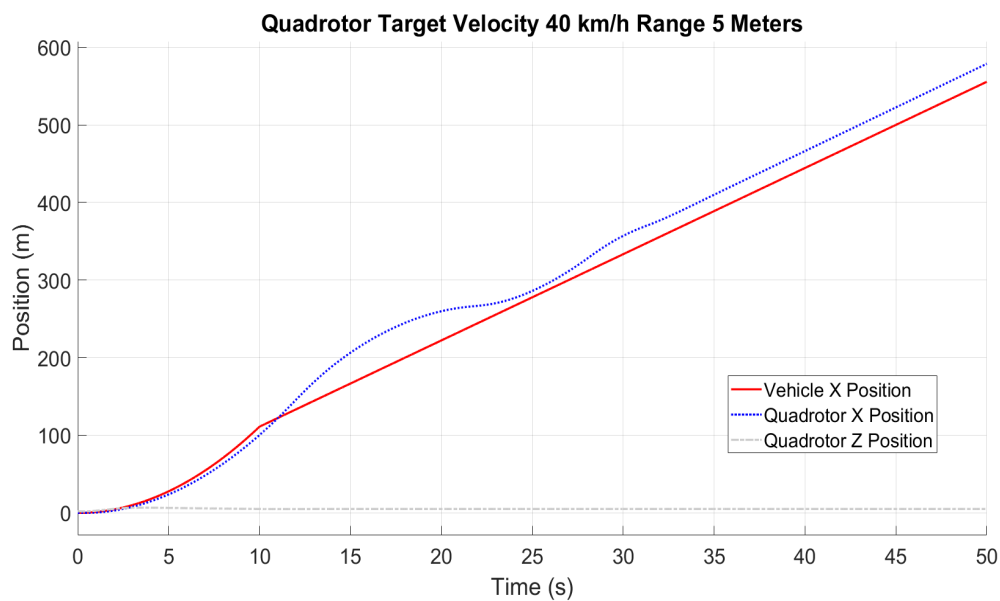


Figure 7.70: Scenerio 1 Quad. Range=5 meters and Target Velocity=40km/hours

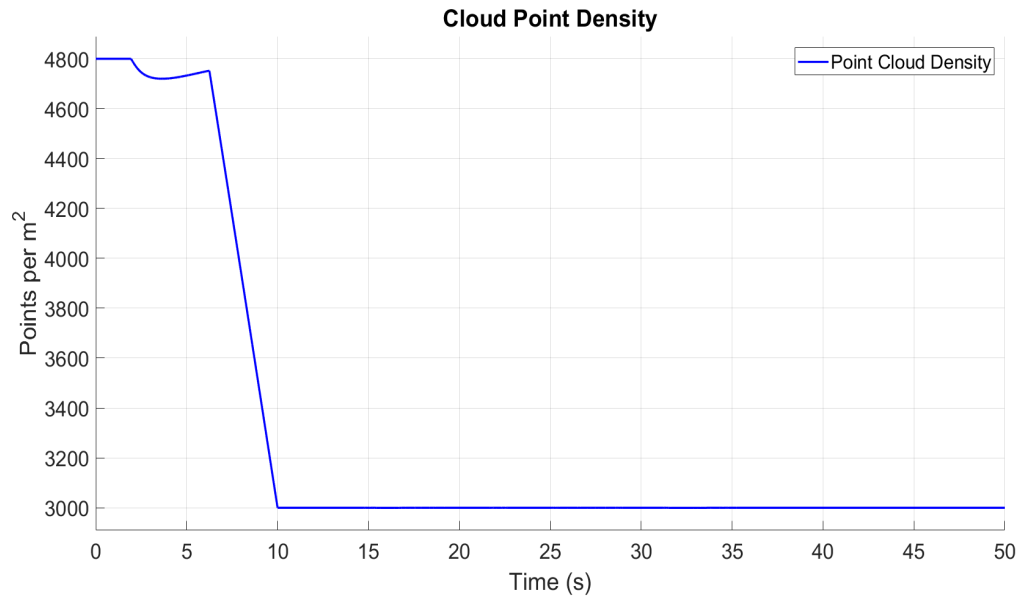


Figure 7.71: Cloud Point Density for Scenerio 1 (Quad Range=5 meter, Velocity=40km/h)

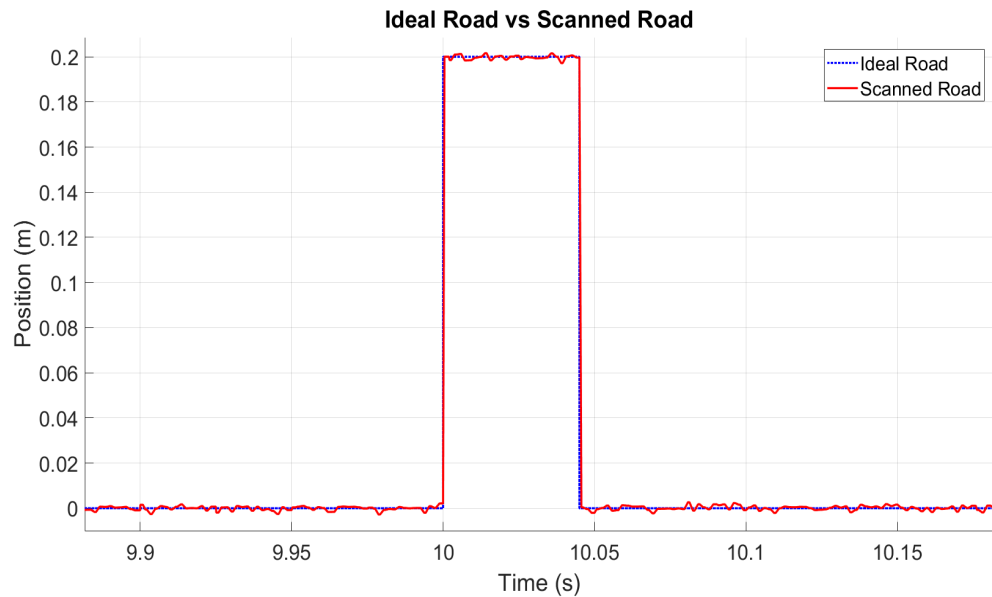


Figure 7.72: Scanned Road vs Ideal Road for Scenerio 1 (Quad Range=5 meter, Velocity=40km/h)

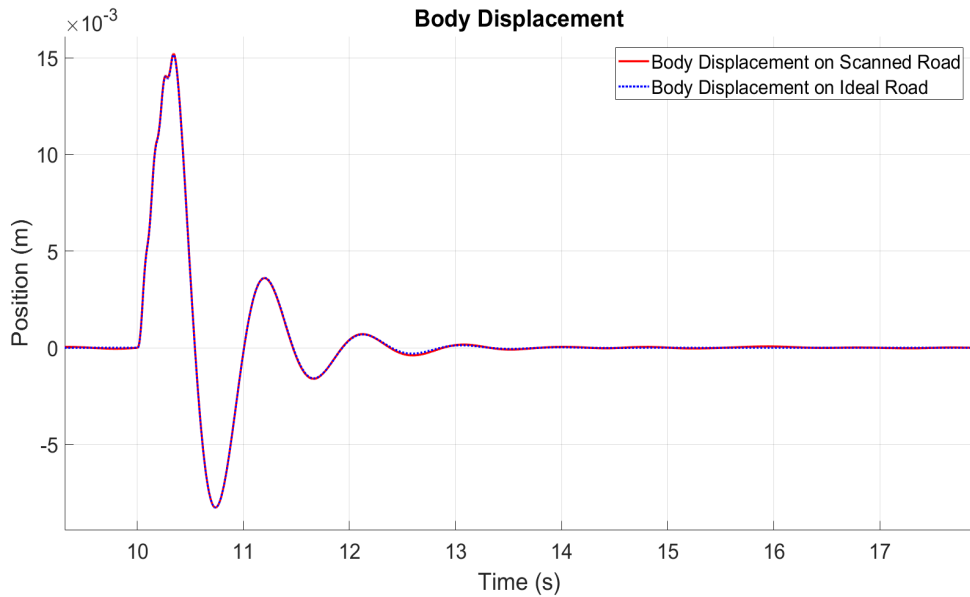


Figure 7.73: Body Displacements for Scanned Road and Ideal Road

7.4.8.2 Scenario 2: Speed 40 km/h Range 100 Meters

In order to see the suspensions responses more clearly, the quadrotor is flied at an altitude of 100 meters, thus, the error values are increased. The scenario 2 is generated to investigate the "maximum error" situations, which refers the error when the quadrotor flies at an altitude of 100 meters for the given speed based on the vehicle speed. The Figure 7.74 shows the second scenario.

Figure 7.76 shows the scanned road under maximum error conditions and the ideal road. The disruption for the road is clearly seen in the figure. At this time the maximum distance between two scanned points is around 8.891 centimeters. Figure 7.75 also shows the scanned points per meter square under the maximum error conditions. Finally, Figure 7.77 shows the preview suspension response to the road which is scanned with the maximum error.



Figure 7.74: Scenerio 2 Quad. Range=100 meters and Target Velocity=40km/hours

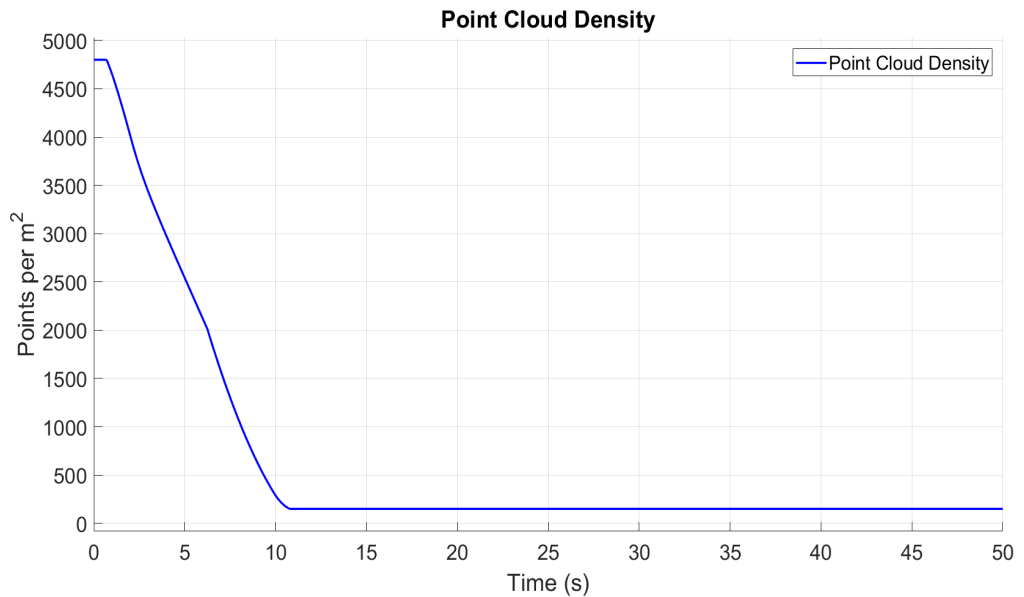


Figure 7.75: Cloud Point Density for Scenerio 2 (Quad Range=100 meter, Velocity=40km/h)

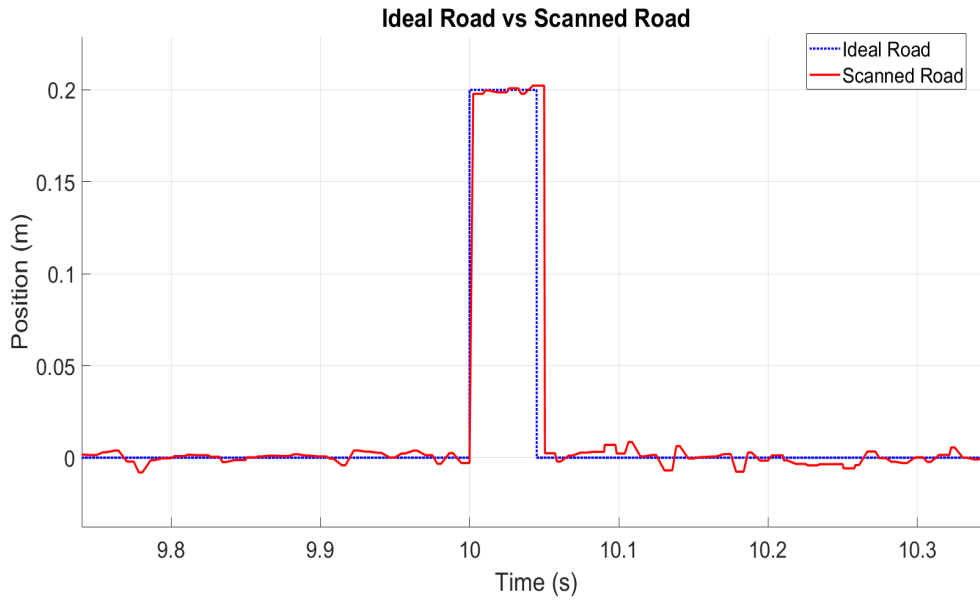


Figure 7.76: Road Profile with Max. Error vs Zero Error

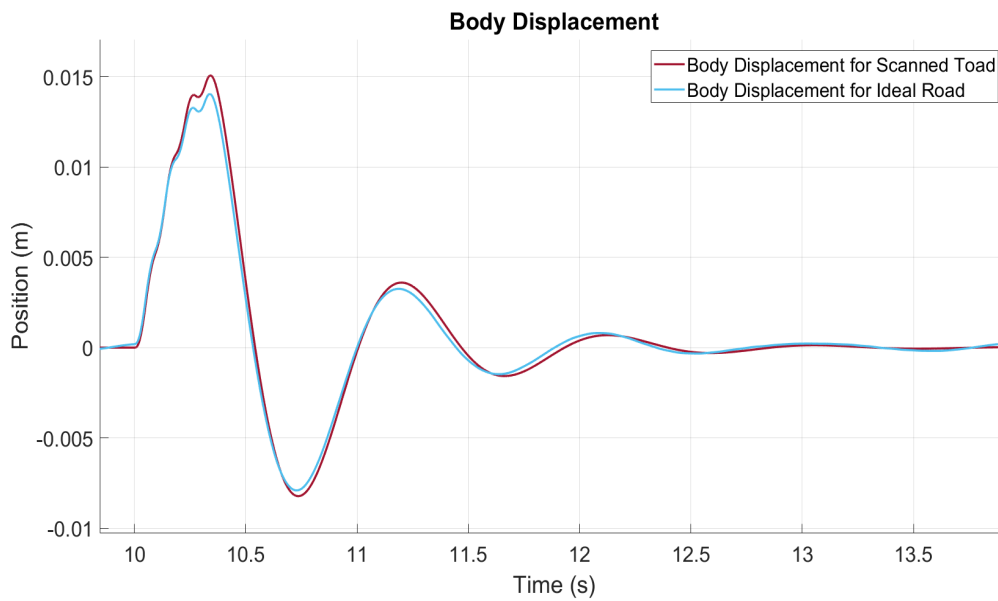


Figure 7.77: Suspension Behavior with Road Profile with Max. Error

7.4.9 Roll Channel Analysis

In roll channel analysis, a sinusoidal road is used to investigate the roll improvements of the vehicle by using the preview suspension system. In this simulations, only right

side of the vehicle is subjected to a sinusoidal bump series, which have bump length of 1 meter and bump amplitude of 40 centimeters, with a speed of 10 km /hours for the vehicle. Time of drive is 50 seconds. Figure 7.78 shows the road profile.

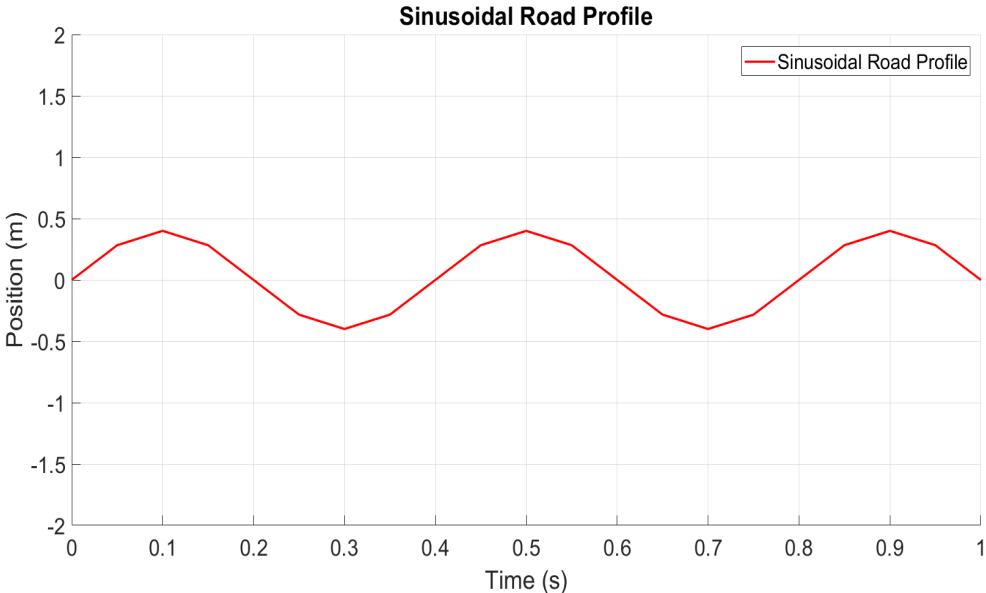


Figure 7.78: Sinusoidal Road Profile

Figure 7.79, Figure 7.80 and Figure 7.81 show the roll acceleration, vertical body acceleration and pitch acceleration for all suspension types, respectively.

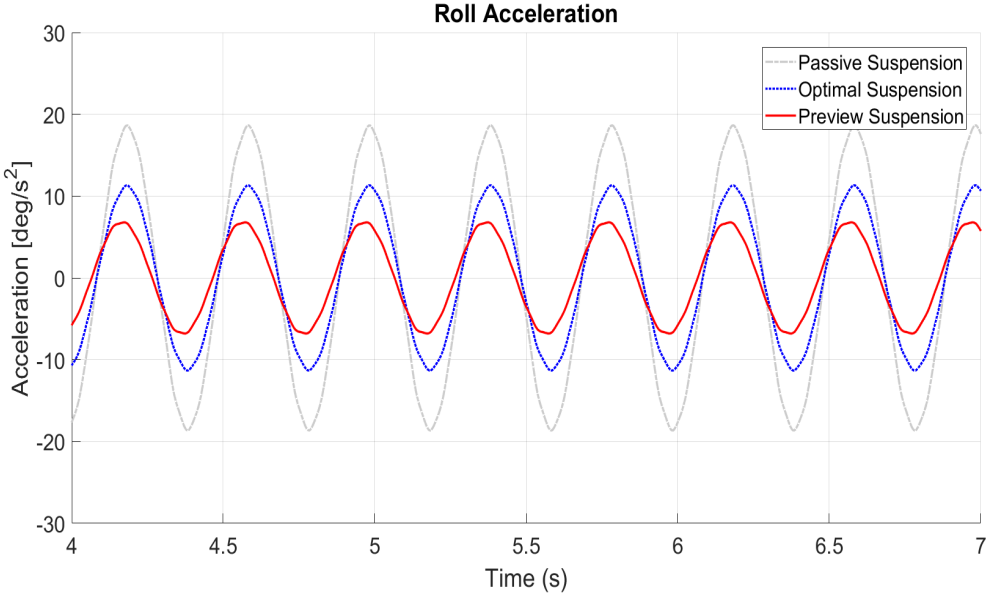


Figure 7.79: Roll Acceleration

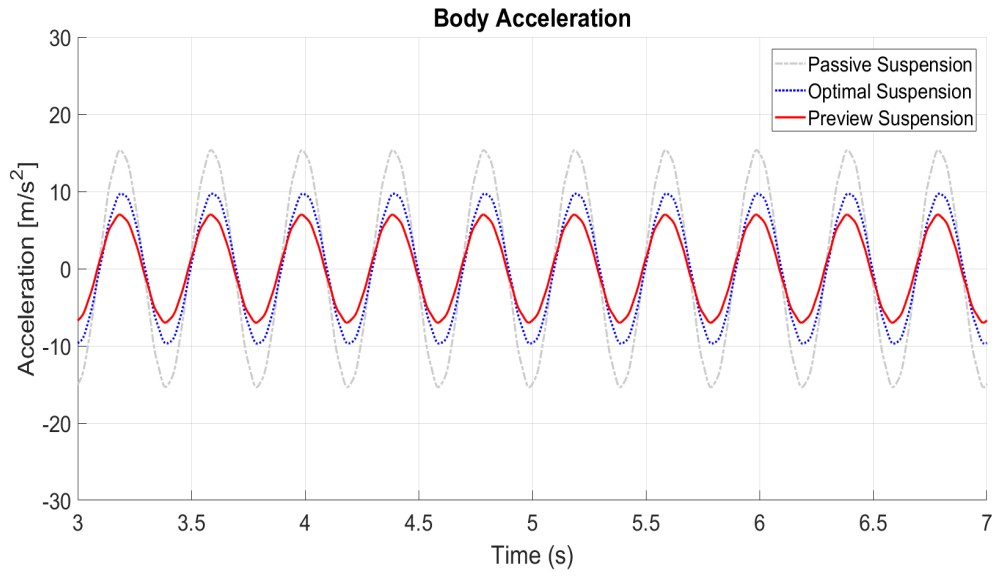


Figure 7.80: Body Acceleration

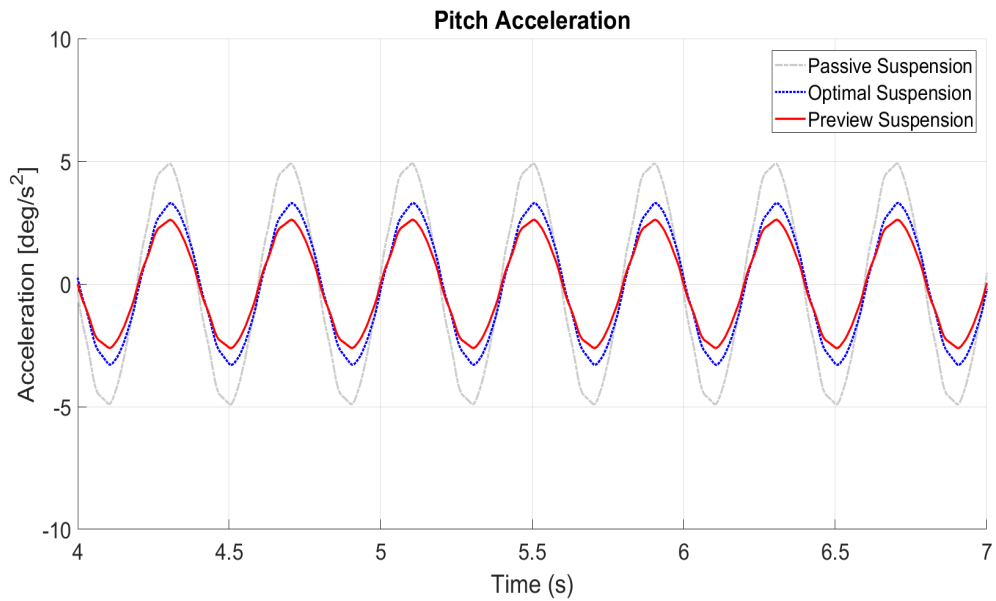


Figure 7.81: Pitch Acceleration

Figure 7.82 and 7.83 show the actuator forces for all tires and suspension travel for the tire 1, respectively.

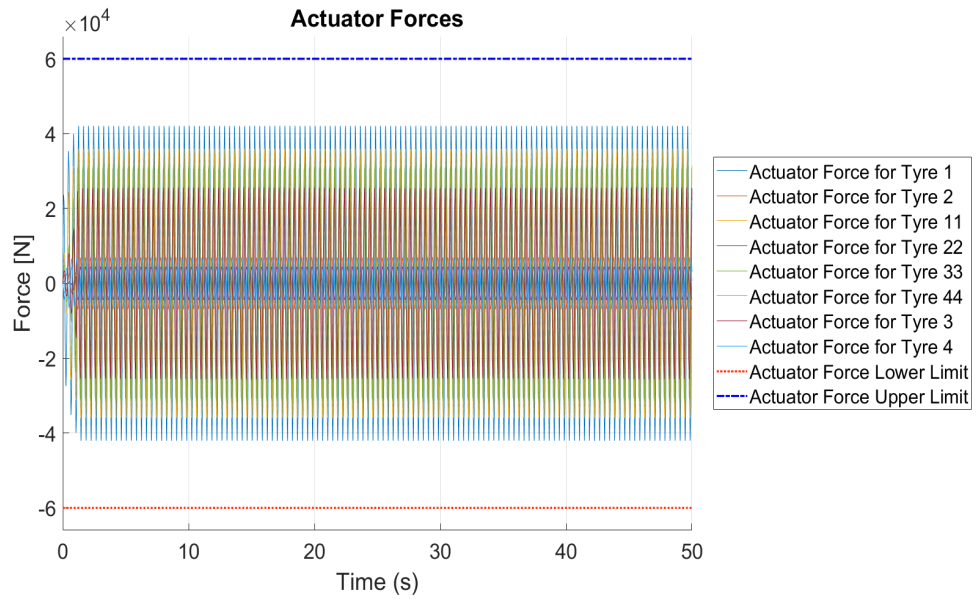


Figure 7.82: Actuator Forces

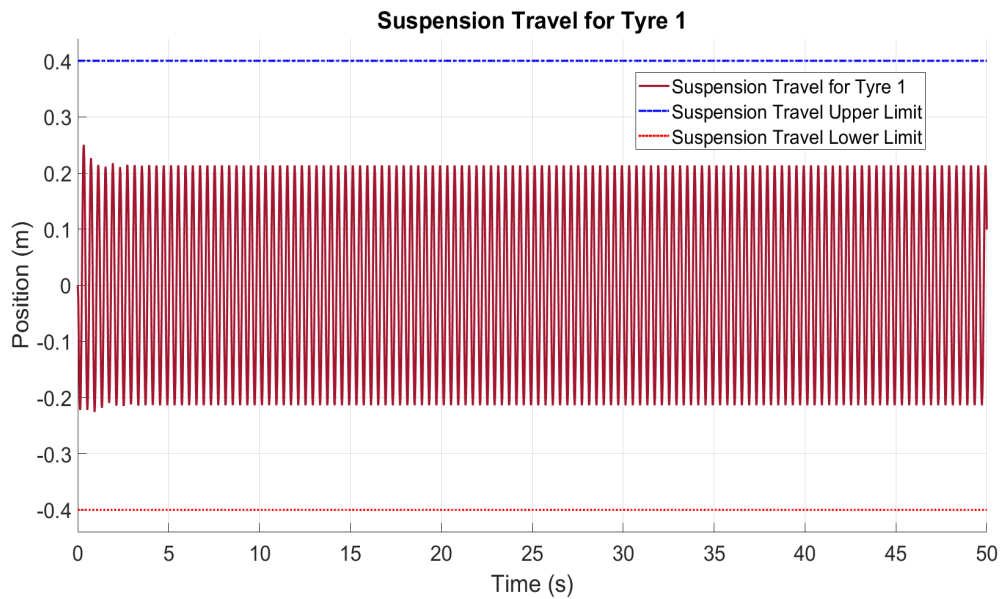


Figure 7.83: Suspension Travel for Tyre 1

Table 7.27 and Table 7.28 summarize the performances of the different suspension system types against the sinusoidal road with the speed of 10 km/h. The meanings and the consequences of the values are explained in detail in the discussion section.

Table 7.27: Time Domain Analyzes Results for Sinusoidal Road

Time Domain Analyzes Results						
Susp. Types	Vertical Acc.		Roll Acc.		Pitch Acc.	
	RMS	Max	RMS	Max	RMS	Max
Vehicle Velocity 10 km/h						
Passive Suspension	10.6785	15.7827	12.8839	18.8324	3.4298	5.1025
Optimal Suspension	6.8215	9.9881	7.8165	11.4507	2.2721	3.4307
Preview Suspension	4.8404	7.1787	4.7537	6.8812	1.8104	2.7251

Table 7.28: Time Domain Analyzes Results for Sinusoidal Road (Percental)

Time Domain Analyzes Results (Percental)						
Susp. Types	Vertical Acc.		Roll Acc.		Pitch Acc.	
	RMS	Max	RMS	Max	RMS	Max
Vehicle Velocity 10 km/h						
Passive Suspension	-	-	-	-	-	-
Optimal Suspension	36.12%	36.71%	39.33%	39.20%	33.75%	32.76%
Preview Suspension	54.67%	54.52%	63.10%	63.46%	47.22%	46.59%

7.5 Discussions

In order to discuss the vibrational evaluation of all of the suspension types, three different information is generated by combining the ISO 2631 standard [51] and US Army body vibration procedure [52] with simulation results, which are stated in the Results part. The first one is the maximum operation duration time, which is calculated by obtaining the intersection point between the weighted RMS value and the lower line of the whole body vibration health guidance zone [51]. Figure 7.10 shows the graph which is used to obtain operation duration information. The second information is used to make easier to understand the reactions to the various magnitudes of vibration. For this information, the weighted RMS values are compared with the intervals in the Table 7.2 based on the ISO 2631 standard. Final information based

on the deterministic results is the absorb power information based on the frequency domain. In the NATO reference mobility model [52], the maximum allowable speed for the military vehicles is obtained by using the total average absorb power value, which are calculated in the Results part. The procedure says that the maximum speed is the speed when the total average absorb power value reaches an upper limit of 6 watts [52]. Additionally, by using the stochastic results, the feasibility of the using of quadrotor for the road scanning process is tried to understand under both minimum error condition and maximum error condition.

H Type Road:

H type road is the most drastic road condition according to the ISO 8608 road characterization standard [50]. Since the actuators have the most difficulty with this type of road, the controller parameters such as Q and R matrices are determined at the maximum speed at which 3 suspensions can be reached on this type of road. Therefore, 5 km/h vehicle speed on H type of road refers the controller design condition. Since the the maximum speed at which 3 suspension systems can be evaluated at the same time is 5 km/h, the maximum operation duration is obtained at the continuous speed of 5 km/h. While the maximum operation duration of the passive suspension system is less than 10 minutes, it is between 25 and 30 minutes for the optimal suspension system and between 40 and 45 minutes for the preview suspension system. It can be easily said that the comfort level increases from the "extremely uncomfortable" level to the "uncomfortable" level by using preview suspension system, even though all three types are on this road surface and at this speed is stated as uncomfortable based on the Table 7.2. Since this is a 8x8 military vehicle, this result is quite understandable. By using the frequency domain results, maximum allowable speed of the suspension systems are calculated when the total average absorb power value reaches an upper limit of 6 watts. According to this information and the results, while the maximum allowable speed is less than 5 km / h for the passive suspension system, it is between 15 km / h and 20 km / h for the optimal suspension system, and between 20 km / h and 25 km / h for the preview suspension system. Table 7.3 and Table 7.4 summarizes the improvements for the optimal suspension system and preview suspension system against the passive suspension system with respect to vertical motion and pitch motion.

Finally stochastic results reveal that the usage of the quadrotor system is feasible even under maximum error conditions, since the performance derogation is under 1 percent, which does not make any significant effect on the suspension responses. In other words, it is seen that the accuracy and precision and the hardware capability of the laser scanner system is enough to scan the road surface accurately and sufficiently for the suspensions.

Table 7.29 summarizes the most important discussions for the H type road.

Table 7.29: Vibration Evaluation for the H Type Road

Deterministic Results			
	Time Domain Analysis		Frequency Domain Analysis
	Weighted RMS Acceleration Information		Absorb Power Information
	Max. Operation Duration w.r.t ISO 2631 Health Guidance Caution Zone @ 5 km/h [32]	Comfort Reaction to Vibration Environments w.r.t ISO 2631 @ 5 km/h [32]	Max. Vehicle Speed w.r.t NATO Reference Mobility Model [33]
Passive	less than 10 Minutes	Extremely Uncomfortable	less than 5 km/h
Optimal	25-30 Minutes	Very Uncomfortable	between 15 km/h & 20 km/h
Preview	40-45 Minutes	Uncomfortable	between 20 km/h & 25 km/h
Stochastic Results			
	Performance Derogation w.r.t. Vertical Acceleration		
	Scenario 1 Quad Range 5 m Quad Velocity 20 km/h	Scenario 2 Quad Range 100 m Quad Velocity 20 km/h	
Preview	less than 0.5%		between 0.5% and 1%

G Type Road

G type road is the second level highly off-road condition according to the ISO 8608 road characterization standard [50]. Since the the maximum speed at which 3 suspen-

sion systems can be evaluated at the same time is 20 km/h, the maximum operation duration is obtained at the continuous speed of 20 km/h. While the maximum operation duration of the passive suspension system is between 25 and 30 minutes, it is approximately 60 minutes for the optimal suspension system and between 2 and 2.5 hours for the preview suspension system. It can be observed that the comfort level increases from the "very uncomfortable" level to the "fairly uncomfortable" level by using preview suspension system, even though all three types are on this road surface and at this speed is stated as uncomfortable based on the Table 7.2. Since this is a 8x8 military vehicle, this result is quite understandable. By using the frequency domain results, maximum allowable speed of the suspension systems are calculated when the total average absorb power value reaches an upper limit of 6 watts. According to this information and the results, while the maximum allowable speed is between 20 km/h and 25 km/h for the passive suspension system, it is between 60 km / h and 70 km / h for the optimal suspension system, and it is more than 80 km/h for the preview suspension system. Since the upper velocity limit for this 8x8 military vehicle is 80 km/h, the maximum allowable speed for the preview suspension system is stated as 80 km/h on this road surface. Table 7.11 and Table 7.12 summarizes the improvements for the optimal suspension system and preview suspension system against the passive suspension system with respect to vertical motion and pitch motion.

When we consider the stochastic results, it is observed that the usage of the quadrotor system is again feasible even under maximum error conditions, since the performance derogation is again under 1 percent, which does not make any significant effect on the suspension responses. In other words, it is seen that the accuracy and precision and the hardware capability of the laser scanner system is again enough to scan the road surface accurately and sufficiently for the suspensions.

Table 7.30 summarizes the most important discussions for the G type road.

Table 7.30: Vibration Evaluation for the G Type Road

Deterministic Results			
	Time Domain Analysis		Frequency Domain Analysis
	Weighted RMS Acceleration Information		Absorb Power Information
	Max. Operation Duration w.r.t ISO 2631 Health Guidance Caution Zone @ 20 km/h [32]	Comfort Reaction to Vibration Environments w.r.t ISO 2631 @ 20 km/h [32]	Max. Vehicle Speed w.r.t NATO Reference Mobility Model [33]
Passive	25-30 Minutes	Very Uncomfortable	between 20 km/h and 25 km/h
Optimal	Approx. 1 Hour	Uncomfortable	between 60 km/h & 70 km/h
Preview	between 2 & 2.5 Hours	Fairly Uncomfortable	Upper Speed Limit 80 km/h
Stochastic Results			
	Performance Derogation w.r.t. Vertical Acceleration		
	Scenario 1 Quad Range 5 m Quad Velocity 40 km/h	Scenario 2 Quad Range 100 m Quad Velocity 40 km/h	
Preview	less than 0.5%	between 0.5% and 1%	

B Type Road

B type road is generated to simulate the paved road conditions according to the classification, which is represented in the ISO 8608 standard. Since the B type of road simulates the asphalt road conditions, the results reveals that the vibrational effects on the human body is quite low. Although the improvements seen in the Table 7.19 and Table 7.20 are relatively high both as a value and as a percental, it can be said that all values are quite low to be felt by human body. Therefore, according to the whole body vibration health guidance zone [51], the operation time for all of the suspension system is more than 8 hours. Additionally, since all of the weighted RMS value for all of the suspension types are less than $0,315m/s^2$, the comfort reaction is evaluated

as "not uncomfortable" for all suspension types based on the Table 7.2. In the light of the frequency domain analysis, the absorb power for all of the suspension types are calculated at the upper limit of the vehicle, which is 80 km/h and it is seen that the absorb power for all of the suspension types is less than 6 watts. Therefore, all of the suspension types can be used at the maximum vehicle speed.

When we consider the stochastic results, it is observed that the the performance derogation is much more in percental in comparison with the H type road and G type road. This is because all of the calculated values are quite small and even the derogation is around 10 percent for the maximum error condition, there is no significant effect on the suspension responses and therefore it can still be said that the accuracy and precision and the hardware capability of the laser scanner system is again enough to scan the road surface accurately and sufficiently for the suspensions.

Table 7.31: Vibration Evaluation for the G Type Road

Deterministic Results			
	Time Domain Analysis		Frequency Domain Analysis
	Weighted RMS Acceleration Information		Absorb Power Information
	Max. Operation Duration w.r.t ISO 2631 Health Guidance Caution Zone @ 80 km/h [32]	Comfort Reaction to Vibration Environments w.r.t ISO 2631 @ 80 km/h [32]	Max. Vehicle Speed w.r.t NATO Reference Mobility Model [33]
Passive	more than 8 hours	Not Uncomfortable	Upper Speed Limit 80 km/h
Optimal	more than 8 hours	Not Uncomfortable	Upper Speed Limit 80 km/h
Preview	more than 8 hours	Not Uncomfortable	Upper Speed Limit 80 km/h
Stochastic Results			
	Performance Derogation w.r.t. Vertical Acceleration		
	Scenario 1 Quad Range 5 m Quad Velocity 40 km/h	Scenario 2 Quad Range 100 m Quad Velocity 40 km/h	
Preview	less than 2%	less than 10%	

Bump Road

A bump road input, which is at a height of 0.2 meters and at a width of 1 meters, is used to evaluate the pitch motion improvements by using the optimal suspension system and preview suspension system against the passive suspension system. It is observed that using optimal suspension systems increases the performance by around 30-40 percent compared to the passive suspension system and using the preview suspension system increases the performance by 50-60 percent against passive suspension system with respect to vertical motion and pitch motion. All of the values can be found in the Table 7.24 and Table 7.25.

In the stochastic simulations, for the small bump obstacles, it is seen that the accuracy

and precision of the laser scanner system is enough to scan the bump accurately and sufficiently for the suspensions. Although the error is maximum, the Figure 7.76 reveals that the bump part of the road is still scanned sufficiently and accurately for the suspensions. Therefore, the Figure 7.77 shows that the response to the bump part of the road for the ideal road and the scanned road is almost the same.

Sinusoidal Road

The final road type is the sinusoidal road, which is used to evaluate the roll motion improvements. Only the right side of the vehicle is subjected to the sinusoidal road profile. The length of one of the sinusoidal bumps is 1 meter and the amplitude of one of the sinusoidal bumps is 40 centimeters. According to the Table 7.27 and 7.28, it is observed that using optimal suspension systems increases roll, pitch and vertical motion performances by around 30-40 percent compared to the passive suspension system. On the other hand, the preview suspension system increases the performance of the roll motion by around 60 percent and vertical and pitch motion performances by around 50 percent.

CHAPTER 8

CONCLUSION AND FUTURE WORKS

8.1 Conclusion

The first objective of this study is to understand the usage of the air vehicles for the purpose of road scanning. It is observed that quadrotor systems have more advantages for the road scanning process because of the improved stability and payload capacity. Moreover, considering the reliability, availability and maintainability, quadrotor system comes into prominence. Payload based design is made and theoretically a working quadrotor system is obtained with all of the electrical, mechanical and optical components. When the theoretical design is completed, by using the input parameters, which are obtained at the end of the design, the modeling and simulation of the quadrotor is made in order to built a high-fidelity simulation for more accurate error analyzing. At this point, one of the important challenges is to design the controllers for the designed heavy weight carrying quadrotor. After tuning the PID terms for attitude controllers for the quadrotor, based on the motion of the quadrotor, the scanned points distribution curves are obtained depend on the range and speed of the quadrotor. These studies prove that a laser scanner system can be mounted on a quadrotor system in order to scan the road effectively and accurately for tuning the suspension parameters to improve personnel comfort.

After completing the quadrotor, payload and road scanning processes, the vertical vehicle model is modeled o simulate the suspension responses. The vehicle studies is done for 8x8 high tonnages land vehicle. An LQR optimal gain is calculated for the active suspension system and this optimal gain is improved with the help of the

prescanned road input. Additionally, since the actuators have physical limitations, the energy boundedness of the control input signal is implemented to the model.

Quadrotor and vehicle models are integrated in order to provide a simulation medium. For the simulations a bump, which has appropriate sizes for the analyzes of 8x8 military vehicle, is used as a first road profile. The second and third road profiles are generated by using the ISO 8608 standard. According to the ISO 8608 standards, a "G" type highly terrain road and "B" type paved road are used. Additionally, according to the road type, different vehicle speeds are used for the simulations and the vehicle speed is simulated by using phase delay for the road profile.

The simulations reveals that using the proposal method for the prescan suspension system increases the personnel comfort performance of the vehicle suspension system especially for the off-road conditions(See Section 7.5, Tables 7.29, 7.30). Usage of the laser scanner mounted on the quadrotor system improves the personnel comfort significantly. For the simulations, the predicted mission conditions is used for the quadrotor motion. According to the generated mission scenarios, the range of the quadrotor is at an altitude of 5 meters and the speed of the quadrotor is controlled by the vehicle. For the maximum error conditions, the range of the quadrotor is used as 100 meters. Also, using different vehicle speeds shows that the performance worsens as the speed increases. For all speed conditions it is shown that the prescan suspension has the best performance and the passive suspension system has the worst performance. Even, under the maximum error conditions, for the bump road, it is proved that the proposal methodology for the prescan suspension system improves the performance of the suspension system for the personnel comfort. Moreover, for the asphalt road and the off-road condition, the analyzes also show that the performance is significantly improved by using the prescan sensor carrying quadrotor system as compared to passive suspension system and standard optimal system.

8.2 Future Works

In this thesis a quadrotor system is used to carry the laser scanner system as a payload and with the help of the laser scanner system and prescanned road information

the suspensions of a 8x8 vehicle is optimized. Since the vehicle model has only the 8x8 vertical vibration model for the suspension analyzes, all of the analyzes are conducted along the X axes and the speed of the vehicle is simulated by using the phase delays. As a future work the vehicle model may be improved by adding the lateral and longitudinal force models, tyre and steering models and also the braking and the acceleration models. By doing this, the suspension analyzes can be conducted for any conditions such as going down or up to the hill, turning, braking and accelerating. On the other hand, quadrotor system has the capability for analyzing along any axes. Moreover, in the scope of this thesis, only the vertical displacement and the vertical acceleration is evaluated for the personnel comfort. Pitch and roll capability may also be investigated as a future work.

Additionally, as a future works, different controller type may be developed for both quadrotor system and the vehicle system. Sliding mode control, fuzzy logic control and backstepping can be considered as additional control methodologies and all of the control methodologies may be evaluated in order to create a benchmark study.

In this study, since the LQR algorithms directly produce the actuator forces for 8 suspension systems for the 8x8 vehicle, only blocks that create the physical limitations and saturation for the actuators are used. As a future works hydraulic actuators may be modeled in detail and the behavior of the actuators can be analyzed.

In the literature reviews for the air vehicles, it is seen that coaxial systems are also used for the heavy weight carrying. Because of the military conditions and maintenance advantages of the quadrotor system is used but as a future work coaxial octocopter can also be built and evaluated for carrying the laser scanner system.

Final and most important future work is the manufacturing and testing of the both quadrotor and 8x8 prescan active suspension system and verifying all of the models with real test data.

REFERENCES

- [1] Modeling and control active suspension system for a full car model Rosheila Darus-Yahaya Sam - 2009 5th International Colloquium on Signal Processing Its Applications - 2009
- [2] Types of Multirotor . (2018, January 16). Retrieved from <https://oscarliang.com/types-of-multicopter/>
- [3] Schmidt, Michael David, "Simulation and control of a quadrotor unmanned aerial vehicle" (2011). University of Kentucky Master's Theses. 93.
- [4] Professional gimbal damper system (2018, January 24). Retrieved from <http://damperzen.com/wp/>
- [5] LN-200 FOG Family. (2018, January 24). Retrieved from <http://www.northropgrumman.com/Capabilities/LN200FOG/ln200.pdf>
- [6] Airborne Systems Options and Specifications. (2018, January 24). Retrieved from <http://www.resonon.com/Products/airborneoptionsandspecifications.html>
- [7] TW5340 Multi-Constellation GNSS Smart Antenna . (2018, January 28). Retrieved from <https://www.amtechs.co.jp/product/TW5340-datasheet-Rev3.0.pdf>
- [8] VN-200 GPS Aided INS (2018, January 29). Retrieved from <https://www.vectornav.com/products/vn-200?gclid=wcB>
- [9] PPS PLUS. (2018, February 3). Retrieved from <http://www.lehmann-partner.de/technology/pps-plus?L=6>
- [10] Laser Crack Measurement System (LCMS). (2018, February 4). Retrieved from <http://www.pavemetrics.com/applications/road-inspection/laser-crack-measurement-system/>
- [11] Mobile Survey. (2018, February 4). Retrieved from <http://www.phnx-sci.com/PPS/Home.html>
- [12] N., Pfeifer, C., Briese. (2007). LASER SCANNING PRINCIPLES AND APPLICATIONS SUMMARY.

- [13] Cahalane, C., Mcelhinney, C., Lewis, P., Mccarthy, T. (2014). MIMIC: An Innovative Methodology for Determining Mobile Laser Scanning System Point Density. *Remote Sensing*, 6(9), 7857-7877. doi:10.3390/rs6097857
- [14] RIEGL VUX-1HA. (2018, February 5). Retrieved from <http://www.riegl.com/products/newriegl-vux-1-series/newriegl-vux-1ha/>
- [15] MN701S KV135 System Specifications. (2018, February 5). Retrieved from <http://store-en.tmotor.com/goods.php?id=627>
- [16] Alpha 60A HV System Specifications. (2018, February 7). Retrieved from <http://store-en.tmotor.com/goods.php?id=582>
- [17] Tattu 30000mAh 22.2V 25C 6S1P Lipo Battery Pack. (2018, February 9). Retrieved from <https://www.genstattu.com/tattu-30000mah-22-2v-25c-6s1p-lipo-battery-pack.html>
- [18] Yih, C. (2016). Flight control of a tilt-rotor quadcopter via sliding mode. 2016 International Automatic Control Conference (CACs). doi:10.1109/cacs.2016.7973885
- [19] Ji, Y., Yu, Y., Zhang, W., Sun, C. (2015). Attitude control of a quadrotor unmanned aerial vehicle based on linear extended state observer. The 27th Chinese Control and Decision Conference (2015 CCDC). doi:10.1109/ccdc.2015.7162128
- [20] Severinghaus, R., Kaniarz, J. (2015). Quadrotor for Increased Situational Awareness for Ground Vehicles. doi:10.21236/ada613195
- [21] PID Controller. (2018, February 9). Retrieved from <https://en.wikipedia.org/wiki/PIDcontroller>
- [22] Choi, S. B., Lee, H. S. and Park, Y. P., Hinf Control Performance of a Full-Vehicle Suspension Featuring Magnetorheological Dampers. *Vehicle System Dynamics* 38 (2002) 341-360.
- [23] Genç, S., Synthesis and Properties of Magnetorheological (MR) fluids. Ph. D. Thesis. University of Pittsburgh, 2002.
- [24] Paré, C. A., Experimental Evaluation of Semiactive Magneto-Rheological Suspensions for Passenger Vehicles. M. Sc. Thesis. Virginia Polytechnic Institute and State University, 1988.
- [25] Spencer, B. F., Dyke, S. J., Sain, M. K. and Carlson, J. D., Phenomenological Model of a Magnetorheological Damper. *ASCE Journal of Engineering Mechanics* 3 (1996) 201-221.

- [26] Krüger, W., Integrated Design Process for the Development of Semi-Active Landing Gears for Transport Aircraft. Ph.D. Thesis. University of Stuttgart, 2000.
- [27] Active Automotive Suspensions. (n.d.). Mechanical Engineering Series Vehicle Dynamics and Control, 325-355. doi:10.1007/0-387-28823-6-11
- [28] Donahue, M. D., Implementation of an Active Suspension, Preview Controller for Improved Ride Comfort. M. Sc. Thesis. University of California at Berkeley, 2001.
- [29] Chantranuwathana, S. and Peng, H., Adaptive Robust Force Control for Vehicle Active Suspensions. *International Journal of Adaptive Control and Signal Processing* 18 (2004) 83-102.
- [30] Pang, L., Kamath, G. M., and Wereley, N. M., Analysis and Testing of a Linear Stroke Magnetorheological Damper. *AIAA/ASME/AHS Adaptive Structures* 4 (1998) 2841-2856.
- [31] Shen, X. and Peng, H., Analysis of Active Suspension Systems with Hydraulic Actuators. *Proceedings of the IAVSD Conference, Atsugi*, 2 (2003) 546-556.
- [32] Yi K. and Song B. S., Observer Design for Semi-Active Suspension Control. *Vehicle System Dynamics* 32 (1999) 129-148.
- [33] Park, J. H. and Kim, Y. S., Decentralized Variable Structure Control for Active Suspensions based on a Full-Car Model. In: *Proceedings of the International Conference on Control Applications, Trieste* (1998) 383-387.
- [34] Valasek, M., Novak, M., Sika, Z. and Vaculin, O., Extended Ground-Hook - New Concept of Semi-Active Control of Truck's Suspension. *Vehicle System Dynamics* 27 (1997) 289-303.
- [35] Rettig, U. and Stryk, O., Optimal and Robust Damping Control for Semi-Active Vehicle Suspension. In: *Proceedings of the Fifth EUROMECH Nonlinear Dynamics Conference, Eindhoven University of Technology*, MS 20-316, 2005.
- [36] Sampson, D. J. M., Active Roll Control of Articulated Heavy Vehicles. Ph.D. Thesis. University of Cambridge, 2000.
- [37] Taghirad, H. D. and Esmailzadeh, E., Automobile Passenger Comfort Assured Through LQG/LQR Active Suspension. *Journal of Vibration and Control* 4 (1998) 603-618.
- [38] ABC Active Body Control / MBC Magic Body Control. (2018, March 03). Retrieved from <http://500sec.com/abc-active-body-control-mbc-magic-body-control/>

- [39] Magic Body Control. (2018, March 4). Retrieved from <https://www.mercedes-benz.com/en/mercedes-benz/innovation/magic-body-control/>
- [40] Hydractive 3. (2018, March 5). Retrieved from <http://www.citroenet.org.uk/miscellaneous/hydraulics/hydraulics-13.html>
- [41] Trikande, M., Karve, N., Raj, R. A., Jagirdar, V., Vasudevan, R. (2016). Semi-active vibration control of an 8x8 armored wheeled platform. *Journal of Vibration and Control*, 24(2), 283-302. doi:10.1177/1077546316638199
- [42] The Simple Pendulum. (2018, March 5). Retrieved from <http://m-newton.ex.ac.uk/research/qsystems/people/sque.togo/physics/simple-pendulum/>
- [43] Hamersma, H. A., and Els, S. (2015). A Comparison of Quarter, Half and Full Vehicle Models With Experimental Ride Comfort Data. Volume 3: 17th International Conference on Advanced Vehicle Technologies; 12th International Conference on Design Education; 8th Frontiers in Biomedical Devices. doi:10.1115/detc2015-47180
- [44] Nguyen, T. A. (2006). Application of optimization methods to controller design for active suspensions (Unpublished master's thesis). Cottbus, Techn. University, Diss.
- [45] Paucer, W. J., Casas. (2013). DYNAMIC ANALYSIS AND OPTIMIZATION OF VIBRATIONS CONTROL BY LINEAR QUADRATIC REGULATOR ALGORITHM ON A COMPLETE VEHICLE MODEL. 22nd International Congress of Mechanical Engineering. Retrieved 2013.
- [46] J., Marek. (n.d.). Choosing Between Electromechanical and Fluid Power Linear Actuators in Industrial Systems Design. Manuscript, Thomson Industries, Inc..
- [47] Precision Linear Actuators [PDF]. (n.d.). Thomson Inc.
- [48] Gillespie, T. D., 1992. *Fundamentals of Vehicle Dynamics*. Society of Automotive Engineers.
- [49] Tmoney Commercial Brochure. (n.d.). Retrieved from [http://www.timoneygroup.com/Libraries/Brochures/Downloads/Timoney Commercial Brochure.sflb.ashx](http://www.timoneygroup.com/Libraries/Brochures/Downloads/Timoney%20Commercial%20Brochure.sflb.ashx)
- [50] Mechanical vibration – Road surface profiles – Reporting of measured data(2018, April 10). Retrieved from <https://www.iso.org/standard/71202.html>
- [51] International Organization for Standardization. (1997). *Mechanical vibration and shock – Evaluation of human exposure to whole-body vibration (Standard No. 2631)*. Retrieved from <https://www.iso.org/standard/7612.html>

- [52] US Army ride dynamics and evaluation of human exposure to whole body vibration procedure. (n.d.). Retrieved from <http://www.dtic.mil/dtic/tr/fulltext/u2/a559451.pdf>
- [53] Gabasa, H.M.L., 2009. LQR controller tuning by using particle swarm optimization, Master of Engineering (Electrical – Mechatronics and Automation Control), Faculty of Electrical Engineering, Universiti Teknologi Malaysia, Malaysia.
- [54] Goodall, R. M., Kortüm, W. (1983). Active Controls in Ground Transportation A Review of the State-of-the-Art and Future Potential. *Vehicle System Dynamics*, 12(4-5), 225-257. doi:10.1080/00423118308968755
- [55] A.G. Thompson, "Design of active suspensions", *Proc. Instn. Mech. Engrs.*, 185:553-563, 1970-1971.
- [56] Rao, K. D. (2014). Modeling, Simulation and Control of Semi Active Suspension System for Automobiles under MATLAB Simulink using PID Controller. *IFAC Proceedings Volumes*, 47(1), 827-831. doi:10.3182/20140313-3-in-3024.00094
- [57] Lin, J., Kanellakopoulos, I. (1996). Adaptive Nonlinear Control in Active Suspensions. *IFAC Proceedings Volumes*, 29(1), 2738-2743. doi:10.1016/s1474-6670(17)58090-8 Finland; 2004
- [58] Robert L.W. Kent L.L. (1997). *Modeling and Simulation of Dynamic System?*, Second Edition, Prentice-Hall Website, "<http://www.sice.jp/english/>"
- [59] Baran, J. (2016). Disturbance observer based control of active suspension system with uncertain parameters. *Przełąd Elektrotechniczny*, 1(12), 196-199. doi:10.15199/48.2016.12.50
- [60] M.M.M. Salam and Ayman A. Aly, "Fuzzy control of a quarter-car suspension system", *International Conference in Mechanical Engineering, ICME*, pp. 258-263, Tokyo, Japan, May 27-29, 2009.
- [61] Xie, X. (2002). Absorbed power as a measure of whole body vehicular vibration exposure (Unpublished master's thesis).

APPENDIX A

DRONE PART

Write your Appendix content here.

A.1 Motor Technical Specifications

Table A.1: Test Report Table for the Chosen Motor MN701s KV280

Throttle%	Voltage (V)	Current (A)	Input Power (W)	RPM	Torque(N.m)	Thrust(g)	Efficiency (g/W)
40	23.55	8.7	204.89	2161	0.66	2189	10.68
42	23.5	9.8	230.3	2236	0.73	2351	10.21
44	23.46	11.1	260.41	2336	0.81	2603	10
46	23.41	12.4	290.28	2433	0.88	2854	9.83
48	23.33	14	326.62	2536	0.97	3100	9.49
50	23.27	15.9	369.99	2642	1.03	3376	9.12
52	23.21	17.6	408.5	2757	1.09	3675	9
54	23.13	19.5	451.04	2835	1.16	3879	8.6
56	23.05	21.4	493.27	2923	1.24	4144	8.4
58	22.97	23.8	546.69	3024	1.3	4441	8.12
60	22.9	25.3	579.37	3089	1.37	4612	7.96
62	22.81	27.7	631.84	3164	1.44	4831	7.65
64	22.72	30.4	690.69	3265	1.51	5180	7.5
66	22.65	32	724.8	3322	1.58	5355	7.39
68	22.58	34.1	769.98	3391	1.64	5555	7.21
70	22.5	36.3	816.75	3457	1.74	5782	7.08
75	22.24	43	956.32	3634	1.92	6390	6.68
80	22.05	48.8	1076.04	3773	2.08	6860	6.38
90	21.58	63.7	1374.65	4076	2.4	8005	5.82
100	21.11	80.6	1701.47	4333	2.66	9040	5.31

A.2 Quadrotor Inertia Calculations

Moment of Inertia:

Inertia about each axis for only the motor:

$$J_{x_{motor}} = M_{motor} * R_{motor}^2 + \frac{4}{3} * M_{motor} * H_{motor}^2 + 2 * M_{motor} * X_{motor2cg}^2 \quad (A.1)$$

$$J_{y_{motor}} = M_{motor} * R_{motor}^2 + \frac{4}{3} * M_{motor} * H_{motor}^2 + 2 * M_{motor} * X_{motor2cg}^2 \quad (A.2)$$

$$J_{z_{motor}} = 2 * M_{motor} * R_{motor}^2 + 4 * M_{motor} * X_{motor2cg}^2 \quad (A.3)$$

Inertia about each axis for for only the ESCs:

$$J_{x_{ESC}} = \frac{M_{ESC} * W_{ESC}^2}{6} + \frac{M_{ESC} * L_{ESC}^2}{6} + 2 * M_{ESC} * X_{ESC2cg} \quad (A.4)$$

$$J_{y_{ESC}} = \frac{M_{ESC} * W_{ESC}^2}{6} + \frac{M_{ESC} * L_{ESC}^2}{6} + 2 * M_{ESC} * X_{ESC2cg} \quad (A.5)$$

$$J_{z_{ESC}} = \frac{M_{ESC} * (W_{ESC}^2 + L_{ESC}^2)}{3} + 4 * M_{ESC} * X_{ESC2cg}^2 \quad (A.6)$$

Inertia about each axis for only the hub:

$$J_{x_{Hub}} = \frac{1}{4} * M_{Hub} * R_{Hub}^2 + \frac{1}{12} * M_{Hub} * H_{Hub}^2 \quad (A.7)$$

$$J_{y_{Hub}} = \frac{1}{4} * M_{Hub} * R_{Hub}^2 + \frac{1}{12} * M_{Hub} * H_{Hub}^2 \quad (A.8)$$

$$J_{z_{Hub}} = \frac{1}{2} * M_{Hub} * R_{Hub}^2 \quad (A.9)$$

Inertia about each axis for only arms:

$$J_{x_{ARM}} = \frac{3}{2} * M_{arm} * R_{arm}^2 + \frac{2}{3} * M_{arm} * L_{arm}^2 + 2 * M_{arm} * X_{arm2cg} \quad (A.10)$$

$$J_{y_{ARM}} = \frac{3}{2} * M_{arm} * R_{arm}^2 + \frac{2}{3} * M_{arm} * L_{arm}^2 + 2 * M_{arm} * X_{arm2cg} \quad (A.11)$$

$$J_{z_{ARM}} = M_{arm} * R_{arm}^2 + \frac{4}{3} * M_{arm} * L_{arm}^2 + 4 * M_{arm} * X_{arm2cg} \quad (A.12)$$

Total inertia about each axis:

$$\begin{aligned} J_{x_{TOTAL}} &= J_{x_{motor}} + J_{x_{ESC}} + J_{x_{Hub}} + J_{x_{arm}} \\ J_{x_{TOTAL}} &= 0.1806 + 0.0015 + 0.0592 + 0.0191 \\ J_{x_{TOTAL}} &= 0.2604kg/m^2 \end{aligned} \quad (A.13)$$

$$\begin{aligned} J_{y_{TOTAL}} &= J_{y_{motor}} + J_{y_{ESC}} + J_{y_{Hub}} + J_{y_{arm}} \\ J_{y_{TOTAL}} &= 0.1806 + 0.0015 + 0.0592 + 0.0191 \\ J_{y_{TOTAL}} &= 0.2604kg/m^2 \end{aligned} \quad (A.14)$$

$$\begin{aligned} J_{z_{TOTAL}} &= J_{z_{motor}} + J_{z_{ESC}} + J_{z_{Hub}} + J_{z_{arm}} \\ J_{z_{TOTAL}} &= 0.3594 + 0.0031 + 0.0887 + 0.0380 \\ J_{z_{TOTAL}} &= 0.4892kg/m^2 \end{aligned} \quad (A.15)$$

Finally:

$$\begin{aligned} J^{body} &= \begin{bmatrix} J_{x_{TOTAL}} & 0 & 0 \\ 0 & J_{y_{TOTAL}} & 0 \\ 0 & 0 & J_{z_{TOTAL}} \end{bmatrix} \\ &= \begin{bmatrix} 0.2604kg/m^2 & 0 & 0 \\ 0 & 0.2604kg/m^2 & 0 \\ 0 & 0 & 0.4892kg/m^2 \end{bmatrix} \end{aligned} \quad (A.16)$$

J^{body} is the total inertia matrix of the quadrotor system.

Motor rotation inertia for the rotating components (J_m) is expressed in the next equation. In this equation, it is assumed that the mass of rotating components is 50 percent of the total mass of the motor and propeller systems.

$$J_m = \frac{1}{2} \left(\left(\frac{1}{2} M_{motor} \right) R_{motor}^2 \right) \quad (\text{A.17})$$

$$J_m = 6.8183 * 10^{-4} \text{kg/m}^2$$

where M_{motor} , M_{ESC} , M_{Hub} and M_{arm} are the masses of the motor, ESC, hub and arm respectively. L_{motor} , L_{ESC} , L_{Hub} and L_{arm} are the lengths of the motor, ESC, hub and arm respectively. R_{motor} , R_{Hub} and L_{arm} are the radius of the motor, hub and arm respectively. H_{motor} and H_{Hub} are the heights of the motor and hub respectively. Finally, $X_{motor2cg}$, X_{ESC2cg} and X_{arm2cg} are the distances between the motor, ESC, arm and the center of gravity of the quadrotor respectively.

APPENDIX B

VEHICLE PART

B.1 Actuator Comparison

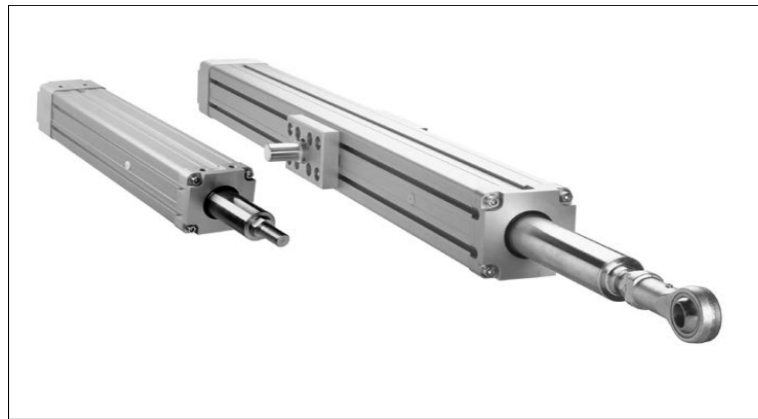


Figure B.1: T Series Actuator

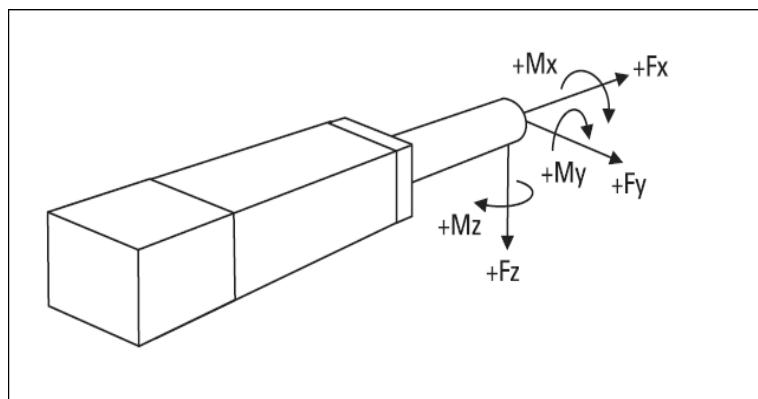


Figure B.2: Definition of Forces

Table B.1: Actuator Comparison Table [47]

Electrical Actuators vs. Hydraulic Actuators and Pneumatic Actuators			
	Electrical Linear Actuators	Hydraulic Actuators	Pneumatic Actuators
Installation	All electric operation requires simple wiring.	Requires expensive plumbing, filtering, pumps, etc.	Requires expensive plumbing, filtering, pumps, etc.
Accuracy	Very repeatable (to $\pm 0,013$ mm) and rigid, multi-stop capabilities.	Requires expensive position sensing and precise electrohydraulic valving to implement. Has tendency to creep.	Difficult to achieve. Requires expensive position sensing and precise valving to implement. Has tendency to creep.
Control	Directly compatible with standard programmable controls, allowing easy, automatic operation of complex motion sequences.	Requires electronic/fluid interfaces and exotic valve designs. Hysteresis, dead zone, supply pressure and temperature changes complicate control.	Inherently non-linear, compressible power source severely complicates servo control.
Speed	Smooth, variable speed from 0 to 2 m/s with controlled acceleration.	Difficult to control accurately. Varies with temperature and wear. Stick slip can be a problem.	More susceptible to stick slip and varying load. Well-suited for light, high-speed applications.

Table B.1 continued from previous page

Electrical Actuators vs. Hydraulic Actuators and Pneumatic Actuators	
Reliability	<p>Repeatable, reproducible performance during the entire product life. Very little maintenance required</p> <p>Up to 60 000 N</p> <p>Up to millions of cycles at rated load. Easy to predict.</p> <p>Moderate initial cost, very low operating cost.</p> <p>Standard models rated for -30 to +70 °C. Inherently clean and energy efficient.</p>
Force	<p>Very contamination sensitive. Air sources require proper filtration. Good reliability, but usually many system components are involved</p> <p>Up to 25 000 N. Typically used below 6000 N.</p>
Life Expectancy	<p>Very contamination sensitive. Require regular maintenance. Seals are prone to leak. Reliable with diligent maintenance</p> <p>Virtually unlimited force. Most powerful.</p> <p>Dependent on design and seal wear, usually good.</p> <p>Components often cost less, but installation and maintenance are increased. Hydraulic power unit cost is high if not pre-existing.</p> <p>Temperature extremes can be a major problem. Seals are prone to leak. Waste disposal is increasingly problematic.</p>
Cost	<p>Dependent on design and seal wear, usually good.</p> <p>Components often cost less, but installation and maintenance are increased.</p> <p>Temperature extremes can be a major problem. Seals prone to leak. Air borne oil can be a problem.</p>

Table B.1 continued from previous page

Electrical Actuators vs. Hydraulic Actuators and Pneumatic Actuators		
Load holding	Acme screw units are self-locking if power fails. Fail-safe brakes available for ball screw models.	Complex back up safety devices must be used.
		Complex back up safety devices must be used.

B.2 A Matrix

$$A_{(:,1)} = \left\{ \begin{array}{c} 0 \\ 0 \\ 0 \\ 0 \\ 0 \\ 0 \\ 0 \\ 0 \\ 0 \\ 0 \\ 0 \\ -\frac{kf_1T_f^2}{l_r} - \frac{kf_2T_f^2}{l_r} - \frac{kf_{11}T_f^2}{l_r} - \frac{kf_{22}T_f^2}{l_r} - \frac{kf_{33}T_r^2}{l_r} - \frac{kf_{44}T_r^2}{l_r} - \frac{kf_3T_r^2}{l_r} - \frac{kf_4T_r^2}{l_r} \\ -\frac{kf_1T_f a}{l_p} + \frac{kf_2T_f a}{l_p} - \frac{kf_{33}T_f d}{l_p} + \frac{kf_{44}T_f d}{l_p} + \frac{kf_{33}T_p e}{l_p} - \frac{kf_{44}T_r e}{l_p} + \frac{kf_3T_r b}{l_p} - \frac{kf_4T_r b}{l_p} \\ -\frac{kf_1T_f}{m_s} + \frac{kf_2T_f}{m_s} - \frac{kf_{33}T_f}{m_s} + \frac{kf_{44}T_f}{m_s} - \frac{kf_{33}T_p}{m_s} + \frac{kf_{44}T_r}{m_s} - \frac{kf_3T_r}{m_s} + \frac{kf_4T_r}{m_s} \\ \frac{kf_1T_f}{muf_1} \\ -\frac{kf_2T_f}{muf_2} \\ \frac{kf_{11}T_f}{muf_{11}} \\ -\frac{kf_{22}T_f}{muf_{22}} \\ \frac{kf_{33}T_r}{muf_{33}} \\ -\frac{kf_{44}T_r}{muf_{44}} \\ \frac{kf_3T_r}{muf_3} \\ -\frac{kf_4T_r}{muf_4} \end{array} \right. \quad (\text{B.1})$$

$$A_{(:,4:7)} = \left\{ \begin{array}{cccc}
0 & 0 & 0 & 0 \\
0 & 0 & 0 & 0 \\
0 & 0 & 0 & 0 \\
0 & 0 & 0 & 0 \\
0 & 0 & 0 & 0 \\
0 & 0 & 0 & 0 \\
0 & 0 & 0 & 0 \\
0 & 0 & 0 & 0 \\
0 & 0 & 0 & 0 \\
0 & 0 & 0 & 0 \\
\frac{kf_1 T_f}{l_r} & -\frac{kf_2 T_f}{l_r} & \frac{kf_{11} T_f}{l_r} & -\frac{kf_{22} T_f}{l_r} \\
\frac{kf_1 a}{l_p} & \frac{kf_2 a}{l_p} & \frac{kf_{11} d}{l_p} & \frac{kf_{22} d}{l_p} \\
\frac{kf_1}{m_s} & \frac{kf_2}{m_s} & \frac{kf_{11}}{m_s} & \frac{kf_{22}}{m_s} \\
-\frac{kf_1}{\mu f_1} - \frac{kf_1}{\mu f_1} & 0 & 0 & 0 \\
0 & -\frac{kf_2}{\mu f_2} - \frac{kf_2}{\mu f_2} & 0 & 0 \\
0 & 0 & -\frac{kf_{11}}{\mu f_{11}} - \frac{kf_{11}}{\mu f_{11}} & 0 \\
0 & 0 & 0 & -\frac{kf_{22}}{\mu f_{22}} - \frac{kf_{22}}{\mu f_{22}} \\
0 & 0 & 0 & 0 \\
0 & 0 & 0 & 0 \\
0 & 0 & 0 & 0 \\
0 & 0 & 0 & 0
\end{array} \right\} \quad (\text{B.4})$$

$$A_{(:,8:11)} = \left(\begin{array}{cccc}
0 & 0 & 0 & 0 \\
0 & 0 & 0 & 0 \\
0 & 0 & 0 & 0 \\
0 & 0 & 0 & 0 \\
0 & 0 & 0 & 0 \\
0 & 0 & 0 & 0 \\
0 & 0 & 0 & 0 \\
0 & 0 & 0 & 0 \\
0 & 0 & 0 & 0 \\
0 & 0 & 0 & 0 \\
\frac{kf_{33}T_r}{l_r} & -\frac{kf_{44}T_r}{l_r} & \frac{kf_3T_r}{l_r} & -\frac{kf_4T_r}{l_r} \\
-\frac{kf_{33}e}{l_p} & -\frac{kf_{44}e}{l_p} & -\frac{kf_3b}{l_p} & -\frac{kf_4b}{l_p} \\
\frac{kf_{33}}{m_s} & \frac{kf_{44}}{m_s} & \frac{kf_3}{m_s} & \frac{kf_4}{m_s} \\
0 & 0 & 0 & 0 \\
0 & 0 & 0 & 0 \\
0 & 0 & 0 & 0 \\
0 & 0 & 0 & 0 \\
-\frac{kf_{33}}{\mu f_{33}} - \frac{ktf_{33}}{\mu f_{33}} & 0 & 0 & 0 \\
0 & -\frac{kf_{44}}{\mu f_{44}} - \frac{ktf_{44}}{\mu f_{44}} & 0 & 0 \\
0 & 0 & -\frac{kf_3}{\mu f_3} - \frac{ktf_3}{\mu f_3} & 0 \\
0 & 0 & 0 & -\frac{kf_4}{\mu f_4} - \frac{ktf_4}{\mu f_4}
\end{array} \right) \quad (\text{B.5})$$

$$A_{(:,12)} = \left\{ \begin{array}{c} 1 \\ 0 \\ 0 \\ 0 \\ 0 \\ 0 \\ 0 \\ 0 \\ 0 \\ 0 \\ 0 \\ -\frac{bf_1T_f^2}{l_r} - \frac{bf_2T_f^2}{l_r} - \frac{bf_{11}T_f^2}{l_r} - \frac{bf_{22}T_f^2}{l_r} - \frac{bf_{33}T_r^2}{l_r} - \frac{bf_{44}T_r^2}{l_r} - \frac{bf_3T_r^2}{l_r} - \frac{bf_4T_r^2}{l_r} \\ -\frac{bf_1T_f a}{l_p} + \frac{bf_2T_f a}{l_p} - \frac{bf_{33}T_f d}{l_p} + \frac{bf_{44}T_f d}{l_p} + \frac{bf_{33}T_p e}{l_p} - \frac{bf_{44}T_r e}{l_p} + \frac{bf_3T_r b}{l_p} - \frac{bf_4T_r b}{l_p} \\ -\frac{bf_1T_f}{m_s} + \frac{bf_2T_f}{m_s} - \frac{bf_{33}T_f}{m_s} + \frac{bf_{44}T_f}{m_s} - \frac{bf_{33}T_p}{m_s} + \frac{bf_{44}T_r}{m_s} - \frac{bf_3T_r}{m_s} + \frac{bf_4T_r}{m_s} \\ \frac{bf_1T_f}{\mu f_1} \\ -\frac{bf_2T_f}{\mu f_2} \\ \frac{bf_{11}T_f}{\mu f_{11}} \\ -\frac{bf_{22}T_f}{\mu f_{22}} \\ \frac{bf_{33}T_r}{\mu f_{33}} \\ -\frac{bf_{44}T_r}{\mu f_{44}} \\ \frac{bf_3T_r}{\mu f_3} \\ -\frac{bf_4T_r}{\mu f_4} \end{array} \right\} \quad (\text{B.6})$$

$$A_{(:,13)} = \left\{ \begin{array}{c} 0 \\ 1 \\ 0 \\ 0 \\ 0 \\ 0 \\ 0 \\ 0 \\ 0 \\ 0 \\ 0 \\ -\frac{bf_1T_f a}{l_r} + \frac{bf_2T_f a}{l_r} - \frac{bf_{11}T_f d}{l_r} + \frac{bf_{22}T_f d}{l_r} + \frac{bf_{33}T_r e}{l_r} - \frac{bf_{44}T_r e}{l_r} + \frac{bf_3T_r b}{l_r} - \frac{bf_4T_r b}{l_r} \\ -\frac{bf_1a^2}{l_p} - \frac{bf_2a^2}{l_p} - \frac{bf_{33}d^2}{l_p} - \frac{bf_{44}d^2}{l_p} - \frac{bf_{33}e^2}{l_p} - \frac{bf_{44}e^2}{l_p} - \frac{bf_3b^2}{l_p} - \frac{bf_4b^2}{l_p} \\ -\frac{bf_1a}{m_s} - \frac{bf_2a}{m_s} - \frac{bf_{33}d}{m_s} - \frac{bf_{44}d}{m_s} + \frac{bf_{33}e}{m_s} + \frac{bf_{44}e}{m_s} + \frac{bf_3b}{m_s} + \frac{bf_4b}{m_s} \\ \frac{bf_1a}{muf_1} \\ \frac{bf_2a}{muf_2} \\ \frac{bf_{11}d}{muf_{11}} \\ \frac{bf_{22}d}{muf_{22}} \\ -\frac{bf_{33}e}{muf_{33}} \\ -\frac{bf_{44}e}{muf_{44}} \\ -\frac{bf_3b}{muf_3} \\ -\frac{bf_4b}{muf_4} \end{array} \right\} \quad (\text{B.7})$$

$$A_{(:,14)} = \left\{ \begin{array}{c} 0 \\ 0 \\ 1 \\ 0 \\ 0 \\ 0 \\ 0 \\ 0 \\ 0 \\ 0 \\ 0 \\ -\frac{bf_1T_f}{l_r} + \frac{bf_2T_f}{l_r} - \frac{bf_{11}T_f}{l_r} + \frac{bf_{22}T_f}{l_r} - \frac{bf_{33}T_r}{l_r} + \frac{bf_{44}T_r}{l_r} - \frac{bf_3T_r}{l_r} + \frac{bf_4T_r}{l_r} \\ -\frac{bf_1a}{l_p} - \frac{bf_2a}{l_p} - \frac{bf_{33}d}{l_p} - \frac{bf_{44}d}{l_p} + \frac{bf_{33}e}{l_p} + \frac{bf_{44}e}{l_p} + \frac{bf_3b}{l_p} + \frac{bf_4b}{l_p} \\ -\frac{bf_1}{m_s} - \frac{bf_2}{m_s} - \frac{bf_{33}}{m_s} - \frac{bf_{44}}{m_s} - \frac{bf_{33}}{m_s} - \frac{bf_{44}}{m_s} - \frac{bf_3}{m_s} - \frac{bf_4}{m_s} \\ \frac{bf_1}{muf_1} \\ \frac{bf_2}{muf_2} \\ \frac{bf_{11}}{muf_{11}} \\ \frac{bf_{22}}{muf_{22}} \\ \frac{bf_{33}}{muf_{33}} \\ \frac{bf_{44}}{muf_{44}} \\ \frac{bf_3}{muf_3} \\ \frac{bf_4}{muf_4} \end{array} \right\} \quad (\text{B.8})$$

$$A_{(:,15:22)} = \left(\begin{array}{cccccccc}
0 & 0 & 0 & 0 & 0 & 0 & 0 & 0 \\
0 & 0 & 0 & 0 & 0 & 0 & 0 & 0 \\
0 & 0 & 0 & 0 & 0 & 0 & 0 & 0 \\
1 & 0 & 0 & 0 & 0 & 0 & 0 & 0 \\
0 & 1 & 0 & 0 & 0 & 0 & 0 & 0 \\
0 & 0 & 1 & 0 & 0 & 0 & 0 & 0 \\
0 & 0 & 0 & 1 & 0 & 0 & 0 & 0 \\
0 & 0 & 0 & 0 & 1 & 0 & 0 & 0 \\
0 & 0 & 0 & 0 & 0 & 1 & 0 & 0 \\
0 & 0 & 0 & 0 & 0 & 0 & 1 & 0 \\
0 & 0 & 0 & 0 & 0 & 0 & 0 & 1 \\
\frac{bf_1 T_f}{l_r} & -\frac{bf_2 T_f}{l_r} & \frac{bf_{11} T_f}{l_r} & -\frac{bf_{22} T_f}{l_r} & \frac{bf_{33} T_r}{l_r} & -\frac{bf_{44} T_r}{l_r} & \frac{bf_3 T_r}{l_r} & -\frac{bf_4 T_r}{l_r} \\
\frac{bf_1 a}{l_p} & \frac{bf_2 a}{l_p} & \frac{bf_{11} d}{l_p} & \frac{bf_{22} d}{l_p} & \frac{bf_{33} e}{l_p} & \frac{bf_{33} e}{l_p} & \frac{bf_{44} b}{l_p} & \frac{bf_{44} b}{l_p} \\
\frac{bf_1}{m_s} & \frac{bf_2}{m_s} & \frac{bf_{11}}{m_s} & \frac{bf_{22}}{m_s} & \frac{bf_{33}}{m_s} & \frac{bf_{44}}{m_s} & \frac{bf_3}{m_s} & \frac{bf_4}{m_s} \\
-\frac{bf_1}{\mu f_1} & 0 & 0 & 0 & 0 & 0 & 0 & 0 \\
0 & -\frac{bf_2}{\mu f_2} & 0 & 0 & 0 & 0 & 0 & 0 \\
0 & 0 & -\frac{bf_{11}}{\mu f_{11}} & 0 & 0 & 0 & 0 & 0 \\
0 & 0 & 0 & -\frac{bf_{22}}{\mu f_{22}} & 0 & 0 & 0 & 0 \\
0 & 0 & 0 & 0 & -\frac{bf_{33}}{\mu f_{33}} & 0 & 0 & 0 \\
0 & 0 & 0 & 0 & 0 & -\frac{bf_{44}}{\mu f_{44}} & 0 & 0 \\
0 & 0 & 0 & 0 & 0 & 0 & -\frac{bf_3}{\mu f_3} & 0 \\
0 & 0 & 0 & 0 & 0 & 0 & 0 & -\frac{bf_3}{\mu f_3}
\end{array} \right) \quad (\text{B.9})$$

$$B_{1(:, :)} = \begin{bmatrix}
0 & 0 & 0 & 0 & 0 & 0 & 0 & 0 \\
0 & 0 & 0 & 0 & 0 & 0 & 0 & 0 \\
0 & 0 & 0 & 0 & 0 & 0 & 0 & 0 \\
0 & 0 & 0 & 0 & 0 & 0 & 0 & 0 \\
0 & 0 & 0 & 0 & 0 & 0 & 0 & 0 \\
0 & 0 & 0 & 0 & 0 & 0 & 0 & 0 \\
0 & 0 & 0 & 0 & 0 & 0 & 0 & 0 \\
0 & 0 & 0 & 0 & 0 & 0 & 0 & 0 \\
0 & 0 & 0 & 0 & 0 & 0 & 0 & 0 \\
0 & 0 & 0 & 0 & 0 & 0 & 0 & 0 \\
\frac{T_f}{l_r} & -\frac{T_f}{l_r} & \frac{T_f}{l_r} & -\frac{T_f}{l_r} & \frac{T_r}{l_r} & -\frac{T_r}{l_r} & \frac{T_r}{l_r} & -\frac{T_r}{l_r} \\
\frac{a}{l_p} & \frac{a}{l_p} & \frac{d}{l_p} & \frac{d}{l_p} & -\frac{e}{l_p} & -\frac{e}{l_p} & -\frac{b}{l_p} & -\frac{b}{l_p} \\
\frac{1}{m_s} & \frac{1}{m_s} & \frac{1}{m_s} & \frac{1}{m_s} & \frac{1}{m_s} & \frac{1}{m_s} & \frac{1}{m_s} & \frac{1}{m_s} \\
-\frac{1}{\mu f_1} & 0 & 0 & 0 & 0 & 0 & 0 & 0 \\
0 & -\frac{1}{\mu f_2} & 0 & 0 & 0 & 0 & 0 & 0 \\
0 & 0 & -\frac{1}{\mu f_{11}} & 0 & 0 & 0 & 0 & 0 \\
0 & 0 & 0 & -\frac{1}{\mu f_{22}} & 0 & 0 & 0 & 0 \\
0 & 0 & 0 & 0 & -\frac{1}{\mu f_{33}} & 0 & 0 & 0 \\
0 & 0 & 0 & 0 & 0 & -\frac{1}{\mu f_{44}} & 0 & 0 \\
0 & 0 & 0 & 0 & 0 & 0 & -\frac{1}{\mu f_3} & 0 \\
0 & 0 & 0 & 0 & 0 & 0 & 0 & -\frac{1}{\mu f_4}
\end{bmatrix} \tag{B.10}$$